

Uncovering the Formation of Galaxies Using Their Stellar Populations

By

Thomas Davison

A THESIS SUBMITTED IN PARTIAL FULFILMENT
OF THE REQUIREMENTS FOR THE DEGREE OF
DOCTOR OF PHILOSOPHY

Jeremiah Horrocks Institute for Maths, Physics and Astronomy
University of Central Lancashire

November 2021

Declaration

Award: Doctor of Philosophy

School: School of Natural Sciences

Concurrent registration for two or more academic awards

I declare that while registered as a candidate for the research degree, I have not been a registered candidate or enrolled student for another award of the University or other academic or professional institution.

Material submitted for another award

I declare that no material contained in the thesis has been used in any other submission for an academic award and is solely my own work.

No proof-reading service was used in the compilation of this thesis.

A handwritten signature in black ink, appearing to read 'Davison', with a long, sweeping horizontal stroke above it.

Thomas Davison

Abstract

The following thesis explores the stellar populations of Early Type galaxies, and in doing so develops a viable method by which to identify ex-situ stars in both spatially resolved and unresolved galaxies. Using simulated data from the EAGLE simulations, this thesis first lays a theoretical groundwork for the subsequent chapters by building predictions of ex-situ fraction in galaxies according to galaxy mass and size, as well as more readily observable properties such as surface brightness. Following this, the focus shifts to observational datasets of galaxies. The basics of a methodology with which to extract ex-situ fractions of galaxies is tested on MUSE data of NGC 7135, finding increases in ex-situ fraction with radius, in line with predictions from the EAGLE simulations. This methodology is improved upon and expanded in order to map the ex-situ populations present within 13 galaxies observed with MUSE. These are shown to display an increase in ex-situ fraction with mass and radius, with high gradients of increase in ex-situ material for the most massive and most extended galaxies. A similar methodology is finally applied to a large statistically representative sample of spatially unresolved galaxies from the SDSS survey. This provides a lower galactocentric resolution view of the mass size plane but with a vastly improved sample size. With this study it is demonstrated that the smaller MUSE sample is a representative sample of galaxies and accurately demonstrates changes in ex-situ fraction with average galaxy mass and size. The results found in the chapters point to evidence of the ‘two-phase’ scenario of galaxy formation, and present means to explore this further observationally.

Contents

Declaration	ii
Abstract	iii
1 Introduction	1
1.1 The Early Universe	1
1.2 Early Type Galaxies	4
1.2.1 History of Observation	4
1.2.2 Classification and Kinematics	6
1.3 Galaxy Accretion	10
1.4 Spectral Analysis	16
1.4.1 Stellar Models	21
1.5 Galaxy Simulation	25
1.5.1 Simulation Techniques	26
1.5.2 EAGLE	30
1.5.3 Simulated Mergers	31
1.6 Galaxy Observation	32
2 Accreted Stars in the EAGLE Simulations	36
2.1 Remarks	36
2.2 Chapter Abstract	36

2.3	Chapter Introduction	37
2.4	Methodology	40
2.4.1	Simulations Overview	40
2.4.2	In/Ex-Situ Classification	41
2.4.3	Galaxy Properties and Classification	43
2.4.4	The EAGLE Galaxy Sample	45
2.4.5	Summary of Other Quantities	47
2.5	Results	50
2.5.1	Ex-situ Fraction as a Function of Galaxy Properties	50
2.5.1.1	Ex-situ Fraction as a Function of Galaxy Mass	50
2.5.1.2	Ex-Situ Fractions across the Mass-Size Plane	54
2.5.1.3	Ex-situ Fraction as a Function of Parent Halo Mass	58
2.5.2	Ex-situ Fraction across Galaxies' bodies	61
2.5.2.1	Ex-situ Fraction as a Function of Radius	61
2.5.2.2	Ex-situ Fraction as a Function of Surface Brightness	61
2.6	Discussion	68
2.7	Conclusions	73
3	NGC 7135, A Case Study	75
3.1	Remarks	75
3.2	Chapter Abstract	75
3.3	Chapter Introduction	76
3.4	Observations and data reduction	78
3.5	Methodology	79
3.6	Results	81
3.6.1	Stellar Properties	83
3.6.2	Gas Properties	85
3.6.3	Stellar Population Mapping	91

3.6.4	Accreted Populations	98
3.7	Discussion	102
3.8	Conclusions	106
4	Observing Ex-situ Populations Across the Mass-Size Plane with MUSE	108
4.1	Remarks	108
4.2	Chapter Abstract	108
4.3	Chapter Introduction	109
4.4	Methodology	116
4.4.1	Observations and Analysis	117
4.4.1.1	Voronoi Binning	118
4.4.1.2	Elliptical Binning	119
4.4.1.3	Full Spectral Fitting	120
4.4.2	Ex-Situ Fraction Estimation	122
4.4.2.1	Mass dependent SFH and chemical evolution	124
4.4.2.2	Model mass fractions and uncertainties	126
4.5	Results	127
4.6	Discussion	133
4.7	Conclusion	144
5	Probing the Mass-Size Plane with SDSS	145
5.1	Chapter Abstract	145
5.2	Chapter Introduction	146
5.3	Methodology	147
5.3.1	Sample and Reduction	147
5.3.2	Full-Spectral Fitting	152
5.3.3	Ex-situ Fraction Estimation	155

5.4	Results	157
5.5	Discussion and Conclusions	161
6	Thesis Overview and Discussion	167
6.1	Discussion	167
6.2	Conclusions	178
A	Appendix of Chapter 2	180
A.1	Confirmation of Host Halo Properties	181
A.2	Tabulated Values	186
B	Appendix of Chapter 3	198
C	Appendix of Chapter 4	200
C.1	Galaxy Sample - Interesting Cases and Points of Note	201
C.1.1	IC1459	201
C.1.2	NGC1316	201
C.1.3	NGC1404	204
C.1.4	NGC2992	204
C.1.5	NGC4594	204
C.1.6	NGC4696	205
C.1.7	NGC5846	205
C.2	Verification of Metallicity Effects	207
C.2.1	Eagle Simulation Verification	207
C.2.2	Adaptive Metallicity Gradient Modelling	208
C.3	Galaxy Full Plots	213
	Acknowledgements	227

Chapter 1

Introduction

1.1 The Early Universe

Galaxies are some of the most immense and beautiful objects in the Universe, and yet they grew from unimaginably small quantum fluctuations in space. Immediately after the Big Bang, and during the first picoseconds of the Universe, small quantum fluctuations rendered the material of the universe inhomogeneous and anisotropic on all but the largest scales. These seeds of ever-so-slight differences in space became fluctuations in the density of primordial material. Over-densities were able to collapse due to gravitational dominance, forming the first galaxies. These areas continued to collapse and to collect baryonic matter, forming the large-scale structure of the universe.

Such structure has been revealed by galaxy redshift surveys such as the 2dF Galaxy Redshift Survey (Colless et al. 2003) and the Sloan Digital Sky Survey (SDSS) (York et al. 2000), which have built maps of vast areas of the observable Universe, and have revealed immense structures across the cosmos. These structures were hinted at initially by a gargantuan void discovered in Boötes (Kirshner et al. 1981), and then backed up by further structure discovered during the 1980's (see Rood (1988) for a review of voids and other features discovered before the advent

CHAPTER 1

of large galactic redshift surveys). From the galactic redshift data, filamentary structure quickly became apparent. Evidence for the fluctuations that built these structures can be seen especially well in measurements of the Cosmic Microwave Background Radiation (CMBR) (Ade et al. 2016). This radiation traces structure that was present at the time the Universe became transparent to radiation ($\approx 370,000$ years after the Big Bang, $z=1100$). As matter recombined and became distributed enough to allow radiation to propagate, photons were free to radiate. These same photons are the ones imaged by CMBR surveys, and thus this is considered to be a 'baby picture' of our Universe.

Slight differences in density were exacerbated over time, with dark matter (DM) acting under gravity, collapsing to areas of higher density and decoupling from the expansion of the universe (Hawking & Ellis 1973). Unlike baryonic matter, DM does not interact electromagnetically and as such during the time of matter and radiation equivalence, DM was able to collapse. Baryonic matter being equally as susceptible to gravity was then drawn into these gravitational wells after recombination. Baryonic matter however is able to dissipate energy via radiation, thus allowing it to collapse to much denser scales. After the initial recombination in the early universe there was a long dark period without stars, lasting until ~ 200 or 300 million years after the Big Bang. With the universe now transparent to radiation, gas further cooled, finding it increasingly efficient to coalesce into the vast gravitational wells already organised by collapsing DM, transitioning the universe to matter (rather than radiation) dominated. The first stars (and so we can assume galaxies) formed when the universe was around $400-700$ million years old (Lewis et al. 2016). This would continue with the 'rich becoming richer' due to an increased gravitational well likewise increasing influential range and power of attraction. This baryonic action would become the birthing grounds for the first galaxies.

This star formation continued increasing until approximately ~ 3.5 Gyr after the

CHAPTER 1

Big Bang (Madau & Dickinson 2014). The universal star formation rate (SFR) peaked at 3.5Gyr, or $z \approx 1.9$, and has been declining ever since. This indicates that we have missed the party and are currently within a decreasing SFR period. This is perhaps odd considering observations show there is an abundance of pristine and recycled gas remaining in the interstellar and intergalactic mediums (ISM, IGM) available to be converted to stars.

The widely adopted cold dark matter model of the universe points to a hierarchical assembly of matter. This describes a Universe in which small structure first forms, then coalesces to form larger structures, further increasing the influence of the gravitational well. For baryonic matter however this does not scale perfectly with dark matter density due to the effects of feedback from various sources such as active galactic nuclei (AGN), supernovae and radiation pressure from star formation which can interact with baryons, disrupting movement and preventing an increase in baryonic density. These effects result in galaxies which can have entirely different morphologies depending on the local environment, timescale of gas infall, and galaxy mass.

One suggestion of the hierarchical growth model is that galaxy merger rates are expected to decline as the universe ages, as has been observed (see e.g. Shankar et al. 2015). Extrapolating backwards we expect to see that mergers were more frequent early in the universe, an effect which is exhibited in deep images such as the Hubble ultra deep field, in which a much higher percentage of galaxies appear to be interacting or to be recently disturbed (Beckwith et al. 2006). A further prediction of this is that the stellar populations of Early Type galaxies, which have often been without star formation for billions of years, should consist of vast fractions of ex-situ stars; stars which originated in other galaxies, but have then been ‘cannibalised’ by larger galaxies during galaxy mergers.

1.2 Early Type Galaxies

When Edwin Hubble attempted to classify galaxies morphologically, he did so with his now famous ‘Hubble Tuning Fork’ diagram. In this classification scheme, galaxies were separated into the ‘Early Type Galaxies’ (ETGs) and ‘Late Type Galaxies’ (LTGs). LTGs encompass those galaxies that show beautiful large scale structure, such as spiral arms and bars, whilst ETGs show smooth elliptical isophotes and little or no organised substructure (Hubble 1926). Though modern definitions of ETGs have advanced, the fundamental divisions of galaxy by visual morphology hold.

ETGs are characterised as galaxies that most commonly consist of very old stellar populations compared to spiral galaxies which are more frequently associated with younger stars and active star formation at $z=0$. The stellar populations of Early Types are also kinematically distinct, with velocity dispersion found to be a much more significant method of support in comparison to spirals.

The Early Type classification includes elliptical and S0 type galaxies. Literature largely agrees that many if not most S0 galaxies are spirals which have been starved of gas (Barr et al. 2007; Cortesi et al. 2013). This is supported by Hubble Space Telescope observations revealing that spirals are far more common (by a factor of $\approx 2-3$) in distant clusters than nearby ones. As a general rule, S0 galaxies become much rarer with greater distance (Fasano et al. 2000). The implication of this is a transition over time of spiral types to S0s in which star formation effectively halts. However, at present there is no consensus in the literature as to the cause of the truncation of star formation in spiral galaxies.

1.2.1 History of Observation

The classification of galaxies as ‘late-’ and ‘early-’ types is a well known misnomer. The original classification by Hubble came from his belief that galaxy types represented a smooth transition from the apparently unstructured ellipticals, to the

CHAPTER 1

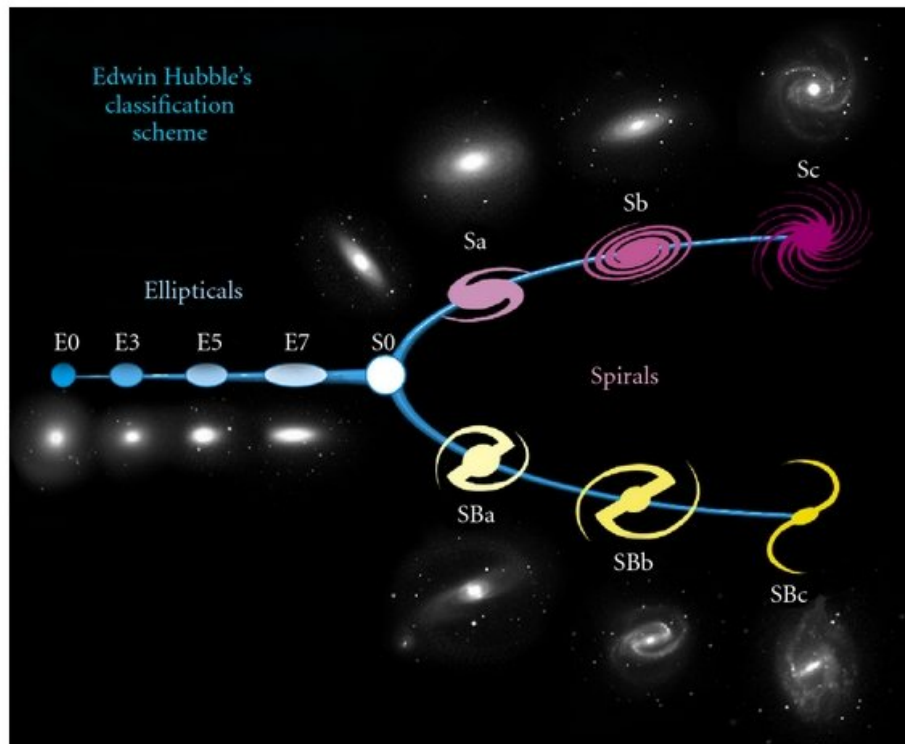


Figure 1.1: A view of the so called 'Hubble Tuning Fork', displaying the basics of galaxy classification as defined in Hubble (1927). Early types are shown on the right of the diagram under the 'Ellipticals' heading. This encompasses the morphological types from E0 to S0. The right hand of the diagram shows two prongs of the tuning fork. These are the Late Types, encompassing spirals, both barred and non-barred. Credit: NASA and ESA

CHAPTER 1

marginally structured S0 type galaxies (these were undiscovered in Hubble’s classification era but were hypothesised by himself), and finally on to the well structured spirals and barred-spirals. Upon viewing this apparent transition between galaxy types, Hubble hypothesised that ETGs evolved throughout their lives, becoming closer to spiral galaxies over time (Hubble 1927).

It is now understood that any temporal hypotheses regarding the Hubble tuning fork are mistaken, as evolution to spirals or elliptical are fundamentally different branches in a possible evolutionary tree, rather than the beginning and end points of the same branch; and though there may be transition between types, this is by no means a linear and irreversible timeline. The Hubble tuning fork was subsequently found to represent an excellent demonstration of the separation of galaxies by rotation, rather than age. The nearly rotationless ellipticals give way to S0 galaxies with embedded rotating disks, and finally to fully coherent rotation found in spirals.

Ideas regarding galaxy rotation emerged slowly in the decades following Hubble with the use of long-slit spectroscopy. This allowed the determination of rotation curves for both spiral and elliptical galaxies alike.

1.2.2 Classification and Kinematics

The light distributions of Early Type Galaxies are frequently described by their Sersic profile (equation 1.1) (Sersic 1968). This function is able to characterise the variation in intensity of a galaxy from the core to some given distance from the centre. The resultant Sersic index ‘n’ that best fits a given galaxy can be tied to important galaxy kinematic parameters such as strength of an embedded disk as well as fundamental characteristics such as total galaxy luminosity. Variations in this profile can be used as diagnostic properties for galaxy formation history such as higher than expected central intensity of a galaxy, a likely result of a ‘wet’ merger event causing a rapid and dense starburst event (Kormendy et al. 2009).

CHAPTER 1

The Sersic equation is represented as follows:

$$I_n(R) = I_e \exp \left\{ -b_n \left[\left(\frac{R}{R_e} \right)^{1/n} - 1 \right] \right\}, \quad (1.1)$$

$$b_n \approx 2n - 0.324 \quad (1.2)$$

where I_e is the intensity of light at the effective radius (R_e), representing the radius at which half the total light of the galaxy is enclosed. The variable b_n is derived from n through the fitting formula shown in equation 1.2 (Ciotti 1991) (or by similar formulae) and is commonly used with a fractional error of less than 0.001 within the expected range for the Sersic index ($1 < n < 10$) (Ciotti & Bertin 1999).

Galaxy colour can also be considered a proxy for morphological type. The colour of a galaxy shifts on average from redder on the ETG side of the Hubble sequence, to bluer on the LTG side. This is highly visible in a colour magnitude diagram of galaxies, akin to the stellar HR diagram, but for galaxies. This shows how galaxies can be largely separated into two groups, namely the ‘Red Sequence’ and the ‘Blue Cloud’, which respectively contain the Early Types and the Late Types.

The dividing area between the two regions is known as the green valley (see Figure 1.2). This area represents a transition between the two galaxy types and is an area of particular ongoing study. Work on specific green valley galaxy examples has highlighted how these objects can represent a change in galaxy star formation patterns. This is demonstrated for example in Thilker et al. (2010) wherein NGC 404 is shown to have had a recent star formation event likely caused by merger-induced rejuvenation. This has pushed the galaxy away from the red sequence and further towards the blue cloud galaxies. Thus the green valley can be seen as a region of galaxies undergoing significant changes, and the transition zone between the red and blue clouds.

The cause of the colour shift along the Hubble sequence is mostly the result of

CHAPTER 1

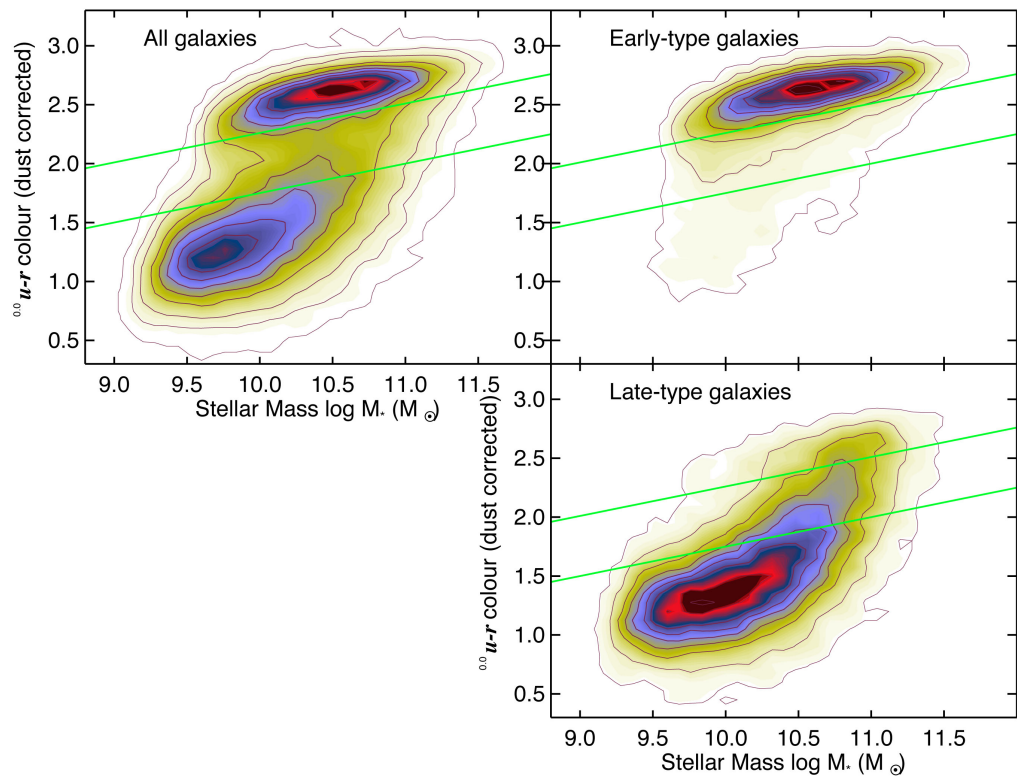


Figure 1.2: View of the galaxy u-r colour-mass diagram of SDSS galaxies from Schawinski et al. (2014). Galaxies of Early or Late Type generally separate into two distinct regions, however a region of ambiguity (shown between two green lines) represents an overlap in these separate galaxy types. Notably, both Early and Late Type galaxies can be found across the entire general galaxy distribution, showing that purely cutting a sample either below or above the green valley is insufficient for limiting to a single galaxy type.

CHAPTER 1

mean stellar age, with metallicity and extinction also affecting the colour. Early types are dominated by old stars with naturally redder colours. This is in contrast to spiral galaxies and other LTGs which consist of a far higher fraction of younger luminous blue stars which outshine the more massively dominant underlying older populations.

A further possible means of division of galaxies is by using specific quantities such as mass and size. These galaxy values are amongst the most important factors, as almost every galaxy quantity can be correlated in some way to mass and/or size. For this reason it can be instructive to view galaxies on a ‘mass-size’ plane. This arranges galaxies two dimensionally with a diagonal increase in galaxy density.

The present day size and mass of a galaxy is highly dependent on the specific galaxy history and assembly. Depending on the rates and longevity of star-formation, which themselves are dictated by abundances and availability of fresh gas, initially similar galaxies can evolve to highly divergent final masses and densities. As such, the final position of a galaxy on the mass-size plane can be used as a means of separating different assembly paths and evolution to the final state. It is for this reason that other quantities are often found embedded in galaxy mass-size correlations. Rate of stellar accretion, chemical abundances and kinematics are all found to have mass-size correlations as a result of assembly history (Li et al. 2018; Rosito et al. 2019).

The assembly history of a galaxy will also leave lasting imprints on galaxy kinematics, with merger history and local environment heavily affecting present day kinematics (Hung et al. 2016; Pelliccia et al. 2019; Nevin et al. 2021). This has been shown very clearly in our own Milky Way with data from GAIA, that has evidenced historical mergers by examining tell-tale signatures of merging in Milky Way stellar kinematics (Mackereth et al. 2019; Wu et al. 2021).

Amongst the most important kinematic components for galactic archaeology are

CHAPTER 1

velocity (V), velocity dispersion (hereafter referred to as σ), and the Gauss-Hermite moments. After accounting for the expansion of the Universe, the velocity component is used to study aspects such as rotation and counter rotation. Disruption in the gas kinematics of galaxies can provide key indications of merger events. One of the most readily identifiable signatures of a past or ongoing galaxy merger is the presence of counter rotating components, with up to 40% of S0 galaxies displaying counter rotation of stars (Rubin 1994; Davis et al. 2011; Coccato et al. 2015; Bassett et al. 2017). The velocity dispersion, or σ , is also a key component in galaxy kinematic studies, playing an especially prominent role in the study of elliptical galaxies. σ measures the dispersion value of stellar velocities represented within a spectrum. As ETGs are primarily supported by stellar dispersion (as opposed to ordered disks) the peak value of σ can be used as a proxy for stellar mass as dictated by the Virial theorem. This value is closely tied to the galaxy dark matter halo (Zahid et al. 2018). Finally the Gauss-Hermite moments represent differences in the velocity map with respect to the mean. For instance the values of the h3 moment is representative of the ‘skewedness’ of the velocity from the mean. This is highly useful for determining areas that are rotating at a different expected velocity, even if that velocity is in the same general direction as the mean. For instance, this would be useful for identifying an embedded stellar disk rotating faster than the surrounding stars. The h4 moment represents the kurtosis of the velocity. This identifies how narrow or broad the velocity distribution is with respect to a normal Gaussian profile.

1.3 Galaxy Accretion

The dominant tool for exploring galaxy accretion in the past decade has been through the use of simulation. Simulators have a ‘God’s eye view’ of stars passing between galaxies, and can view this temporally; a luxury not afforded to observers.

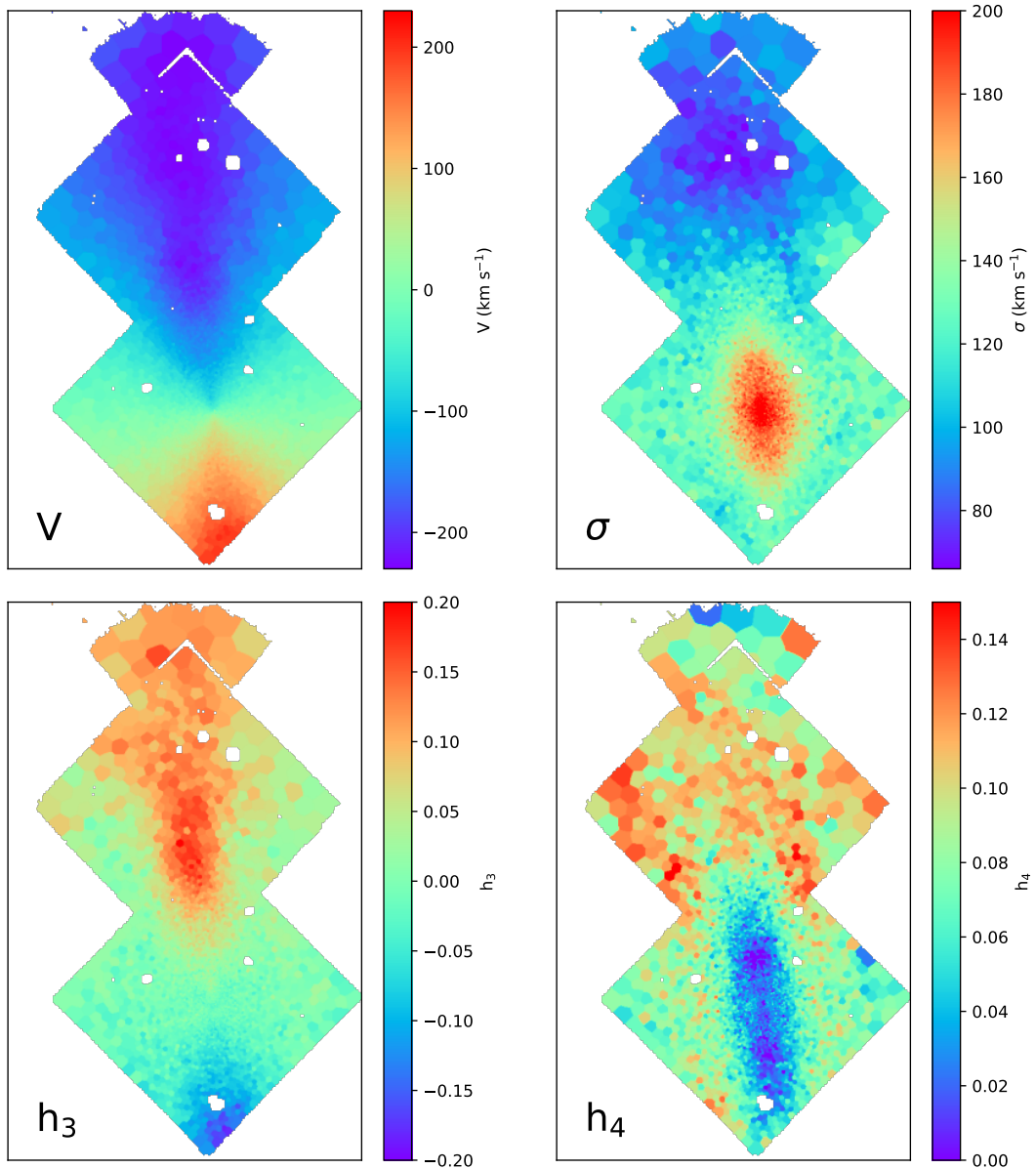


Figure 1.3: Kinematic views of the galaxy NGC 1380 derived from MUSE data (details in Chapter 4). Panels show velocity, velocity dispersion (σ), and two Gauss-Hermite polynomial moments h_3 and h_4 . One can see an ordered rotation across the galaxy in velocity, with the transition from the advancing components to receding components about the galaxy centre. The σ map shows a clear galaxy core with higher velocity dispersion, with σ decreasing with radius. The h_3 component shows the asymmetric deviation from the Gaussian value, whilst h_4 shows the symmetric deviation (i.e. the kurtosis) from the Gaussian value.

CHAPTER 1

As such, simulations offer an unobstructed view into the quantities and locations of ex-situ stars in any simulated galaxy. This has led to remarkable insights into galaxy formation, including the development of the ‘two-phase’ scenario of galaxy formation.

The ‘two-phase’ scenario provides a view of galaxy formation in which a dense in-situ core is built up at high redshift (Oser et al. 2010). Over time, this core can accrete stellar material from less massive galaxies through both galaxy mergers and tidal stripping. This forms the ex-situ component of stars, and rapidly becomes the dominant source of mass growth for the most massive galaxies, overtaking in-situ star formation in the core (Trujillo & Pohlen 2005; Auger et al. 2011; Pérez et al. 2013; Van Der Burg et al. 2015).

In- and ex-situ classifications separate stars into two groups. Those formed within the main progenitor branch host (in-situ), and those formed in other galaxies which are then stripped and accreted onto the host (ex-situ). Simulations have shown that high mass galaxies of mass $>10^{11}M_{\odot}$ are composed of significant fractions of ex-situ stars, with fractions up to 90% (Rodriguez-Gomez et al. 2016). This high fraction is indicative of frequent or massive merger events in the past.

Whilst the accreted stars can usually be found throughout the galaxy (and can be expected to be found in all regions of massive galaxies), ex-situ stars maintain more extreme orbits post merger event, and therefore can preferentially lie in the outer regions of the galaxy (Van Dokkum et al. 2014; Pillepich et al. 2015). This picture is far from clear, and evidence suggests that many factors can affect the locations of ex-situ stars in a galaxy, such as the relative angles of galaxy mergers and the mean direction of angular momentum (Bassett et al. 2017; Karademir et al. 2019).

Whilst simulations have dominated the conversation regarding galaxy accretion history, there are many discrepancies between models. Differing subgrid physics

CHAPTER 1

and especially controversial parameters such as feedback values seem to affect the ex-situ fractions of galaxies and the transition radius (see e.g. figure 3 of Rodriguez-Gomez et al. 2016). Whilst modern simulations almost entirely agree that there is an increase in ex-situ fraction with galaxy mass, and with galactocentric radius, the magnitudes of these trends are still debated (Pillepich et al. 2015; Pulsoni et al. 2020; Davison et al. 2020; Remus & Forbes 2021). It therefore falls to observation to constrain the ex-situ fractions of galaxies, and to confirm or deny the findings from simulation.

For many years, simulations and observations have pointed to huge amounts of interaction between galaxies (e.g. Lacey & Cole 1993, 1994; Lotz et al. 2011). In the majority of galaxies examined through deep imaging, large scale structure can be found at large radii, suggestive of tidal events, interactions, and merging (Duc et al. 2015; Kado-Fong et al. 2018; Hood et al. 2018; Mancillas et al. 2019; Rampazzo et al. 2020; Kluge et al. 2020; Martinez-Delgado et al. 2021). Even in our own Milky Way we find evidence of stellar streams originating from satellite galaxies currently being consumed by our Galaxy (see e.g. Belokurov et al. 2006; Bernard et al. 2014; Shipp et al. 2018; Malhan et al. 2018).

In a perfect observational method, stars could be identified as in- or ex-situ for a given galaxy in the same way as for simulation. This would require obtaining imaging or spectroscopy of spatially resolved stars throughout the target galaxy. Technological constraints prevent this currently for all but the nearest galaxies, and even then only for outer regions where stars are more easily distinguishable (Dalcanton et al. 2012; Johnson et al. 2013; Lewis et al. 2015). To obtain any view of general galaxy evolution we must seek a far larger sample than only the nearest few galaxies, and therefore we must move beyond galaxies in which stars are resolved. This presents issues as any spectrum taken from a portion of these more distant galaxies will contain the summed light from both in-situ and ex-situ stars,

CHAPTER 1

rendering classification of individual spectra meaningless. In order to quantify the ex-situ populations in a given area of galaxy, we must be able to separate a spectrum into its constituent component spectra.

The complexities and degeneracies of decomposition of spectra have led to a number of alternative methods to estimate the locations and quantities of ex-situ stars. Aspects such as the Sersic fit of galaxy light, metallicity profiles, and kinematic profiles have all been investigated as a means of exploring accreted populations. One particularly pursued quantity is the location of the ‘transition radius’. This marks the point at which the mass or brightness (depending on definition) of ex-situ stars becomes greater than that of the in-situ stars (Arnold et al. 2011; Huang et al. 2013a; Oyarzún et al. 2019; Gupta et al. 2020). These methods provide key insights into likely relative ex-situ fractions between galaxies, but fall short in central regions of galaxies where even multiple Sersic fits fail to accurately reproduce the light profile (dos Reis et al. 2020). Furthermore, some studies suggest that the transition radius is a poor proxy for quantifying ex-situ stars and their locations, as galaxies can sometimes show multiple transition radii (Remus & Forbes 2021), and literature estimates of the standard transition radius can range wildly even at fixed mass. In Remus & Forbes (2021) the authors demonstrate that between the Illustris, IllustrisTNG, and Magneticum simulations, the transition radius for a galaxy of stellar mass $M_{\star} = 10^{11}M_{\odot}$ can range between 0 and $> 8r_e$ (see Figure 1.4).

Evidence for the two-phase galaxy assembly process also comes in the form of the observed bimodality of globular star clusters (GCs) in colour and metallicity. Examination of the distribution and orbits of GCs has shown that the two GC sub-populations typically found around massive galaxies may be associated with the two phases; redder metal-rich GCs with the in-situ burst of formation in the main progenitor, and bluer metal-poor GCs with the later accretion of lower mass

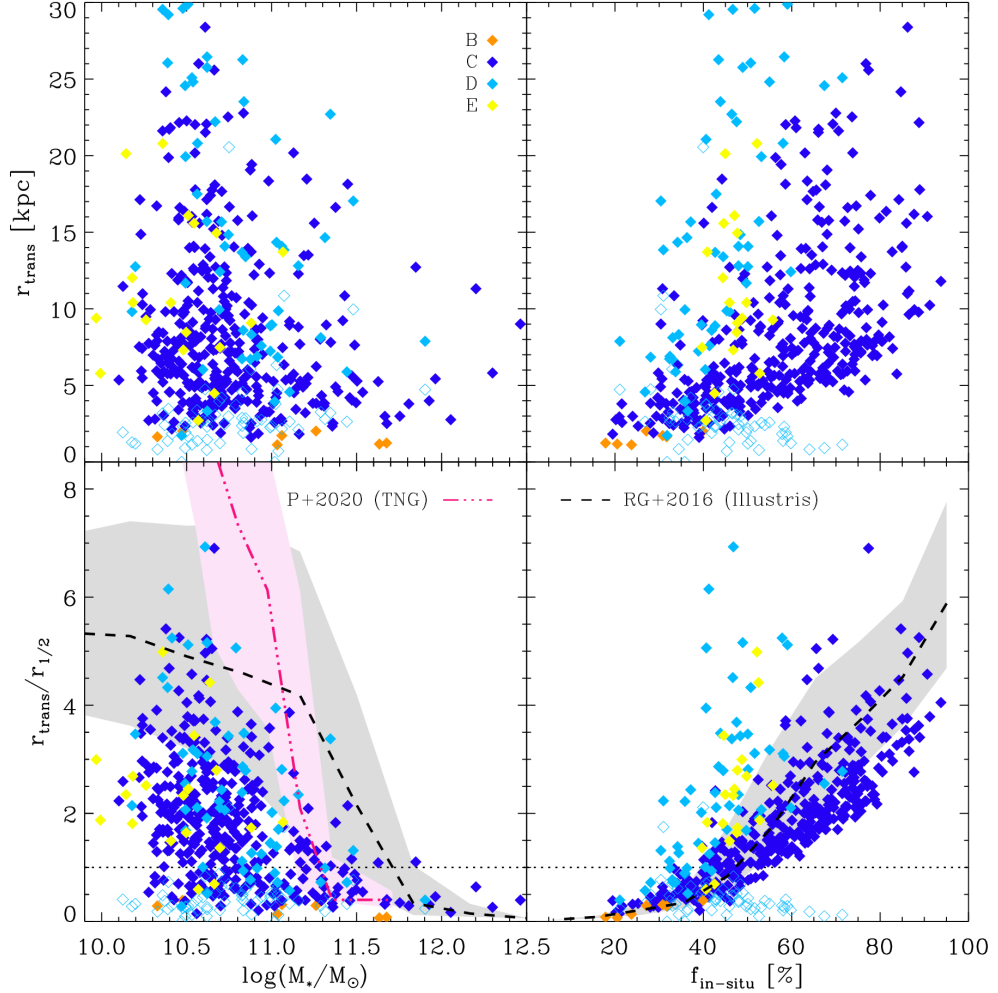


Figure 1.4: Figure from Remus & Forbes (2021) showing the transition radius of Illustris galaxies. Galaxies are separated into classes and shown as different colours according to the galaxy transition radii. Class B galaxies (orange diamond) are accretion dominated from the centre outwards. Class C galaxies (blue diamond) are ‘classic’ profiles with accreted fraction increasing and dominating at some radius away from the core. Class D galaxies (cyan diamond) show two transition radii, the inner radii are shown as open diamonds, the outer radii are shown as filled diamonds. Class E galaxies (yellow diamond) show roughly equal distribution of ex-situ and in-situ stars throughout the galaxy radial profile. Dashed black lines and shaded areas show the results from the Illustris simulation (Rodríguez-Gomez et al. 2016), and the dashed pink line and shaded area are the results found for Illustris-TNG (Pulsoni et al. 2020).

CHAPTER 1

galaxies hosting lower metallicity GC systems (e.g. Forbes et al. 2011; Romanowsky et al. 2012; Pota et al. 2015; Beasley et al. 2018; Kruijssen et al. 2018; Fahrion et al. 2020). GCs are found to display colour bimodality in nearly every massive galaxy system studied (Brodie & Strader 2006; Peng et al. 2006). Merging low-mass systems frequently produce GCs of low-metallicity, in stark contrast to in-situ metal rich GCs (Choksi et al. 2018; Forbes & Remus 2018). Hence, these GC properties can be used to diagnose both merger history as well as gradients of ex-situ fraction (Forbes et al. 2015; Kruijssen et al. 2018; Mackey et al. 2019), however this is complicated by uncertain mappings between colour and metallicity, and uncertain ages of old GCs in systems outside the Local Group.

1.4 Spectral Analysis

A galaxy spectrum can be considered as the sum of the spectra of all its stars, with modification by dust and gas within the galaxy, between the galaxy and the detector, and including skylines and other atmospheric alteration if the detector is on Earth. The specific ingredients to build that exact spectra are unique and extraordinarily complex. As a result, there are huge difficulties in decomposing a galaxy spectra into its constituent individual stellar spectra, dust, and gas emission components. Perhaps most difficult of all is the high degree of degeneracy, with many possible combination of different stellar spectra able to reproduce a galaxy spectra at current spectral resolutions and sensitivities. This was a problem especially for earlier techniques of population decomposition in which colours were used as a means of determining galaxy age and population. Galaxy colour changes both with age and metallicity through a non-exclusive function, meaning the quantities of age and metallicity are highly degenerate with colour. As such, if viewing the evolution of a star in a 2D plane of optical colours (such as R-I against B-V), one will find positions in the colour diagram that represent a multitude of overlapping ages and

CHAPTER 1

metallicities along the evolutionary track.

One current popular method by which to decompose a galaxy spectrum and to avoid much of this colour degeneracy is to fit single stellar population (SSP) models to a spectrum. SSPs represent the spectrum from a stellar population with a single age and single metallicity. By combining a weighted grid of SSPs covering all possible stellar ages and metallicities, one should theoretically be able to reproduce the spectrum from a galaxy. This is shown in a simplified form in Figure 1.5. The difficulty arises in correctly identifying the weight of all SSPs in the grid to reproduce the spectrum.

This can be pictured as the sound from an orchestra. What we may hear in totality as Beethoven's Symphony No.5 in C minor is really the coalescence of woodwind, brass, strings and percussion. Not only that but each instrument section may have different weights of instruments such as 3 trombones and 1 contrabassoon and any number of violins. Each instrument gives its very own sound to the piece, with more or less quantities of a specific instrument leading to a greater or lesser dominance of the total sound. In hearing the orchestra together we appreciate the entire summed sound from each instrument, in the same way we see a galaxy as the summed light from its stars. If we know the exact sound profile produced by each instrument, we can guess which combinations of each profiles will produce the final total music. When the right combination of instruments, and number of each instrument is found, the reconstructed and the original sound profiles will match almost precisely (providing the instrument sound profiles are accurate and there are no defects or noise in the recording).

When dealing with galaxies, there are far more components (SSPs) than for an orchestra, and therefore far more possible combinations. The combination of weighted component SSPs can be estimated via a linear least squares method. This is the method of full-spectral fitting used throughout this thesis, particularly using

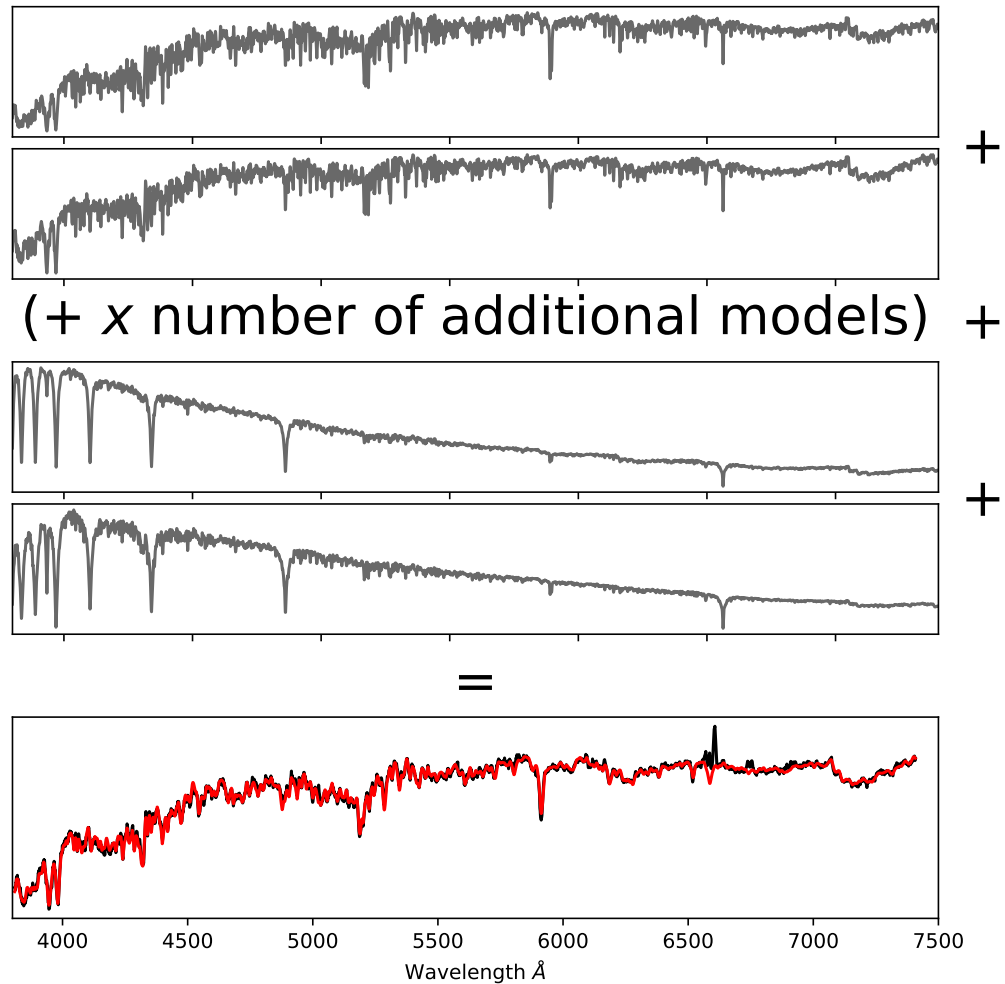


Figure 1.5: A demonstration of the summation of SSP models to produce a final spectrum. The figure shows four example SSP models in grey, with SSP models representing older ages seen in the first two panels, and SSP models representing younger ages seen in the central two panels. The lower panel shows the resultant weighted sum of a number of SSP models in red, fit to an input spectrum shown in black. Real combinations of models would use variable amounts of multiplicative and additive models and would vary the input weights. Furthermore, other ingredients would be considered to treat sky lines and gas/dust emission. The first two spectra are both from old populations, the first with a higher metallicity and the second with a lower metallicity. The third and fourth spectra are from young populations, the third with a lower metallicity, and the fourth with a higher metallicity.

CHAPTER 1

the existing full spectral fitting software Penalized PiXel-Fitting (pPXF) described in Cappellari & Emsellem (2004) and upgraded in Cappellari (2017).

The pPXF method described by Cappellari (2017) generalises a galaxy spectrum as a product of model stellar spectra, convolved to match the galaxy line-of-sight velocity distribution, and combined with orthogonal polynomials and sky spectra. This is described as:

$$G_{mod}(x) = \sum_{n=1}^N w_n \left\{ [T_n(x) * \mathcal{L}_n(cx)] \sum_{k=1}^K a_k \mathcal{P}_k(x) \right\} + \sum_{l=0}^L b_l \mathcal{P}_l(x) + \sum_{j=1}^J c_j \mathcal{S}_j(x) \quad (1.3)$$

where T_n is the N number of templates used in the fitting, x are the spectral elements, and $.$ Each is adjusted according to the line of sight velocity distribution (LOSVD) represented by \mathcal{L}_n . These can be optionally multiplied by multiplicative orthogonal polynomials of order K and then again optionally added to by additive polynomials of order L . Finally to complete the observed spectrum, sky spectra (\mathcal{S}_j) can be introduced if necessary. In theory this should well reproduce a given galaxy spectrum.

The software pPXF estimates the correct combination of weighted templates to reproduce an input spectrum using a maximum penalized likelihood approach. An in depth description of this can be found in Cappellari (2017). One advantage of pPXF over other available software is the well implemented optional use of regularisation. Regularisation offers a way in which to physicalise the solution obtained by full spectral fitting. By definition the acquisition of a solution from fitting models is an ill-posed inverse problem. A result of this is that many degenerate solutions can be found to provide an apparent solution to the spectral fit. Regularisation aims to reduce the impact of these degenerate solutions, by finding a smooth solution

CHAPTER 1

amongst the degenerate noisy solutions. Nonphysical solutions will often show strong weights in highly localised templates at apparently random positions on the age-metallicity grids. We know this to be nonphysical as galaxies will evolve according to age-metallicity relations and show a spread of ages and metallicities over a greater area than the grid resolution. Furthermore, the reasonable error associated with estimations of populations are larger than these noisy grid pixels; even a true rapid star formation event would be seen as a reasonably broad population spread with current methodology.

Regularisation chooses the smoothest solution up to a limit defined by the regularisation parameter. If regularisation is handled correctly, the final solution should in theory be the most physical amongst many apparently equally valid solutions. One also has to consider the effects of over-regularisation in which the solution can be too smooth. This results in a loss of resolution regarding changes in age and metallicity and therefore can hide events such as star-bursts or rapid accretion.

Using a population map of a galaxy derived from full spectral fitting, we are able to harness the age metallicity relation (AMR) to identify accreted stars. Galaxies exhibit a clear age metallicity relation (Twarog 1980; Carraro et al. 1998; Layden & Sarajedini 2000) due to supernovae injecting higher metallicity material into the ISM and the resultant gradual enrichment of the galaxy. By pulling out fractional populations of stars, those with discontinuities in metallicity from the original progenitor group become distinct, as they lie away from the AMR. Stars which lie out of the AMR are most likely to have formed in another galaxy under different metallicity environments and have been merged or stripped onto the host galaxy. Alternatively, these could be stars formed in-situ from gas stripped from galaxy fly-bys. Stars born of the accretion of new gas (a so called wet merger) are roughly as distinct and separate from the AMR, though such stars are virtually indistinguishable from ex-situ stars of the same source despite being truly in-situ.

CHAPTER 1

Using ex-situ fractions, one can theorise formation mechanisms of galaxies. For example, Early Types with high fractions of ex-situ stars have likely been perturbed by the constant harassment and merging of galaxies, and as such have lost gas from the ISM into the IGM or ICM.

1.4.1 Stellar Models

Single-age, single-metallicity stellar populations (SSPs) are spectra representing stars of a specific age and metallicity. SSPs are a product of understanding both the evolution history and the spectra of stars of all size, ages and types. Whilst many complex caveats can affect the spectra of a star, the spectrum at any time is essentially a function of mass and initial composition. To model the spectra of a star using known inputs we must use three basic properties. These are the Initial Mass Function (IMF) which describes the distribution of stellar masses; the expected evolutionary paths of stars dependent on their initial mass and composition, given in the forms of stellar isochrones; and the stellar spectral libraries describing the expected spectra at various ages and metallicities.

The stellar spectral libraries are themselves produced as a function of stellar metallicity, surface gravity, and effective temperature. The resultant SSP model can be described as:

$$f_{SSP}(t, Z) = \int_{m_{lo}}^{m_{up}(t)} f_{star} [T_{eff}(M), \log g(M)|t, Z] \Phi(M) dM, \quad (1.4)$$

Where f_{SSP} is the output SSP spectrum, M is the stellar initial mass, $\Phi(M)$ is the IMF, and f_{star} is the stellar spectrum.

One of the most commonly used empirical stellar spectral libraries with which to build SSP spectra from are the Medium resolution INT [Isaac Newton Telescope] Library of Empirical Spectra (MILES) (Falc3n-Barroso et al. 2011). These models use

CHAPTER 1

a combination of both photometric libraries and stellar spectra to produce high resolution spectra using the prescribed ingredients (such as surface gravity and effective temperature). Empirically derived spectra offer numerous benefits compared to theoretically derived spectra. They are real observed quantities, and therefore exactly follow the physical outputs of stars, even for aspects that are not fully understood such as complex convection processes. They are however subject to observational errors and complications such as sky-lines and offset calibrations. Furthermore, the constructions of such libraries are at the statistical mercy of local populations, with some locally rare stars being poorly or not at all represented in a library. The MILES spectral library is considered amongst the most complete spectral libraries with over 985 stars used to provide spectra. Despite good coverage, all empirical spectral libraries struggle to provide spectra from metal poor young stars ($<1\text{Gyr}$) and metal rich older stars, as a result of the scarcity of these stars in the Milky Way. As such full spectral fitting with empirical spectral alone can provide a poor insight into young populations.

In Vazdekis et al. (2010), the authors are able to mitigate some of these issues by interpolation of models across the Hertzsprung-Russell (HR) diagram. The authors use stellar evolution isochrones in order to build a high resolution set of stellar spectra using the MILES models as a base. Thus the authors build spectra representing a grid of stars ranging from 0.06 to 18Gyr, and with a metallicity range of $+0.22$ to -2.32 [Fe/H].

Isochrones are used to track the expected evolution of any given star across the HR diagram. Numerous descriptions of isochrones have been presented in literature, all claiming to demonstrate a more accurate modelling of stellar evolution than the other (Pietrinferni et al. 2004; Pietrinferni et al. 2006; Cordier et al. 2007; Dotter et al. 2008; Marigo et al. 2008; Percival et al. 2009; Pietrinferni et al. 2009; Salaris et al. 2010; Bressan et al. 2012; Morton 2015; Spada et al. 2017). Truthfully no

CHAPTER 1

model of an isochrone will perfectly capture the evolution of all stars, due to small complexities in evolution that can adjust the path taken across the HR diagram. One example of this would be the existence of binary systems. Close binary pairs can adjust properties over a lifetime through mass transfer, meaning an assumed initial mass will give only approximate results (Conroy et al. 2009a; Li & Han 2008). Rotation of a star alone can strongly affect the surface gravity of a star, and binaries again play a part in changing the rotation of a star through tidal interaction. Rotation causes further problems in assumed starting quantities, as rotation can mix stellar material to a higher degree, supplying the stellar core with lighter elements and sustaining the lifetime of a star (Shaviv & Salpeter 1973; Claret & Torres 2016). These are examples of some of the simplest complications, and as such no isochrone model to date can accurately account for the complexities of stellar evolution.

Despite these caveats, stellar isochrones are able to give a general overview of stellar evolution. Especially for large samples of populations (such as in galaxies) many of the inconsistencies are smoothed out by a majority consensus of stars that follow the expected isochrones to a close degree. Two of the most frequently used isochrones are the Padova isochrones (Bressan et al. 2012) and the BaSTI isochrones (Pietrinferni et al. 2006). These consider various sub-processes in stellar evolution and are considered to be amongst the most accurate descriptions of stellar evolution in current use. One BaSTI isochrone version further considers ‘overshooting’ in which the variability of convection (outside of the Schwarzschild criterion) is considered. These evolutionary paths are shown in Figure 1.6.

The isochrones used throughout this document are of BaSTI type using scaled-solar and α -enhanced isochrones without overshooting. The age range of these isochrones is between 0.03 and 14Gyr in steps of 0.05 dex.

The third and arguably most influential ingredient for SSP model creation is the IMF. The debate regarding the correct IMF to use has been ongoing for decades

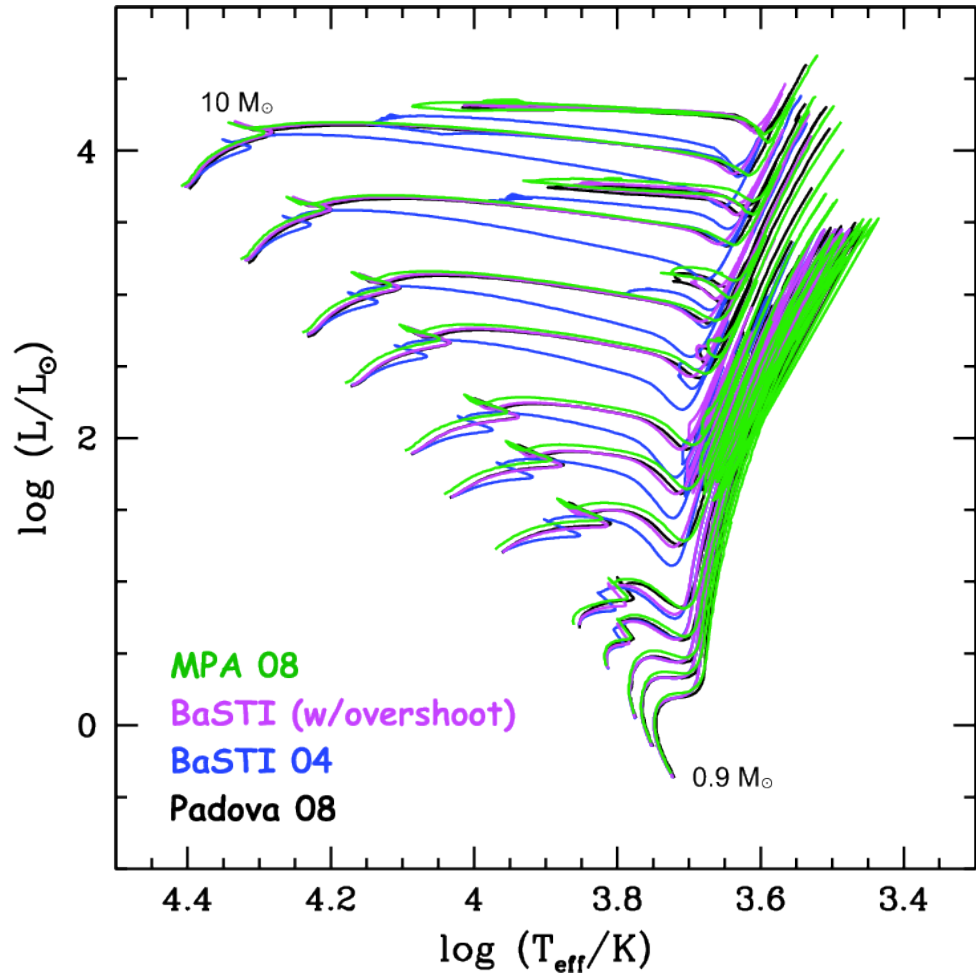


Figure 1.6: Examples of MPA, BaSTI and Padova isochrones of stellar evolution. Examples are shown for BaSTI isochrones both with and without consideration of overshooting. Image by S. Charlot.

CHAPTER 1

with debate only accelerating in recent times (some of the most widely cited IMF literature is added here, though there is a staggering amount of literature regarding this topic. Smith (2020b) provides a comprehensive modern overview) (Scalo 1986; Kroupa 2001, 2002; Padoan & Nordlund 2002; Chabrier 2003). The choice of IMF will dictate the distribution of stellar masses used to build SSP models. Variations in IMF will provide differing contributions to the total stellar light from low-mass stars relative to high-mass stars. During the course of this thesis, all SSP models will assume a Kroupa model with an IMF slope value of $\mu = 1.3$ (Kroupa 2001). Sections regarding the EAGLE simulations assume a Chabrier IMF (Chabrier 2003).

1.5 Galaxy Simulation

Observational astrophysics can give us physical insights into the properties and mechanics of galaxies. This is however restricted temporally to a snapshot of the universe as it is today. We have a sample of exactly 1 Universe, so if we wish to explore spatial physics of galaxies at $z \approx 0$, we have the Milky Way, the few resolved local galaxies around us, and little else. Of course, higher statistics can be yielded by looking further afield, though as we do, we also look through layers of time and must be wary about properties that change with galaxy age. Furthermore, the more distantly we observe, the poorer our spatial resolution, and the more prone we are to brightness limited biases, giving us samples of only the brightest galaxies in the younger universe.

The simple solution to this problem is to observe more universes. If we construct approximations of universes, we can explore them with a ‘God’s eye view’, where time and distance are no limitation. This is where cosmological simulations of galaxy formation are key. In these simulations we may advance time, sliding through 13.8 billion years of simulated history in an instant to watch galaxies form, collide and evolve. Furthermore, we may create as many of these simulations as we would like,

CHAPTER 1

giving us immense statistical resolution. And as we can travel instantly through these samples, any galaxy can be treated as either local or a distant object.

Unsurprisingly there are limitations in creating a model universe. If the model universe had the same volume, resolution, and physics as our Universe, it would run at the speed of time (assuming perfectly efficient computation). This is also known as the Universe. Therefore in order to view temporally we must lower the resolution and approximate the physics. A number of methods are able to achieve this and these are described below. Whilst these techniques give us good temporal access to the evolution of a volume of universe, approximations and low resolution have a trade off in physicality. This makes it particularly difficult to simulate physics that are highly dependent on small scale turbulence such as AGN outflows and magnetohydrodynamics (Ragone-Figueroa et al. 2013; Marinacci & Vogelsberger 2015). To treat these difficulties, approximations must be used which can provide some semblance of the ‘randomness’ attributed to especially turbulence.

Though Moore’s Law died in the early 2000’s, modern computing has continued to advance largely through the improvement of load and power leakage on processors. As such, cosmological simulations are also scaling with an increase in available computing power. This allows astronomers to work with either higher resolution or larger volume simulations, which are increasingly revealing surprising aspects of galaxy formation and evolution.

1.5.1 Simulation Techniques

N-Body simulation is a technique in which virtual particles are ascribed with the laws of physics. Arguably the first N-body simulation was performed by Erik Holmberg in 1941 in which he placed light bulbs at various intervals, using the propagation of light as a proxy for gravitational interaction. From this he was able to explore the properties of interactions between stars in interacting galaxies (Rood 1987).

CHAPTER 1

In computational N-body simulations, each particle will interact with others according to physical laws, and move throughout a simulation space physically. This is advantageous in cosmological simulation, especially for components such as dark matter (DM), which is expected to only interact through gravity. This makes it an ideal property to study through N-Body simulation, as the particles only need to calculate the gravitational force which they impart and experience in order to simulate physical movements of dark matter. [Note: This methodology works regardless of the correctness of the dark matter interpretation of the ‘missing mass’ issue, as the final conditions of a galaxy can be well approximated with dark matter particles, regardless of the validity of the existence of dark matter.] Particles are assigned initial conditions and densities, and then the simulation is allowed to run. Small incremental time units are progressed, with the expected motion of each DM particle updated according to laws of motion imparted on the particles from every other particle in the simulation.

This pair-wise method is computationally expensive and runs with an $O(N^2)$ execution time, meaning a parabolic increase in computing time with particle number. This can be improved however, especially in large volume simulations. One of the most common and basic ways to improve this is to use a tree algorithm (also known as a Barnes-Hut algorithm; Barnes & Hut 1986). This uses the assumption that from the perspective of particles in a central frame, other particles that are at long distances away, but physically located close together will appear as only a small angular area. This small area exerts the sum gravitational force of all of those distant particles. As such, the group of distant particles can be assumed to be a single particle with the summed mass, reducing computational complexity to $O(N \log N)$. This method works well providing the maximum angular resolution of the particles is not too large. The smaller this maximum angular resolution, the more accurate the calculated force, but the slower the computation. Considering this trade-off is

CHAPTER 1

key for maximising both the efficiency and the physicality of a simulation.

Smoothed particle hydrodynamical (SPH) simulations utilise a concept in which many particles approximate a fluid. The particles are ‘smoothed’ according to a smoothing function h , which controls a smoothing length. The smoothing length adapts so that areas of higher density, and thus higher detail, will have shorter smoothing lengths compared to less dense areas of lower detail, which will have longer smoothing lengths. This ensures that dense and detailed regions in a simulation will be treated with high resolution computation, whilst more sparse regions with little detail can afford lower resolution and thus less computing time. The computational technique of smoothed particle hydrodynamics (SPH) was developed in 1977 by Gingold, Monaghan and Lucy in order to simulate astrophysical environments (Gingold & Monaghan 1977; Lucy 1977), but has since been used to simulate a vast array of mechanical processes, both within astrophysics, and without.

SPH simulations offer a variety of benefits in comparison to purely particle based simulations. Firstly they are better able to resolve finely detailed fluid physics and complex processes such as feedback, star formation and black-hole growth. This is something rarely present in purely particle based codes which lack the ability to track large regions of low density material such as gas present in the interstellar or intergalactic medium. Considering the importance of many of these processes for galaxy evolution, SPH models are amongst the most frequently used in galaxy evolution simulation. Despite this improved description of galaxy processes, SPH simulation requires significantly more computational power than particle models of the same resolution. This is often considered a fully worthwhile cost considering the advantages granted in the form of far more physical final conditions. Further complications arise from assigning complex and poorly understood physics to the SPH codes. One particular example of this is in the modelling of stellar feedback. This process is extremely complex and cannot be described well with current fluid

CHAPTER 1

models at reasonable resolutions. As such this has to be approximated, and the strength/process of feedback in simulations is perhaps the most distinct and varying feature between competing SPH simulations. The computing requirements often mean that SPH resolution will poorly constrain some fluid mechanics, especially features such as fluid instability and shocks. These shortcomings are being rapidly improved upon using advanced and increasingly accurate subgrid models, as defined below.

Simulations using SPH come in largely two flavours; Large Volume, or Zoom-in. Zoom-in simulations model a large volume of space at very low resolution. They then pick a smaller area of this volume, zoom in and re-simulate the smaller volume at a substantially higher resolution, using the low-resolution initial conditions as a guide. This can be performed multiple times, giving a final extremely high resolution view of a very small volume of space. This is very useful for viewing subgrid processes such as supernovae or aspects of star clusters, which are usually below the resolution of non-zoom SPH codes. The downside of this method is it eliminates the high statistics often associated with cosmological simulations.

In comparison, large volume simulations provide extraordinarily good statistics, usually with the intention of providing far better statistics than would be available from volume limited observational samples. These operate at much lower resolution due to the computational demand, however provide good results for larger systems such as galaxies and galaxy filaments. To simulate the mechanics that are controlled by processes smaller than the resolution, subgrid models can be used. These approximate the output from smaller resolution areas using known averages, without modelling the true output as a zoom-in simulation would. Though this only approximates the final processes, these approximations have advanced to the degree that they accurately portray many aspects of galaxy formation and evolution.

Resolution vs volume is the dominating factor when judging the usefulness of

CHAPTER 1

a simulation. On the one hand, a high volume is paramount to reach any statistical certainty in most galaxy studies. Nonetheless, if this is at the cost of a low resolution, the simulation will match poorly to observational results. One way that the simulations can be tested in order to confirm that the resolution is high enough to capture the galaxy physics is to use a double resolution simulation. In these usually smaller volume simulations, resolution is increased to at least double and the simulation re-run. If the final product is significantly different to the standard resolution simulation then the original resolution is not high enough to capture important physics. If however the double resolution volume appears to be simply a sub-volume of the original simulation, then the original resolution is successfully approximating the physics, and resolution does not have to be scaled down.

1.5.2 EAGLE

The EAGLE (Evolution and Assembly of GaLaxies and their Environments) simulations are a suite of cosmological hydrodynamical simulations created with the aim of understanding the co-evolution of galaxies and supermassive black holes within a cosmologically representative volume of a standard Λ cold dark matter Universe. The simulations were built and run using the extensively modified gadget-3 tree-SPH code. A description of gadget-3 can be found in Springel (2005) and for a comprehensive overview of the full suite of simulations see Schaye et al. (2015); Crain et al. (2015).

Subgrid feedback parameters were calibrated to ensure $z = 0$ reproduction of the galaxy stellar mass function, disc sizes, and the $M_{BH} - M_*$ relation. Further studies make comparisons to other observational properties, showing close matches (Schaye et al. 2015; Furlong et al. 2015; Lagos et al. 2015). Detailed descriptions of the calibration procedure and the influence of parameter variation are given by Crain et al. (2015). The EAGLE simulations use a Chabrier initial stellar mass

CHAPTER 1

function (Chabrier 2003) and were run with a modified version of the gadget-3 smoothed particle hydrodynamics code. The subgrid treatments are well explained in McAlpine et al. (2016).

The EAGLE suite of simulations have various volumes and resolutions, with the main suite of simulations using cubic volumes of 25 to 100 comoving megaparsecs (cMpc). This suite has initial baryonic particle masses ranging from $2.26 \times 10^5 M_\odot$ for the smallest volume simulation, to $1.81 \times 10^6 M_\odot$ for the larger volume, with various intermediate combinations of volume and initial particle mass. Key to the resolutions of the EAGLE simulations is that it resolves the Jeans scales in the warm ($T \simeq 10^4 \text{K}$) ISM for all simulations allowing for accurate modelling of the ISM and associated processes.

The cosmological parameters of the Λ CDM environment are gathered from the Planck Collaboration et al. (2014), with values of $\Omega_0=0.307$, $\Omega_b=0.04825$, $\Omega_\Lambda=0.693$, $\sigma_8=0.8288$, $n_s=0.9611$, $h=0.6777$, $Y=0.248$.

1.5.3 Simulated Mergers

Cosmological simulations have lead the field in helping to understand the merger processes of galaxies. The high number statistics as well as ability to trace stars back to their galaxies of origin has allowed simulations to provide crucial insights into galaxy mergers, and the impact of such mergers on galaxy growth. To understand such evolution, simulated galaxies at any given snapshot must be linked with historical merger information in order to understand the effects of galaxy collision and accretion. To do this, galaxy merger trees are utilised.

Merger trees are a record of all galaxies that combined together to form the galaxy up to a specific snapshot. As this analysis can be performed after the completion of the simulation, these trees will often also include future merger history, such as which subhalo the viewed galaxy will end up in by $z=0$. In the EAGLE simulations,

CHAPTER 1

this is performed using the D-Trees algorithm (Jiang et al. 2014). This tracks the transfer of particles between halos that are gravitationally self bound. The halo in a given snapshot that has received the most mass from other candidate halos is marked as the descendent, and will be considered the main galaxy of the merger. This can happen with thousands of galaxies over the evolution of a main branch galaxy, with a single final descendant at $z=0$, but thousands of progenitors. Each of the progenitor galaxies will also retain information regarding their own progenitors. This is shown in Figure 1.7 as an overview for one galaxy in the EAGLE simulation.

1.6 Galaxy Observation

Galaxy spectroscopic observation is a key requirement in the study of galaxy evolution. A harmonious collaboration between observation and simulation is necessary to mutually constrain and verify theory. Whilst the field of simulation has expanded in line with computational advance, so has the field of observation in line with technological advance.

Over recent decades, one of the most important advances in technology for astronomers studying galaxies has been the advent of large field of view integral field spectrographs (FoV $\gtrsim 1$ arcminute) (e.g. SAURON at the WHT, GCMS on the 2.7m Harlan J. Smith telescope and MUSE at the VLT, Bacon et al. 2001; Hill et al. 2008; Bacon et al. 2010). These and similar instruments allow the simultaneous measurement of high signal-to-noise spectra across a range of galactocentric distances, facilitating unprecedented maps of spectroscopically-derived stellar populations across galaxies (see e.g. Gu erou et al. 2016).

Integral Field Spectroscopy has proven particularly useful in exploring galaxy kinematics and populations. Integral Field Units (IFUs) have provided spatially resolved maps of galaxies which can be used to diagnose population differences and kinematic effects as a result of mergers. This has been shown to be effective in

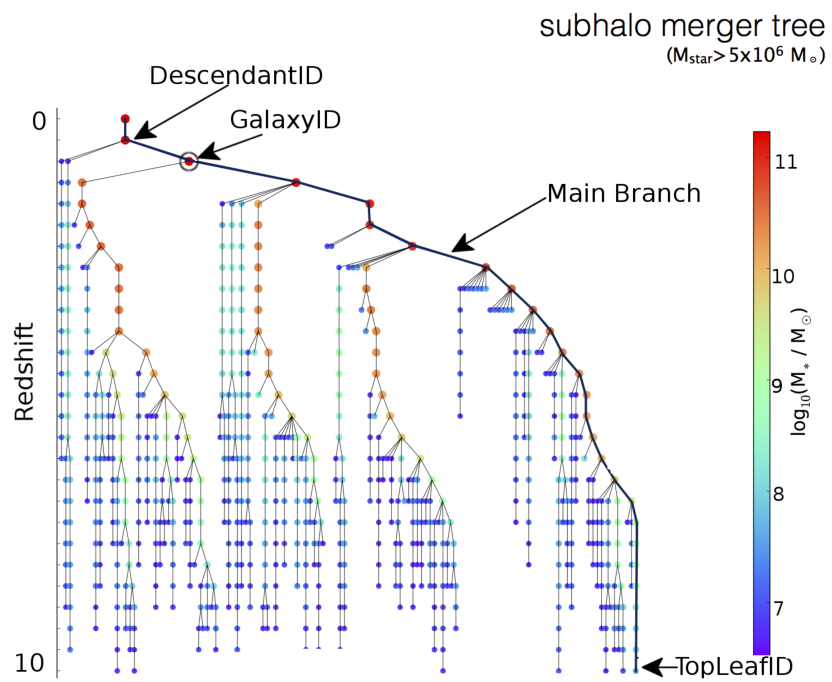


Figure 1.7: Merger history of an EAGLE galaxy with stellar mass $M_{*} = 10^{11} M_{\odot}$ at $z = 0.18$, as shown in McAlpine et al. (2016). Colour shows the logarithmic stellar mass and a solid black line shows the main branch following the most influential subhalo at every snapshot.

CHAPTER 1

numerous observational cases (see e.g. Guérou et al. 2016; Faifer et al. 2017; Ge et al. 2019).

One of the most well regarded IFUs is MUSE, an $\sim 1 \times 1$ arc-minute FoV IFU with a spectral range of 4560-9200 Å. The instrument comprises of 24 individual IFU units which each receive one horizontal slice of the full FoV. Each of these horizontal slices are further sliced both horizontally and vertically in each IFU, resulting in 48 slices per spectrograph unit and 1152 final slitlets.

Whilst IFUs are able to map resolved galaxies, when it comes to building numerically superior samples, astronomers turn to sky surveys. These surveys have lower depth and resolution than dedicated targeting instruments, however the vast number of galaxies that they image can provide many other advantages. The Sloan Digital Sky Survey (SDSS) (York et al. 2000) is one of the largest digital surveys and archives available as a public release. Spectroscopic data are available on more than 3 million objects, with 500 million photometric objects available (as of DR15, Aguado et al. 2018). Data are collected with the use of a dedicated 2.5m optical telescope based at Apache Point, New Mexico, USA.

30 2048x2048 CCD chips are placed to drift scan the sky. Drift scanning movement is used instead of regular tracking as a means to eliminate large CCD readout overheads. Chips are covered with an optical filter with 6 chips of each filter. Filters are defined as the SDSS photometric filters, and are specified as $u'=354\text{nm}$, $g'=475\text{nm}$, $r'=622\text{nm}$, $i'=763\text{nm}$, $z'=905\text{nm}$ (York et al. 2000; Gunn et al. 1998).

As part of the SDSS survey, the Mapping Nearby Galaxies at Apache Point Observatory (MaNGA) project has been producing spatially resolved spectral surveys of nearby galaxies and has more than 10'000 galaxies mapped (Bundy et al. 2014; Law et al. 2015). This is a powerful tool for galactic archaeology, in which populations can be mapped spatially across a galaxy.

When studying galaxies, Signal to Noise (SN) is a key data aspect to consider.

CHAPTER 1

Poor SN will result in equally poor confidence in results. Despite this, many galaxy observations will show poor SN and as such, the observations must be binned to a lower spatial resolution in order to increase SN.

Voronoi binning is a data binning technique in which data are binned into Voronoi diagram partitions, known as Voronoi cells or bins. Using this method it is possible to group data on a 2d plane, such that a third parameter sums to a desired minimum value (ζ) within the bin. This is done with maximum efficiency wherein the area of the spaxel is at a minimum though still sums to the minimum desired third parameter value ζ . The actual final summed value of the bin is usually larger than ζ and is referred to here as ζ' .

One particular use of this method is to group low SN objects to sum to a higher SN, whilst keeping physical size and mass differences between the binned objects at a minimum, or instead to bin spatial pixels of an image to a lower spatial resolution but higher SN. Cappellari & Copin (2003) describes three requirements needed to be satisfied in order to make the Voronoi tessellation well formed. First is a topological requirement. Bins should cover the plane in entirety, without overlapping or missing areas. Second is a morphological requirement in which the shape of the bin has to be as ‘round’ as possible. In essence, this requires the boundaries of a bin to be at the minimum distance from the central bin seed, whilst still containing enough data to sum to ζ . Third is a uniformity requirement, in which the disparity between ζ' values from bin to bin should be as small as possible. Whilst it is rarely possible to sum to exactly ζ , bins should aim to sum to as close to this minimum as possible. When ζ' is much larger than ζ (even if the other conditions are satisfied) then the uniformity requirement has not been met.

Chapter 2

Accreted Stars in the EAGLE Simulations

2.1 Remarks

The following chapter includes published work from Davison et al. (2020), with additions to the published document where appropriate.

2.2 Chapter Abstract

Modern observational and analytic techniques now enable the direct measurement of star formation histories and the inference of galaxy assembly histories. However, current theoretical predictions of assembly are not ideally suited for direct comparison with such observational data. This chapter examines the contribution of ex-situ stars to the stellar mass budget of simulated galaxies, extending prior work. The predictions are specifically tailored for direct testing with a new generation of observational techniques by calculating ex-situ fractions as functions of galaxy mass and morphological type, for a range of surface brightnesses. These enable comparison with results from large FoV IFU spectrographs, and increasingly

CHAPTER 2

accurate spectral fitting, providing a look-up method for the estimated accreted fraction. Furthermore, predictions are provided of ex-situ mass fractions as functions of galaxy mass, galactocentric radius and environment. Using $z = 0$ snapshots from the 100cMpc³ and 25cMpc³ EAGLE simulations, this chapter corroborates the findings of prior studies, finding that ex-situ fraction increases with stellar mass for central and satellite galaxies in a stellar mass range of $2 \times 10^7 - 1.9 \times 10^{12} M_{\odot}$. For those galaxies of mass $M_{*} > 5 \times 10^8 M_{\odot}$, we find that the total ex-situ mass fraction is greater for more extended galaxies at fixed mass. When categorising non-central galaxies by their parent group/cluster halo mass we find that the ex-situ fraction decreases with increasing parent halo mass at fixed galaxy mass for the densest environments. This apparently counter-intuitive result may be due to high passing velocities within large cluster halos inhibiting efficient accretion onto individual galaxies.

2.3 Chapter Introduction

The recent simultaneous advancement of improved observational technology and stunningly detailed theoretical simulations has significantly expanded and deepened the scientific repertoire available to study galaxy formation.

One of the key insights inferred from large cosmological simulations of galaxy formation (e.g. the EAGLE, Illustris, Horizon-AGN, and Fire simulations; Dubois et al. 2014; Hopkins et al. 2014; Vogelsberger et al. 2014; Crain et al. 2015; Schaye et al. 2015) is that galaxies (particularly massive elliptical galaxies) undergo a ‘two-phase’ process of assembly (see e.g. Oser et al. 2010), in which they initially form a relatively compact core of stars formed in-situ in the main progenitor from infalling cosmological cold gas and gas returned to the ISM by stellar evolution. Following this period (at $z \lesssim 3$, Oser et al. 2010) simulations indicate continuing accretion of stars from smaller galaxies outside of the virial radius via mergers and tidal

CHAPTER 2

stripping, resulting in a build up of ex-situ stars. These simulations indicate that the ex-situ fraction is a strong function of the mass and formation history of the galaxy, with galaxies of $M_*=10^9 M_\odot$ being almost entirely composed of stars formed in-situ, while in contrast $\approx 90\%$ of the stellar mass of the most massive galaxies ($M_\odot > 1.7 \times 10^{11} M_\odot$) can have originated in previously distinct progenitors (Oser et al. 2010; Lackner et al. 2012; Rodriguez-Gomez et al. 2016; Pillepich et al. 2018).

Observational evidence has accumulated to support the two-mode scenario of in-situ and ex-situ stellar assembly from a variety of sources. The most obvious is the observation that many galaxies, if not most, including our own Milky Way, exhibit streams of stars attributable to the remains of tidally disrupted dwarf galaxies (see e.g. Belokurov et al. 2006; Martínez-Delgado et al. 2008; Jennings et al. 2015; Hood et al. 2018). Examination of the distribution and orbits of globular clusters (GCs) has shown that the two GC sub-populations typically found around massive galaxies can be associated with the two phases; metal-rich GCs with the in-situ burst of formation in the main progenitor, and metal-poor GCs with the later accretion of lower mass galaxies hosting lower metallicity GC systems (e.g. Forbes et al. 2011; Romanowsky et al. 2012; Pota et al. 2015; Beasley et al. 2018; Kruijssen et al. 2018; Fahrion et al. 2020). Investigations of the radial gradients of stellar populations in massive early-type galaxies shows that the outskirts of such galaxies are composed of older, lower metallicity, alpha-enhanced stars indicative of accretion from lower mass progenitors (e.g. Greene et al. 2012; La Barbera et al. 2012; Martin et al. 2018). The same mode of galaxy assembly has also been suggested by independent observational means such as supermassive black hole growth (Krajinović et al. 2018). Finally, observations indicate that at earlier epochs galaxies were considerably more compact than galaxies of comparable mass today, an observation that can in part be explained by the later addition of accreted stars to the outer regions of galaxies (van der Wel et al. 2014; van Dokkum et al. 2014).

CHAPTER 2

Recently, observational technology and analytical techniques have advanced sufficiently that the opportunity now exists to infer in detail the star formation and mass assembly histories of galaxies on an individual basis. This advancement is largely due to three developments:

1. The advent of integral field spectrographs with a large field of view ($\gtrsim 1$ arcminute) (e.g. SAURON at the WHT, GCMS at the 2.7m Harlan J. Smith telescope, KCWI at Keck, and MUSE at the VLT, Bacon et al. 2001; Hill et al. 2008; Bacon et al. 2010). These and similar instruments enable the simultaneous measurement of high signal-to-noise spectra out to large galactocentric distances, delivering unprecedented spatially-resolved measurements of spectroscopically-derived stellar population parameters across galaxies (see e.g. Guérou et al. 2016; Mentz et al. 2016).
2. The development of full spectral fitting methods (e.g. pPXF, STARLIGHT, VESPA etc; Cappellari & Emsellem 2004; Cid Fernandes et al. 2005; Tojeiro et al. 2007; Cappellari 2017) to extract temporally resolved star formation histories from the integrated light measurements made by spectrographs (see e.g. Onodera et al. 2012; Norris et al. 2015; Ferré-Mateu et al. 2017; Kacharov et al. 2018; Ruiz-Lara et al. 2018, for demonstrations of the application of this approach).
3. The development of techniques to use the information provided by the full star formation and chemical enrichment histories provided by 2) to infer galaxy accretion histories (Boecker et al. 2020b; Kruijssen et al. 2019) or to provide additional constraints on assembly history in combination with kinematic information (e.g. a population-dynamical approach; Poci et al. 2019).

In order to aid the understanding of the huge quantity of information provided by the combination of these technologies and techniques, it is necessary to have more

CHAPTER 2

detailed predictions from simulations with which to compare to the observations. To date, most studies of the assembly histories of galaxies have focused on examining the underlying physics from a more theoretical direction (e.g. Oser et al. 2010; Rodriguez-Gomez et al. 2016; Qu et al. 2017). In this chapter we use the EAGLE simulations to develop predictions for the fraction of stars that formed in-situ and ex-situ, in terms of observable quantities most useful to observers e.g. galaxy stellar mass, galaxy type (roughly early or late type), environment (specifically halo mass), and most usefully, surface brightness. This study therefore builds on that of Qu et al. (2017) whose analysis of EAGLE found that typically, galaxies of mass $M_* < 10^{10.5} M_\odot$ assemble less than 10% of their mass from ex-situ sources, whilst those of $M_* > 10^{11} M_\odot$ typically exhibit ex-situ mass fractions of $\sim 20\%$ (though with a large scatter in these values).

This chapter is organised as follows. In Section 2.4 we describe the EAGLE simulations we are utilising, as well as the methodology for classifying star particles as in- or ex-situ. In Section 2.5 we present the results of our investigation into the dependence of in- and ex-situ mass fractions as functions of various observable properties of galaxies, and of galactocentric radius. Furthermore we provide tabulated data for use when comparing to observational studies. In Section 2.6 we discuss some of the implications of our results in light of expectations and previous studies. Finally in Section 2.7 we provide some concluding remarks.

2.4 Methodology

2.4.1 Simulations Overview

For the present work we focus on two simulations, Recal-L025N0752 (hereafter Recal-025) and Ref-L0100N1504 (hereafter Ref-100). The Ref-100 simulation is a periodic volume, 100cMpc on a side, realised with 1504^3 dark matter particles and

CHAPTER 2

an initially equal number of gas particles, described as ‘intermediate resolution’. The resultant initial baryonic particle mass is $1.81 \times 10^6 M_{\odot}$; the dark matter particle mass is $9.70 \times 10^6 M_{\odot}$; the gravitational softening length is 2.66ckpc (co-moving kiloparsecs) limited to a maximum proper length of 0.7pkpc (proper kiloparsecs).

Recal-025 is the higher resolution of the two simulations and the parameters of the Recal model were re-calibrated to achieve a similarly good match to the observational data as the Reference model. This simulation is 25cMpc on a side, realised with 752^3 dark matter and gas particles. The resultant initial baryonic particle mass is $2.26 \times 10^5 M_{\odot}$; the dark matter particle mass is $1.21 \times 10^6 M_{\odot}$; the gravitational softening length is 1.33ckpc limited to a maximum proper length of 0.35pkpc.

For our analysis we focus on the final $z = 0$ snapshots for both simulations, where the simulated galaxies are comparable to local galaxies (see e.g. Schaye et al. 2015; Trayford et al. 2015). These specific simulations are chosen for their complementary ability to adequately resolve the formation of lower mass ($M < 10^9 M_{\odot}$) galaxies (Recal-025), and to provide sufficient statistics on the properties of rarer high mass galaxies (Ref-100). We limit our analyses to only those galaxies which contain a minimum count of >500 bound stellar particles at $z = 0$, to ensure reasonable sampling errors on derived properties.

2.4.2 In/Ex-Situ Classification

The classification of any simulated star (or dark matter) particle as ‘in’ or ‘ex’-situ is a matter of some debate in the literature, with several schemes implemented to date (see e.g. Oser et al. 2010; Pillepich et al. 2015; Rodriguez-Gomez et al. 2016; Qu et al. 2017; Clauwens et al. 2018; Monachesi et al. 2019). In this current work we implement a scheme to classify each particle as described below.

CHAPTER 2

In common with most modern cosmological simulations, the EAGLE simulations track galaxy merger histories by post-processing halo and subhalo catalogues to produce ‘merger trees’. The structures are connected at different epochs using the D-Trees algorithm (Jiang et al. 2014) which tracks linked particles to identify progenitors and descendants. As galaxies merge, the total mass of each branch forming that galaxy is summed, and the larger branch mass is defined as the ‘main progenitor’.

In our scheme, the subhalo that an initial gas particle is a member of (if any) in the snapshot immediately before conversion to a star particle is identified. Following this, the unique identifier of that progenitor, as determined by the merger tree, is assigned to the particular star particle. If the particle happens to be unbound at that snapshot, the earliest snapshot after star formation in which the particle resides in a subgroup as a member is defined as its host.

We then compare the particle progenitor identifier to the identifier of the subhalo the particle is a member of at $z = 0$. If the subhalo at the snapshot prior to star formation is in the main branch of the final galaxy, the particle is considered in-situ. If the progenitor galaxy is not in the main branch it is defined as ex-situ.

The result is that each of the particles comprising a simulated galaxy at $z = 0$ has a flag denoting the nature of its origin. This is performed for all particles and data can be limited to a chosen aperture as usual along with other properties. In addition to this flag, and to the standard properties recorded for each EAGLE particle in its snapshot (e.g. stellar mass, metallicity, coordinates); we also calculate the distance from the galaxy centre (defined by the position of the minimum of the gravitational potential, itself the position of the most bound particle) for each particle. From this information it is trivial to compute spherically averaged stellar half-mass radii ($r_{1/2}$). This can be achieved simply by summing stellar particles in order of absolute distance to the galaxy centre until half the total mass within a

CHAPTER 2

chosen aperture (in this study, 100pkpc) has been reached. Using this information it is then possible to search for correlations between in/ex-situ fraction and a host of final galaxy properties.

Combining the status of the particle origin with other EAGLE particle properties allows us to mask to in-situ or ex-situ stars. We use this to examine ensemble properties as a function of radius, stellar mass and halo mass for individual galaxies. Figure 2.1 shows a single high mass galaxy where we have divided the stellar components by both origin and galactocentric distance to demonstrate the Age-Metallicity relations of these populations.

2.4.3 Galaxy Properties and Classification

A further property that is of interest to observers is the morphological type of galaxy under study. This is especially true in this work as morphological transformation has long been thought to be related to merger history (see e.g. Querejeta et al. 2015; Martin et al. 2018), and in fact the addition of ex-situ stars is suggested as the main mode of mass assembly for large early-type galaxies (Martin et al. 2018).

Using the co-rotational stellar energy parameter κ_{co} made available as part of the EAGLE data release (see e.g. Thob et al. 2019) for each galaxy in the simulations, we separate galaxies into the ‘blue sequence’ of disk starforming galaxies ($\kappa_{co} > 0.4$) and ‘red sequence’ of more spheroidal passively evolving galaxies ($\kappa_{co} < 0.4$) as advocated by Correa et al. (2017). The method is based on earlier development in Sales et al. (2010) in which rotational energy is quantified as the fraction of kinetic energy invested in ordered rotation. However the Correa et al. (2017) method instead uses co-rotational energy, defined as:

$$\kappa_{co} = \frac{K_{co}^{rot}}{K} = \frac{1}{K} \sum_{i, L_{z,i} > 0} \frac{1}{2} m_i \left(\frac{L_{z,i}}{m_i R_i} \right)^2 \quad (2.1)$$

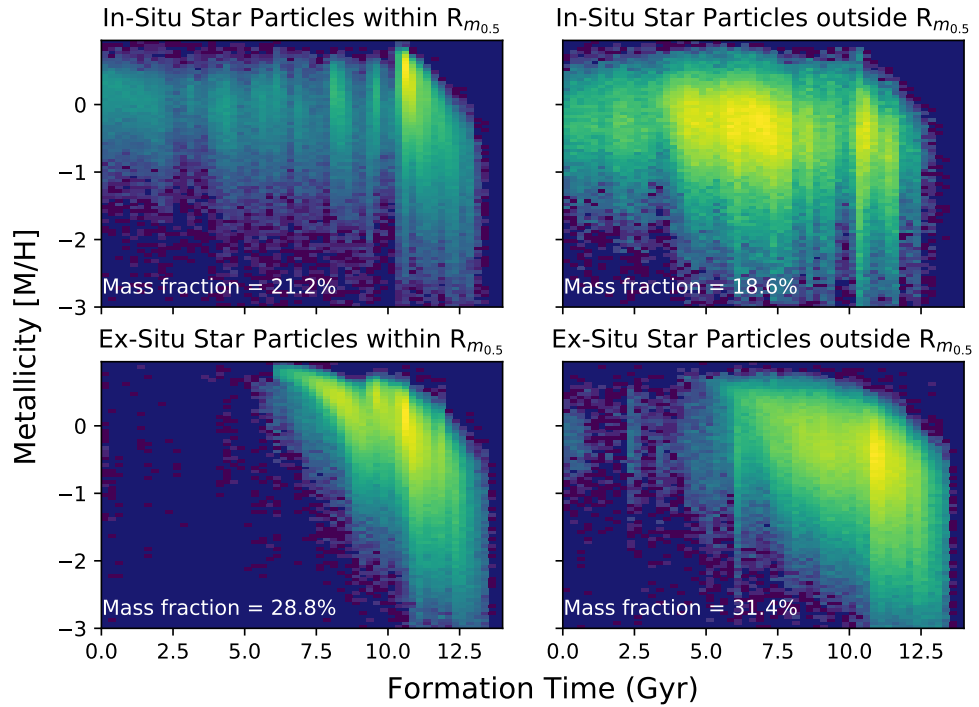


Figure 2.1: The age-metallicity plane for a single massive ($M_* = 4.5 \times 10^{11} M_\odot$) EAGLE galaxy, separated by in and ex-situ populations, as well as the location of stars inside or outside of the half-mass radius. Metallicity was calculated using the stellar particles only, assuming $Z_\odot=0.012$ for consistency with yields from the wider EAGLE project. The percentage share of the total galactic stellar mass is provided in the lower left corner of each panel. Colour demonstrates point density of particles within a bin, and is normalised to 1 individually for each panel. As can be seen for this galaxy ex-situ stars dominate at all radii, but especially outside the half mass radius.

CHAPTER 2

where ($L_{z,i} > 0$) defines all co-rotating stellar particles within 100 pkpc of the galactic centre, and R_i is the 2-dimensional radius in the plane normal to the rotation axis. This is shown to be efficient in classifying galaxies in the EAGLE simulations (Correa et al. 2017).

As an independent check of this morphological classification we also apply a separation based on specific star formation rate (sSFR). By plotting stellar mass vs sSFR for the EAGLE galaxy sample, a boundary sSFR of 0.01 Gyr^{-1} is found to effectively separate the blue sequence and red sequence. Applying this selection only alters the classification of 6.35% of galaxies, relative to the κ_{co} selection, leading to no significant changes of any of our findings. Therefore, to maintain consistency with other studies using EAGLE simulations we use the κ_{co} classification in all further analyses.

2.4.4 The EAGLE Galaxy Sample

The histogram in the upper panel of Figure 2.2 shows our final sample of EAGLE galaxies. Sharp discontinuities in the apparent distribution of galaxies are the result of the previously described lower particle limit of 500 stellar particles per galaxy. This equates to a minimum stellar mass within 100pkpc of $4.01 \times 10^7 M_\odot$ and $3.48 \times 10^8 M_\odot$ at $z = 0$ for the Recal-025 and Ref-100 simulations respectively. The most massive galaxies in the two samples have mass $1.12 \times 10^{11} M_\odot$ (Recal-025) and $1.93 \times 10^{12} M_\odot$ (Ref-100). As can clearly be seen, the Recal-025 and Ref-100 simulation sample different parts of the mass distribution, owing to their differing resolutions and volumes. Recal-025 provides high numbers of low-mass galaxies in the range $\sim 10^{7.5} M_\odot$ - $10^{9.5} M_\odot$, with the Ref-100 simulation taking over (with overlap) to provide galaxies in the range $\sim 10^{8.5} M_\odot$ - $10^{12} M_\odot$. Though Recal-025 provides some small number of galaxies of mass $> 10^{9.5} M_\odot$, the fraction is barely noticeable compared to those provided by Ref-100.

CHAPTER 2

The lower two panels of Figure 2.2 show the distribution of objects across the mass-size plane. The half-mass radius is determined following the prescription provided in Section 2.4.2. These panels display observational best fit lines from Lange et al. (2015) produced for the Galaxy And Mass Assembly (GAMA) survey, in which $M_* - r_{1/2}$ relations are built for ‘red’ and ‘blue’ sequence galaxy samples using a double power-law function described by Shen et al. (2003)

$$r_{1/2} = \gamma \left(\frac{M_*}{M_\odot} \right)^\alpha \left(1 + \frac{M_*}{M_0} \right)^{\beta-\alpha}. \quad (2.2)$$

We choose to overplot the K-band fits due to the fact that the K-band has been shown to be a good stellar mass tracer due to its relative insensitivity to both extinction and the effects of young hot stars which bias mass-to-light measurements in the optical (e.g. McGaugh & Schombert 2014; Norris et al. 2016). Hence we expect that K should provide the closest match between the simulations which output stellar mass, and the observationally inferred values. The parameters for Equation 2.2 are provided in Shen et al. (2003) for K band. For the blue sample, these parameters are $\gamma = 0.1$, $\alpha = 0.16$, $\beta = 1.00$ and $M_0 = 33.62 \times 10^{10} M_\odot$. Parameters for the red sample are $\gamma = 0.12$, $\alpha = 0.1$, $\beta = 0.78$ and $M_0 = 2.25 \times 10^{10} M_\odot$.

As Figure 2.2 demonstrates, the simulated galaxies appear to be slightly more extended at fixed mass than real galaxies. This has a number of potential explanations. One is the result of over-efficient feedback within the EAGLE simulations (see e.g. Crain et al. 2015) which moves galaxies of fixed M_* into haloes of higher M_{200} (Mass within an aperture of 200kpc) potentially extending the galaxies. A second explanation is described in Ludlow et al. (2019), wherein if a simulation contains particle species of differing mass (such as the lower mass baryonic and higher mass dark-matter particles in EAGLE), 2-body scattering can be artificially inflated. This occurs when higher mass species effectively transfer kinetic energy to lower mass species, artificially raising their energy. This may contribute to the

CHAPTER 2

greater extent of the EAGLE galaxies compared to observation that we see in Figure 2.2, especially in lower mass galaxies.

2.4.5 Summary of Other Quantities

Units and conversions are kept consistent with prior EAGLE analysis works. An aperture of 100pkpc is considered for all objects unless otherwise stated. This ensures that galaxies of $M_* > 10^{11} M_\odot$ are properly considered, as demonstrated in figure 4 of Schaye et al. (2015). For subhalo mass units, only the baryonic stellar component is used; however when analysing halo mass (such as in section 2.5.1.3) we use the total mass within the corresponding group Crit200 radius, where group Crit200 defines the radius at which mass is equal to 200 times the critical mass of the universe.

In order to use the EAGLE simulations to provide robust predictions for observational studies, we provide estimates of the ex-situ mass fraction as a function of more readily observable quantities. To achieve this, each simulated galaxy is analysed to determine the ex-situ fraction as a function of visual (i.e. V-band) surface brightness. The results of this are discussed in Section 2.5.2.2

To estimate surface brightness quantities, galaxies are projected in the xy plane, effectively randomising the viewing angle relative to the observer. This is intended to give an accurate representation of galaxies compared to real observing conditions. Each galaxy is set at a fiducial distance of 16.5Mpc (the approximate distance to the Virgo cluster). Following this, the luminosity of each particle is calculated by matching each to interpolated stellar mass-to-light relations built from the single stellar population models of Maraston (2005).

Derivation of projected ellipticity is completed using the formulae described by Lagos et al. (2018). Here, r-band luminosity is used to calculate the projected ellipticity by:

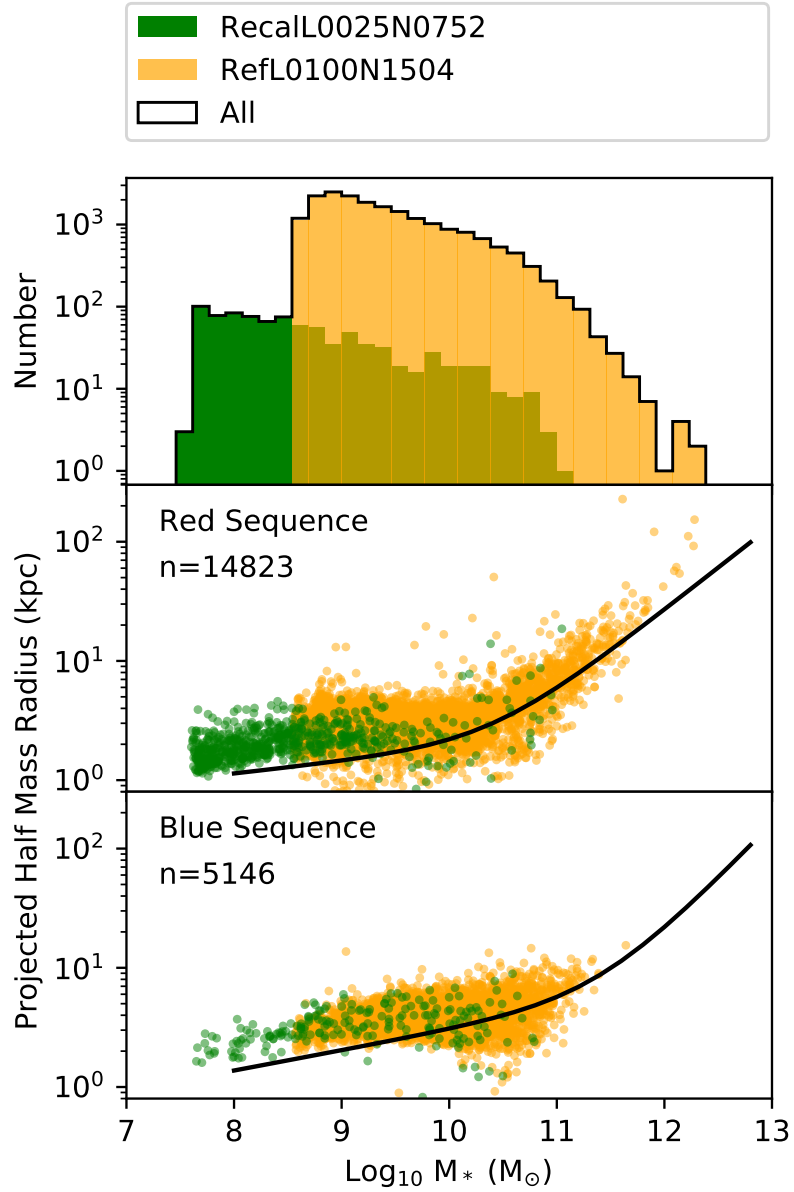


Figure 2.2: Origin of all objects used in subsequent mass size plots. The upper panel shows a histogram of the mass distribution of simulated galaxies across the (\log_{10}) stellar mass axis. The centre and lower panels show the same distribution in the mass-size plane, with objects separated into Red sequence and Blue cloud populations, using the κ_{co} parameter (see section 2.4.3). The radius shown is projected half mass radius, averaged over the three orthogonal projections. Fit lines show the double power law mass-size trend of the observed galaxy population in K-band, as described in Lange et al. (2015). A similar figure for only the Ref-100 simulation can be found in Furlong et al. (2016) with comparison to measurements from van der Wel et al. (2014) and Shen et al. (2003).

CHAPTER 2

$$\epsilon = 1 - \sqrt{\frac{b^2}{a^2}} \quad (2.3)$$

Where,

$$a^2 = \frac{\bar{x}^2 + \bar{y}^2}{2} + \sqrt{\left(\frac{\bar{x}^2 - \bar{y}^2}{2}\right)^2 + \bar{x}\bar{y}} \quad (2.4)$$

$$b^2 = \frac{\bar{x}^2 + \bar{y}^2}{2} - \sqrt{\left(\frac{\bar{x}^2 - \bar{y}^2}{2}\right)^2 + \bar{x}\bar{y}} \quad (2.5)$$

And,

$$\bar{x}^2 = \frac{\sum_i L_i x_i^2}{\sum_i L_i} \quad (2.6)$$

$$\bar{y}^2 = \frac{\sum_i L_i y_i^2}{\sum_i L_i} \quad (2.7)$$

$$\bar{x}\bar{y} = \frac{\sum_i L_i x_i y_i}{\sum_i L_i} \quad (2.8)$$

In which L is the r-band luminosity, and x and y are the particle coordinates in the projected frame (with the centre of the galaxy set to 0,0). The position angle of the elliptical fit is given by:

$$\theta_{PA} = \frac{1}{2} \tan^{-1} \left(\frac{2\bar{x}\bar{y}}{\bar{x}^2 - \bar{y}^2} \right) \quad (2.9)$$

Adaptive bins measure the luminosity of each galaxy from the centre outwards. Particles are binned in order of distance (weighted by ellipticity) from the centre, with every 75 particles justifying a new bin. Area and the sum of the luminosity of particles within each bin is calculated, allowing us to build a luminosity profile across the galaxy. Ellipse major axis positions, corresponding to the mid-point between integer magnitudes, are read from the luminosity profile (e.g., choosing inner and outer elliptical radii of 22.5 and 23.5 magnitudes for a magnitude of 23). With these boundaries we define new concentric elliptical bins with the total luminosity

of particles contained in a bin providing magnitudes per square arcsecond. Using the previously described ex- or in-situ classification of each particle, we can then determine the ex-situ fraction at any desired surface brightness value.

This method is detailed in Figure 2.3.

2.5 Results

2.5.1 Ex-situ Fraction as a Function of Galaxy Properties

2.5.1.1 Ex-situ Fraction as a Function of Galaxy Mass

In order to examine the reliability of our methodology, we first examine the dependence of ex-situ fraction on various other properties. This allows us to compare to the results of previous studies, and therefore provides confidence in the reliability of our later predictions.

Figure 2.4 displays the stellar mass dependence of the ex-situ fraction for our EAGLE sample along with a selection of other literature sources. The layout follows that of Figure 3 of Rodriguez-Gomez et al. (2016) in which the same analysis is performed on simulated galaxies from the Illustris simulations (Genel et al. 2014; Vogelsberger et al. 2014; Nelson et al. 2015).

As can be seen in Figure 2.4 our sample exhibits the same overall trend as found by previous studies (Oser et al. 2010; Rodriguez-Gomez et al. 2016; Qu et al. 2017; Clauwens et al. 2018), in that ex-situ fraction increases with increasing galaxy mass. In common with Qu et al. (2017), we find that EAGLE galaxies display systematically higher ex-situ fractions than Illustris (Rodriguez-Gomez et al. 2016) at all stellar masses, though the two samples are consistent within their mutual scatters. IllustrisTNG displays almost identical results as EAGLE at high mass ($>2 \times 10^{11} M_{\odot}$) (Tacchella et al. 2019). Our sample also displays only marginally lower ex-situ fractions at fixed mass than either Oser et al. (2010) or Clauwens

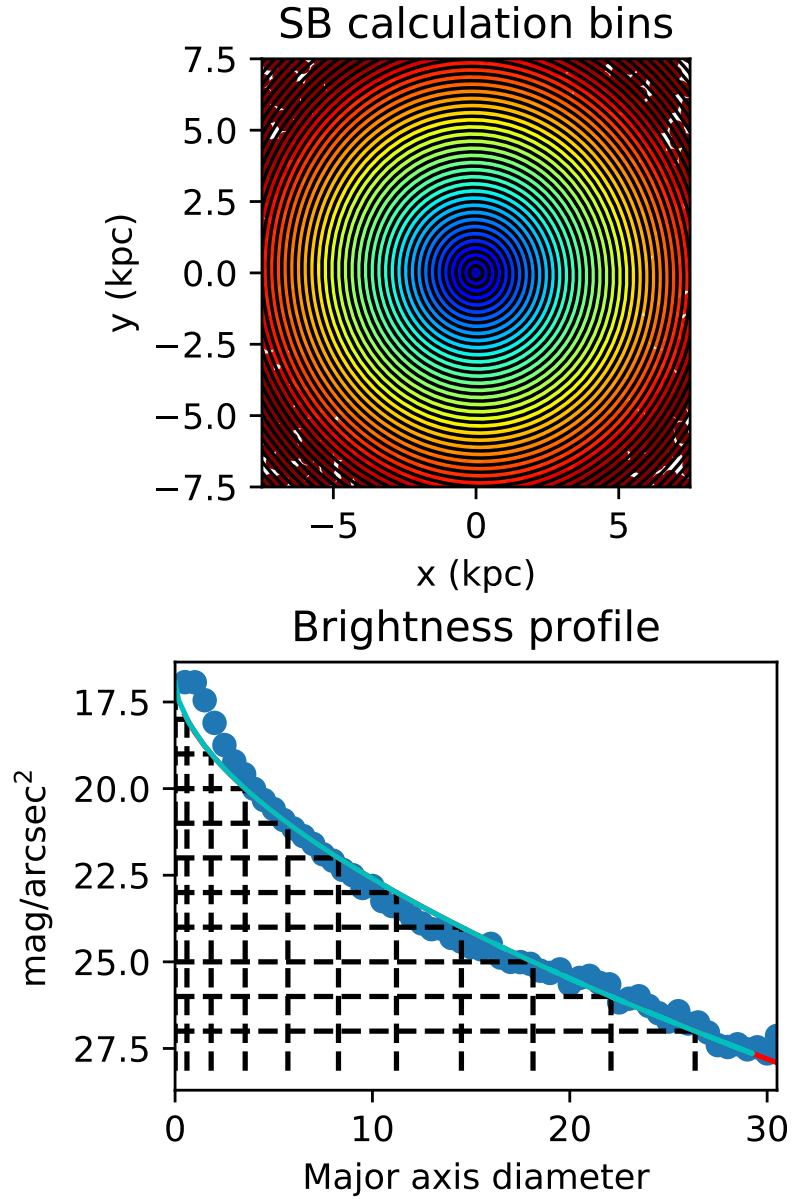


Figure 2.3: Surface brightness determination methodology of a randomly selected Recal-025 galaxy of stellar mass $1.01 \times 10^{11} M_{\odot}$. The upper panel shows elliptical bins used to calculate the surface brightness profile. Boundaries expand from the centre, binning particles from the inside out with respect to the galaxy ellipticity. Coloured points show the distance of a given stellar particle from the closest point on the ellipse boundary for an ellipse with major axis 100kpc. The lower panel shows the surface brightness profile calculated from the binning, in units of apparent magnitudes per square arcsecond. Blue points show the average brightness within each bin, approximated by a function overlaid as a solid line. Integer magnitudes, and the major axis diameter at which these magnitudes occur, are marked with dashed lines. This method is used for all galaxies in the sample.

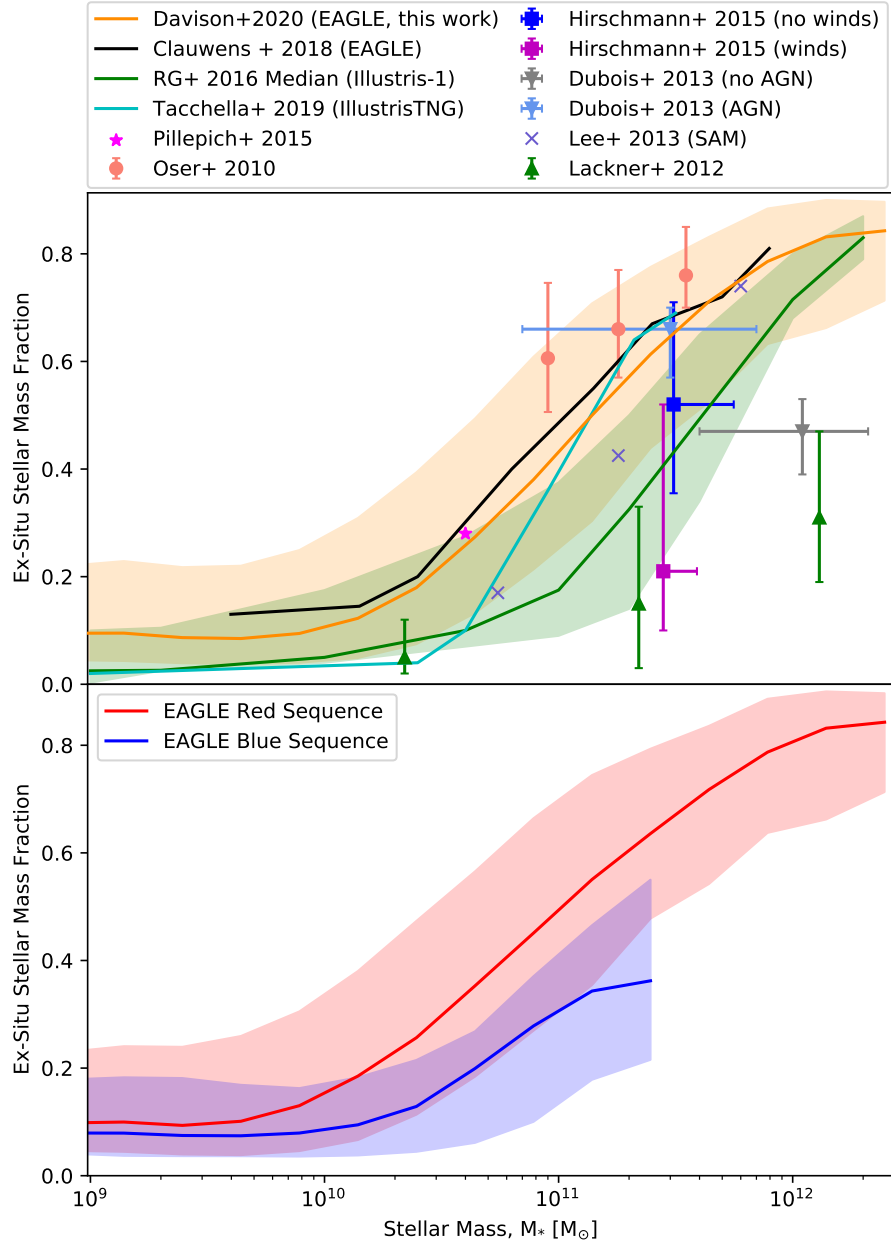


Figure 2.4: This figure (modelled after figure 3 from Rodriguez-Gomez et al. (2016)) shows ex-situ fraction as a function of stellar mass and adds $z=0$ EAGLE data for comparison. EAGLE data consists of a sample built from the Recal-025 and Ref-100 simulations as detailed in Figure 2.2. The upper panel compares the full sample of EAGLE galaxies to previous studies. The lower panel separates the EAGLE sample into blue sequence and red-sequence components using the κ_{c_0} parameterisation. Shaded regions show 1σ percentile scatter in the ex-situ plane. To reproduce accurately the Rodriguez-Gomez et al. (2016) figure, median ex-situ fraction is calculated with 0.25 dex mass bins with a minimum bin population of 8 (the highest mass bin) and a maximum bin population of 3172. Only particles inside of 100pkpc are considered.

CHAPTER 2

et al. (2018). The analysis of Clauwens et al. (2018) makes use of the same Ref-100 EAGLE simulation as this work, although it applies an independent method of classifying in- and ex-situ fraction. The fact that two independent methods for determining ex-situ fraction agree so well, when looking at the same simulation, is encouraging.

The origins of the differences between the ex-situ mass fractions of EAGLE and Illustris are explored by Qu et al. (2017), with the preponderance of the differences likely caused by differing stellar and AGN feedback treatment. Minor differences between values from our analysis and those of Clauwens et al. (2018) can be attributed to the systematic uncertainty associated with using differing methods to classify the origin of stars within a galaxy, such as assigning the particle to a progenitor galaxy prior to or after star formation occurs, as well as a difference in samples examined, with Clauwens et al. not including Recal-025 as we do. The fact that our results agree so closely with those found by several independent analyses of several independent simulations gives confidence that our sample is reliably capturing the underlying behaviour.

The lower panel of Figure 2.4 shows the same data but now split by our morphology classification. Unfortunately the number of ‘blue sequence’ galaxies drops off dramatically above $10^{11} M_{\odot}$, which is where the significant increase in ex-situ fraction with mass becomes apparent for the full sample. However, within the stellar mass range where both galaxy types have sufficient numbers for analysis ($M_{*} < 10^{11} M_{\odot}$), there is a statistically significant difference in the two distributions (the Kolomogorov-Smirnov test gives a p-value of $p < 10^{-6}$, therefore the hypothesis that the samples come from the same distributions can be rejected). This difference is characterised in the sense that blue sequence galaxies have a lower ex-situ fraction compared to red sequence galaxies of the same mass. This finding is consistent with that of (Rodriguez-Gomez et al. 2016), who found a similar trend for Illustris

CHAPTER 2

galaxies.

2.5.1.2 Ex-Situ Fractions across the Mass-Size Plane

We next examine the behaviour of the ex-situ fraction across the galaxy mass-size plane. To display this information, data are projected onto mass-size axes with colour denoting the ex-situ fraction. The great variety in the density of the galaxies across the mass-size plane is mitigated using a tessellated hexagonal binning approach. Bins are adjusted such that they remain of equal size on log-log axes. Galaxies falling within each bin are identified, and the median of the ex-situ fraction for all galaxies within the bin is calculated. Bins have a minimum of 3 galaxies, and the most populated bin contains 1007 galaxies.

We separate particles by radial location within a galaxy, respective to the half mass radius $r_{1/2}$. In the upper left panel of Figure 2.5 we show the ex-situ fraction of particles within $r_{1/2}$, and in the centre left panel only particles with a distance from the galaxy centre greater than $2r_{1/2}$ ($r < 100\text{pkpc}$). Finally, in the lower left panel, we show all particles within an aperture of 100pkpc . A LOESS (Locally Weighted Scatterplot Smoothing) smoothing function (Cappellari et al. 2013) is applied to the image, this implements 2D local adaptive smoothing across the plane (Cleveland & Devlin 1988) to reduce the influence of outlier points.

Examination of Figure 2.5 reaffirms the finding from Figure 2.4 that as stellar mass increases, so does ex-situ fraction. This trend is clearly present for stars in both the inner and outer regions of galaxies, though clearly ex-situ stars comprise a larger fraction of those found at larger radii. This finding is therefore consistent with those of previous studies which indicate that the majority of ex-situ stars are deposited on the outer regions of galaxies (see e.g. Oser et al. 2010; Rodriguez-Gomez et al. 2016).

CHAPTER 2

As a further extension to this analysis we also examine potential relations between ex-situ fraction and galaxy size. To do this at fixed mass we split the galaxy population into three equal bins (by number of galaxies) of galaxy radius, and then calculate the median ex-situ fraction for each bin. These median lines represent the 33% most extended, 33% most compact, and 33% intermediate radius galaxies respectively. The radii separated by the bins varies with stellar mass, such that there are always a third of the galaxies at fixed mass within each bin. The right-hand panels of Figure 2.5 show the result of this procedure. As can be clearly seen there is a distinct separation of the median ex-situ fractions of compact, mid-sized and extended galaxies, for all galaxies at all masses. This separation is apparent both for the stars contained within $r_{1/2}$, and even more so for those beyond $2r_{1/2}$.

The fact that at fixed mass, more extended galaxies exhibit higher ex-situ mass fraction supports the idea that they are larger because they accreted more stars during generally “dry” mergers after the initial burst of in-situ star formation that formed the inner regions of the galaxy. The stars accreted during galaxy-galaxy mergers or fly-by interactions will preferentially be deposited at larger radii leading to an increase in the half-mass radius of the galaxy (see e.g. Oser et al. 2010; Rodriguez-Gomez et al. 2016). In contrast, gas accreted during “wet” galaxy interactions can find its way to the inner regions of the galaxy, as it is dissipative. There it can increase the number and density of in-situ stars, potentially even decreasing the half-mass radius of the galaxy (see e.g. Du et al. 2019).

In Figure 2.6 we view the variance of each bin. For all regions examined the variance was small. Outlier areas showed a maximum variance of 0.2, however the mean variance is a tiny 0.043. Variance is smallest for the largest regions considered which is indicative of the larger sample size.

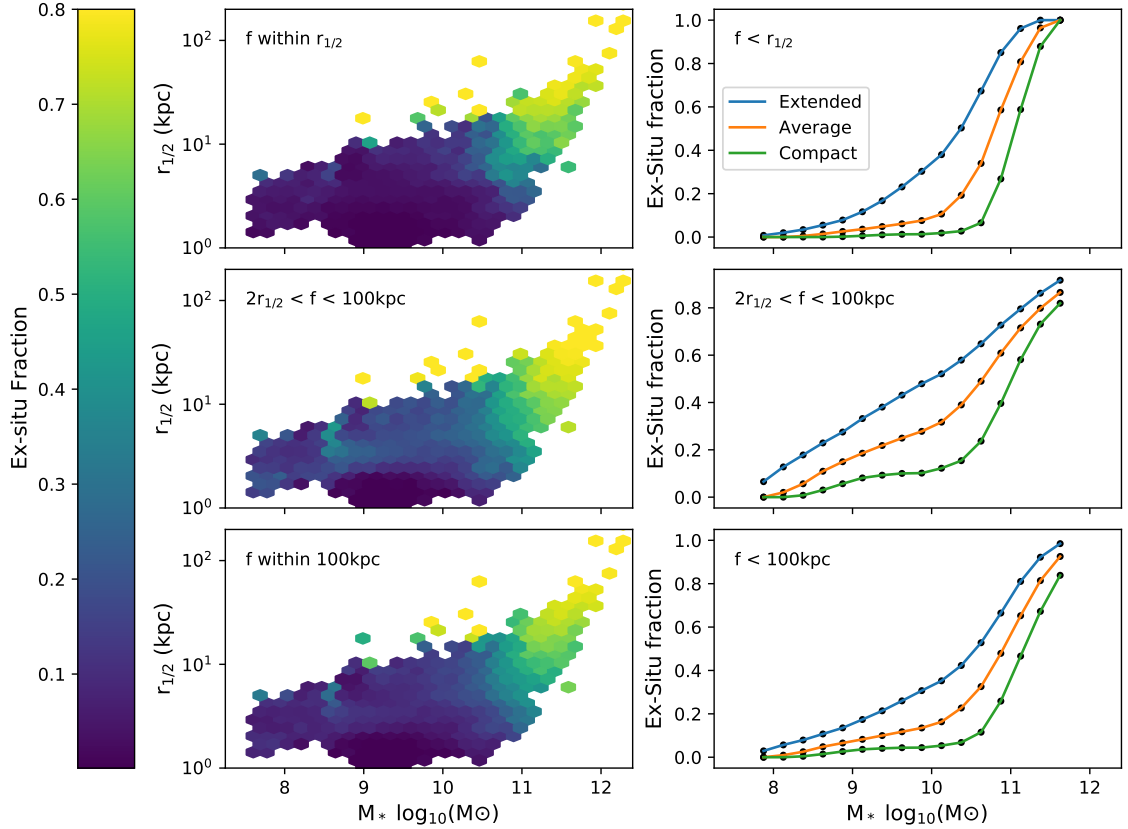


Figure 2.5: On the left panels, binned $z=0$ simulated galaxies are shown on the mass-size plane with colouration by ex-situ fraction. The upper-left panel limits to only star particles up to $r_{1/2}$, and the middle-left panel limits to all particles outside of $2r_{1/2}$ ($r < 100\text{pkpc}$). Finally the lower left panel includes all particles within an aperture of 100pkpc . The panels use a 2D LOESS smoothing function to remove small fluctuations, and to better display the general trend. Colour is given by the median of ex-situ values within a hexagonal bin, with a minimum of 3 objects in a bin, a maximum of 1007 objects in a bin, and an average of 57 objects in a bin. The right-hand panels show mass against ex-situ fraction, when separated into 3 bins of galaxy radius at fixed mass. The ‘Extended’ line collects the upper 33% of particles spatially on the y axis. The ‘Average’ line represents the central 33% and the ‘Compact’ line collects the lowest 33% of objects. The stellar mass axis is binned into 0.25dex bins, with a minimum of 17 objects in a bin.

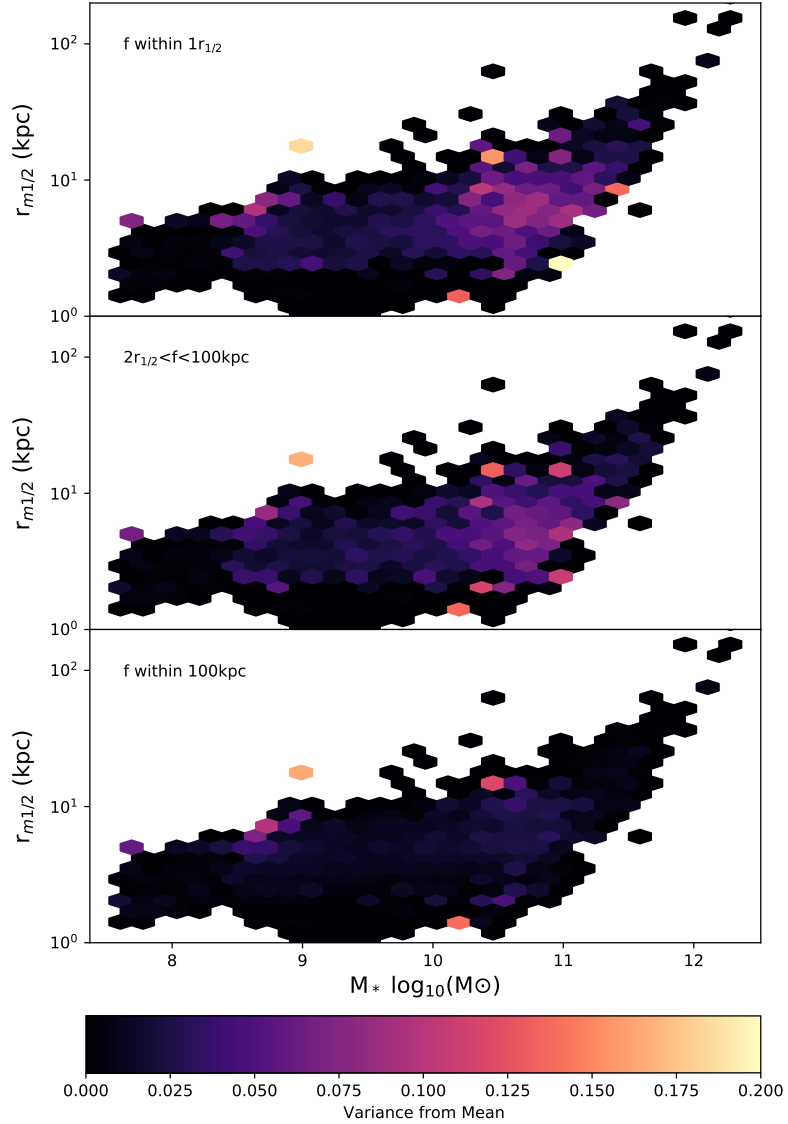


Figure 2.6: Binned $z=0$ simulated galaxies are shown on the mass-size plane with colouration by variance of ex-situ fraction. The top panel limits to only star particles up to $r_{1/2}$, and the middle panel limits to all particles outside of $2r_{1/2}$ ($r < 100\text{pkpc}$). Finally the lower panel includes all particles within an aperture of 100pkpc . The panels use a 2D LOESS smoothing function to remove small fluctuations, and to better display the general trend. Colour is given by the median of ex-situ values within a hexagonal bin, with a minimum of 3 objects in a bin, a maximum of 1007 objects in a bin, and an average of 57 objects in a bin.

2.5.1.3 Ex-situ Fraction as a Function of Parent Halo Mass

To probe for differences in ex-situ fraction with halo mass, we next limit the sample to include only satellite galaxies (with >500 stellar particles) and separate by the mass of the halo they reside in. Figure 2.7 shows the result of this analysis for all satellites. Analysis was also performed for the centrals only. Though similar effects as discussed below were present, statistical resolution was strained and so the analysis was excluded from this study. We see in Figure 2.7 that ex-situ fraction appears to be highest in objects with a lower parent halo mass, becoming especially distinct at $\sim M_* > 10^{10.5} M_\odot$. At first glance this may seem counter-intuitive, considering that one might reasonably expect more merger activity within denser environments such as those of rich clusters. However, such trends have been hinted at in previous analyses, for example in Pillepich et al. 2018, where their figure 12 shows a similar flattening of the ex-situ fraction increase for the most massive haloes, and indeed a drop in ex-situ fraction for stars in the inner regions of galaxies in the highest mass haloes.

In order to check the robustness of this seemingly counter-intuitive result we examine the dependence of ex-situ fraction when considering the maximum of the circular velocity curve with z , $v_{\max}(z)$ (V_{\max}). We use this rather than halo mass as an independent estimator of galaxy environment. The choice to use the maximum of the circular velocity curve reached at any point in the history of a galaxy ensures that we are not misled by potential stripping at $z = 0$. Such an assumption could potentially lead to temporary increases or decreases in the estimated circular velocity. Therefore, using the maximum of V_{\max} (most often occurring at between $z = 0$ and $z = 1$) by tracking V_{\max} back down the merger history and finding the peak value we secure a secondary robust method to characterise the galaxy environment potential. This analysis showed an overall trend consistent with that seen in Figure 2.7. Again we find it is generally the intermediate mass haloes

CHAPTER 2

(identified as those with lower peak V_{max}) which display maximum ex-situ fraction at fixed galaxy mass. Possible mechanisms for this effect are discussed in section 2.6. Further clarifications of the robustness of this result with respect to known Subfind issues are found in the Appendix.

The fact that we observe significant differences in ex-situ fraction as a function of parent halo mass suggests a possible explanation for the observation that blue sequence galaxies display lower ex-situ fraction than red sequence galaxies of the same stellar mass (see Figure 2.4); that it is the result of the red sequence galaxies living preferentially in denser regions. To test this hypothesis we undertake the following test; we produce samples of red and blue sequence galaxies in fixed stellar mass bins which have the same halo stellar mass distribution. In practice this means that within each stellar mass bin we randomly sub-select red sequence galaxies (which are more common in the simulations), to match the observed halo mass distribution of the blue galaxies. In the rare cases where no red sequence galaxy of the appropriate stellar mass has the parent halo mass of a particular blue sequence galaxy, both galaxies are removed from their respective samples. Though this significantly reduces the number of objects available in the subset, the halo distributions match one-to-one.

With this subset, we repeat the same analysis as section 2.5.1.1 as a function of stellar mass for both galaxy types. This allows us to examine whether samples of early and late type galaxies, matched in mass and halo mass, still display different ex-situ fractions. In Figure 2.8 we see that the new sub-selected sample shows no preference for higher or lower ex-situ fraction compared to the original sample. Thus persists the systematic trend that early types have a larger ex-situ fraction. We employ 50 Monte-Carlo simulations to estimate error from our random selection, and all original positions are well within these errors. This is possibly a result of the large uncertainties in ex-situ fraction, though the general trends are highly

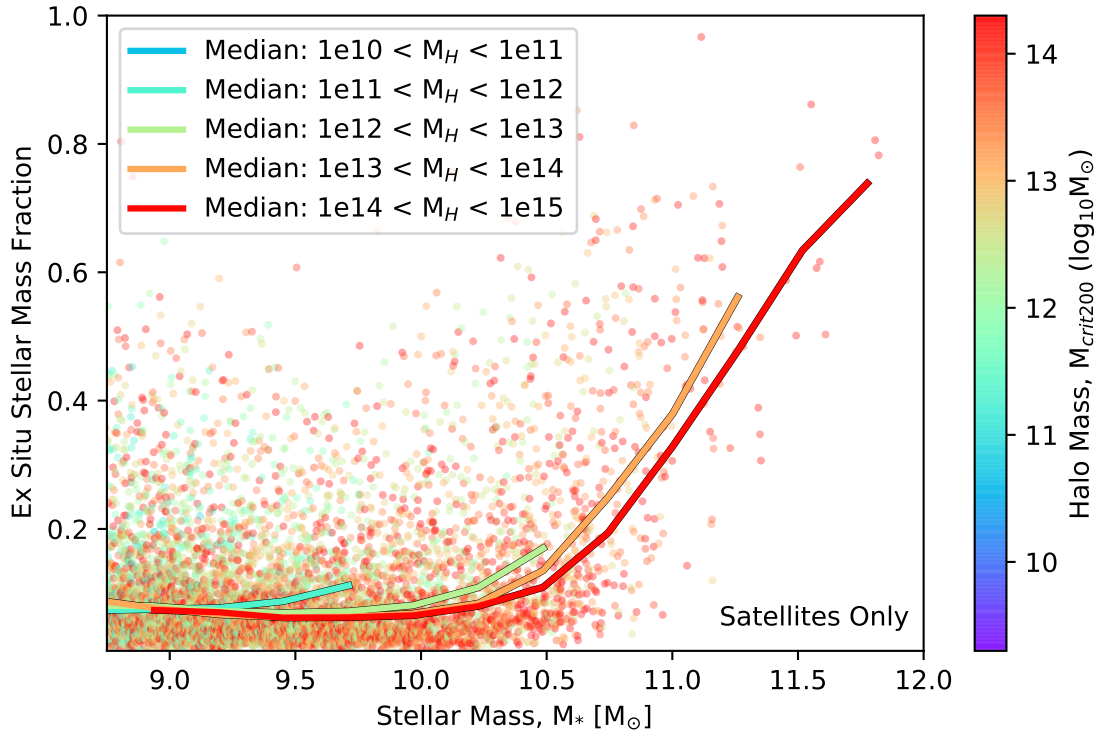


Figure 2.7: Ex-situ fraction within 100kpc for all $z=0$ satellite galaxies with >500 stellar particles against stellar mass, and split by total halo mass (M_H). Individual objects are coloured by the mass of the halo to which they belong. Solid lines show the median position of the ex-situ fraction for objects within 5 bins of parent halo mass, across 0.25 dex wide bins of stellar mass. There are a minimum of 5 objects per bin, and an average of 220 objects per bin. The $1e10$ - $1e11$ halo mass bin is obscured due to its similar location to the $1e11$ - $1e12$ halo mass line.

CHAPTER 2

consistent. As a result we can be reasonably sure that the differences in ex-situ fraction between red and blue galaxies at fixed mass do not appear to be driven by systematic differences in halo mass distribution.

2.5.2 Ex-situ Fraction across Galaxies' bodies

2.5.2.1 Ex-situ Fraction as a Function of Radius

We produce an analysis of all galaxies of > 500 particles as a function of individual subhalo galactocentric distance. When binned by stellar mass, this allows us to see the increase of ex-situ fraction with radius, for each stellar mass bin. This is shown in Figure 2.9.

From Figure 2.9 we see that for less massive galaxies ($10^9 M_{\odot}$ - $10^{10} M_{\odot}$) not only does the mass fraction of ex-situ stars increase with galactocentric radius, so does the rate of increase. For more massive galaxies ($10^{11} M_{\odot}$ - $10^{12} M_{\odot}$) the ex-situ fraction increase is linear with galactocentric radius, with even the most central regions containing an average ex-situ fraction of $> 65\%$. This can also be seen in the Illustris simulations, as is shown by Rodriguez-Gomez et al. (2016) in their figure 10.

2.5.2.2 Ex-situ Fraction as a Function of Surface Brightness

By linking the ex-situ fraction to the surface brightness (described in section 2.4.5), we create an observationally comparable parameter. This allows us to create predictions of ex-situ fraction which are verifiable observationally. The calculated surface brightness is paired with mass and size parameters of the simulated galaxies, adding a further dimension to the plots. Similarly to the analysis performed to investigate halo mass effects, the galaxies are split by stellar mass. Figure 2.10 shows the separation of EAGLE galaxies by mass, along with their average position in the surface brightness/ex-situ fraction plane.

CHAPTER 2

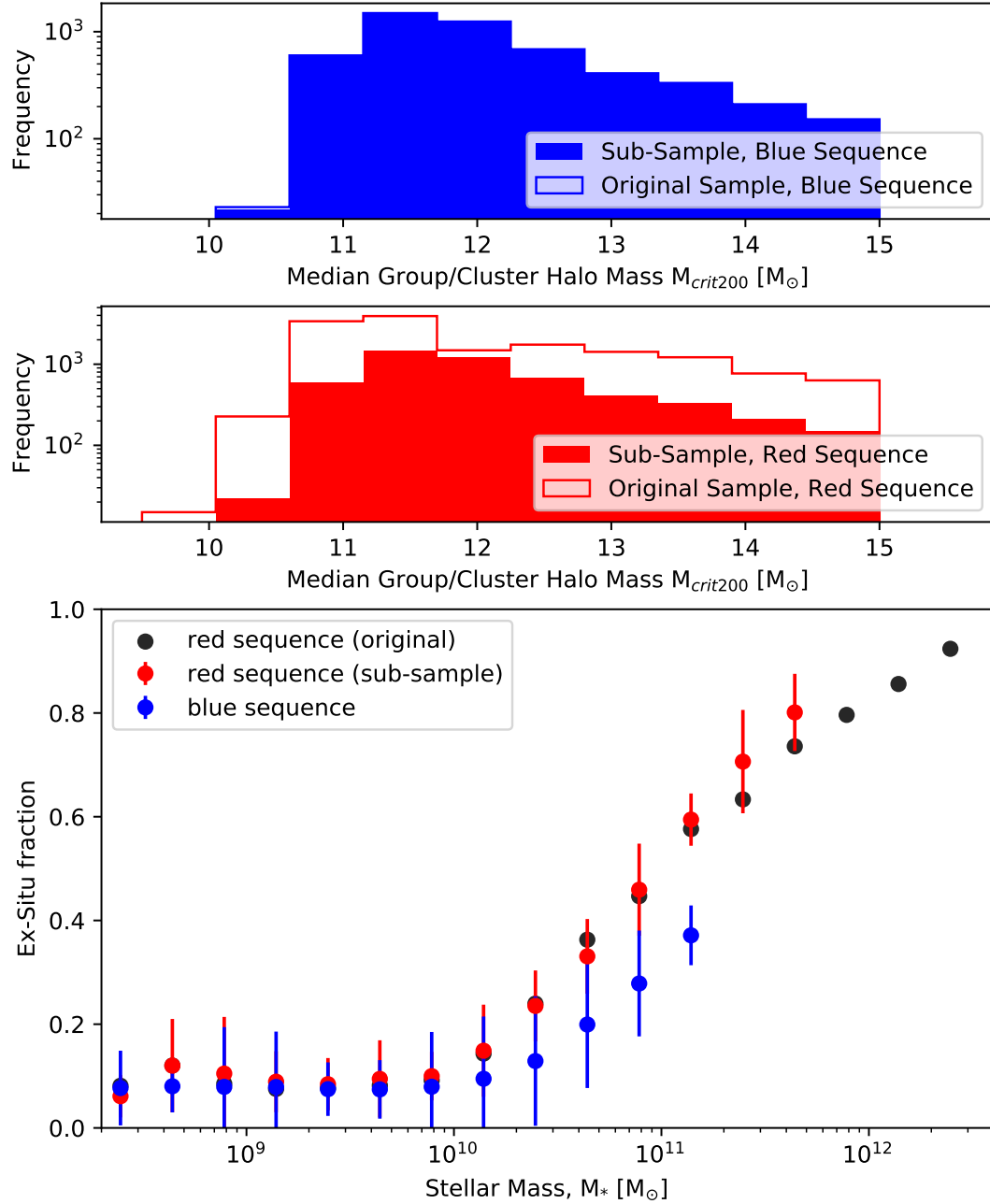


Figure 2.8: Ex-situ fraction of sub-selected galaxies, such that the halo mass distributions of red and blue sequence samples match. Top panels show original and new sample histograms. There are no residual differences between the two samples, as shown in the histograms. The lower panel shows the results of the stellar-mass-ex-situ distribution after the re-sampling with values binned in 0.25dex bins of stellar mass. There is no significant difference between the original data-set of red sequence galaxies, and the re-sampled data-set of red sequence galaxies

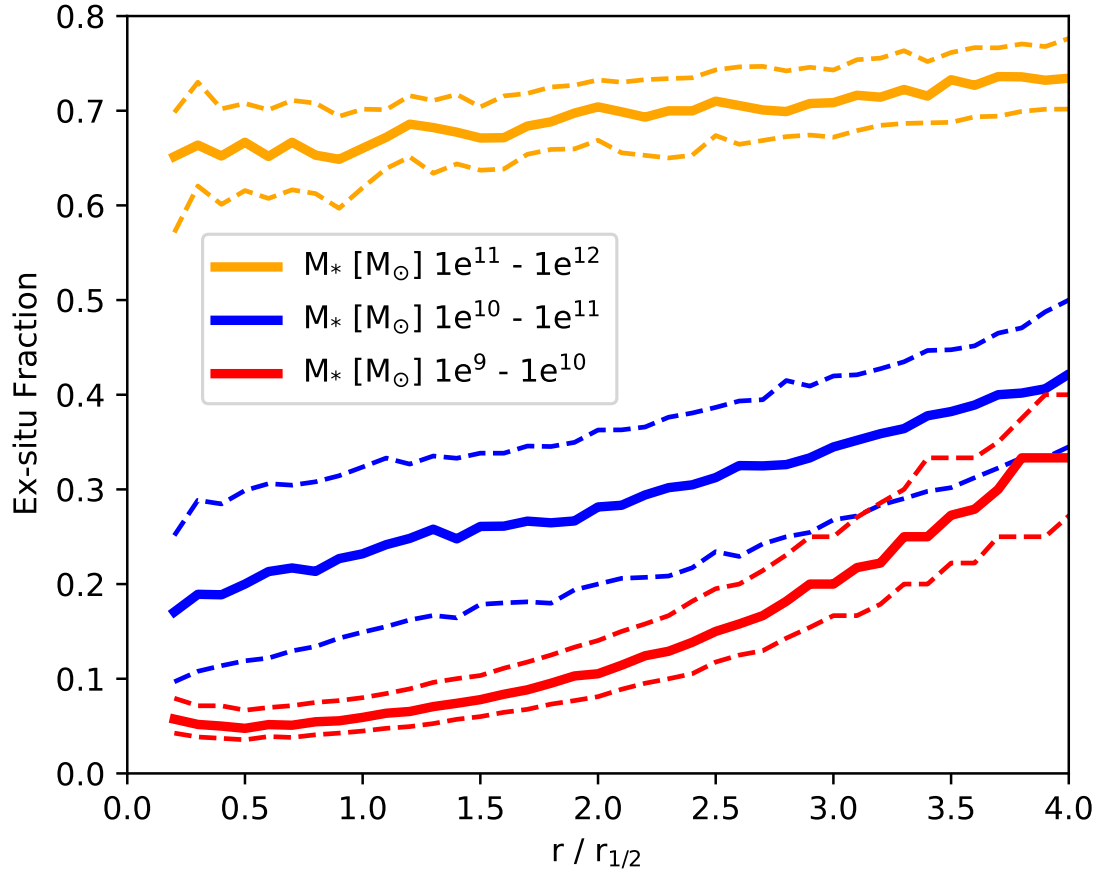


Figure 2.9: Ex-situ fraction as a function of galactocentric radius, normalised to individual subhalo half mass radius ($z=0$). Galaxies are binned by total stellar mass. Solid lines show the average ex-situ fraction for a galaxy within the stellar mass bin. Dashed lines show 1σ percentile lines of the ex-situ scatter. Mean values are calculated from bins of size $0.1r_{1/2}$ with 6421 objects in the 10^9 - $10^{10}M_\odot$ sample, 1418 objects in the 10^{10} - $10^{11}M_\odot$ sample and 263 objects in the 10^{11} - $10^{12}M_\odot$ sample.

CHAPTER 2

The Figure shows a mostly low ex-situ fraction, whilst surface brightness increases up to a stellar mass of $10^{10} - 10^{11} M_{\odot}$. At this turning point, as mass increases, surface brightness decreases, whilst ex-situ fraction rises. This is consistent with our picture of galaxy evolution, in which average surface brightness within $r_{1/2}$ increases with stellar mass initially. Then beyond a stellar mass of $\sim 10^{10} - 10^{11} M_{\odot}$ ex-situ fraction begins to rapidly increase. As this occurs, the average surface brightness density decreases. This lends weight to the idea that ex-situ stars are preferentially accreted to the outskirts, where they increase the half-light radius, extending the galaxy and thereby reducing the average surface brightness within the effective radius. This can be seen in Figure 2.9 where high fractions of ex-situ stars are present at large galactocentric radii compared with the galaxy centres.

We then move to generating predictions for the ex-situ mass fraction as a function of galaxy mass and surface brightness. To ensure that all generated data can be quickly and intuitively compared to observed galaxies, our analysis is performed by examining the ex-situ fractions within radial bins containing like surface brightnesses.

Using the method described in Section 2.4.5, magnitudes per square arcsecond (calculated for an assumed distance of 16.5Mpc, the approximate distance to the Virgo cluster) are linked to the ex-situ fractions within the magnitude bins. These values are used to examine the median ex-situ fraction with mass, for constant surface brightnesses.

This is shown in Figure 2.11, where surface brightnesses of magnitudes 19 - 27 per square arcsecond are considered for V band. Sigmoid functions are fit to the data of the form:

$$\frac{c}{1 + e^{-a(x-b)}} + d \quad (2.10)$$

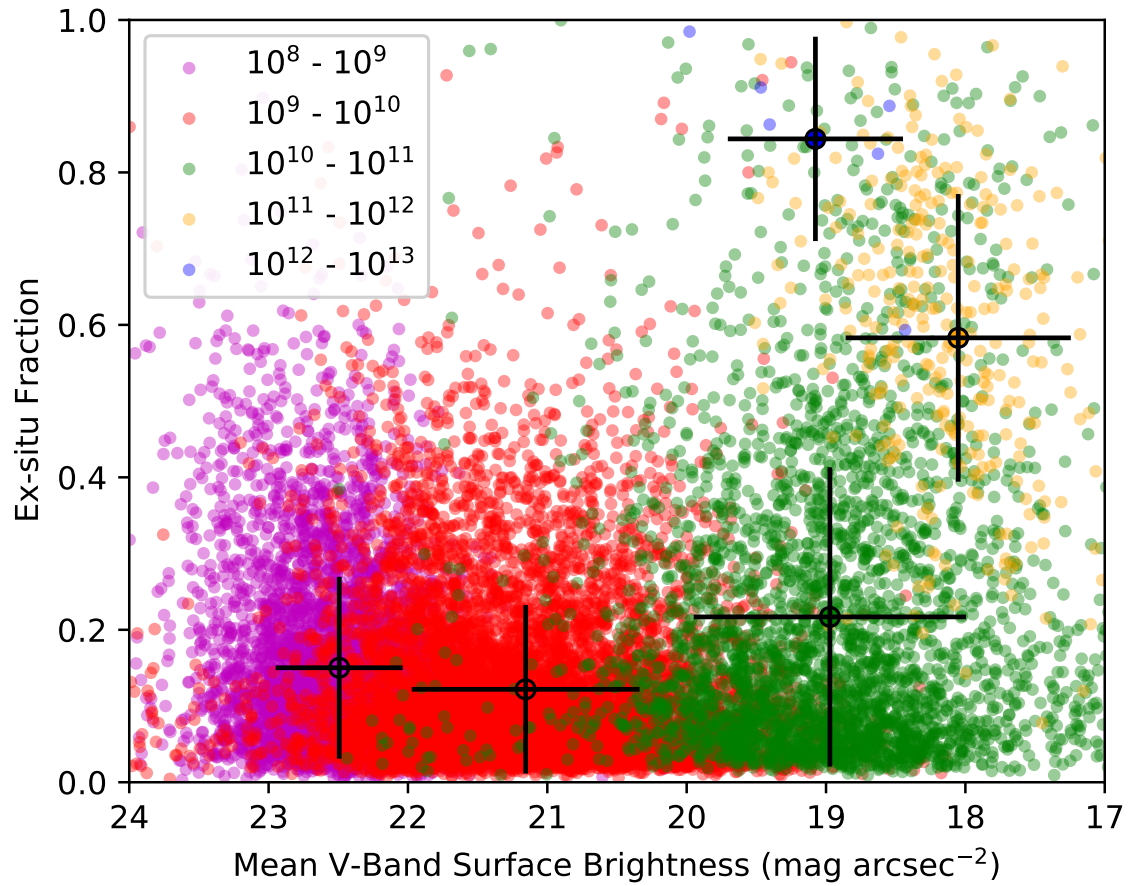


Figure 2.10: Ex-situ fraction of the $z=0$ EAGLE galaxies (centrals and satellites) as a function of mean V-band SB within $r_{1/2}$, with separation by mass. The legend shows colour division of stellar mass ranges (M_{\odot}). Mean values are overplotted in a larger sized point with 1σ standard deviation bars attached. Note that points are plot in order of mass, thus overlapping regions are obscured by higher mass points.

CHAPTER 2

where a, b, c and d are constants tabulated in Table 2.1. This allows the expected ex-situ fraction at any stellar mass ($8 < \log_{10}(M_{\odot}) < 12.5$) to be calculated according to the function at a particular surface brightness. Shaded error bars show the 1σ scatter in the ex-situ values within each bin, which are provided as a co-variance matrix of the form shown below, where all elements are tabulated in Table 2.2.

$$\begin{bmatrix} \alpha & \beta & \gamma & \delta \\ \beta & \epsilon & \zeta & \eta \\ \gamma & \zeta & \theta & \iota \\ \delta & \eta & \iota & \kappa \end{bmatrix} \quad (2.11)$$

The purpose of Fig 2.11, and the tabulated constants is to provide predictions which may be compared directly to forthcoming observational studies. Tabulated constant values are shown in Table 2.1 for surface brightnesses of 19 - 27 magnitudes per square arcsecond for V band. Values for filters Johnson-Cousins V, B and R; and Sloan g, r and i, are also available and can be found in Appendix A.2.

CHAPTER 2

Table 2.1: Constants for V band surface brightness to ex-situ fraction functions for the stellar mass range $8 < \log_{10} M_{\odot} < 12.5$ in Equation 2.10. Surface brightnesses (μ_V) of 19 - 27 magnitudes per square arcsecond are shown.

μ_V	a	b	c	d
Red Sequence Galaxies				
19	2.252	11.135	0.842	-0.030
20	3.050	10.892	0.788	-0.006
21	3.534	10.732	0.790	0.010
22	3.461	10.645	0.795	0.031
23	3.458	10.509	0.801	0.034
24	3.535	10.419	0.787	0.054
25	3.507	10.309	0.783	0.073
26	3.219	10.151	0.780	0.085
27	2.886	10.009	0.756	0.110
Blue Sequence Galaxies				
19	12.756	10.960	0.302	0.037
20	14.823	10.946	0.305	0.082
21	3.490	11.185	0.852	0.025
22	2.838	11.258	1.142	0.027
23	2.663	11.040	0.975	0.034
24	3.574	10.653	0.740	0.054
25	4.713	10.502	0.655	0.098
26	4.242	10.375	0.709	0.086
27	5.161	10.157	0.671	0.102

CHAPTER 2

Table 2.2: Constants for V band co-variance matrix (Equation 2.11) to surface brightness functions for the stellar mass range $8 < \log_{10} M_{\odot} < 12.5$. Surface brightnesses (μ_V) of 19 - 27 magnitudes per square arcsecond are shown.

μ_V	α	β	γ	δ	ϵ	ζ	η	θ	ι	κ
Red Sequence Galaxies										
19	3.919	-0.281	-0.776	0.287	0.141	7.11E-02	6.86E-03	0.177	0.177	3.33E-02
20	4.972	-0.041	-0.448	0.207	0.060	5.81E-03	1.33E-02	0.057	0.057	1.85E-02
21	5.670	-0.041	-0.315	0.138	0.043	4.60E-03	8.11E-03	0.032	0.032	1.07E-02
22	5.076	-0.048	-0.270	0.112	0.043	5.40E-03	6.98E-03	0.028	0.028	8.89E-03
23	4.735	-0.046	-0.226	0.091	0.041	5.04E-03	6.06E-03	0.023	0.023	7.41E-03
24	4.607	-0.057	-0.180	0.063	0.038	5.77E-03	4.22E-03	0.018	0.018	5.00E-03
25	4.534	-0.046	-0.171	0.065	0.039	4.61E-03	4.56E-03	0.017	0.017	5.20E-03
26	3.665	-0.029	-0.163	0.069	0.043	3.18E-03	5.78E-03	0.017	0.017	6.06E-03
27	2.945	-0.012	-0.161	0.076	0.052	1.49E-03	7.71E-03	0.018	0.018	7.16E-03
Blue Sequence Galaxies										
19	220.933	-0.256	-0.769	0.219	0.011	2.72E-03	1.19E-03	0.008	-0.002	1.88E-03
20	439.691	-0.331	-1.018	0.259	0.012	2.97E-03	1.15E-03	0.009	-0.002	2.01E-03
21	9.661	-1.224	-1.852	0.169	0.225	3.03E-01	-1.35E-02	0.449	-0.030	6.45E-03
22	5.746	-1.500	-2.413	0.129	0.497	7.72E-01	-2.43E-02	1.245	-0.048	6.31E-03
23	4.264	-0.985	-1.273	0.100	0.321	3.75E-01	-1.46E-02	0.475	-0.028	5.56E-03
24	5.745	-0.343	-0.457	0.065	0.061	4.38E-02	3.19E-04	0.055	-0.007	3.32E-03
25	10.459	-0.202	-0.326	0.057	0.030	1.37E-02	1.45E-03	0.021	-0.003	2.48E-03
26	7.935	-0.172	-0.303	0.063	0.034	1.39E-02	2.02E-03	0.024	-0.005	3.34E-03
27	13.924	-0.125	-0.306	0.080	0.026	7.37E-03	2.39E-03	0.018	-0.004	3.63E-03

2.6 Discussion

In this study we explore the relation of ex-situ material to galaxy properties, both global and local. In Figure 2.4 we plot stellar mass against ex-situ fraction. An increase in ex-situ fraction with stellar mass matches existing expectations (drawn from complementary simulations) about galaxies of larger mass possessing greater fractions of stars accreted from other galaxies. Likewise, less massive galaxies have been shown to have few or even no ex-situ stars (Fitts et al. 2018). When all galaxies are considered, at the highest mass bin limits, the average ex-situ fraction reaches

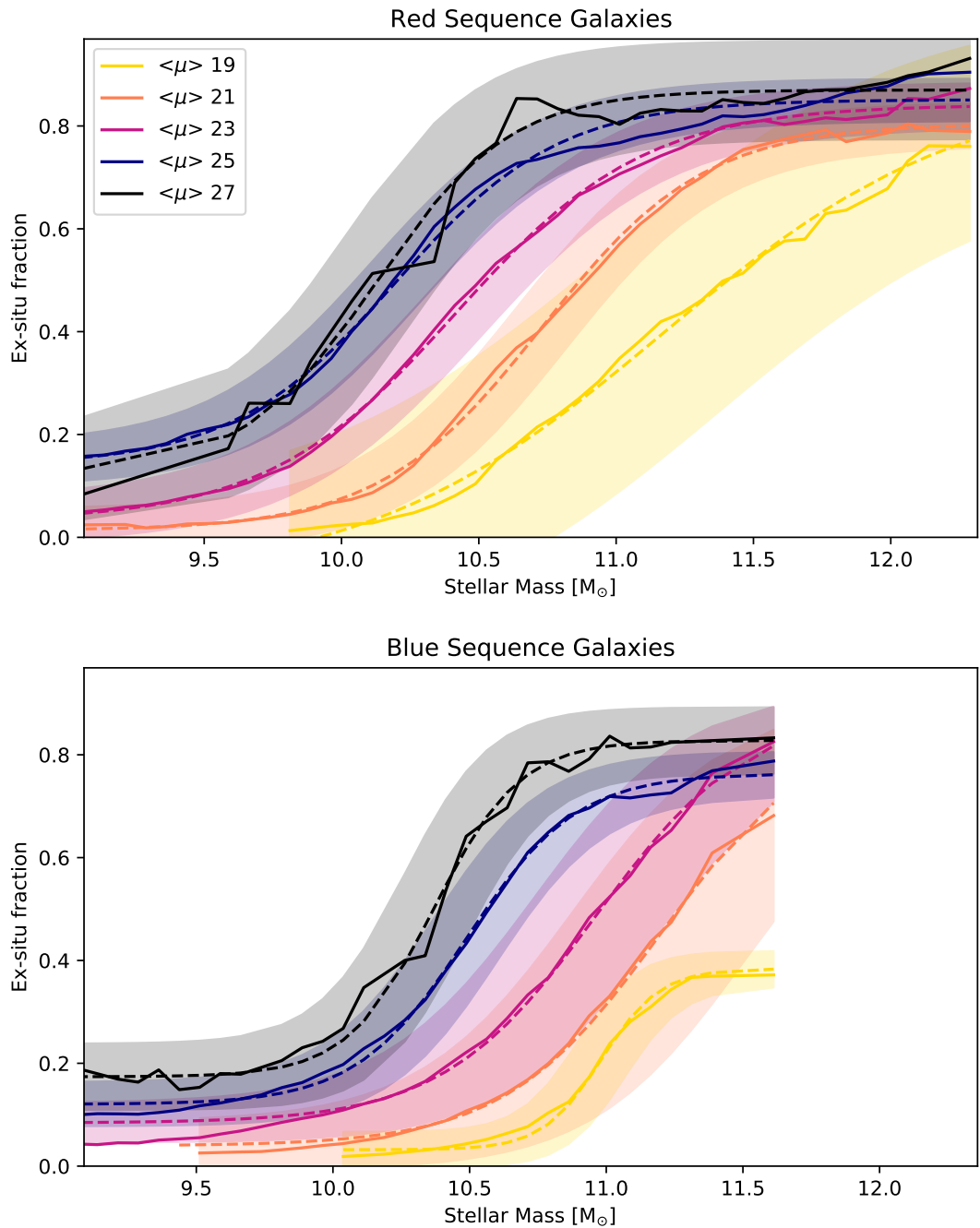


Figure 2.11: Mass and ex-situ fraction for all $z=0$ objects, considering only particles within integer magnitudes per square arcsecond projected ellipses in V band. Solid lines show the true data, dashed lines show a fitting function. Sigmoid functions are fit to the data as described in Section 2.5. Five different magnitudes-per-square-arcsecond ($\langle \mu \rangle$) bins are shown here, with additional values tabulated in Table 2.1. Shaded regions show the 1σ distribution of ex-situ scatter.

CHAPTER 2

as high as $\approx 84.2\%$. This is almost identical to the fraction recovered at the highest mass bin by Rodriguez-Gomez et al. (2016) for the Illustris simulations as discussed in Section 2.5.1.1.

When comparing to other analyses of the EAGLE simulations, we see small differences between those results and our own. A likely reason for the small differences between analyses of the same simulation are due to differences in ex-situ and in-situ classification. In our method we trace all particles through their entire merger history from formation to $z = 0$, resulting in identification of origin. It is possible for a few particles to be mistakenly labelled as ex-situ when swapping between subhaloes during mergers, however this possible over-estimation of ex-situ fraction is negligible and does not impact on the statistics of our sample.

A second parameter which correlates with ex-situ fraction was found to be the total mass of the halo which hosts a satellite galaxy. By forming a sub-sample of satellite galaxies split by the mass of their parent halo we were able to compare the effects of halo mass on ex-situ fraction. As seen in Figure 2.7 there is a variation with halo mass such that satellite galaxies within the most massive haloes possess consistently lower ex-situ fractions on average compared to those of the same stellar mass in the next lowest halo mass bin. Objects within intermediate mass haloes ($M_{*,halo} > 1 \times 10^{13} M_{\odot}$) seem to experience especially efficient accretion of stars onto galaxies.

As a general rule, at fixed stellar mass, satellite galaxies residing in highest mass haloes have lower ex-situ fraction within 100 kpc. This is unexpected when we consider the vastly larger potential wells of larger and likely older haloes. The effect is also visible in similar environmental analyses of other simulations, such as in figure 12 of Pillepich et al. (2018), in which the IllustrisTNG simulation shows the same effect. Though present in the plot, this is not commented upon, possibly due to the subtle nature of the effect.

CHAPTER 2

Initially the proposed explanation for this effect was as the result of overcooling (Crain et al. 2015), in which the most-massive haloes cease to display efficient AGN feedback, leading to artificially high in-situ fractions. This was eliminated as a potential mechanism by running the same analyses, though ignoring stars born after $z = 1$. The result shows the same effect as in Figure 2.7 in which satellite galaxies within the more massive haloes contain an ex-situ fraction that is lower than galaxies of the same mass in less massive haloes.

A number of mechanisms could be responsible for the effect that satellite galaxies within higher mass haloes have lower ex-situ fraction. One is that because passing velocities in clusters are so high, true mergers are rare, and it becomes more likely that material gets pulled out and added to the intra-cluster light than actually incorporated into another galaxy (Moore et al. 1996; Makino & Hut 1997). In contrast, within groups the passing velocities are lower and mergers are more likely (Bahcall et al. 1994). Although we might expect clusters to be built from groups and thus have a similar fraction, it is possible we are instead seeing an influence of survivor bias. This could occur where groups that fell into clusters did so, on average, long ago and ceased merging, whereas surviving groups today have had much longer to continue to merge.

Evidence for this mechanism can be found in literature (e.g. Gu et al. 2018) where stellar population models are fit to spectra of intra-cluster light (ICL). The velocity dispersion of the stars indicate that many ICL stars are dissociated from individual galaxies and are instead influenced by the gravitational potential of the cluster as a whole. The authors of the study suggest tidal stripping as a potential formation mechanism for the ICL, where flybys of massive galaxies can expel significant amounts of matter into the ICM.

Another mechanism for this effect could be partly due to differences in galaxy formation efficiency driven by assembly bias. At fixed halo mass, galaxies that form

CHAPTER 2

earlier do so more efficiently, because the central density is higher and outflows find it harder to escape (Gunn & Gott 1972). As such, earlier forming galaxies end up with a higher M_*/M_{sub} ratio, where M_{sub} is the stellar mass contained in solely subhalos. The satellites of the most massive clusters will have formed the earliest on average, since they are part of higher sigma peaks, and so these could be systematically more efficient at star formation. At fixed M_* , we are then looking at systematically lower subhalo mass fractions (as a fraction of the halo mass) as we transition from groups to clusters, and as such you could expect a lower ex-situ fraction.

By separating galaxies based on their half mass radius, we investigate and compare spatial differences regardless of galaxy size. The increase in ex-situ fraction (as seen in Figure 2.5) is present both in the central ($<r_{1/2}$) region and outer regions ($>2r_{1/2}$). For both central and outer regions this is the case at all masses, though ex-situ fraction increases negligibly with extent for central regions below a mass of $M_* < 5 \times 10^8 M_\odot$. This situation is perhaps to be expected, as higher mass haloes are thought to be assembled through a higher fraction of mergers (Maller et al. 2006).

When looking solely at the central region of galaxies, more diffuse galaxies have accreted a higher fraction of stars than their denser counterparts. This difference is as equally pronounced for the outer regions of the same galaxies, with fractions between 5-30% greater at all masses where $M_* > 5 \times 10^8 M_\odot$. The increase in ex-situ fraction at all masses for the outer regions is indicative of stripped ex-situ stars preferentially remaining in the disk and halo and infrequently migrating to the core. This is supportive of the ‘two phase’ scenario wherein an initial core of in-situ stars accretes stars via mergers and tidal stripping.

Once above $M_* > 2 \times 10^9 M_\odot$ the ex-situ fraction of the outer regions quickly surpasses 50% for the most diffuse galaxies, and all galaxies of mass $M_* > 2 \times 10^{11} M_\odot$ contain more than 50% constituent ex-situ stars, regardless of radius.

2.7 Conclusions

We have analysed two EAGLE simulations of volumes 25cMpc^3 and 100cMpc^3 within the sample stellar mass range of $(2 \times 10^7 - 1.9 \times 10^{12} M_{\odot})$ for both central and satellite galaxies. From these we have extracted ex-situ fraction information at $z = 0$ with respect to spatially resolved galaxy parameters. We have investigated how ex-situ fraction changes with stellar mass, and at fixed mass with changes in half mass radius. Furthermore we have examined ex-situ changes with group/cluster halo mass by separating satellite galaxies by the mass of the group/cluster halo they reside in. Lastly we have used mass to light ratios to determine the expected ex-situ fractions for galaxies at a specific mass and surface brightness value.

Our main findings are summarised as follows:

- We find that more massive galaxies gain proportionally more stellar mass from ex-situ sources. This is in common with previous findings in literature (e.g. in Oser et al. 2010; Qu et al. 2017; Rodriguez-Gomez et al. 2016; Pillepich et al. 2018). For the most massive galaxies included in the sample ($> 1 \times 10^{12} M_{\odot}$), ex-situ fraction was found to be, on average, $>80\%$; and for individual cases at these masses the ex-situ fraction could be as high as $>90\%$.
- At fixed galaxy mass, when separated by its parent group/cluster halo mass, there is a consistently lower ex-situ fraction for satellite galaxies within the highest mass group/cluster halos. One interpretation of this is that the high passing velocities present in massive clusters disfavour true mergers and stellar accretion. Instead of material being added to a galaxy during a close pass/merger, the material is instead removed from the original galaxy and spread amongst the ICM. Another interpretation is that the effect is the result of differences in feedback efficiency with time, where tightly bound group/cluster halos possess denser circumgalactic medium as a result of less

CHAPTER 2

efficient feedback. This in turn causes a higher rate of in-situ formation. Similar effects were seen in analysis of a purely central sample, however statistics were too poor to explore this result with any certainty. This remains a point of investigation for larger samples in the future.

- At all galaxy stellar masses there is an increase in ex-situ fraction with increasing galaxy stellar size, thus showing how at fixed mass, more diffuse galaxies are more likely to contain a greater ex-situ fraction. This supports the idea that physically more extended galaxies are more extended because they have accreted more material preferentially onto their outskirts. This is especially clear in the right hand panels of Figure 2.5 where bins of the most diffuse, most compact and average galaxies remain separated from the lowest until the very highest mass extent of the simulation.
- We have also produced predictions for the accreted fraction as a function of galaxy mass and surface brightness. These predictions show estimated ex-situ fractions for the same sample of galaxies, but limited to elliptical isophotes of specific surface brightness values. Combined with stellar mass, these can be used to estimate the ex-situ fraction for observed galaxies of similar surface brightness and mass. This can also be readily compared to observational data processed by new analytic techniques such as recently advanced full spectral fitting methods, for both spatially resolved, and non-spatially resolved galaxies. See Table 2.1 for the tabulated data for V-band. Other bands are also available.

Chapter 3

NGC 7135, A Case Study

3.1 Remarks

The following chapter includes published work from Davison et al. (2021a), with additions to the published document where appropriate.

3.2 Chapter Abstract

The simultaneous advancement of high resolution integral field unit spectroscopy and robust full-spectral fitting codes now make it possible to examine spatially-resolved kinematic, chemical composition, and star-formation history from nearby galaxies. In the following chapter we take new MUSE data from the Snapshot Optical Spectroscopic Imaging of Mergers and Pairs for Legacy Exploration (SOSIMPLE) survey to examine NGC 7135. With counter-rotation of gas, disrupted kinematics, stellar streams, and asymmetric chemical distribution, NGC 7135 is consistent with an ongoing merger. Though well hidden by the current merger, we are able to distinguish stars originating from an older merger, occurring 6-10 Gyr ago. We further find a gradient in ex-situ material with galactocentric radius, with the accreted fraction rising from 0% in the galaxy centre, to $\sim 7\%$ within 0.6 effective radii.

3.3 Chapter Introduction

Galaxy merger research has shown how fundamental merging is to galaxy evolution, with past and ancient merger rates generally increasing with galaxy mass (Bundy et al. 2009; Schawinski et al. 2010; L’Huillier et al. 2012; Pillepich et al. 2018). Distant galaxies ($z \approx 2$) are often quoted as being a factor of 2-5 times smaller than those found locally (Daddi et al. 2005; Van Dokkum et al. 2008; Saracco et al. 2009; van der Wel et al. 2014). As such it is widely assumed that a large amount of mass-assembly after $z \approx 2$ is a result of hierarchical growth through galaxy mergers and accretion which has been widely corroborated from galaxy evolution models. Not only does merger history impact on almost all other aspects of galaxy evolution, but many galaxies have experienced large mergers throughout their history with around 50% of galaxies experiencing a major merger (Maller et al. 2006) (where major here is a merger with mass ratio larger than 1:4), and essentially all surviving galaxies experiencing minor mergers, with frequency increasing with merger mass-ratio (Lotz et al. 2011). The exception for these cases are some rare pristine galaxy types ($\lesssim 0.1\%$ of galaxies according to Quilis & Trujillo 2013) which have likely experienced no outside interaction or accretion events (Trujillo et al. 2013).

Modelling is an excellent way to delve into the mechanics and subsequent effects of galaxy mergers. Using simulations, the ex-situ mass fraction of accreted galaxies has been explored in depth (Pillepich et al. 2015; Qu et al. 2017; Davison et al. 2020). This is useful for defining expected current merger rates to be compared to observationally. A challenging aspect of observational astronomy is demonstrating the merger history of observed nearby galaxies to verify these models, particularly if potential mergers occurred several Gyr ago.

The impact of mergers and merger history on galaxy evolution is an important aspect to understand. For one thing, mergers are known to drive gas towards the galaxy centre (Mihos & Hernquist 1995), causing AGN activity and black hole

CHAPTER 3

growth, which in turn can shut down or suppress star formation in the galaxy (Cales & Brotherton 2015; Choi et al. 2015). On the other hand, mergers can cause sudden and significant bursts of star formation due to the disruption of previously unperturbed gas kinematics (Di Matteo et al. 2008; Ellison et al. 2013; Moreno et al. 2015; Capelo et al. 2015). Disruption in the gas kinematics of galaxies can leave key fingerprints in identification of merger events. One of the most readily identifiable features of a recent or ongoing merger is counter rotating components, with up to 40% of S0 galaxies displaying signatures of counter-rotation (Rubin 1994; Davis et al. 2011; Coccato et al. 2015; Bassett et al. 2017). Galaxy-galaxy mergers of the right combination can change the very morphological type of a galaxy. As such, mergers hold the power to define entire galaxy futures.

The S01-pec galaxy NGC 7135 (AM 2146–350, IC 5136) in the constellation of Piscis Austrinus is a merger remnant galaxy (Keel 1985) that is likely en route to forming an S0 galaxy. It currently displays several immediately striking visual features including an extended tail, shell features, and curved structure (Figure 3.1) based on photometry from the Carnegie-Irvine Galaxy Survey (Ho et al. 2011).

NGC 7135 was first described as having ‘a curious jet and shell’ in Malin & Carter (1983) with the ‘jet’ later shown to be a tail in Rampazzo et al. (2003). The shell structures of the galaxy were found to be particularly clear in UV (Rampazzo et al. 2007; Marino et al. 2011), with FUV gas structure further linked to an accretion event that also likely formed the shells. Ueda et al. (2014) found CO emitting gas that was unassociated with the nucleus, along with 3 mm continuum associated with the nucleus. Despite speculation, NGC 7135 was determined to have no active nucleus as shown in Zaw et al. (2009) through optical spectra analysis. Analysis in Keel (1985) identifies NGC 7135 as a merger galaxy, and in Rampazzo et al. (2003) NGC 7135 is shown to possess an elongated, asymmetric gas structure relative to the stellar material.

CHAPTER 3

The local environment of NGC 7135 is described by Samir et al. (2016) as being ‘low density’, with the classification of ‘low density’ (Annibali et al. 2010) a result of the richness parameter $\rho_{xyz}=0.32 \text{ gal Mpc}^{-3}$ (Tully & Fisher 1988). Early type galaxies in low density environments are known to possess on average younger populations ($\sim 2\text{Gyr}$ younger) than similar galaxies in higher density environments (Thomas et al. 2003), a likely result of more recent mergers and star formation. The galaxy has an estimated mass of $10^{11.0}M_{\odot}$ to $10^{11.5}M_{\odot}$

This chapter presents observations of the galaxy NGC 7135, recently obtained with MUSE. At a distance of 38 Mpc, the angular resolution is 0.182kpc per arcsecond, giving good resolution on the MUSE imaging surface. The chapter shows that NGC 7135 is currently undergoing a major merger, with a history of older mergers underlying in the galaxy populations. The chapter is ordered as follows: In Section 3.4 we describe the motivation behind the observations, as well as the data reduction and limitations. In Section 3.5 we describe our methodology, including the use of regularisation during spectral fitting. In Section 3.6 we present the resultant maps of stellar populations and kinematics, as well as gas properties similarly derived, including rotation differences between the two components. In Section 3.7 we discuss the implications of the results and finally in Section 3.8 we provide a summary and concluding remarks.

3.4 Observations and data reduction

We observed NGC 7135 with the Multi Unit Spectroscopic Explorer (MUSE, Bacon et al. 2010, 2014) at the Very Large Telescope (VLT) as part of the Snapshot Optical Spectroscopic Imaging of Mergers and Pairs for Legacy Exploration (SOSIMPLE) survey (Program ID: 0103.A-0637(A), PI: B. Husemann). The aim of the SOSIMPLE survey is to provide complementary IFU observations for an ongoing Hubble filler gap snapshot imaging program (Program ID: 15446, PI: J. Dalcanton). HST

CHAPTER 3

imaging of NGC 7135 is not yet taken due to the filler nature of the HST program, thus these MUSE observations act as a first look at the data, to which HST data can be compared to at a later date. Combining IFU spectroscopy with a large set of high-quality ancillary data will hopefully provide observational and theoretical insights into the evolution of merging systems.

The MUSE observations were conducted on 6 July 2019 during dark sky conditions and split into 3×560 s dithered pointings along with a 300 s dedicated blank sky field exposure for background subtraction of this extended galaxy. Rotations of 90° were applied between exposures covering approximately 3.4 arcmin^2 as shown in Fig 3.1. The seeing during the observations maintained at $\sim 1''$, and the sky was covered with thin clouds during strong wind conditions from the North-West.

The data were reduced with the standard ESO pipeline (Weilbacher et al. 2020) which performs detector calibrations, flat-fielding, wavelength calibration, flux calibration as well as sky subtraction, exposure alignment, and cube reconstruction of the combined exposures. We performed an additional correction for residual sky lines using a simple Principal Component Analysis (PCA) algorithm. The MUSE pixel scale is $0.2 \text{ arcsec pixel}^{-1}$, with a mean spectral resolution of $\sim 2.5 \text{ \AA}$ though this can vary across the wavelength range (see figure 5 of Husser et al. 2016). The resulting mean Signal-to-Noise (S/N) ratio of the spaxels in the MUSE image within a wavelength range of $4759\text{--}6849 \text{ \AA}$ (limited from $4759\text{--}9300 \text{ \AA}$) is 9.5, with a maximum spaxel S/N of 131.

3.5 Methodology

Spaxels were Voronoi binned to a minimum S/N of 50 per \AA , thereby poor signal regions were made available for analysis, whilst higher S/N spaxels remained unbinned. This optimally allowed for spatial investigation of spectral properties,

CHAPTER 3

without losing valuable high resolution data at high S/N locations. Angular resolution ranged from the unbinned size of $0.182\text{kpc}/''$ to larger bins at a maximum of around $4.0\text{kpc}/''$.

The wavelength was restricted to $4759 - 6849 \text{ \AA}$ for all spaxels to ensure the strongest Balmer lines were included, and to exclude noisier sky-dominated regions at redder wavelengths. All spectra of spaxels within a bin were summed into a single spectra representing the area covered by the bin. An area containing a foreground star was masked from analysis in the West of the image (see Figure 3.1).

To analyse the spectra from the binned NGC 7135 data we utilised the Penalized PiXel-Fitting (pPXF) method, described in Cappellari & Emsellem (2004) and upgraded in Cappellari (2017). With this method, single-age single-metallicity stellar population (SSP) models are fit to spectra to build a map of stellar populations across age and metallicity space. By identifying the combination of SSP models that approximate a given spectrum, the estimated constituent populations are extracted, as well as velocity and dispersion. Stellar models are weighted as per the estimated fraction of the population present in the galaxy. As a result, output weights of stellar models indicate the fractions of specific stellar populations present in the spectrum. The output model of combined spectra is made more physical by the use of template regularisation (see e.g. section 3.5 of Cappellari 2017), the methodology of which is explained in detail below. Standard pPXF cleaning algorithms were included to mask emission lines where necessary.

A total of 552 MILES SSP models (Vazdekis et al. 2010) were used to fit to galaxy spectra. These models were of Kroupa revised initial mass function (log slope of 1.3, $M_{max}=100M_{\odot}$) using BaSTI isochrones, with a metallicity range of -2.27 to $+0.4$ [M/H] in 12 non-linear steps, and an age range of 0.1 to 14.0 Gyr in 46 non-linear steps, at scaled-solar abundances (Kroupa 2001; Cassisi et al. 2005; Pietrinferni et al. 2006; Falc3n-Barroso et al. 2011; Vazdekis et al. 2012). The solar

CHAPTER 3

abundances assumption is possibly unrealistic for this galaxy due to its differing type from the Milky Way, however our tests have shown that model abundance differences give little discernible difference in results, and nothing above standard errors associated with spectral fitting such as age-metallicity grid resolution.

Application of regularisation allows smoothing over stellar model weights to reproduce a population map consistent with physical results. See Section 1.4 for an explanation of this. Regularisation has been shown in literature to be an accurate and useful method of galaxy population extraction (see e.g. Comerón et al. 2015; Norris et al. 2015; Guérou et al. 2016; Faifer et al. 2017; Ge et al. 2019; Boecker et al. 2020a).

In this work an iterative routine is applied to extract the optimal regularisation parameter. For the best possible fit, the χ^2 of the solution is expected to be approximately equal to the number of available voxels in the spectrum, N (i.e. the number of voxels available after any masking). To obtain this optimal solution, the χ^2 must be increased from the unregularised χ^2 (referred to as χ_0^2) by $\sqrt{2N}$.

After rescaling noise from the unregularised solution such that $\frac{\chi^2}{N} = 1$, we make a number of primary guesses at the regularisation parameter. We find the $\Delta\chi^2$ of these initial guesses and fit a function to the input regularisation guesses and output $\Delta\chi^2$ values. By doing so we can precisely find the optimal regularisation parameter such that $\chi^2 = \chi_0^2 + \sqrt{2N}$. This action is performed for every bin, resulting in optimal solutions across the entire image map.

3.6 Results

We separate the analysis of NGC 7135 into three components; the stellar component analysis, encompassing the stellar kinematics; the gaseous component analysis, encompassing gas kinematics, emission lines and star formation aspects; and the

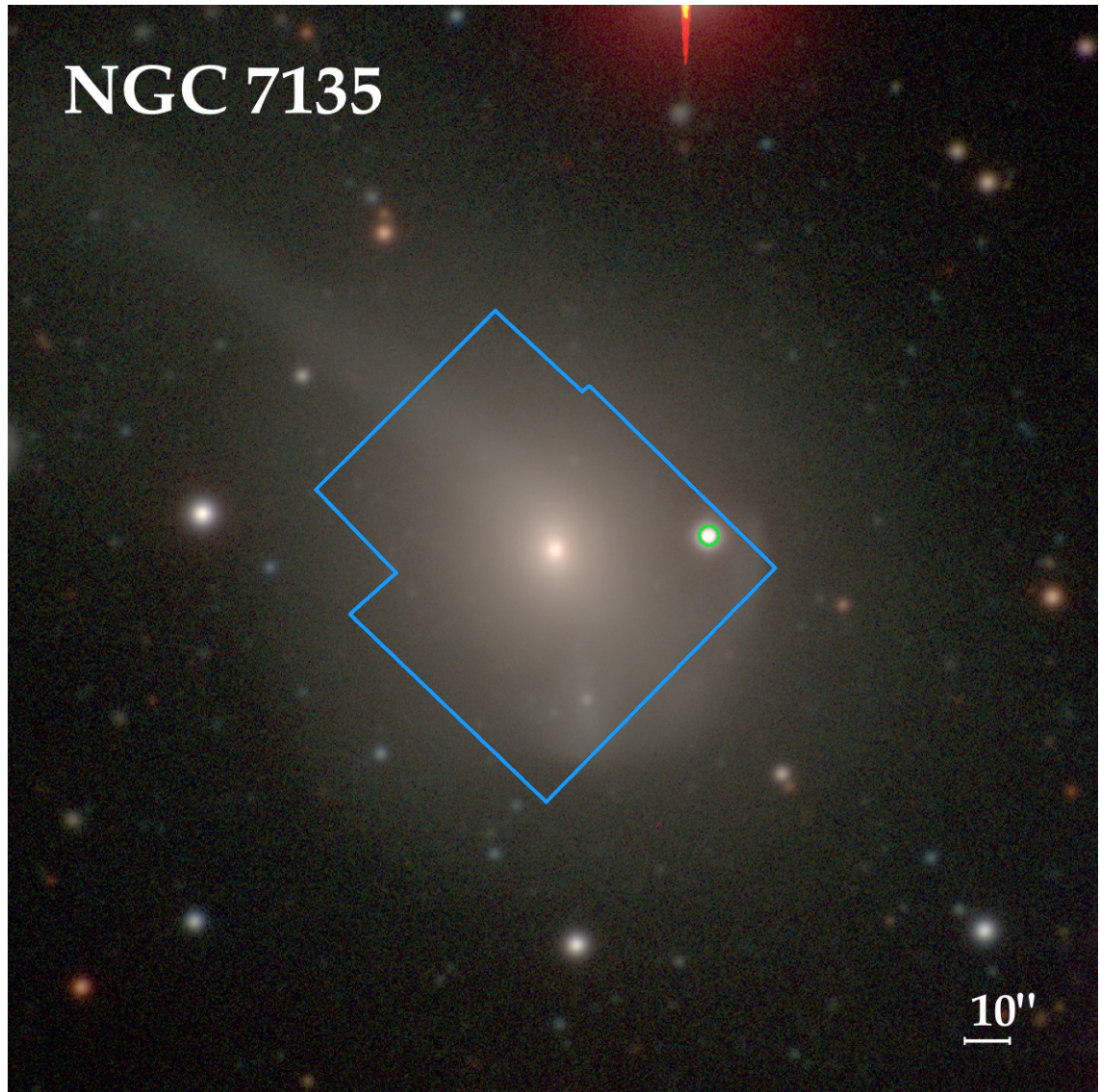


Figure 3.1: A false colour image of NGC 7135 showing the MUSE cube footprint. Photometry of NGC 7135 is from the Carnegie-Irvine Galaxy Survey (Ho et al. 2011). The blue border shows the boundaries of the reduced MUSE IFU data used in this study. A green circle traces an area containing a bright foreground star that was entirely excluded from the analysis. B, V and I filters are used as B, G and R colour filters respectively.

CHAPTER 3

population analysis, examining the various stellar populations and the resulting implications for the assembly history of NGC 7135.

To examine the stellar component we utilise Voronoi binning as described in Section 3.5. From this we are able to examine the stellar rotation and bulk velocities, as well as mean age and metallicities spatially across the galaxy (Fig 3.2). To investigate details related to the gaseous component we use regular binning to view the gas velocities and rotation, as well as the line strengths of $H\alpha$ and $H\beta$ emission lines (Fig 3.3). Though we see reasonable amounts of $H\alpha$ emission, there is scant additional evidence for significant ongoing star formation. This is explained in detail in Section 3.6.2. Finally, in Section 3.6.3 we further analyse age and metallicity distributions for sampled regions across the galaxy to diagnose assembly history and current merger status, then go on to examine underlying metal poor populations in Section 3.6.4.

3.6.1 Stellar Properties

Application of the pPXF method to the NGC 7135 data cube provides mean kinematic properties which are extracted from each bin. Demonstrations of this for velocity and velocity dispersion of the galaxy are found in the top panels of Figure 3.2. Application of regularisation and mass-to-light ratios produce maps of the constituent stellar populations within each bin of the galaxy. From these bins we can derive mean mass-weighted stellar age and metallicity values, as demonstrated in the lower panels of Figure 3.2.

The stellar kinematic, age, and metallicity maps of NGC 7135 reveal much about the galaxy. Stellar rotation is immediately visible. This is of key interest when comparing to gas which rotates counter to the direction of stellar rotation. This is explored in detail in Section 3.6.2. One prominent kinematic feature, perhaps most clearly seen in the velocity map (top left panel) of Figure 3.2, is an arc of

CHAPTER 3

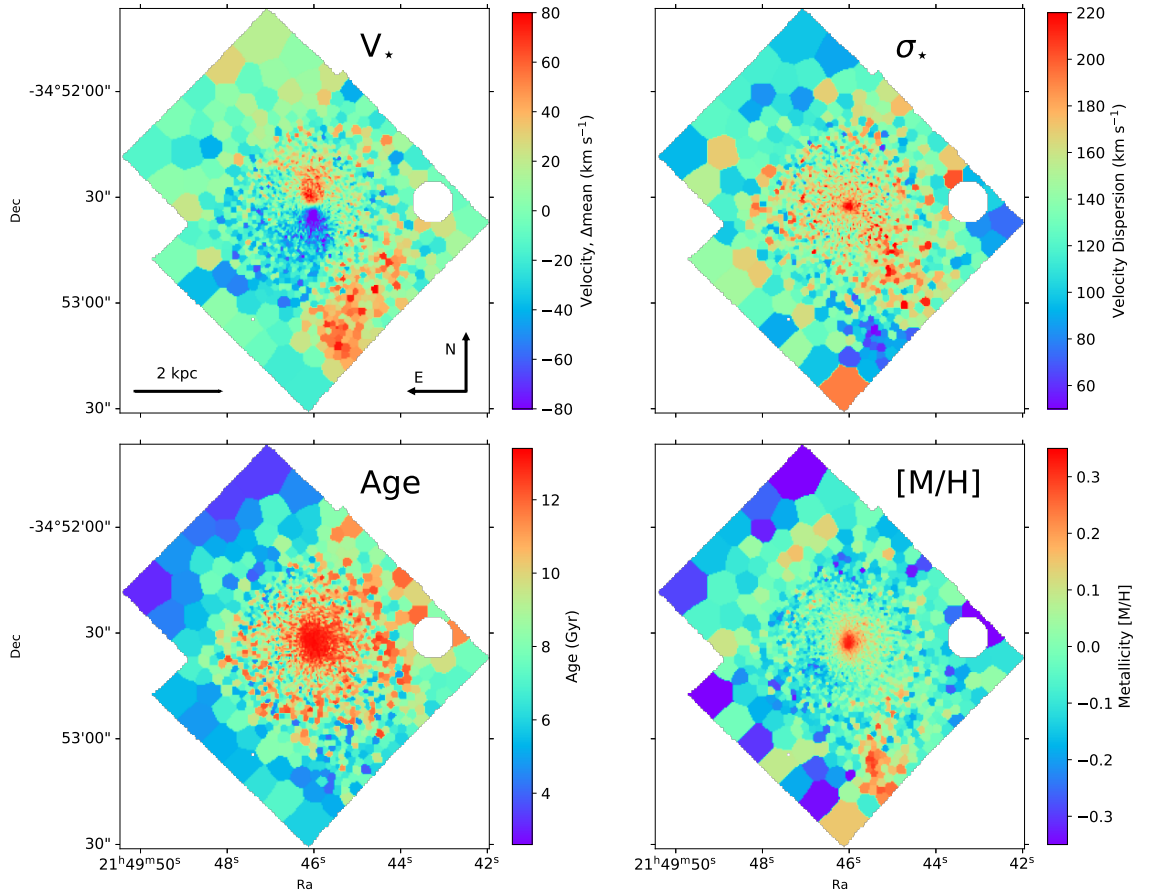


Figure 3.2: Voronoi map of NGC 7135 showing 4 different stellar kinematic or mass-weighted population properties. The top left panel shows the mean velocity in km/s for each bin. The top right panel shows mean velocity dispersion within bins in km/s . The lower left panel shows the mean age of populations within the bin in Gyr. Finally the lower right panel shows mean metallicity within each bin. North is to the top of the image, and East is to the left. The stars show clear rotation in the centre. Velocity dispersion, age and metallicity all increase towards the galaxy centre. Distinct kinematics and metallicity south of the centre highlight a distinct component associated with the disrupting galaxy.

CHAPTER 3

incongruous material at higher than average velocity, stretching from the South West of the Figure to the West. The Southern end of this arc is matched in the metallicity map (lower right panel, Figure 3.2) by a higher metallicity region, which is also distinct in velocity and velocity dispersion. Upon inspection, this is revealed to be an infalling galaxy currently merging onto NGC 7135. This can be clearly seen in photometry shown in Figure 3.7, and even more compelling evidence comes from population analysis below.

3.6.2 Gas Properties

To explore gas kinematics and distribution in NGC 7135, regular binning was employed to avoid biases caused by the stellar light controlling Voronoi binning. Large square bins containing 64 pixels were selected across the face of the data cube, and spectra within a given bin were summed and analysed with ppxf as described in Section 3.5. Following this, those bins with signal-to-noise that exceeded the minimum detection threshold were re-binned to a higher resolution. This adaptive ‘zoom’ binning gave high resolution in areas of strong $H\alpha$ emission. The zoom resolution was limited to central regions of the galaxy, where the finest detail was required.

NGC 7135 displays localised areas of strong Balmer emission, shown in Figure 3.3 with a cropped version showing the galaxy centre in Figure 3.4. As seen from all panels, the gas is asymmetric in distribution as well as in kinematics. The rotation of the gas highlights the decoupled nature of the stellar material in the core. This is shown in Figure 3.5.

Gas is counter-rotating to the stellar component, strongly indicating a disrupted system. A slight deviation to the coherent gas movement is seen in the galaxy centre, giving an ‘S’ shaped gas rotation profile. Counter rotation has long been associated with galaxy mergers (see e.g. Bertola et al. 1988). Total decoupling of gas rotation from stellar components as a result of prograde-prograde merger shocks

CHAPTER 3

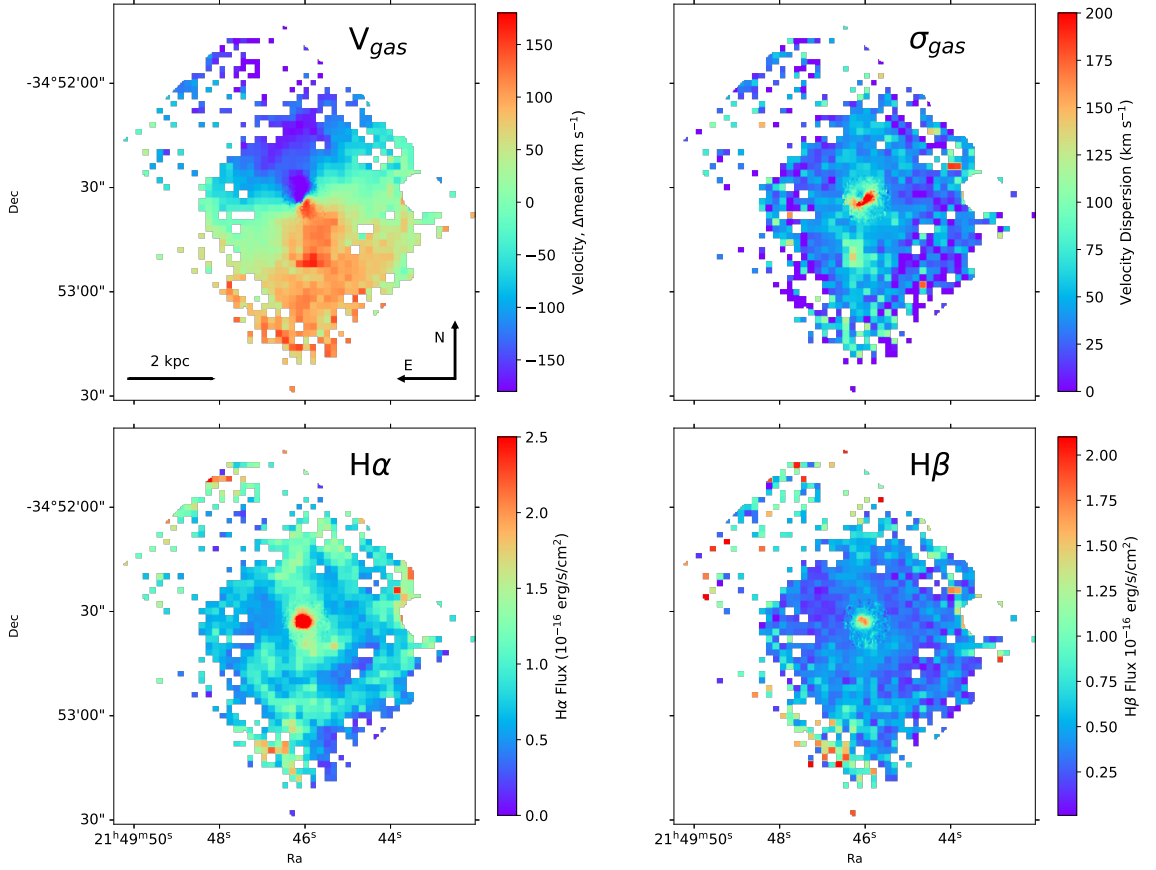


Figure 3.3: Regularly binned map of NGC 7135 showing 4 different gas kinematic and strength properties. The top left panel shows the mean velocity of gas in km/s for each bin. The top right panel shows mean velocity dispersion of gas within bins in km/s . The lower left panel shows the $H\alpha$ flux throughout NGC 7135. The scale has been limited from the true maximum to better display regions of intermediate strength. This limits the core from a true strength of at most $36.2 \times 10^{-16} \text{ erg/s/cm}^2$ (limited to $2.5 \times 10^{-16} \text{ erg/s/cm}^2$). The lower right panel shows $H\beta$ flux throughout NGC 7135. The scale has been limited from the true maximum to better display regions of intermediate strength. This limits the core from a true strength of at most $5 \times 10^{-16} \text{ erg/s/cm}^2$ (limited to $2.1 \times 10^{-16} \text{ erg/s/cm}^2$). The gas velocity shows counter rotation compared to the stellar component, and on a slightly different axis, suggesting a merger origin.

CHAPTER 3

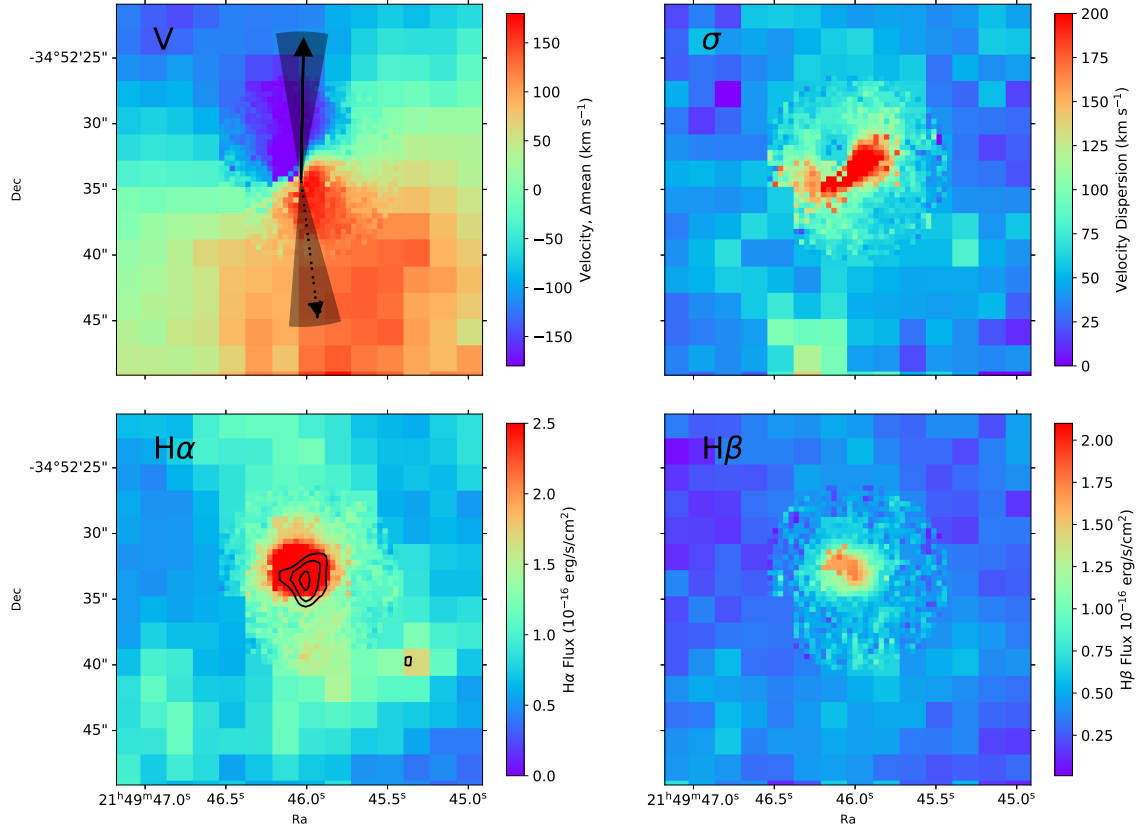


Figure 3.4: Regularly binned and zoomed in map of NGC 7135 showing 4 different gas kinematic and strength properties. The top left panel shows the mean velocity of gas in km/s for each bin. The top right panel shows mean velocity dispersion of gas within bins in km/s. The lower left shows the H α flux throughout NGC 7135. The scale has been limited from the true maximum to better display regions of intermediate strength. This limits the strongest emission near the core from a true strength of at most 36.2×10^{-16} erg/s/cm² (limited to 2.5×10^{-16} erg/s/cm²). The lower right panel shows H β flux throughout NGC 7135. The scale here has also been limited. This limits the strongest emission from a true strength of at most 5×10^{-16} erg/s/cm² (limited to 2.1×10^{-16} erg/s/cm²). In the upper left panel, arrows show the average positive rotation direction. The solid arrow indicates the average stellar component positive rotation whilst the dotted arrow shows the average gas positive rotation direction. Shaded regions show the standard deviation of vectors for both components for bins of 0.1 effective radii. In the lower left panel, contours show integrated CO(J=1-0) emission detected in ALMA observations (Ueda et al. 2014). Contours show the 0.8, 1.0 and 1.2 Jy km s⁻¹ levels. There is pervasive H α emission with a high luminosity and high velocity dispersion component in the centre, though there is little evidence of star formation.

CHAPTER 3

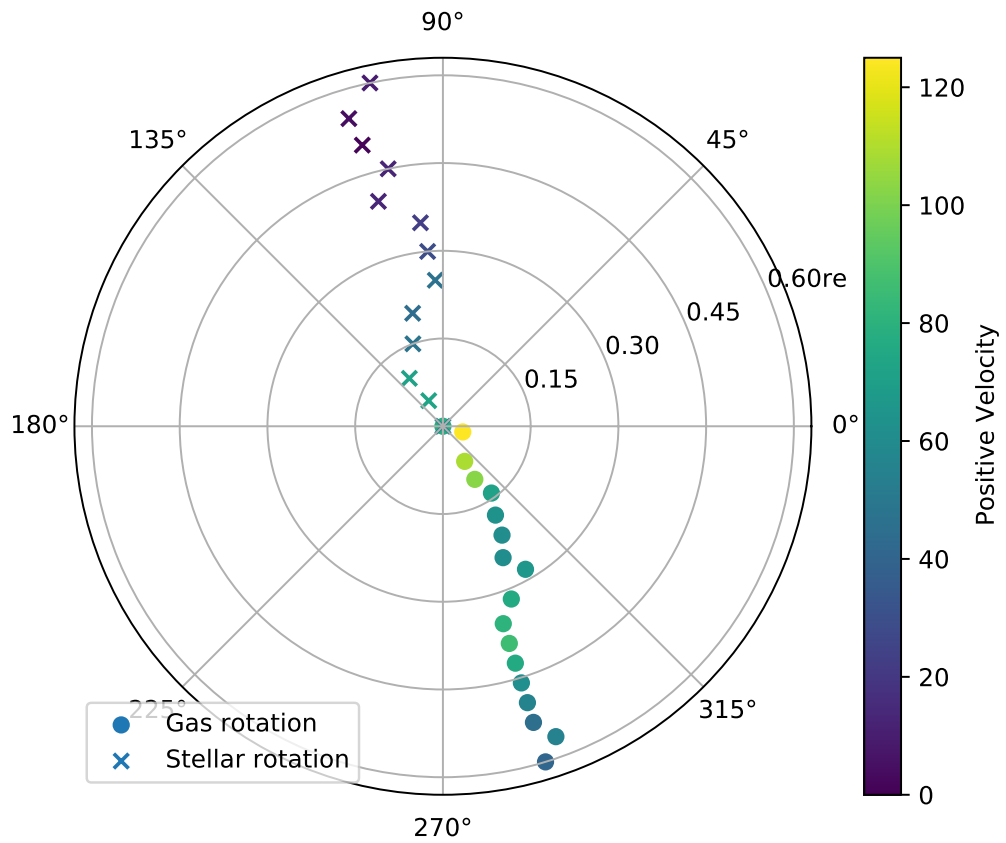


Figure 3.5: Polar view of mean direction of positive rotation for both gas and stars. Gas positions are marked with a cross, and stellar velocities are marked with a circle. Colour shows strength of velocity in the direction of the coordinate angle. Velocities are averages (positive component) over annuli with an inner to outer radius difference of 5 pixels, or approximately 0.04 effective radii.

CHAPTER 3

has been shown in simulation in Capelo & Dotti (2017), and a similar event appears to be in play here, wherein a major merger has resulted in a counter rotation of the gas component. Plausibly this is the result of a previous merger providing counter rotation from a prograde-prograde merger, this is expanded further in section 3.6.3. Alternatively, counter rotation could have arisen as a result of a first pass of the currently infalling galaxy.

Velocity vectorisation of the gas and stars allows us to measure the gas and stellar rotation misalignment. The rotation consensus in the gas is fairly standard, with the gas rotating around the centre. In the stellar component however, matters are complicated by the velocity of the in-falling galaxy, which shifts the positive rotation vector compared to the core. If we consider only the core, the misalignment of gas and stars is 176° , whereas when the entire cube is considered, the misalignment is 139° . This is entirely within the realm of expected values for an interacting galaxy (see e.g. Barrera-Ballesteros et al. 2015; Bryant et al. 2019). This is shown in Figure 3.4 as solid and dashed arrows for the directions of mean positive stellar and gas rotation respectively, with associated errors shown as shaded regions.

Regions of $H\alpha$ emission can be seen in the southern areas of the lower left panel of Figure 3.3. This forms a large arc with patches exhibiting particularly strong emission. These are seemingly matched by arcs in the north in an asymmetrical manner.

Considering the gas asymmetry and the increase in both gas velocity and velocity dispersion, a large amount of gas can be attributed to material stripped from the outskirts of the infalling galaxy and which is currently in the process of accreting onto the host galaxy. This is seen in the largest area of gas velocity dispersion occurring outside the core, located in a tight region south of the galaxy core. This region indicates a quantity of gas that is not associated with the cohort gas of NGC 7135, as it displays a region where infalling gas is interacting with the galaxy

CHAPTER 3

interstellar medium. This area of higher than expected dispersion is in the plane of the galaxy gas rotation, again evidence that gas is infalling, creating high velocity dispersion at the position where in-situ gas meets ex-situ gas.

A strong presence of H α in concentrated regions is consistent with the picture of NGC 7135 as a galaxy that has perhaps recently undergone star formation as suggested in Rampazzo et al. (2007), though at low levels. Despite this, there is little to no evidence of strong ongoing star formation. This can be seen in the emission line diagnostic diagram in Figure 3.6. Almost all the sources of emission are associated with low-ionization nuclear emission-line regions (LINERs). Though a handful of active galactic nuclei (AGN) sources can be seen, they largely lie in the outer noisier regions of the data-cube, which makes the presence of true AGN sources doubtful, as shown in Zaw et al. (2009). This strong bias towards LINER emission is typical of merging systems with shock driven LINER emission (Monreal-Ibero et al. 2010; Rich et al. 2011).

ALMA data (Ueda et al. 2014) showing the $^{12}\text{CO}(J=1-0)$ emission is overlaid in the lower left panel of Figure 3.4. The ALMA observations reveal a significant peak in CO emission offset from the galaxy core with an integrated molecular gas mass of $M_{\text{H}_2} = (5.4 \pm 1.4) \times 10^7 M_{\odot}$ adopting an $\alpha_{\text{CO}} = 4.8 M_{\odot} \text{pc}^{-2} (\text{K km s}^{-1})^{-1}$ (Solomon & Barrett 1991). This cold gas mass would correspond to an expected SFR of only $\sim 0.025 M_{\odot} \text{yr}^{-1}$ if a normal depletion time of 2 Gyr for galaxies is assumed (Bigiel et al. 2011; Leroy et al. 2013). Although there is no similarly distinct ionised gas structure observed with MUSE, there is plenty of ionized gas which may partially originate from star formation despite the LINER-like classification. The extinction-corrected H α flux within the central $r=1''$ is $(4 \pm 0.4) \times 10^{-13} \text{erg s}^{-1} \text{cm}^{-2}$ which would correspond to $\text{SFR} = 0.5 \pm 0.05 M_{\odot} \text{yr}^{-1}$ following Kennicutt Jr (1998). So only 5% of the central H α would need to be hidden among LINER-like classified ionised gas to be in agreement with ongoing star formation. Such a low fraction of

CHAPTER 3

star formation would not alter the line diagnostics significantly and would remain hidden. Hence, we cannot rule out ongoing star formation based on the central cold gas mass observed by Ueda et al. (2014). Given the highly disturbed kinematics, the possibility that dynamical suppression of star formation is preventing cold gas collapse cannot be tested by our observations.

3.6.3 Stellar Population Mapping

Populations of a galaxy evolve in metallicity over time, gradually enriching with age. The expected quantities and rates of this enrichment are well known (Cararo & Chiosi 1994; Layden & Sarajedini 2000; Pont & Eyer 2004), with the rate of enrichment directly tied to galaxy mass resulting in the mass-metallicity relation. Thus, we can quickly establish whether a galaxy has followed the standard enrichment of its population as would be expected from an isolated galaxy.

In reality, galaxies are more often than not experiencing regular disturbances in the form of mergers, fly-bys and intracluster medium interaction such as ram-pressure stripping (Lotz et al. 2011; Sinha & Holley-Bockelmann 2012; Ebeling et al. 2014; Ventou et al. 2017). One effect of this is the variation of the age-metallicity relation of a galaxy from the modelled form. This is most strikingly clear when a galaxy accretes material from a lower mass galaxy (Spolaor et al. 2009; Leaman et al. 2013a). Due to the lower metal enrichment rate of lower mass galaxies than that of larger mass galaxies, one finds that in general a smaller mass galaxy will exhibit far lower values of metallicity at late ages. Because of the ability for full spectral fitting methods to identify populations based on age and metallicity models, one would see these two populations as distinct and separate areas on an age-metallicity diagram. This is dependent on the difference in mass of the mergers however, as if two galaxies of similar mass were to merge, the separation of populations on the age-metallicity diagram would be too little to distinguish at the current resolutions

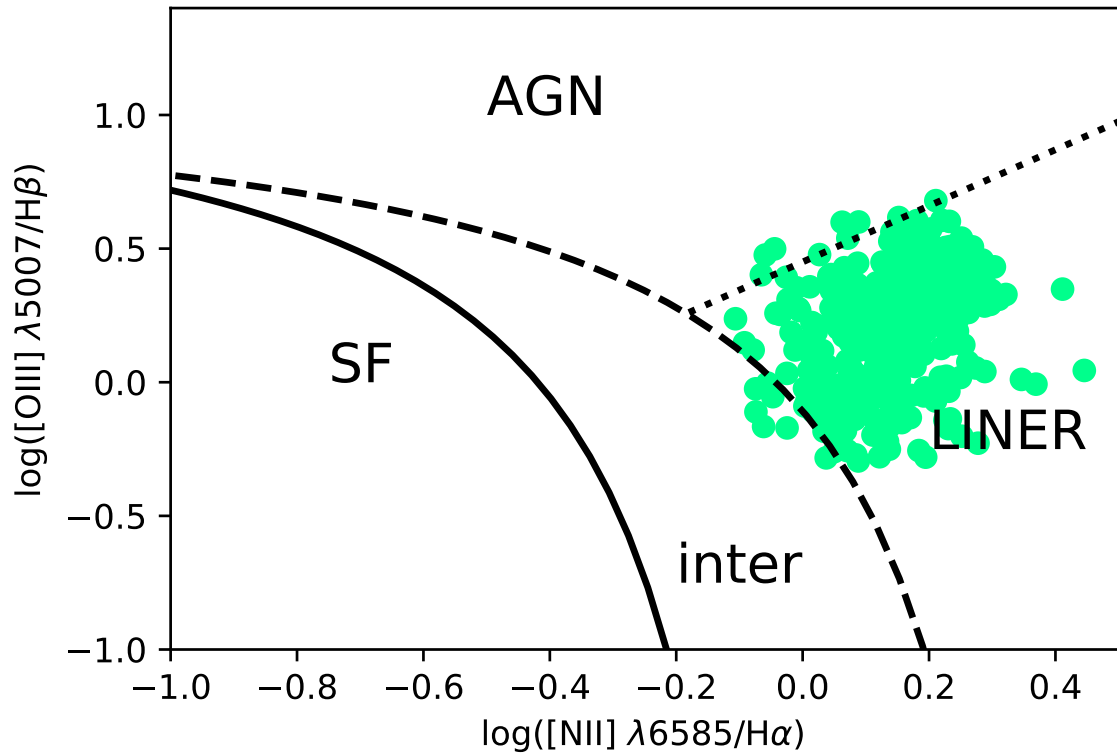


Figure 3.6: An emission line diagnostic diagram (Baldwin et al. 1981) divided into various sources. Each bin is shown as a point according to its emission ratios of $[\text{NII}]/\text{H}\alpha$ and $[\text{OIII}]/\text{H}\beta$ allowing for the identification of regions of star formation, AGN emission or Low-ionization nuclear emission-line region (LINER) emission. Detailed description of the line equations can be found in Park et al. (2013). NGC 7135 shows no bins where current star formation is clear in the emission. Slight overlaps outside the LINER emission bin are unlikely to be genuine, but rather likely arise because of noise and intrinsic variations. The galaxy emission is overwhelmingly LINER type.

CHAPTER 3

of full-spectral fitting methods. Using these principles we can estimate which of the populations present are those which have accreted onto the host galaxy, and are therefore ex-situ in origin.

There is potential to be misled by my mischaracterisation by models. For instance if intrinsic differences in natural in-situ stellar metallicity distributions are present in a galaxy, they could be misidentified as ex-situ fraction gradients. This is explained in detail in Section C.2, with no adverse impacts found by the models used.

We apply these principles to the population maps of NGC 7135 in order to derive the history of formation and evolution. In Figure 3.7, nine regions are marked with sequential letters corresponding to population maps, which are similarly sequentially lettered, with maps taken from the Voronoi bin below the labelled cross. Each position marks an area of interest or standard uniformity across the maps of Figure 3.2 with which we can build a picture of the assembly and current status of NGC 7135. Region ‘A’ marks the core of NGC 7135. Regions ‘B’ and ‘C’ sample the tidal tail clearly seen in the unsharp mask image (lower right panel of Figure 3.7), with increasing galactocentric radius. Regions ‘D’, ‘E’, and ‘F’ also sample with increasing galactocentric radius, however they do so outside of any prominent tidal features. These are assumed to be a ‘control’ sample which are chosen to represent the underlying galaxy, though show signs of probing accreted material. Regions ‘G’ and ‘H’ sample the tidal regions opposite the tail, with ‘H’ particularly covering unstripped remnants of the infalling galaxy. Finally region ‘K’ covers the core of the infalling galaxy.

Starting with region ‘A’, we see a very high metallicity, very old population associated with the galaxy core. This is to be expected and is commonly seen in galaxy cores (see e.g. Gu erou et al. 2016). There is little obvious evidence for accreted populations as expected, as shown by the old and high metallicity population, and lack of any clear population bimodality.

CHAPTER 3

Moving along the main tidal tail in region ‘B’ we see a much younger population at high metallicity. When comparing to regions not associated with tidal features but at similar radius such as ‘E’ and ‘F’, we see that the population of ‘B’ is not similar to ‘E’ or ‘F’. This is largely due to a lack of older material that would be expected to be associated with the host galaxy. Plausibly this is the result of the vast majority of the stellar material originating in the infalling galaxy and comprising the tidal tail, and thus the populations visible are instead associated with this infalling object, rather than original populations of NGC 7135. A small amount of material is also visible as a young and metal poor population. This can be attributed to ex-situ material that merged onto either NGC 7135 or the infalling galaxy in the past prior to the current merger, and thus shows a separate population signature.

As we move further out along the tidal tail to region ‘C’, many of the features become more prominent. For one thing, the high metallicity population associated with the stripped material from the infalling galaxy remains. Furthermore, low metallicity ex-situ populations increase in the fraction of contributed mass (as seen as a distinctly separate low metallicity population). Care must be taken in comparison due to colour normalisation differences on the plot, however the maximum low metallicity ex-situ fraction increases from $\sim 0.5\%$ in ‘B’ to $\sim 1.0\%$ in ‘C’, with a higher sum total of ex-situ material. This increase is to be expected, as ex-situ material commonly increases in fraction with galactocentric radius (La Barbera et al. 2012; Martin et al. 2018; Davison et al. 2020). It is unclear whether this ex-situ population is associated with NGC 7135 or the infalling galaxy, however it could plausibly be from both, as models of hierarchical growth suggest both galaxies would have undergone historical minor mergers in all but the rarest cases (Fakhouri et al. 2010). A burst of star formation is also seen in the final Gyr history. This is suggestive of a rapid star formation event, most likely triggered as a result of the galaxy interactions. Following this, no star formation is noticed in any bin. A

CHAPTER 3

shutdown of star formation after a major merger is discussed widely in literature (see e.g. Bekki 2001; Barr et al. 2007; Cortesi et al. 2013; Querejeta et al. 2015; Puglisi et al. 2021).

Region ‘D’ samples an inner region of NGC 7135. It shows similar populations as in ‘A’, however extends slightly to lower ages and metallicities as expected following galaxy population age gradients. Little to no ex-situ material is clear. Moving further out in radius, we come to region ‘E’. This also shows the expected populations previously seen in ‘A’ and ‘D’. This time however there is a more significant low metallicity ex-situ population, which as mentioned previously is expected as one reaches regions further from the galaxy centre according to galaxy simulations. Also prominent in region ‘E’ is a population of intermediate age and high metallicity stars. As shown below in region ‘H’, this is almost certainly associated with the infalling galaxy.

Region ‘F’ samples at a slightly greater radius than ‘E’, again with more prominent features, though in similar positions to ‘E’. We see an increase in the low metallicity ex-situ population radially along the tidal tail (‘A’, ‘B’ and ‘C’) and well as radially in areas not associated with tidal features (‘D’, ‘E’ and ‘F’).

The final regions sample the galaxy shell and associated infalling object. Region ‘G’ examines an area of tidal shell seemingly also originating from the infalling galaxy. The region almost identically matches ‘H’ which is placed to examine the outskirts of the infalling object, in regions that have yet to be stripped. The fact that these two populations are quite so similar suggests they are of the same origin, and that the tidal shells and tails are the result of scattered accreted material from the infalling galaxy.

Finally region ‘K’ examines the core of the infalling galaxy at approximately 0.5 effective radii from the centre of NGC 7135. It shows a highly metal rich and old population with the exact tendencies of a galaxy nucleus. It shows largely the same

CHAPTER 3

properties as the nucleus of NGC 7135, though with marginally lower metallicity and a greater extent in age, suggesting a lower mass.

The velocity dispersion of region ‘K’ (seen in Fig 3.2) is at a much lower average velocity dispersion than the host galaxy, again suggesting a lower mass of the merging galaxy compared to NGC 7135. This is curious considering its high metallicity. One explanation would be that the in-falling galaxy is the remnant of a galaxy core stripped of its halo, which would explain both its relatively high brightness and high metallicity. This is also supported by the large amounts of seemingly ex-situ gas that are seen in Figure 3.3, where this gas would have formed the outer regions of the infalling galaxy as explained further in section 3.6.2.

The velocity dispersion (Fig 3.2) increases significantly midway between the accreting galaxy core and the host galaxy core. This further lends weight to the idea that material is accreting onto the host galaxy, as the high velocity dispersion area indicates a region where accreted material begins encountering large amounts of in-situ material, and the difference in velocities becomes more evident, inflating the velocity dispersion, prior to mixing.

In summary, the population maps are indicative of three distinct galaxy populations, in which two significant merger events are present. The first merger is ongoing, with an intact core of a second galaxy currently in close proximity to NGC 7135, with material being stripped off, accreted onto NGC 7135, and creating large tidal features. These make up the high metallicity populations at intermediate ages. Yet another population is consistently present, as a low metallicity, intermediate to old aged population. As discussed previously, chemical enrichment and mass-metallicity relations mean this population is not associated with either galaxy. Therefore we attribute these stars to older historical mergers, now mixed loosely with the main populations. It is unclear which of these two present galaxies these populations accreted to, however as mentioned previously, the ex-situ population is likely present in

CHAPTER 3

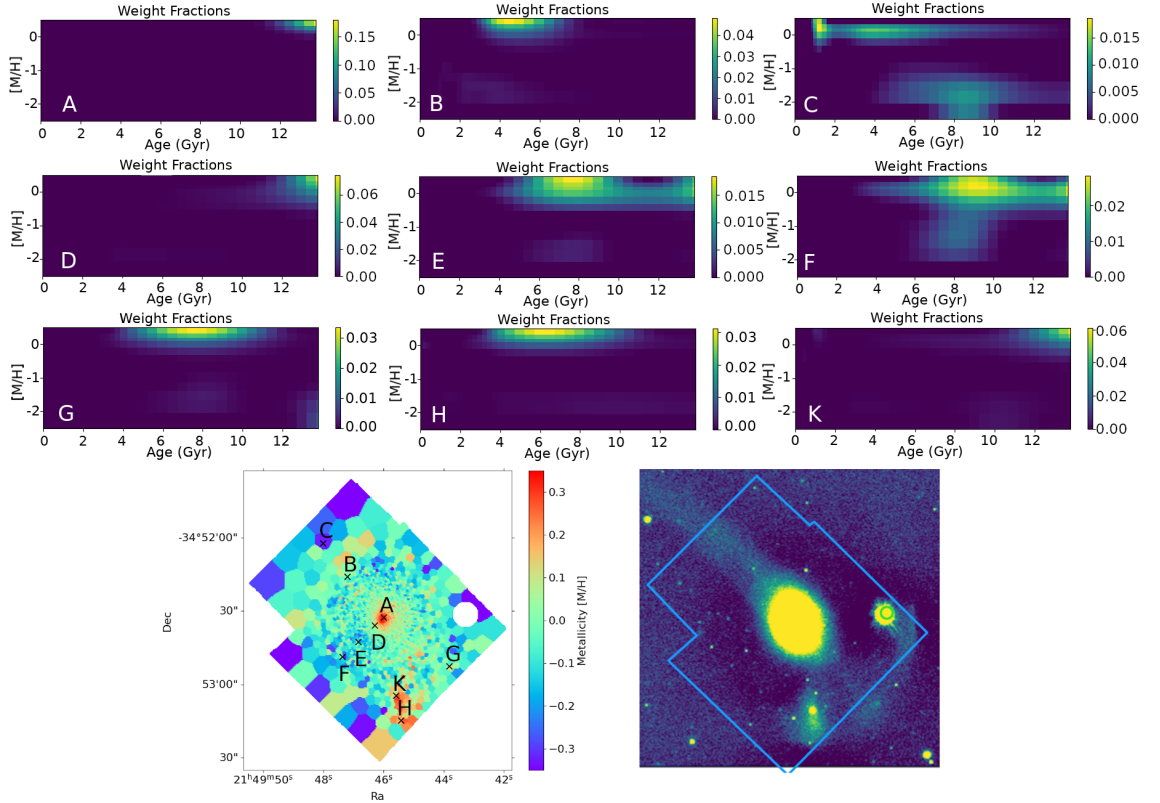


Figure 3.7: NGC 7135 population sampling diagram. The upper nine panels display mass weighted metallicity space of NGC 7135 for various regions. Corresponding regions are marked in the lower left panel with crosses marking the position extracted, and the corresponding letter. The lower right panel shows the same region as an unsharp masked image to highlight tidal features. Data for the unsharp masked image are taken from the VST ATLAS survey (Shanks et al. 2015). The diagrams build a narrative in which a recent and ongoing merger creates large tidal features in NGC 7135. There are also populations of far lower metallicity which are well mixed in the galaxy. These populations indicate historical mergers of high merger-mass ratio.

both galaxies independently, and was captured by each prior to this ongoing merger.

3.6.4 Accreted Populations

As seen in Figure 3.7, many bins display a bimodality in population distribution (see e.g. panels ‘B’, ‘C’, ‘E’, ‘F’, ‘G’, and ‘H’). Such a strong separation in populations suggests stellar material being obtained from more than a single source. Galaxies not associated with the main galaxy will evolve with a different metallicity due to the mass metallicity relation. As such, when the galaxies merge, there will be a distinct separation in the Age-Metallicity relation of each galaxy. The most obvious explanation for the bimodal populations seen in Figure 3.7 would be the merger of a less massive, lower metallicity galaxy to the host galaxy or onto the infalling galaxy. Stars from this galaxy were formed from around ~ 10 Gyr ago, though considering there is a peak of star formation from both galaxies, it is likely that the merger occurred between 10-6 Gyr ago. Furthermore, the fact that the bi-modality of populations is seen at almost all positions across the galaxy outside of the cores (panels ‘B’, ‘C’, ‘E’, ‘F’, ‘G’, and ‘H’) suggests that this material has been well mixed and is distributed throughout the galaxy, with the exception of the two galaxy cores (see panels ‘A’, ‘D’, and ‘K’).

To explore the population bi-modality, the fraction of stars not associated with the main host population was determined from each bin. To identify two discontinuous populations, a dividing line was sought across the population map, which would follow the lowest saddle points. This ‘path of least resistance’ then divided the populations into two distinct sources; one being material from NGC 7135 and the in-situ material of the infalling galaxy; and the other source being low metallicity populations accreted onto both galaxies at earlier times. This can be imagined as the valley between two hills, with the dividing line taking the natural path of a river at the lowest potential. This is visualised in Figure 3.8 with a red line showing

CHAPTER 3

the calculated separation path for one random bin, separating the populations into two sources.

Application of this to all bins provides a map such as in Figure 3.9, where we can examine the fraction of stellar material associated with the lower metallicity source. Figure 3.9 shows a polar view of NGC 7135 to better examine radial features. By examining fraction across the galaxy we can infer regions of higher or lower concentration of the accreted material.

At the centre of NGC 7135 we see no accreted material suggesting the core is dominated by in-situ stars. The density of accreted material rises with radius which is indicative of galaxy mergers depositing material on the outer regions of the galaxy. The material seems to be unevenly radially mixed, with proportionally higher quantities of ex-situ material deposited between 0 and 1 radians from North. This is likely a projection effect, as the area at the south of the galaxy (the left and right extents of Figure 3.9) aligns with the previously mentioned high metallicity galaxy, with the stream of stellar material obscuring the host galaxy structure, and dominating the spectral light.

We can further see evidence of the division of the various populations by examining stellar mass estimates per population, determined with the division of the age-metallicity plane in combination with mass-to-light ratios. We show this in Figure 3.10, with three regions of different populations separated roughly. The panel labelled ‘1’ corresponds to intermediate age stars with high metallicity which were associated with the infalling galaxy. This is confirmed in the first map in the Figure (panel 2) in which there is a noticeably higher stellar mass associated with the infalling object for only this population. This panel also encompasses much of the stellar material of NGC 7135 near to the centre though at a slight distance, as is expected from standard galaxy age gradients. Though effects from the pointing overlaps are visible, it is notable that we see a small amount of material tracing

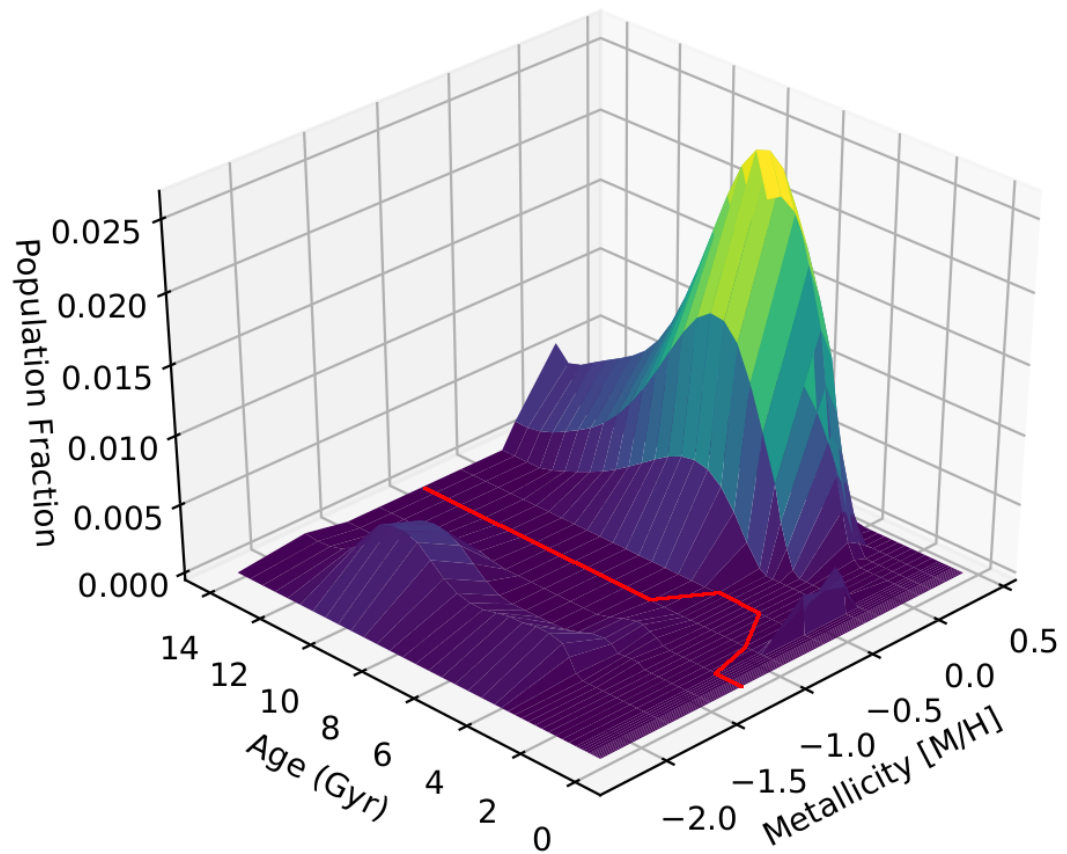


Figure 3.8: Population map of one bin projected on 3D axes. A line is sought for each map to bisect the lower metallicity population from the older using low saddle points. For this example, the path is marked by a red line.

CHAPTER 3

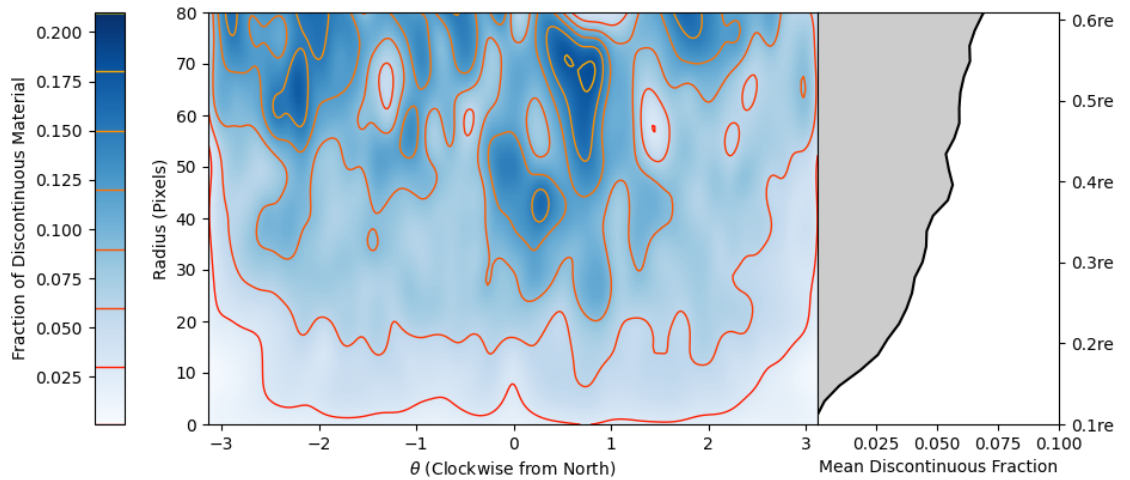


Figure 3.9: The left panel shows a polar oriented map of NGC 7135. Blue colour shows the mass fraction of derived material not associated with the host galaxy population, with contouring shown in red-orange-yellow. The angle is shown with 0 radians as the North of the image and positive angle increase showing clockwise movement around the galaxy. Gaussian smoothing has been applied to show more clearly larger structures of ex-situ material. The radius from centre has been limited to include only radii in which a complete circle can be arranged within the image. The adjoining right-hand panel shows the same radial positions as the left side, however it shows the mean discontinuous mass fraction for a complete circle for the radii. Mean fraction was calculated using circular annuli of radius 3 pixels with a moving average. The effective radius is taken from table 1 of Marino et al. (2011). The fraction of accreted material increases with radius, with a roughly 7% increase within 0.6 effective radii.

CHAPTER 3

the tidal tail and other tidally derived features. This suggests that the intermediate age material and tidal tail is associated with the infalling galaxy exclusively, though further data analysis from a higher resolution stellar model grid would be required for verification of this.

In the second labelled map (panel 3) we see that the most metal rich and oldest material is associated heavily with the host galaxy, with a strong gradient from the galaxy centre. This in-situ population is generally undisturbed and centrally concentrated, in comparison to the largely ex-situ population represented in the 1st map. Finally in the third labelled map (panel 4), we see again a gradient of stellar mass associated with the host galaxy. This third map shows only stars at far lower metallicities than the majority of the stellar material. This material is assumed to be low mass objects which have historically accreted to NGC 7135, and are now well mixed into the galaxy. It should be noted that these are rigid divisions, and that the true population distributions from each object undoubtedly bleed over into the other divided regions (especially in regions ‘1’ and ‘2’).

3.7 Discussion

Analysis of the galaxy kinematics and gas of NGC 7135 yielded evidence for both historical galaxy mergers, as well as an ongoing disruptive major merger. Despite the kinematics of past mergers being hidden (to the available resolution of data) due to mixing over time, ex-situ populations were extracted from the galaxy using full spectral fitting. This allowed for the identification of a well mixed low-metallicity stellar population relative to the larger fraction of higher metallicity stellar population. Considering expected enrichment patterns, this can only have occurred if either gas or stars (or both) originating in an ex-situ galaxy rapidly accreted or fully merged onto NGC 7135. The lower metal content of this population made it distinct from the original population.

CHAPTER 3

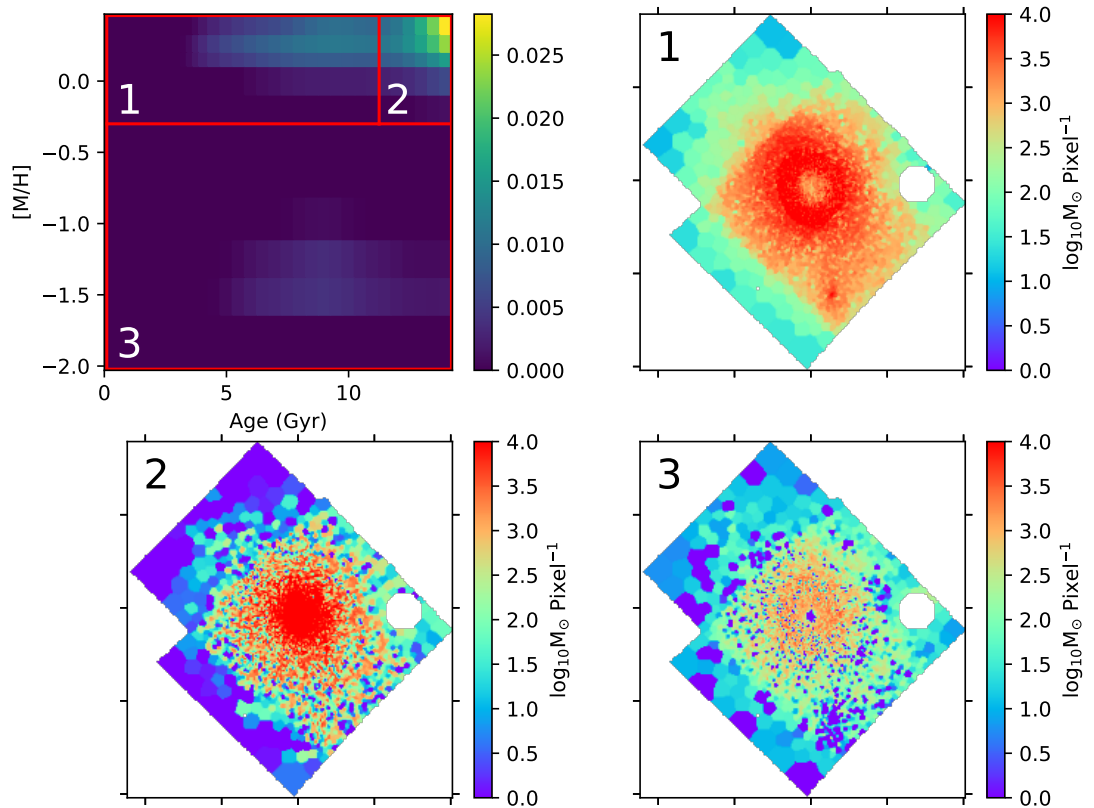


Figure 3.10: The first panel shows a general galaxy age-metallicity map. This is divided by the red boxes into 3 groups of populations to examine the mass associated with each area. Panel labels correspond to the numbers on the age-metallicity map. These show the divided nature of the populations, in which the intermediate age high metallicity population is more strongly associated with the infalling object and tidal features, whilst the older metal rich population is associated with the host galaxy.

CHAPTER 3

Potentially, all the stellar material in this population could have been created in-situ using gas that was accreted from another galaxy. This is highly unlikely however considering the specificity of the age and metallicity of the two distinct populations. Were these stars to be the product of new infalling gas, we would expect to see a mixing of the gas, and for the metallicity of new stars born after the merger event to be at a more intermediate metallicity. Instead, we see the two populations continuing to form stars without a sharp change in metallicity, thus the lower metallicity population stars are considered to be born ex-situ.

The bimodality of these stars allowed for clean separation of the ex-situ and in-situ populations. Thus the relative fraction of ex-situ material could be ascertained. This allowed for the exploration of ex-situ fraction with galactocentric radius, as shown in Figure 3.9. The Figure shows a clear preference for ex-situ material to be located at the outer edges of the galaxy, with no detectable ex-situ material in the centre of the galaxy. This is akin to simulated results showing the same preference for ex-situ fraction increase with galactocentric radius (Schaye et al. 2015; Crain et al. 2015; Rodriguez-Gomez et al. 2016; Davison et al. 2020), as well as observational studies showing the same principles (Forbes et al. 2011; Pillepich et al. 2015; Oyarzún et al. 2019). The mean ex-situ fraction measured for NGC 7135 at approximately 0.6 effective radii (the greatest extent captured by the MUSE image) is 7%. This is only representative of the low metallicity populations from low-mass systems. Higher metallicity populations from mergers of smaller mass-ratio mergers would be disguised amongst in-situ populations.

Limitations of this technique largely arise from the ability to separate populations. At current resolutions of full spectral fitting techniques, populations must be wholly distinct in metallicity to be noticeably separable from the host population. Accreted material with age and metallicity similar to that of the host galaxy would be largely indistinguishable from the main population. Further limitations are the

CHAPTER 3

inability to directly distinguish between stars that are born ex-situ, and those born in-situ but of ex-situ material. As discussed above, these limitations are unlikely to be dominant in this scenario.

One interesting area to consider is the eventual fate of NGC7135. Will it retain some semblance of a spiral structure, or evolve into an S0 or elliptical galaxy? Conversion into an S0 galaxy seems to be a distinct possibility as S0 galaxies with coherent disk kinematics form through merger mechanisms, though the exact merger specifics continue to be debated within the community. Some evidence suggests that S0 galaxies are rarely expected to be formed through major mergers (<4:1 merger ratio) (Bournaud et al. 2005; Lofthouse et al. 2016), with the conclusion given that major mergers are a plausible but non-dominant mechanism for early type formation. Conversely, other arguments suggest that S0 galaxies can indeed be formed from major mergers (Querejeta et al. 2015). Furthermore major mergers can be shown to give rise to much of the inner structure often found in early types (Eliche-Moral et al. 2018). Perhaps the most consistent agreement for the formation requirements of an S0 via mergers is the necessity for a misalignment of angular momentum between the in-situ and ex-situ accreted baryonic components (see e.g. Sales et al. 2012). Considering the existing baryonic misalignment present in NGC 7135 in the form of a counter rotating disk, and considering the seemingly misaligned orbit of the ongoing merger, it is perhaps likely that the ongoing disruption will lead to NGC 7135 tending towards S0 morphology. Plausibly the kinematics would increasingly reflect those of general spheroid galaxies as newly formed stars with an opposing angular momentum to the mean, and those recently accreted, would begin to reduce kinematic coherence. Though this is a distinct possibility, the true future of NGC 7135 will remain unknown until more decisive techniques and modelling are developed. Due to the complex nature of the recent history of NGC 7135, any predictions on future evolution are speculation.

3.8 Conclusions

We have used a Voronoi binned map of NGC 7135 to explore kinematic stellar features such as velocity and velocity dispersion, as well as the distributions of stellar properties such as age and metallicity. Gas properties were also explored in regular bins, with both kinematic gas properties and gas distribution investigated. Gas was shown to be counter rotating compared to stellar material, with significant evidence of disturbance in the galaxy core. This along with population evidence shows a galaxy currently merging onto NGC 7135. Despite gas being present, little to no current star formation was identified. ALMA data of the galaxy core points to a star formation rate of only $0.025 M_{\odot} \text{ yr}^{-1}$ assuming normal depletion times. Strong LINER emission likely obscures emission associated with star formation and as such a higher SFR cannot be ruled out.

During population analysis of NGC 7135 from data provided by the SOSIMPLE project, we have identified both historic and ongoing merger activity. This was achieved using a ‘full spectral fitting’ method to disentangle strong bi-modalities in stellar populations. We show that in a snapshot of a ‘single’ galaxy, we are in reality witnessing the product of three distinct galaxy populations.

An ongoing merger or large accretion event is clear from the stellar kinematic maps, showing a distinct area of stellar material not associated with the host galaxy, but interacting with the galaxy structure. Likewise in gas maps we see large velocity dispersion in areas where ex-situ infalling gas interacts with in-situ gas.

At least one historical large merger event took place that has now mixed into the general galaxy populations. The populations of this merger are born largely at around 6-10 Gyr ago according to star-formation history derived by full spectral fitting. This potentially provided gas with lower enrichment with which NGC 7135 birthed stars of lower metallicity; however the timeline of stellar ages, matched with the likely merger date makes it highly likely that most, if not all of the stars belonging

CHAPTER 3

to this population are ex-situ stars originating in another galaxy. Considering there is no discernible change in the host population metallicity of new stars born after the merger, we assume that all lower metallicity population stars are ex-situ in origin. The timeline of star formation history suggests that this merger caused a general shut-down of star formation in NGC 7135, not long after the merger event.

We calculate the fraction of the ex-situ material as a function of galactocentric radius, finding a steep increase in ex-situ material as we probe further to the outskirts of the galaxy. The centre of the galaxy exhibits no signs of ex-situ material, whilst by 0.6 effective radii, this fraction is at 7%. This is in common with literature expectations of ‘two phase’ galaxy assembly seen both observationally and in simulation, where ex-situ material is preferentially deposited on the outskirts of a galaxy.

Many more SOSIMPLE galaxies are available from the survey, with much left to explore.

Chapter 4

Observing Ex-situ Populations Across the Mass-Size Plane with MUSE

4.1 Remarks

The following chapter includes work published in MNRAS as Davison et al. (2021b), with additions to the published document where appropriate.

4.2 Chapter Abstract

Galaxy mergers are instrumental in dictating the final mass, structure, stellar populations, and kinematics of galaxies. Cosmological galaxy simulations indicate that the most massive galaxies at $z=0$ are dominated by high fractions of ‘ex-situ’ stars, which formed first in distinct independent galaxies, and then subsequently merged into the host galaxy. Using spatially resolved MUSE spectroscopy we quantify and map the ex-situ stars in thirteen massive Early Type galaxies. We use full spectral fitting together with semi-analytic galaxy evolution models to isolate the signatures

CHAPTER 4

in the galaxies' light which are indicative of ex-situ populations. Using the large MUSE field of view we find that all galaxies display an increase in ex-situ fraction with radius, with massive and more extended galaxies showing a more rapid increase in radial ex-situ fraction, (reaching values between $\sim 30\%$ to 100% at 2 effective radii) compared to less massive and more compact sources (reaching between $\sim 5\%$ to 40% ex-situ fraction within the same radius). These results are in line with predictions from theory and simulations which suggest ex-situ fractions should increase significantly with radius at fixed mass for the most massive galaxies.

4.3 Chapter Introduction

There are many indications from both observational and theoretical astrophysics that massive galaxies form 'inside out'. This suggests that galaxies begin as a core of stars formed in-situ, and grow larger through both additional in-situ star formation and through the accretion of smaller galaxies (Trujillo & Pohlen 2005; Auger et al. 2011; Pérez et al. 2013; Van Der Burg et al. 2015). As such, a gradient in stellar population parameters can be imprinted on a galaxy, with the largely in-situ core giving way to a more ex-situ dominated outskirts. Kinematic and population gradients have been found to exist frequently in galaxies (e.g. Norris et al. 2006; Naab et al. 2009; Spolaor et al. 2010; Guérou et al. 2016; Sarzi, M. et al. 2018; Pinna, F. et al. 2019; Dolfi et al. 2020; Simons et al. 2020) however specific treatments to separate intrinsic gradients in the in-situ populations from those resulting from distributions of ex-situ material is a challenging task. This is largely a product of the difficulty in navigating around complex and interconnected secular processes that, additionally to accretion, can provide gradients in stellar populations and kinematics. As a result, disentangling the evidence of mergers is difficult to do via photometry, or from average metallicities and ages.

Evidence of this two-phase galaxy assembly also comes in the form of bimodality

CHAPTER 4

of globular star clusters (GCs) in colour and metallicity. GCs are found to display complex colour distributions in nearly every massive galaxy system studied (e.g. Zinn 1985; Larsen et al. 2001; Brodie & Strader 2006; Yoon et al. 2006; Peng et al. 2006; Faifer et al. 2011; Villaume et al. 2019; Fahrion et al. 2020). Red globular clusters are thought to be closely linked to in-situ formation or very massive mergers with higher metallicities, whereas their blue counterparts are more indicative of acquisition from lower mass galaxies with lower metallicities. A result of this is that merging low-mass systems frequently provide GCs of low-metallicity, in stark contrast to in-situ metal rich GCs (Choksi et al. 2018; Forbes & Remus 2018). These GC properties can be used to diagnose both merger history as well as gradients of ex-situ fraction (Forbes et al. 2015; Kruijssen et al. 2018; Beasley et al. 2018; Mackey et al. 2019), however this is complicated by uncertain mappings between colour and metallicity, and uncertain ages of old GCs in systems outside the Local Group.

Further evidence of a two-phase galaxy assembly scenario is derived from the faint stellar envelopes of massive galaxies. In Huang et al. (2018) (and building on work from Huang et al. 2013b) the authors use deep imaging to study the stellar halos of around 7000 massive galaxies from the Hyper Suprime-Cam (HSC) survey (Aihara et al. 2018) out to $>100\text{kpc}$. The authors find that surface mass density profiles show relative homogeneity within the central 10-20kpc of the galaxies, however the scatter in this profile increases significantly with radius. Furthermore, the authors find that the stellar halos become more prominent and more elliptical with increasing stellar mass. This is in line with a two-phase formation scenario in which central galaxy regions are formed by relatively stable in-situ processes, and the outskirts are formed through far more stochastic accretion and so show a greater scatter in the surface mass density. This is also found to be the case in Oyarzún et al. (2019) in which the authors find a flattening in the metallicity profile of $z < 0.15$ early type galaxies beyond a radius of $1.5r_e$, and conclude the most reasonable explanation of

CHAPTER 4

this is stellar accretion to the galaxy outskirts. This result is also seen for samples of brightest cluster galaxies (Edwards et al. 2020) who likewise find signatures of the two-phase scenario in profiles of kinematics and metallicity.

Simulations of galaxy formation also show strong preferences for galaxies to evolve through frequent mergers, and by accreting material to their outskirts (Kobayashi 2004; Zolotov et al. 2009; Oser et al. 2010; Navarro-González et al. 2013; Rodriguez-Gomez et al. 2016). This is particularly clear for the most massive ellipticals which show strong gradients of increasing ex-situ fraction with galactocentric radius, as well as high total fractions of ex-situ stars (with galaxies of mass $M_{\odot} > 1.7 \times 10^{12} M_{\odot}$ being composed of populations with an ex-situ fraction of $\approx 90\%$) (Oser et al. 2010; Lackner et al. 2012; Rodriguez-Gomez et al. 2016; Pillepich et al. 2018; Davison et al. 2020) and can be seen in Chapter 2. Despite clear trends in ex-situ fraction, these galaxies show a strong overlap between in- and ex-situ populations within 2 effective radii (Pillepich et al. 2015) which causes difficulty in photometric approaches to ex-situ population extraction (see also Remus & Forbes 2021). Modern photometric methods for identification of accreted stars and signatures of interaction (such as tidal features) are able to accurately identify stellar features in the stellar halo (e.g. Duc et al. 2015; Morales et al. 2018; Hood et al. 2018; Martinez-Delgado et al. 2021). Advanced deep-imaging methods can identify features of interaction out to 10 effective radii (Jackson et al. 2021). Despite these ongoing advances in treatments of photometric data, most have difficulty accurately quantifying ex-situ fractions in the centres of galaxies ($< 2r_e$) especially for ancient mergers which have largely diffused in projective space.

Notably, galaxy size seems to be closely linked to galaxy accretion history. Literature has widely shown that galaxies at high redshift are on average far more compact than similar mass galaxies in the local universe (Van Dokkum et al. 2006; Bezanson et al. 2009; Van Dokkum et al. 2014; Belli et al. 2015; Wellons et al. 2016).

CHAPTER 4

Larger galaxies are expected to grow radially as a result of dry-mergers disproportionately extending massive galaxies (Cappellari 2013; Barro et al. 2013). For this reason it can be highly instructive to examine galaxy properties related to accretion in both terms of galaxy radius and galaxy mass.

Analyses of the Illustris simulation (Genel et al. 2014; Vogelsberger et al. 2014; Vogelsberger et al. 2014) have shown the impact of mergers on galaxy populations, and work by Cook et al. (2016) further explored the population gradients in Illustris galaxies. These show clear demonstrations that large galaxies gain the majority of their material from ex-situ sources, rather than in-situ star formation. Particularly, Rodriguez-Gomez et al. (2016) find a cross-over point for nearby galaxies ($z < 1$, $M_* \approx 1-2 \times 10^{11} M_\odot$) wherein galaxies transition from in-situ dominated growth to ex-situ dominated growth. For all galaxies, the authors find a roughly even split of merger mass contribution between major mergers (mass ratio $> 1/4$) and minor/very minor mergers (mass ratio $< 1/4$).

This is similarly shown for the Magneticum simulations in Remus & Forbes (2021) where the mean Magneticum galaxy ex-situ fraction passes 50% at $M_* \approx 8 \times 10^{10} M_\odot$. Here the authors find similar splits in galaxy mass contribution from major and minor mergers, though with different defined mass splits. They show that the major merger mass contribution is consistently larger than minor mass contribution, but this is dependent on galaxy ‘class’ (with division based upon radial stellar density profiles), see their figure 6 for details.

Similarly in analyses of the EAGLE simulations (Schaye et al. 2015; Crain et al. 2015), almost all galaxies are found to contain a non-negligable quantity of accreted stellar mass. Clearly the influence of ex-situ populations from mergers and fly-bys on galaxy evolution is profound, influencing the composition, kinematics and stellar history of a galaxy. Stellar material acquired in mergers has been shown

CHAPTER 4

to be the key contributor to stellar mass in massive galaxies. As shown in Chapter 2, the lowest mass galaxies analysed ($M_* \approx 1 \times 10^9 M_\odot$) comprise $10 \pm 5\%$ ex-situ stars. This increases with mass up to the most massive galaxies in the simulation ($M_* \approx 2 \times 10^{12} M_\odot$) which are comprised of $80 \pm 9\%$ ex-situ stars. Interestingly this work highlighted trends in ex-situ fraction with galaxy density, showing that at fixed mass more extended galaxies would on average contain higher fractions of ex-situ stars.

With the recent advancement in integral field spectroscopy, galaxies are being studied spectroscopically as spatially resolved objects, detailing spectral differences with galactocentric radius, and physical location within a galaxy (see e.g. Guérou et al. 2016; Mentz et al. 2016). Instruments such as SAURON at the WHT, GCMS (VIRUS-P) on the 2.7m Harlan J. Smith telescope, KCWI on Keck, and MUSE (Multi-unit spectroscopic explorer) at the VLT (Bacon et al. 2001; Hill et al. 2008; Bacon et al. 2010) with their ~ 1 arcminute field of views have been critical to the development of this field, and are a few of the integral field units (IFUs) driving this particular area of research. IFUs have significantly widened the field of galactic archaeology for nearby galaxies as they have allowed for more thorough spatial investigations of population distributions. Derived population maps can provide powerful insights into visual features, kinematics, and evolution (see e.g. Comerón et al. 2015; Faifer et al. 2017; Ge et al. 2019; Davison et al. 2021a).

Alongside these advancements in instrumentation are equally important advancements in software. Full spectral fitting has evolved to fit the needs of the extraordinary data taken by IFUs. A number of full spectral fitting codes now exist which can efficiently reconstruct stellar populations present within galaxy spectra. Examples of such software are pPXF (Cappellari & Emsellem 2004; Cappellari 2017), FIREFLY (Wilkinson et al. 2017), STECKMAP (Ocvirk et al. 2006), and STARLIGHT

CHAPTER 4

(Cid Fernandes et al. 2005). Full spectral fitting software combines single-age single-metallicity stellar spectral models (single stellar population models) in a weighted grid in order to reproduce a provided spectrum. For pPXF, a linear least squares algorithm can determine the optimal stable solution of model combinations to reproduce an input spectrum. Template regularisation provides dampening of noise, and allows for a smoothed physical solution which better represents the distribution of ages and metallicity in a single integrated spectrum. With application to resolved spectral datasets of galaxies received from IFUs, it has become possible to extract maps of stellar populations for a given galaxy. This has provided remarkable insight into the stellar kinematic and population properties of galaxies (see e.g. Onodera et al. 2012; Norris et al. 2015; Ferré-Mateu et al. 2017; Kacharov et al. 2018; Ruiz-Lara et al. 2018; Boecker et al. 2020a, for examples of kinematic and population analysis from full spectral fitting).

A method to identify ex-situ stellar populations by exploiting these spectroscopically recovered age-metallicity distributions was proposed in Boecker et al. (2020b). In this method the age-metallicity distribution of each galaxy is determined via full spectral fitting. Chemical evolution templates for galaxies of different masses are calculated, depicting the in-situ star formation and chemical enrichment history of a galaxy. Lower mass galaxies typically have lower metallicities at fixed age than those at higher mass, and as such ex-situ stars can be separated from the recovered age-metallicity distribution of the host galaxy. This technique was applied to mock spectra (3650-7400Å) from simulated galaxies from the EAGLE cosmological simulation suite and demonstrated remarkably accurate results, such that the spectroscopically recovered accretion fractions and merger histories matched the known merger history of individual simulated galaxies.

Literature examining the stellar population profiles of galaxies has proven to be particularly useful for exploring galaxy evolution when considering the two-phase

CHAPTER 4

formation scenario. The MASSIVE survey (Ma et al. 2014) has provided insights into the links between stellar populations of galaxies, and their kinematics and abundance ratio patterns, finding a link between radial anisotropy and metal-poor populations, most likely as a result of minor mergers and accretion (Greene et al. 2013, 2015, 2019). Further population based evidence comes from the MaNGA survey (Zheng et al. 2017; Goddard et al. 2017; Li et al. 2018). In Oyarzún et al. (2019) the authors find variable metallicity gradients and flattening in the outskirts of MaNGA galaxies, suggesting that this is a sign of stellar accretion, and these features are also found in simulated environments (see e.g. Taylor & Kobayashi 2017). The SAMI survey has likewise provided clues of accretion from stellar population profiles (Scott et al. 2017; Ferreras et al. 2019; Santucci et al. 2020).

Work in Spavone et al. (2021) has utilised surface brightness distributions of MUSE galaxies to examine assembly history, with 3 massive galaxies ($M_* > 10^{12} M_\odot$) shown to have ex-situ fractions of $>77\%$. They further suggest that the majority of this ex-situ mass is obtained via major mergers. The work utilises deep imaging in combination with MUSE data in order to speculate on the merger mechanisms and accreted fractions of galaxies, however MUSE coverage is limited to within $\sim 1R_e$.

In this chapter we leverage high quality MUSE IFU data along with new analytic models and full spectral fitting techniques to measure the radial variation in ex-situ fraction across the galaxy mass-size plane. We improve and expand upon the Boecker et al. (2020b) method and chemical evolution templates to allow for a more sophisticated ex-situ fraction determination and uncertainty quantification. Ascertaining how ex-situ fraction correlates with galaxy density will provide indirect understanding of the impact of dry mergers on the host structure as well as stellar populations. Analytic expectations for the size-growth due to dry minor mergers would naively suggest that the least dense massive ellipticals may show stronger stellar population signatures of ex-situ accretion.

CHAPTER 4

We present the analysis of 13 resolved galaxies observed by MUSE. In order to estimate ex-situ fractions of these galaxies, full spectral fitting (Section 4.4.1.3) is used to quantify the ages and metallicities of stars present in each binned area of the galaxy data-cube. Following this, the in-situ and ex-situ stellar components are separated using analytic prescriptions for the expected galaxy assembly pathways so that we may estimate the quantity of ex-situ stars present in a galaxy (Section 4.4.2).

4.4 Methodology

A galaxy sample was obtained by first searching for all galaxies that have been observed with MUSE. A visual inspection of the dataset showed that lower mass resolved galaxies were poorly represented by existing MUSE data. With this in mind a primary mass selection was defined, limiting galaxies to between $1 \times 10^{11} < M_{\odot} < 2.5 \times 10^{12}$ in order to facilitate examining galaxy features with respect to galaxy size at fixed mass. This was then cut to those galaxies with accurate distance estimates (via SN1a, TRGB, or GCLF), and further cut to galaxies with good imaging data, including estimates of effective radius and ellipticity. Requirements were also imposed to only consider targets with MUSE spatial coverage to a minimum of 1.5 effective radii (though preferably to 3), high spatial resolution, and quality data cubes without reduction errors. The distribution of these galaxies against a wider sample is shown in Figure C.1. These selected MUSE data cubes were obtained from the ESO MUSE archive. All final cube mosaics include the galaxy core and extend contiguously to the outer regions. Data-cubes were obtained from the following ESO programs: 094.B-0298 (P.I. Walcher, C.J), 296.B-5054 (P.I. Sarzi, M), 0103.A-0447 & 097.A-0366 (P.I. Hamer, S), 60.A-9303 (SV), 094.B-0321 P.I. (Marconi, A), 094.B-0711 (P.I. Arnaboldi, Magda). Data were taken as pre-reduced data-products in the majority of cases. In some cases where cubes were reduced poorly, cubes were

CHAPTER 4

re-reduced using the standard ESO pipeline (Weilbacher et al. 2020). Reduction applied standard MUSE calibration files and all exposures were reduced with bias subtraction, flat-fielding, and were wavelength calibrated.

Galaxy mass was estimated using relations between J-K colour and K-band stellar mass-to-light-ratios (Υ'_K). J-K and K-band magnitudes were provided by the 2MASS Large Galaxy Atlas (Skrutskie et al. 2006). As shown in Westmeier et al. (2011), using analysis from Bell & de Jong (2001), the J-K to M/L relation is defined as:

$$\log_{10} \left(\Upsilon'_K \right) = 1.434 (J - K) - 1.380 \quad (4.1)$$

and assumes a modified Salpeter IMF (Salpeter 1955; Fukugita et al. 1998).

These stellar mass-to-light-ratios were combined with K-band magnitudes, distances, and errors therein to produce mass estimates. Size was derived from 2MASS LGA J-band half-light radii estimates, in combination with distance estimates. Monte-Carlo simulation of magnitude, distance, apparent radius, and other uncertainties was employed to estimate final uncertainty in mass and size. For each galaxy, Monte-Carlo simulations were run 15000 times, considering all sources of error to produce a probability distribution of mass and size. Distance estimates and errors impacted on the calculation of physical radius, which in turn impacted on the area with which to calculate mass using mass to light ratios.

4.4.1 Observations and Analysis

For all binning methods, a ‘first sweep’ examined the signal-to-noise (S/N) of all spaxels in the datacube. The S/N of each spaxel was defined as the mean variance in a wavelength range of $5450\text{\AA} < \lambda < 5550\text{\AA}$ which allowed an accurate S/N estimate calculated in a region free from the strongest absorption or emission lines. A mask was applied such that any single spaxel with mean S/N < 1.5 within the wavelength range was excluded from further binning. This ensured there would be

CHAPTER 4

no pollution of useful regions of a cube by particularly noisy pixels. Pixels were infrequently masked with the mean quantity of initially masked pixels per target being 1.4%, with the most being masked in NGC 4696 at 6.1% initially masked, and some targets (e.g. NGC 1316) requiring only 5 or 6 initially masked pixels.

Following this, the spaxel mask was built upon to include objects not associated with the galaxy, such as foreground stars or bright background objects. A Moffat function (Moffat 1969) was applied to the galaxy at V-band which was subtracted from the original V-band slice. The resulting image was scanned using ‘photoutils’ routine included in MPDAF (Bacon et al. 2016) with a sigma value defining the threshold for a source to be considered non-continuous with respect to the galaxy light. This threshold varied case by case, depending on aspects such as galaxy brightness, large scale structure, and diskly areas of the galaxy. Any segmented regions above the threshold were added to the general mask of pixels to be excluded whilst binning.

4.4.1.1 Voronoi Binning

The MUSE cubes gathered from the sample presented extremely large datasets, with large variations in S/N. The on-source time of each cube varied between objects and surveys but was at a minimum of 590s per spaxel (central region of NGC 4594) and a maximum of 11400s per spaxel (combined cubes of outer regions of NGC 4696). To overcome issues associated with low S/N spectra we employed Voronoi binning to ensure the correct treatment of lower S/N areas, whilst maintaining the usefulness of high S/N spectra (usually located in the galaxy core).

Voronoi binning of S/N (here specifically using the ‘Vorbin’ package of Cappellari & Copin 2003) gathers data on a 2D spatial plane such that bins reach a minimum summed S/N threshold. Spaxels are optimally arranged into a bin such that the spatial irregularity of a bin is minimised, and simultaneously the sum of the S/N

CHAPTER 4

within a bin minimally above the desired S/N threshold (thus high S/N areas are not wasted).

We use a minimum S/N threshold of 100 per \AA uniformly for all galaxies in the sample. Due to differences in exposure time, galaxy brightness and other data quality aspects, this results in varying numbers of Voronoi bins per unit area of a given galaxy. The brightest and deepest cubes necessitated many more Voronoi bins per unit area, as many pixels were often left unbinned. Dimmer and shallower targets consist of fewer bins, containing a greater number of binned pixels. The spatial variation of Voronoi bins is quite large between all galaxies. In all cases, the centres of galaxies did not necessitate binning, so spatial coverage of a bin was 1 arcsecond. For regions with more pixels binned together, the spatial coverage could reach as high as 200 square arcseconds. At some point, the size of the area covered would yield poor results, due to the area covered representing multiple non-similar galaxy regions. All Voronoi bins in this project were kept within physical limits, and bins that encompassed more than 5% of the pixels within a cube were discarded.

Spectra within a given Voronoi bin were summed, providing a single spectrum representative of the given bin. Final summed spectra were checked to ensure a minimum of S/N=100 was achieved in all bins. This does not however account for spatial co-variance between pixels. Considering the large spatial coverage of the average Voronoi bin (relative to pixel size) spatial correlations are unlikely to impact on derived values in any bin. Furthermore, all Voronoi diagrams are understood to be a general overview of galaxy properties, rather than an exhaustive pixel-perfect map.

4.4.1.2 Elliptical Binning

When investigating features and trends associated with galactocentric radius, it can be more instructive to bin elliptically. We use elliptical binning to explore features

CHAPTER 4

such as ex-situ fraction as a function of radius. This is simply done, with an origin set at the centre of a galaxy. Elliptical rings derived by projected ellipticity are overlaid onto the cube spatial plane with the major axis increasing by defined bin size. Ellipticity and radial increments are derived from 2MASS LGA data, with axes ratios derived from a J+H+K (super) image at the 3-sigma isophote (Jarrett et al. 2003). This allows all pixels to be binned by galactocentric radius. We performed this using fractions of effective radius (as a standard using $0.1r_e$ steps) as the increment of major axes, in order to maintain a comparable increment across all galaxies in the sample. The ratio of pixel size to elliptical bin width varies with galaxy size and apparent radius but has a minimum bin width of 11 pixels, occurring in NGC 1332 due to the elliptical projection as well as the smaller size against the pixel scale. The mean bin pixel width is greatest for NGC 1316 which has a minimum bin pixel width of 45 pixels.

4.4.1.3 Full Spectral Fitting

We fit stellar population models to binned spectra using the Penalised Pixel-Fitting (pPXF) method (Cappellari & Copin 2003; Cappellari 2017). pPXF uses a maximum penalised likelihood approach to extract the stellar kinematics and stellar populations from the spectra of galaxies. Binned spectra are limited to within the wavelength range ($4750 \text{ \AA} < \lambda < 6800 \text{ \AA}$). This optimally avoids wavelengths that are sensitive to the IMF (this is discussed further in Section 4.6) as well as avoiding regions particularly affected by sky lines. The few remaining sky lines and existing IMF sensitive lines are mostly removed by the iterative clipping routine associated with pPXF. The MUSE tested wavelength range has been shown to be successful in recovering stellar populations parameters in Gu erou et al. (2016).

CHAPTER 4

To ensure the output of pPXF population estimate is physical, we use the regularisation method built into pPXF. Regularisation is intended to smooth over the output weights to provide population estimates that are optimally physical. Weighted templates that have been combined to produce a target spectrum will often be localised to a single unphysical solution, with many other valid solutions being overlooked, despite their physicality. These distributions of stellar populations weights are not just unphysical but are beyond the resolution capabilities of modern instrumentation, as standard error can be expected to spread populations to beyond just a single population grid element. To produce more representative distributions, regularisation seeks to smooth the solutions to a physical state. The challenge is to smooth the template weights to a solution that most accurately represents observed conditions, whilst not overlooking genuine fluctuations and details present in the model-fit.

The value of regularisation is adjusted up to a maximum value such that the reduced χ^2 of this smoothest solution is no different than $1-\sigma$ of the unregularised solution (Cappellari 2017). This has been shown in literature to be an accurate and useful method of galaxy population extraction (see e.g. Comerón et al. 2015; Guérou et al. 2016; Faifer et al. 2017; Ge et al. 2019).

We use an iterative method to find the most reasonable value of regularisation for each bin in a galaxy cube. First the noise from the unregularised solution is rescaled so that $\chi^2/N = 1$, where N is the number of voxels in the target spectrum. Next a series of fits using different amounts of regularisation are produced. We record the output $\Delta\chi^2$ for each fit using a particular regularisation, and fit a function to the output $\Delta\chi^2$ values with respect to the input regularisation guesses. From this function we can find the maximum regularisation parameter which corresponds to $\chi^2 = \chi_0^2 + \sqrt{2N}$. We perform this procedure for all bins, obtaining optimal solutions in all cases. The value of the regularisation parameter has little variation for similar

CHAPTER 4

spaxels of the same galaxy, but can differ between distinct galaxies. Tests were run without regularisation and similar, albeit far noisier, results were obtained.

A total of 552 solar-scaled SSP models, constructed from the MILES spectral library, were used to fit to galaxy spectra (Vazdekis et al. 2012). These models were of Kroupa (Kroupa 2001) revised initial mass function (log slope of 1.3) using BaSTI isochrones, with a metallicity range of -2.27 to $+0.4$ [M/H] in 12 non-linear steps, and an age range of 0.1 to 14.0 Gyr in 46 non-linear steps (Cassisi et al. 2005; Pietrinferni et al. 2006; Falcón-Barroso et al. 2011). Models using alternative IMFs were used (Chabrier IMF (Chabrier 2003) and Kroupa universal (Kroupa 2001) were tested) with no conceivable real difference to the final results.

We perform the pPXF routine twice for each bin, once for the robust extraction of stellar kinematics, and a second time for the extraction of stellar populations assuming the fixed kinematics derived during the initial fit. For robust kinematic fitting we use 4th degree additive polynomials. The population analysis uses no additive polynomials, instead using 16th degree multiplicative polynomials and 2nd order regularisation. This has been shown to be effective in kinematic and population analysis (see e.g. Guérou et al. 2016).

A full process example Figure can be found in Figure 4.1 which shows the reduction and analysis for NGC 1407.

4.4.2 Ex-Situ Fraction Estimation

The mass fractions returned by pPXF in age-metallicity space represent the contribution to the galaxy’s integrated spectrum from different stellar populations. A host galaxy’s chemical evolution will typically progress from older and more metal poor stellar populations, to younger more metal rich stellar populations. The rate of this chemical enrichment is a combination of many complex processes including outflow and recycling of gas, as well as production and removal of heavy elements

CHAPTER 4

through stellar evolutionary processes. Many of these processes are dependent on the star formation rate, IMF, and stellar mass of the host galaxy, and this typically results in lower mass galaxies having lower metallicities (particularly at fixed age). These mass dependent age-metallicity trends have been seen in the Milky Way’s globular cluster system, and those of its satellite galaxies (Forbes & Bridges 2010; Leaman et al. 2013a; Massari et al. 2019).

In Boecker et al. (2020b) the authors leveraged these mass dependent chemical evolution trends to identify which regions of the age-metallicity parameter space were likely associated with accreted satellite galaxies of different masses. In that work, the mass fractions in age-metallicity space returned by pPXF’s fit to an integrated spectra were divided into contributions to the light from galaxies of different masses using a simple mass-dependent chemical evolution model. These flexible chemical evolution tracks provided dividing lines in age-metallicity space between galaxies of different masses.

By comparing to mock spectra of EAGLE galaxies where the accretion history was known, Boecker et al. (2020b) showed that this approach could largely identify how much mass from low mass satellites the host galaxy had accreted. There are two key limitations of the simple Boecker et al. (2020b) models which we improve upon here in order to more robustly compute ex-situ fractions in real galaxies.

(1) The mass-dependent chemical evolution templates in Boecker et al. (2020b) assumed a constant star formation history, simple leaky-box self enrichment, and self-similar internal spreads in metals at fixed age.

(2) The association of mass fractions returned by pPXF in age-metallicity space will be non-uniquely attributed to in-situ or ex-situ components of a galaxy when the mass-ratio of a merger is close to unity (and subsequently the chemical evolution pathways are very similar).

The models for estimating ex-situ fractions from full-spectral fitting outputs used

CHAPTER 4

here address both of these aspects, and are presented in full in a forthcoming paper (Leaman et al. in prep.). Below we present the relevant ingredients in brief.

4.4.2.1 Mass dependent SFH and chemical evolution

The end goal of these models is to estimate the probabilistic contribution of accreted (‘ex-situ’) material to every age-metallicity bin, for a host galaxy of a given mass. While low mass accretion events ($\mu \leq 1/10$) may separate cleanly in age-metallicity space from the in-situ component of the massive host, more massive mergers will significantly overlap with the ages and metallicities of the progenitor host galaxy. Here we work to quantify this degeneracy and compute the ex-situ contribution for these galaxies when they are dominated in the limiting case by the most massive accretion event. We compute models where the most massive merger has a stellar mass ratio with respect to the present day galaxy of $\mu_{max} = 1/10, 1/5$ or $1/3$ (e.g., the mass ratios at time of accretion were $\mu_0 = 1/9, 1/4, 1/2$).

The sole input required for computing the model is an estimate of the present day total stellar mass of the galaxy $M_{*,gal}$. The most massive accretion event is specified in terms of stellar mass as $M_{sat,max} = M_{*,gal}\mu_{max}$. The dark matter mass of the host and most massive accreted satellite are assigned stochastically with an empirical (Stellar-to-Halo Mass Relation) SHMR relation set forth in Leauthaud et al. (2012). These are used to specify the likely redshift of infall for the satellite given the DM mass ratio, with functional form and scatter taken from the statistics of subhalo infall in Boylan-Kolchin et al. (2011).

The SFH of the host and most massive satellite are stochastically evolved using empirical relations for galaxy SFRs at different redshifts from Genzel et al. (2015). This study characterises the typical specific star formation rate (sSFR) for galaxies of a given mass and redshift. We use this empirical relation recursively starting from redshift zero with the present day mass of the host used to specify the SFR.

CHAPTER 4

We proceed back in time in steps of 1 Myr, with the assumption of a constant SFR within those intervals, and subtract off the amount of mass formed in that timestep (e.g., $M_{i-1} = M_i - (t_i - t_{i-1})SFR|_{(t_i)}$). A given SFH constructed in this way is obviously approximate, but reproduces the mass dependent evolutionary pathways of galaxies through the star forming main sequence. Each SFH is given correlated noise with a power law slope of $\beta = 2$ to mimic the bursty star formation histories seen in simulated galaxies (Iyer et al. 2020). The stochastic assignment of SFHs using both of these aspects typically results in SFRs that vary by $\sim 50\%$ at any given redshift for a single galaxy’s model.

The nominal mass dependent SFHs of the host and most massive satellite are further augmented by a variable quenching time, after which the SF is terminated. In the case of the host, for any given model iteration this quenching time is drawn uniformly between $t_{young} \leq t_{quench} \leq \min\{t_{young} + 3.5Gyr, t_{Hubble}\}$, where t_{young} is the age of the youngest stellar population detected in the full spectral fit of the observed spectrum. For the satellite galaxy, the quenching time is specified by the time of infall to the host virial radius, plus the orbital decay time as described previously.

The chemical enrichment in any timestep corresponds to a leaky or accreting box prescription with equal probability. The effective yield is given a mass dependent parameterisation as in Boecker et al. (2020b), with the parameters of the mass scalings chosen stochastically in each model from a range that ensures the final galaxies reproduce the global mass-metallicity relation, and its scatter, observed in SDSS and the Local Volume (Gallazzi et al. 2005; Kirby et al. 2013). The gas fraction time evolution, which drives any analytic chemical evolution model, is here coupled to the empirical SFHs by re-expressing this quantity in terms of a sSFR ($t_{gas} = (1 + (t_{dep}sSFR)^{-1})^{-1}$, where we adopt the redshift scaling of depletion time from Tacconi et al. (2013). This allows us to self-consistently use the same relations

CHAPTER 4

to drive the star formation histories and chemical evolution.

4.4.2.2 Model mass fractions and uncertainties

For a single merger history (characterised by the satellite mass ratio and time of accretion) we run 200 iterations of the SFH/chemical model for the host and merging satellite. Due to the stochastic sampling of those model ingredients, the resulting evolutionary tracks in age-metallicity-SFR space span a probable distribution of pathways that a galaxy of that mass might take through this parameter space. These age-metallicity tracks are weighted by the SFR, and the composite density of mass-weights in age-metallicity space are smoothed and binned to the SSP model grid used by pPXF in a metallicity range of -2.27 to $+0.4$ [M/H] in 12 non-linear steps, and an age range of 0.1 to 14.0 Gyr in 46 non-linear steps.

As this is done for the host and the most massive satellite galaxy which merges, for a given cell in age-metallicity space we can ask what is the plausible contribution from overlapping ex-situ/in-situ material. This grid of ex-situ fractions can be multiplied by the mass-fractions returned by pPXF from a full-spectrum fit to an observed galaxy spectrum, to produce an estimate of the contribution of ex-situ material to that galaxy's spectrum. To quantify the uncertainty in these ex-situ fraction estimates, we run 150 merger histories (stochastically producing different quenching and accretion times) for a model corresponding to a given mass-ratio merger (an example of these stochastic histories is shown in Figure 4.2). The variance of these 200x150 models serves as one estimate of the systematic uncertainty in this exercise. The primary uncertainties in the chemical and star formation histories are encompassed within the variations of a single merger history. This is shown for one example in Figure 4.1.

Final ex-situ fraction and uncertainty can be calculated from a given population

CHAPTER 4

as:

$$f_{ex,tot\pm 1\sigma} = \frac{\sum_{t,[M/H]} G_{re} \times (0 \leq avg(f_{ex}) \pm \sqrt{var(f_{ex})} \leq 1)}{\sum_{t,[M/H]} G_{re}} \quad (4.2)$$

Where G_{re} is the product age-metallicity stellar population map derived from full spectral fitting at a given radial annuli.

We stress that while highly approximate, these analytic models are stochastically exploring plausible evolutionary pathways using empirical and physically motivated mass-dependent galaxy scaling relations and theoretical prescriptions. That these models reproduce additional redshift zero scaling relations they were not informed by (scatter and mean of the mass-metallicity relation, SFH-mass relations), is one simple check that they are reasonable ways to characterise the age-metallicity distributions of galaxies. The forthcoming paper (Leaman et al. in prep) will present a detailed description of the model ingredients and calibration checks.

4.5 Results

The application of model ex-situ fraction grids from tailored simulations allows for the extraction of robust and physical ex-situ fractions for every bin of spectra considered. This method is applied to both elliptical and Voronoi binned galaxy maps, granting insights into galactocentric and more general spatial trends respectively.

A comparison of ex-situ fraction with galactocentric radius for all the sample galaxies is presented in Figure 4.4. This shows the various ex-situ profiles associated with galaxies, within limited radii, in units of effective radius. This is presented for three different merger mass ratios (μ) where μ is the ratio of the present day galaxy mass prior to merger, against the mass of the merging galaxy. For each bin, the mean residual value of the ppxf spectrum fit was calculated. Bins with mean residual value of greater than 0.1 (10% difference from input spectrum) were discarded. In the majority of sample galaxies, no bins were discarded by this condition.

CHAPTER 4

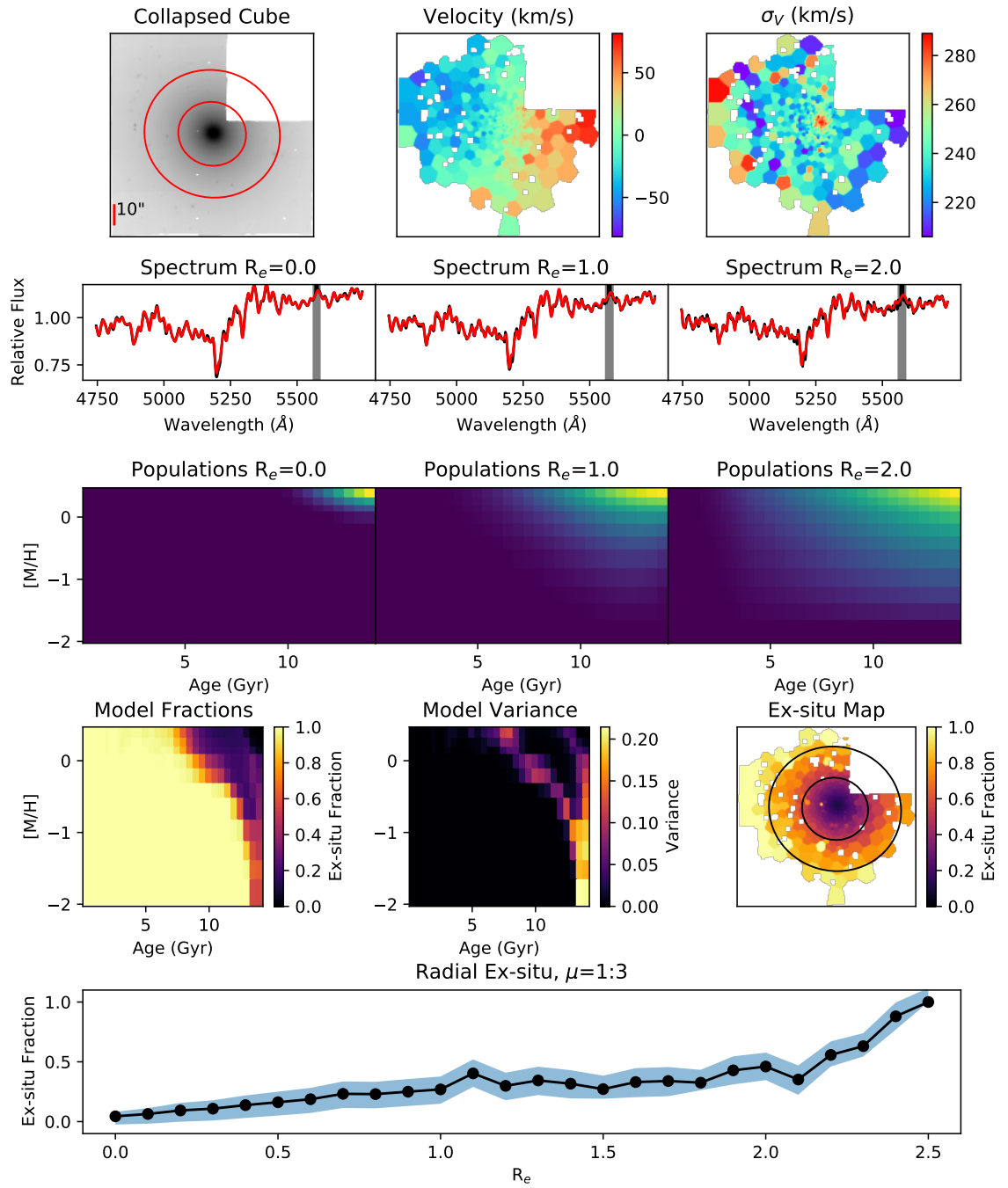


Figure 4.1: Figure caption on following page.

CHAPTER 4

Figure 4.1: An example process for NGC 1407. Here we show the analysis and reduction from the collapsed cube, to the final ex-situ estimation. The leftmost panel in the top row shows a full view of the collapsed cube. Brightness is inverted, and rings of $1r_e$ and $2r_e$ are shown projected onto the cube. The middle panel of the top row shows the stellar velocity as derived by pPXF and applied to a Voronoi binned map of NGC 1407. The rightmost panel in the top row shows the velocity dispersion for the same map. Other kinematic and chemical properties for NGC 1407 can be found in Figure C.11. The spectra at 3 different radii are shown in the second row. The r_e value provided is the lower bound of an annulus with an outer boundary of radius $(n+0.1)r_e$. All spectra within these bounds are summed and shown in the panels, though only a limited region is shown. The black line represents the original summed spectrum, and the red line shows the final reproduced spectrum derived from full-spectral fitting. A grey shaded region represents a mask used to obscure a strong skyline ($[\text{OI}]5577\text{\AA}$). In the third row we show the weighted stellar models in the age-metallicity plane of NGC 1407 for 3 different annuli in units of effective radius, as derived from the full spectral fitting fit. An increasing fraction of younger and lower metallicity stars are apparent with increasing radius. The left panel of the 4th row shows the ex-situ distribution obtained from the model realisation of many $\mu=1:3$ mergers at all radii, whilst the middle panel shows the resultant variance for all age-metallicity bins in the map. Variance is applied to the total age-metallicity map as per equation 4.2. The final Voronoi map of ex-situ stars is shown in the right panel of row 4, again with rings showing $1r_e$ and $2r_e$. This is shown for all galaxies in Figure 4.6. Finally in the 5th row we show the profile of ex-situ fraction in units of r_e .

CHAPTER 4

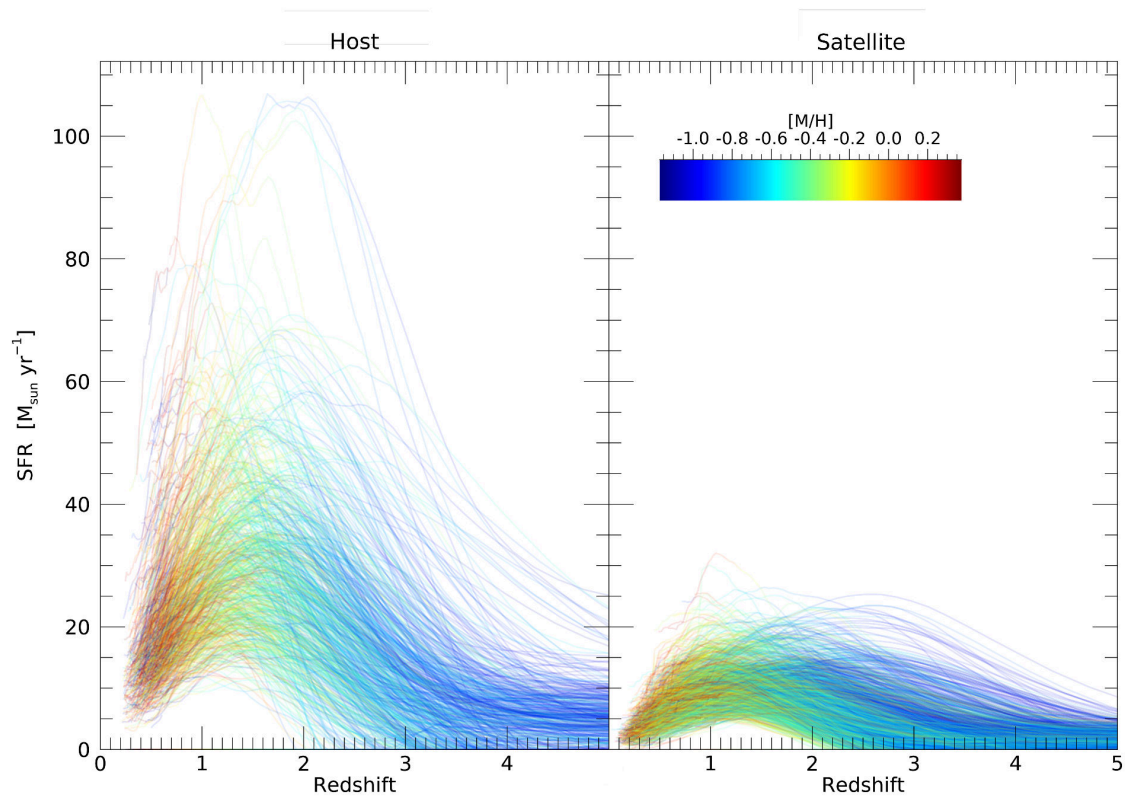


Figure 4.2: Example empirical SFHs for one merger realisation of NGC 1380. Each thread shows the path in SFR- z space of a single model, with many hundreds of stochastically varied models producing a variance map of expected $z=0$ population ages and metallicities. Colour shows the mean metallicity increase within the galaxy over time.

CHAPTER 4

For all galaxies within the sample, and for all mass merger ratios considered, the ex-situ fraction increases with galactocentric radius. This varies from the barely discernible increase of NGC 1404 with a maximum of 4.5% ex-situ fraction at $2.5r_e$; to IC 1459 which displays an increase from 10-18% to 95-98% ex-situ fraction within $1.5r_e$ depending on the assumed merger mass ratio. All galaxies contain fewer or no ex-situ stars in the centres ($0R_e < r < 0.25R_e$), with values starting at no more than 18%, with a mean value of 3.5% across all sample galaxies and merger mass ratios.

The differences in ex-situ fraction that increase with radius can be particularly highlighted by taking slices at specific fractions of effective radii. Figure 4.5 shows the ex-situ fraction for each sample galaxy at 3 different radii. Galaxies are shown as the area enclosing a 1σ error of mass and size. The area is coloured according to the ex-situ fraction. Figure 4.5 clearly shows a trend within the sample of a greater increase in ex-situ fraction with galactocentric radius for galaxies that are both greater in mass, and physical extent at fixed mass.

Metallicity can also be seen to change radially across each galaxy as shown in Figure 4.3. This has the potential to be interpreted in two different ways. Firstly, the gradient in metallicity could be directly linked to the gradient in populations, with ex-situ populations skewing the overall metallicity gradient. Alternatively, there could be an intrinsic metallicity gradient which would cause issues for our analysis. This is discussed thoroughly in Section C.2.

Estimated Voronoi ex-situ bin fractions are shown in Figure 4.6. This demonstrates the ability for the method to extract ex-situ populations for bins of $S/N > 100$. For all galaxies, as shown previously, a gradient can be seen in ex-situ fraction in which the fraction of accreted stars increases with radius. For some galaxies, this is closely tied with radius, for example NGC 1407. This galaxy shows a steady increase in ex-situ fraction at greater radial extents. Other galaxies show both radial

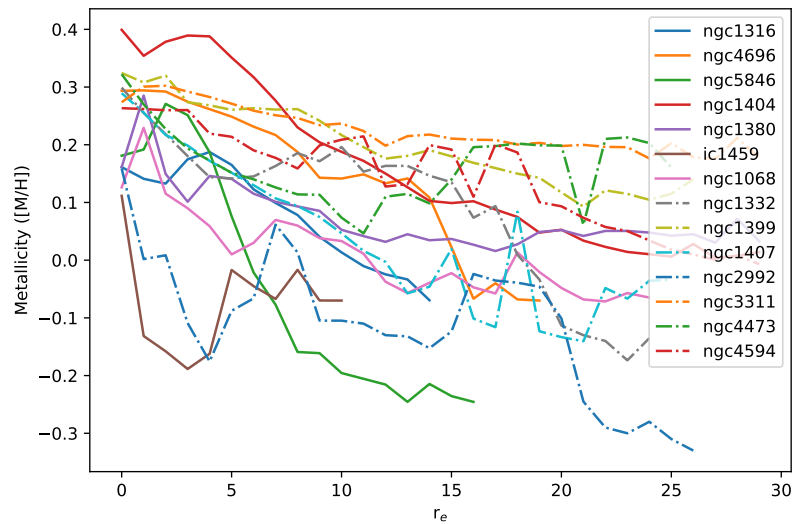


Figure 4.3: Metallicity as a function of galactocentric radius for 13 sample galaxies. A maximum radial extent of 3 effective radii is considered, and a minimum of 1.5 effective radii was a requirement of initial sample definition. Galaxies are split between two line-styles, with division purely for ease of legibility.

CHAPTER 4

and localised increases in ex-situ fraction. For example, NGC 2992 increases slowly in general ex-situ fraction from the centre, however a feature in the lower-left corner shows an increase in ex-situ fraction. This can be linked to a region of younger than average stellar material that is clearly seen in the lower panels of Figure C.12 of the Appendix.

For galaxies with disks such as NGC 1332, NGC 1380, and NGC 2992, inner regions show stellar material formed primarily of in-situ material, relative to their much more ex-situ dominated outskirts. We stress that low ex-situ fractions do not mean that significant mergers have not occurred. Systems with ex-situ fractions of 20% could have gained this material in a 1/4 mass ratio merger which can provide significant modifications to the galaxy structure and kinematics.

Sample size prevents any strong conclusions being drawn regarding general galaxy properties, however Figures 4.4 and 4.5 indicate success in the recovery of ex-situ fraction estimation using population age-metallicity distributions. Below we discuss some aspects of the results with respect to host galaxy properties in this preliminary sample.

4.6 Discussion

When examining the sample as a whole, and considering the properties of the galaxies involved, a number of striking features are revealed. For the 50% least massive and least extended galaxies (those with a half-mass radius $< 3\text{kpc}$), ex-situ fraction remains low throughout, with a mean ex-situ fraction at 2 effective radii of 22% for all merger mass ratios. For the most massive and most extended galaxies (those with a effective radius $> 3\text{kpc}$), ex-situ fractions increase more drastically, with a mean ex-situ fraction at 2 effective radii of more than 58% for the same merger mass ratios.

When viewing galaxies at fixed stellar mass there is a general trend that extended

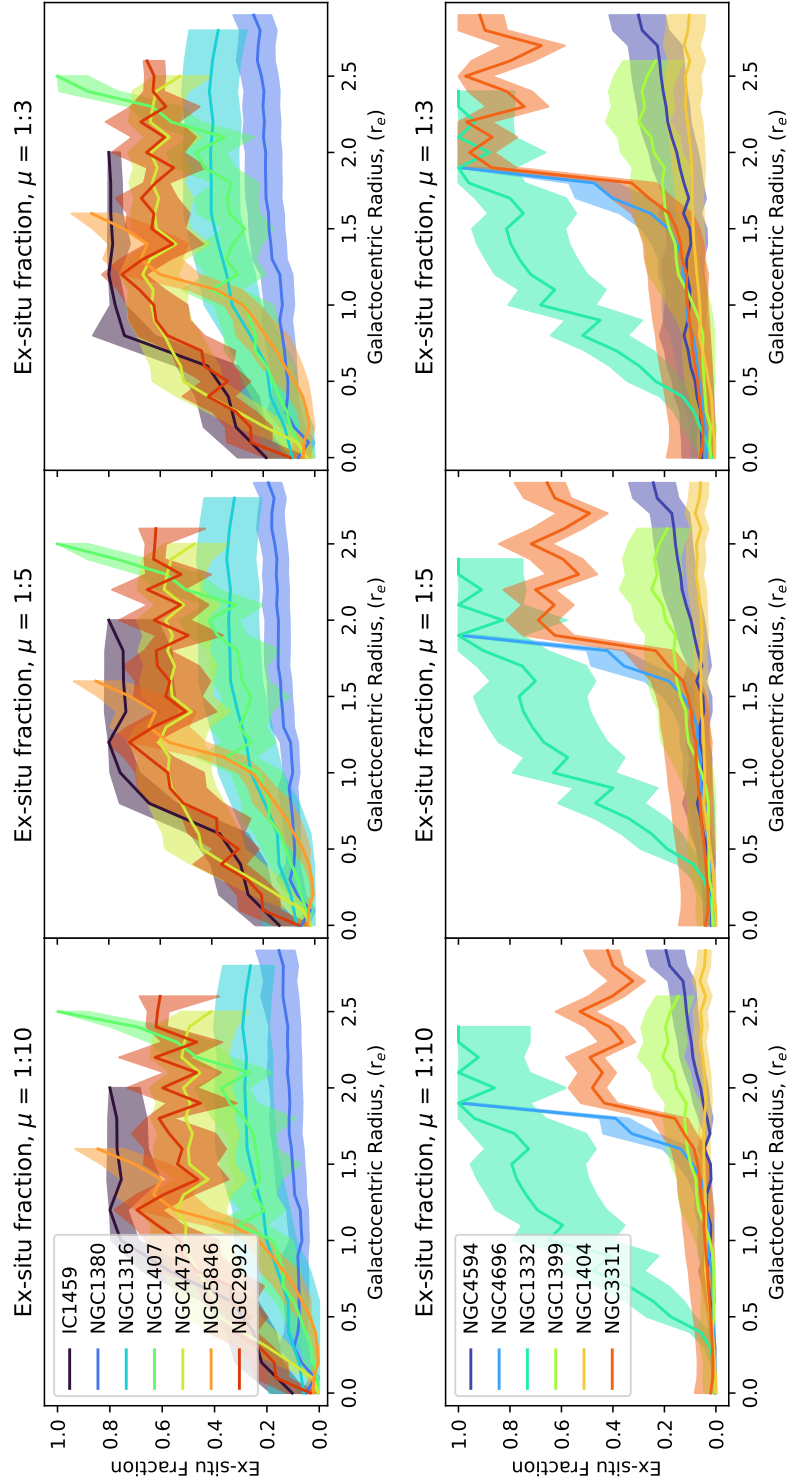


Figure 4.4: Ex-situ fraction as a function of galactocentric radius for 13 sample galaxies, considering 3 different merger mass ratios (μ) where μ is the ratio of the present day galaxy mass prior to merger, against the mass of the merging galaxy. A maximum radial extent of 3 effective radii is considered, and a minimum of 1.5 effective radii was a requirement of initial sample definition. Galaxies are split between two sets of figures (upper row and lower row). Division is done purely for ease of legibility and no meaning is ascribed to the split.

CHAPTER 4

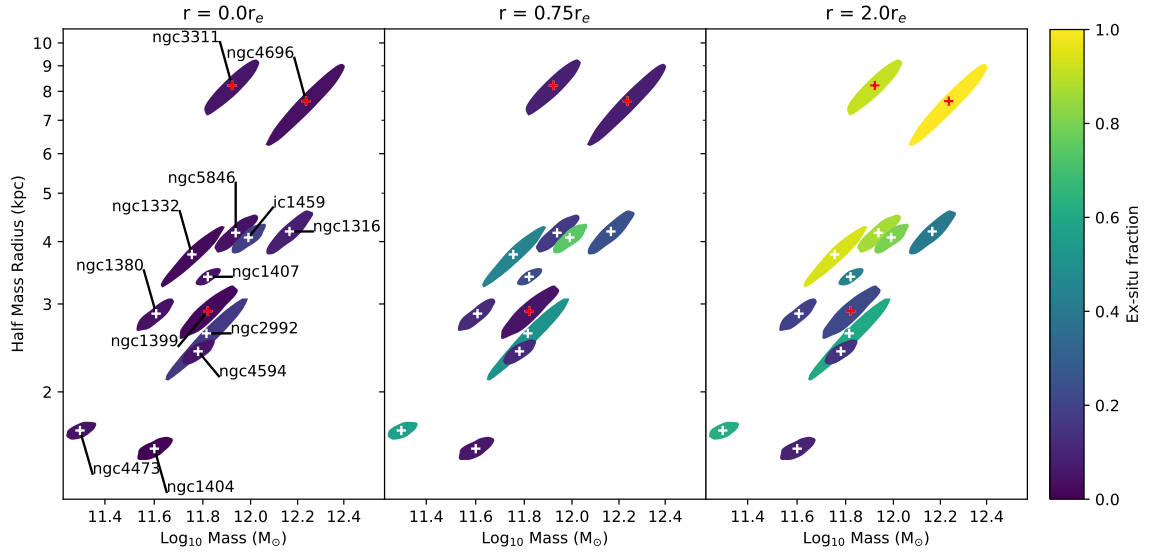


Figure 4.5: Mass size plane of sample galaxies. Colour shows the ex-situ fraction at various radial intervals for a merger mass ratio of 1:3. Three radial bins are shown, representing the ex-situ fraction found in the elliptical annulus at a given galactocentric radius in units of effective radius. Ex-situ fraction is taken as the mean value within $\pm 0.1r_e$ of the specified value. It does not consider ex-situ fraction enclosed within the annulus below the lower bound. Filled ellipses represent the 1σ confidence interval for the uncertainty of the galaxy mass and size. Uncertainty in distance affects radius simultaneous to luminosity elements of mass-to-light calculations used for total mass estimates, hence uncertainty is simultaneous in the xy plane. Central Dominant galaxies are marked with a red cross. For two galaxies with coverage just short of $2r_e$, the final ex-situ measurement taken for the third panel is the most extended point possible within cube coverage. For NGC 4696 this is at $1.8r_e$, and for NGC 5846 this is at $1.7r_e$.

CHAPTER 4

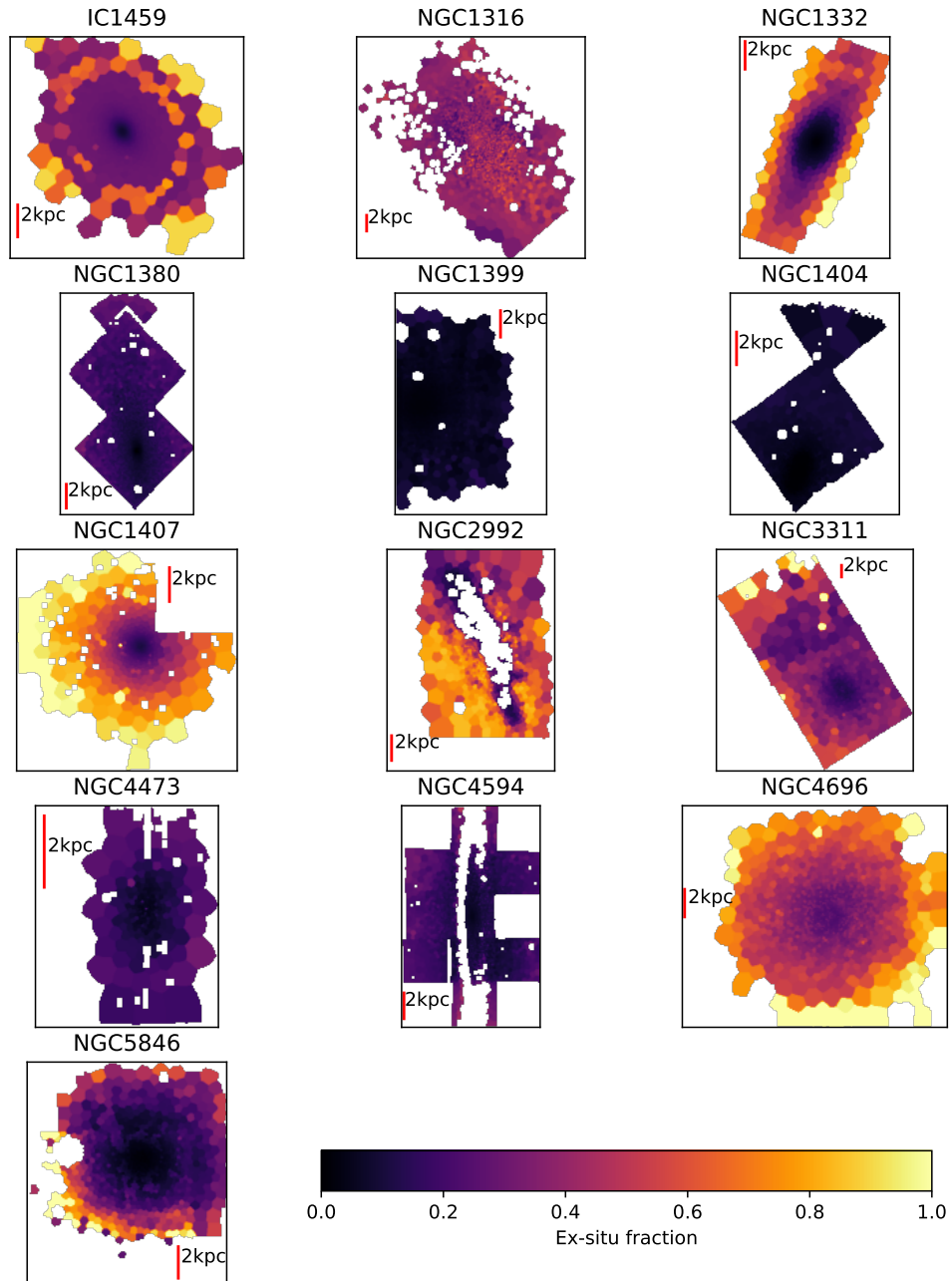


Figure 4.6: Panels show each galaxy in the sample, with colour showing the ex-situ fraction derived using our method. Galaxies are Voronoi binned to a signal-to-noise ratio of at least 100 per bin. This Figure shows the calculated ex-situ fraction per bin with an assumed merger mass ratio of 1:3.

CHAPTER 4

objects experience a greater increase in ex-situ fraction with radius. This is in line with analytic expectations and is seen in the EAGLE simulations (Davison et al. 2020). We directly compare to analysis of the EAGLE simulations in Figure 4.7, using data from Davison et al. (2020). Here we see side by side comparisons of the ex-situ fractions of stars found in galaxies at $2r_e$ with respect to the mass-size plane. We see very similar ranges and differential trends in ex-situ fraction with mass and size between the MUSE analysis of this chapter, and galaxies from the Ref-L0100N1504 EAGLE simulation (Schaye et al. 2015; Crain et al. 2015). The Ref-L0100N1504 simulation is a periodic volume, 100cMpc (co-moving kiloparsecs) on a side, realised with 1504^3 dark matter particles and an initially equal number of gas particles. Stellar particles are traced throughout the simulation providing in- or ex-situ tags for each star present in a given galaxy at $z=0$. The limits of mass and size analysed in this chapter are indicated on the EAGLE panel as a dashed box. It should be noted that Ref-L0100N1504 EAGLE galaxies tend to be slightly more extended at fixed mass than real galaxies. This has a number of potential explanations. One is the result of over-efficient feedback within the EAGLE simulations (see e.g. Crain et al. 2015) which moves galaxies of fixed M_* into haloes of higher M_{200} potentially extending the galaxies. A second explanation is described in Ludlow et al. (2019), where 2-body scattering can artificially inflate galaxies. Regardless of any mass-size offsets, both the theoretical and observational datasets show a clear preference for higher ex-situ fractions in larger and more massive objects. Galaxy density appears to be correlative factor with ex-situ fraction and the gradient of accreted stars with galactocentric radius.

In comparison to Oyarzún et al. (2019) who use stellar metallicity profiles to estimate the ex-situ fractions of MaNGA galaxies, results are reasonably well matched. The results in Oyarzún et al. (2019) similarly show an increase in ex-situ fraction with both mass and galactocentric radius, however the scatter in these values at

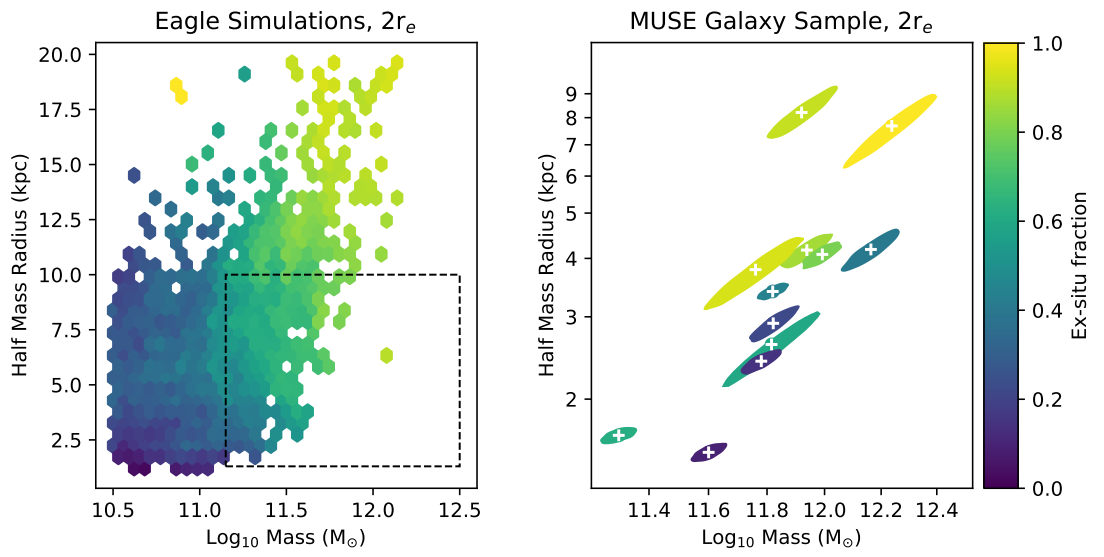


Figure 4.7: A side-by-side comparison of the ex-situ fraction in galaxies from the Ref-L0100N1504 EAGLE simulation, and MUSE galaxies from this chapter. The left panel shows 3643 binned EAGLE galaxies, with each bin showing the mean ex-situ fraction of galaxies between $1.9 < r_e < 2.1$. Only galaxies with a minimum of 500 stellar particles were considered. The right panel shows the ex-situ fraction of MUSE galaxies between $1.9 < r_e < 2.1$. The area covered by rightmost panel is represented as a dotted box in the left panel for comparison. EAGLE galaxies tend to be slightly more extended at fixed mass than real galaxies.

CHAPTER 4

$> 2r_e$ essentially cover the entire ex-situ axis. Similar to population analyses in Edwards et al. (2020) we find population gradients in essentially all the galaxies studied, occurring strongly with both age and metallicity. These gradients are indicative of low-metallicity young stars accreting to the outskirts of the galaxies in this sample. Similarly to Rodriguez-Gomez et al. (2016) we find that in the case of major mergers (assumed in Rodriguez-Gomez et al. (2016) to be $\mu > 1/4$) the contribution to the ex-situ population is significant. In all cases where we assume $\mu > 1/3$ the ex-situ fraction recovered from the sample galaxies was greatest compared to other assumed merger masses.

Final mass-size uncertainties were calculated using a Monte-Carlo approach. Distance and projected size uncertainties impacted on the area with which to calculate mass using mass to light ratios. As such, uncertainties can be seen as a misshapen ellipse enclosing the 1σ mass-size probability, either diagonal in the mass-size plane (distance uncertainty dominated), or more horizontal in the mass axis (mass-to-light ratio uncertainty dominated). Galaxies with more precise distance estimates (such as NGC 1404) exhibit relatively low mass-size uncertainty. Values of mass and size and associated uncertainties can be found in Table 4.1. When considering all mass ratios, the average uncertainty in ex-situ fraction at any radius was $\pm 8.4\%$.

Three of the galaxies included in the sample are considered to be central dominant galaxies (cD) according to literature classifications. All other galaxies in the sample are variously field or satellite galaxies. The three galaxies with cD classification are NGC 1399 (Fornax), NGC 4696 (Centaurus), and NGC 3311 (Hydra) and are marked with a red cross in Figure 4.5. It is perhaps surprising to find that NGC 1399 seems to contain little ex-situ stellar material in the region imaged. This may have to do with the ill-defined and estimated radius for cD galaxies. For such multi-component galaxies, r_e is a simplification, and as such classifying parameters in units of r_e can be misleading. Light on the outskirts of cD galaxies extends

CHAPTER 4

well into the intracluster medium, and the point at which galaxy light transitions to intracluster light is poorly defined if measurable (Seigar et al. 2007). As such, ex-situ estimates for these cD galaxies represent a lower limit of the possible values. Most likely (especially in the case of NGC 1399) the true radius is much larger than normal methods have provided here, and we only probe the very inner regions of NGC 1399. Uncertainty in the radius is clear when we consider just a few of the values provided in literature (such as 1.53' (Jarrett et al. 2003), 4.0' (Lauberts 1982), and 6.0' Vorontsov-Vel'Yaminov & Arkhipova (1974)). Further limitations arise in the age of NGC 1399 and the age of its mergers. Due to poor age resolution in current spectral models, mass accreted onto NGC 1399 in early times could potentially be missed, and therefore much ex-situ mass is misidentified as in-situ mass. Estimates from Spavone et al. (2017) put the total accreted fraction (within $\approx 8r_e$) at a more reasonable 84.4%. On the other hand it is entirely possible that this is an accurate view of NGC 1399. This is a statistically poor sample and we expect a scatter in the true distributions of galaxy ex-situ fraction with galaxy type, mass, and radius. Larger statistically significant samples are necessary to judge this with any certainty.

In the cases of NGC 4696 and NGC 3311 the radial profile of ex-situ fraction increases dramatically over $0.2-0.6r_e$. Both galaxies show similar extents and are the physically largest galaxies by area in the sample. The rate of increase in ex-situ fraction was examined against various galaxy properties such as morphological type and inclination with no convincing correlation found. One possible reason for the increase is the result of dust in the centres of these galaxies. Both the aforementioned galaxies display irregular dusty features in the centre. Potentially this dust skews the age estimate of the full-spectral fitting to older populations as a result of reddening, causing a lower fraction of the stars to be classified as ex-situ. Once the elliptical binning moves outside of this dusty range, the ex-situ estimate

CHAPTER 4

returns to its unaffected state, and gives the impression of a rapid rise in ex-situ fractions. This appears visible in the very few galaxies present with diffuse dusty features. Further tests are needed to help correct for the impact of dust on stellar population properties.

Stellar population models were obtained from the MILES spectral library (Vazdekis et al. 2012). The choice of stellar population models can affect the derived weighted grid, slightly shifting the values of age and metallicity according to SSP differences. Much literature has discussed the differences encountered in using alternative SSP models (Conroy et al. 2009a,b; Conroy & Gunn 2010; Fernandes & Delgado 2010; Delgado & Fernandes 2010; Baldwin et al. 2018; Martins et al. 2019; Knowles et al. 2019). Despite the differences in available SSP models, testing with different models would be unlikely to change results in a differential sense with any significance (see also Boecker et al. 2020a). Though alternative SSP models would possibly give shifted absolute age and metallicity values, in relative terms the populations should remain distinct and separable.

A further parameter that we did not vary was the assumed IMF, which is unlikely to be exactly Kroupa-like for Early-Type galaxies (Vaughan et al. 2018; Smith 2020b). The implications of a variable IMF were particularly explored in Clauwens et al. (2016). At fixed age an SSP with bottom heavy IMF will have more low mass stars and therefore the age recovered with a Milky Way-like IMF would be older. The wavelength range used for the MUSE analysis in this chapter avoids some of the most IMF sensitive regions of the spectrum such as the NaI doublet (Schiavon et al. 1997) and CaI (Smith et al. 2012), and therefore the IMF is not likely to be a hugely impactful factor on the results.

While our approach can only provide approximate separation of the in- and ex-situ components, the benefits of our data and models are two-fold over past approaches. First, the use of spectroscopy allows for recovery of ex-situ components

CHAPTER 4

within the centres (or projected at the centre) of the galaxies, where accretion is still known to deposit ex-situ material. Secondly, the physically and empirically motivated models used to decompose the recovered age-metallicity distribution account statistically for the expected overlap in structure and stellar populations in massive accretion events, which are the most transformative to the host galaxies.

We aim to extend this work further over larger and more representative mass ranges. With complete IFU coverage of galaxies out to 2 effective radii we can endeavour to examine ex-situ fractions of galaxies at every mass range. Better understanding of the influence of environment, as well as cross-validation of our estimates of ex-situ fractions with those of complementary approaches (such as from GC population analysis and photometric imaging of the faintest outer halos Rejkuba et al. e.g. 2014) will allow for a useful census of accreted material in local galaxies. Furthermore, this could allow for testing of galaxies in different environments, with work in EAGLE (Chapter 2) showing variation in ex-situ fractions of galaxies at fixed max, with environment.

Table 4.1: Sample galaxy values used to estimate mass and size. Mass and size values are the mean value from Monte-Carlo simulation considering all available sources of error. Magnitudes and galaxy type were obtained from the 2Mass Large Galaxy Atlas (Skrutskie et al. 2006), whilst distance was taken from various sources:

Galaxy	Type	Ks-band (mag)	\pm Ks	J-K	\pm J-K	Distance (Mpc)	\pm Distance	[Mass] (M_{\odot})	r_e (kpc)
IC1459	E3,AGN	6.928	0.016	0.904	0.03	28.7	1.80	11.99	4.08
NGC1316	SA(rs)b;Sy1;2	5.694	0.016	0.877	0.03	20.8	2.00	12.16	4.18
NGC1332	SAb	7.155	0.016	0.949	0.03	22.9	3.40	11.76	3.79
NGC1380	S(s)0	6.971	0.016	0.911	0.03	18.6	1.40	11.61	2.86
NGC1399	SA0	6.431	0.016	0.924	0.03	18.2	1.75	11.82	2.90
NGC1404	cD;E1;pec	6.941	0.016	0.948	0.03	17.1	0.76	11.60	1.54
NGC1407	E1	6.81	0.016	0.952	0.03	20.6	0.97	11.82	3.40
NGC2992	E0	8.714	0.016	1.123	0.03	38.0	7.70	11.82	2.63
NGC3311	Sa,pec;Sy1	8.154	0.016	0.918	0.029	45.7	5.35	11.92	8.22
NGC4473	SA(s)a;Sy1.9	7.287	0.016	0.906	0.03	15.2	0.57	11.30	1.67
NGC4594	S0-	5.04	0.016	0.933	0.03	8.99	0.52	11.78	2.41
NGC4696	cD;E+2	7.192	0.016	0.972	0.03	38.9	6.59	12.23	7.64
NGC5846	E7/S0	7.044	0.016	0.953	0.03	26.3	2.10	11.94	4.17

4.7 Conclusion

Thirteen MUSE targeted galaxies were analysed to examine the ex-situ populations within galaxies across a small mass-limited area of the mass-size plane. Galaxies were chosen for their large coverage and spatial resolution, allowing for a well resolved examination of ex-situ populations with galactocentric radius. By combining analytic models with weighted populations extracted by full spectral fitting we were able to distinguish ex-situ stellar material that was incongruous to in-situ stellar matter. In all galaxies examined, ex-situ fraction increases with radius. This increase was shown to be particularly strong in more massive galaxies, and more extended galaxies. Whilst less extended and less massive galaxies experienced radial ex-situ fraction increases up to 5-40% at $2R_e$, the more extended and massive galaxies in the sample show radial increases up to 25-100%. The result that the magnitude of radial ex-situ fraction increase seems to correlate with both mass and physical galaxy extent agrees well with existing simulation predictions (see e.g. Davison et al. 2020).

These estimates for the lower-limit of galaxy ex-situ fractions agree with theoretical predictions that expect accreted material from the lowest mass (and hence lowest metallicity) merged galaxies to preferentially remain in the outskirts of galaxies. This reveals how coverage to a minimum of two effective radii is necessary for exploration of galaxy populations, in order to avoid considering only unmixed in-situ portions of massive galaxies.

By estimating and mapping ex-situ stars in a sample of galaxies, we demonstrate the power in tracing accreted populations with IFU spectroscopy. In conjunction with other methods to quantify accreted stars, we now endeavour to utilise the full power of spectroscopically derived full star formation histories. With estimates of the distributions in stellar age and metallicity, we can expect to better constrain and understand galaxy assembly history.

Chapter 5

Probing the Mass-Size Plane with SDSS

5.1 Chapter Abstract

The high number of galaxies available from the Sloan Digital Sky Survey (SDSS) represent an incredible statistical opportunity. This chapter leverages this to explore ex-situ fractions in galaxies with a far greater statistical certainty. Whilst most galaxies in the SDSS survey are at a low spatial resolution in comparison to those examined in Chapter 4, the sheer number of SDSS targets allows us to approach the questions of galaxy ex-situ fraction from another angle. Two samples are formed representing inner and outer stellar populations of the galaxies. In both samples the ex-situ fraction is found to increase with galaxy size, as well as with mass. There is also an increase found with radius, pointing to higher fractions of ex-situ stars in the outer regions of galaxies.

5.2 Chapter Introduction

When investigating general galaxy properties, it is always preferable to have high number statistics. The extraordinary range of galaxy types and uniqueness of each individual galaxy mean that without vast samples of galaxies, one can only infer properties on a case-by-case basis, rather than for galaxies as a whole. When investigating the ex-situ fraction of galaxies with respect to general galaxy properties such as mass or radius, we must use large statistical samples to uncover trends with certainty.

Though current instrumentation is groundbreaking and highly advanced, only the nearest galaxies are sufficiently well resolved to be studied radially with any confidence. This prevents large samples being built, and instead we can only create small samples of specifically targeted objects, and assume this to be a representative sub-sample of the full population. If the trend being studied is strong enough, and the galaxy-galaxy scatter is small, this can hold true, as there is little deviation from the trend even in more unusual target galaxies. However without a view of the larger sample, it is impossible to know if the sub-sample is a true representation of the larger sample. This is further complicated by the fact that many targeted galaxies found in existing archives are chosen specifically for their unusual properties, as they present an ‘interesting case’ for astronomers.

In this chapter we aim to show general trends of ex-situ fraction with galaxy properties such as mass, size and galactocentric radius. By doing this with low-resolution unresolved data we can build a picture of the greater trends present in the data. As such we can estimate if high resolution sub-samples of resolved targets are well sampled. We achieve this using the Sloan Digital Survey, a brightness limited survey covering almost 35% of the sky.

The Sloan Digital Sky Survey (SDSS) (York et al. 2000) is one of the largest digital surveys and archives available as a public release. Spectroscopic data are available

CHAPTER 5

on more than 3 million objects, with 500 million photometric objects available (as of DR16 Ahumada et al. 2020). Data are collected with a dedicated 2.5m optical telescope based at Apache Point, New Mexico, USA. 30 2048x2048 CCD chips image the sky via drift scanning, used instead of regular tracking as a means of eliminating large CCD readout overheads. Chips are covered with an optical filter with 6 filters distributed evenly across the chips (Gunn et al. 1998; York et al. 2000).

SDSS uses fibre-fed spectrographs to spectroscopically image targets on the sky. Up to 1000 optical fibres are manually attached to aluminium plug plates that are drilled to match the observational schedule of a night. Whilst fibre angular diameter has changed throughout the life of SDSS, one output parameter is the fibre magnitude. By comparing this value to the model magnitude (which gives a best estimate of the total galaxy magnitude) one can estimate the total fibre coverage of the galaxy.

5.3 Methodology

5.3.1 Sample and Reduction

We obtained data from the SDSS database by first building a Structured Query Language (SQL) search to request appropriate targets. The query created an index containing any object that matched the following criteria:

$$0.0 < z < 0.05 \tag{5.1}$$

$$\text{Object class : } \textit{Galaxy} \tag{5.2}$$

$$r_{\sigma,DV} < 1.0 \tag{5.3}$$

Where z is redshift and $r_{\sigma,DV}$ is the error associated with the de Vaucouleurs radius estimate (in arcseconds).

CHAPTER 5

The resultant list contained 1,693,858 targets with dereddened colour values provided by SDSS with dereddening applied as described in Schlafly & Finkbeiner (2011). Distance to each target was estimated using the distance calculation as described in Saulder et al. (2015).

Following this, the dataset was divided by three parameters to ensure that largely only early type galaxies remained. The data were first cut on mass-colour as in Figure 5.1. It has been shown that $u-g$ is a useful means of separating galaxy type, especially in dividing star-forming and quiescent galaxies (Baldry et al. 2004). The subsequent cut-off line was placed just above the green valley, ensuring that the remainder of objects was greatly weighted towards early types.

Data were then cut on $H\alpha$ flux, used as a proxy for the presence of star formation. A threshold was set in which any target with $H\alpha$ flux $> 100(\times 10^{17} \text{ ergs cm}^{-2} \text{ s}^{-1})$ was discarded (Lee et al. 2009). Following these cuts, there remained 372,592 galaxies in the sample.

To investigate radial differences of properties within SDSS galaxies, two sub-samples were extracted. These two sub-samples represent spectra encompassing the inner regions of the galaxies, and spectra encompassing both the inner regions and more radially distant regions of the galaxies. By doing so, comparison of final sample properties provides a view into the radial changes of galaxies within the samples. The ratio of the r-band model magnitude of the galaxy against the magnitude of the fibre (hereafter the ‘light fraction’) was used as a proxy for the fractional area of the galaxy covered by the fibre. By separating data by the light fraction, we were able to choose only objects where the fibre captured a specific fraction of the galaxy light.

A sub-sample representing the inner regions of galaxies was selected with a target light fraction of 12.5% (hereafter referred to as r_8), and only the objects with minimum spread from this median were chosen. This contained 37,258 galaxies with

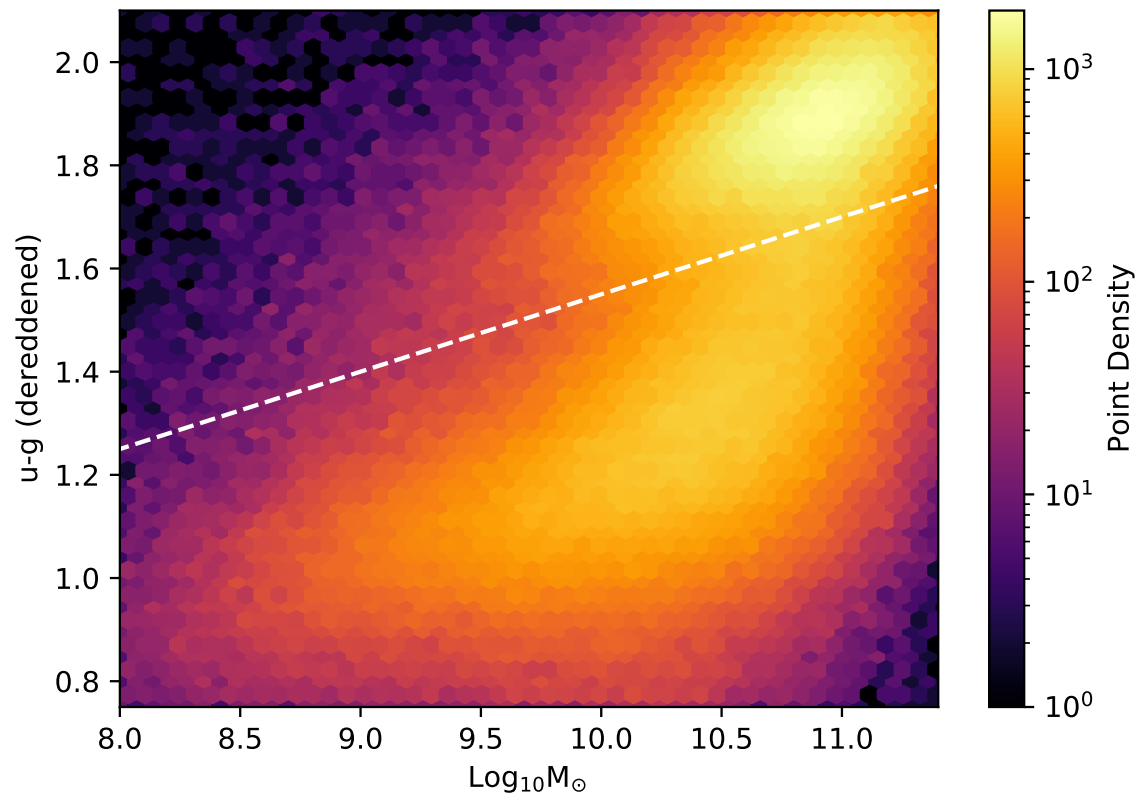


Figure 5.1: Mass-colour diagram of total initial sample, demonstrating the cut-off of objects below the green valley. Galaxies below the white dotted line are removed. Colour shows logarithmic point density of galaxies, with colour indicating the numbers of galaxies present within each hexbin.

CHAPTER 5

a final mean light fraction of 12.49% with a standard deviation of 3.36%. A second sample summing a larger fraction of the galaxy light had a target light fraction of 50.0% (hereafter referred to as r_2). The resultant r_2 sample of 22,557 targets had a median light fraction of 49.98% and a standard deviation of 3.59%. The distribution of light fractions, and the subsequent samples are shown in Figure 5.2.

To examine the parameters of galaxies with respect to their mass and size, it was instructive to view them on a mass size plane. For population analysis, reasonable Signal-to-Noise (S/N) is required. As such, galaxies were binned to a required S/N via a Voronoi binning method on a mass-size plane. This was achieved using a Voronoi binning code from Cappellari & Copin (2003). Whilst Voronoi binning is often used in spatial domains, it is equally transferable to other two-dimensional domains. Voronoi binning galaxies across the age-metallicity plane allows us to gather targets that have the most similar properties, and minimising deviation to extremes of either dimension.

Spectra from galaxies within each Voronoi bin were summed to provide a final spectrum representative of the bin. For this project, the S/N target value was set to 200 to facilitate highly robust full spectral fitting. For the r_8 sample the mean number of galaxies per bin was 238.8, with a maximum and minimum of 1765 and 6 objects per bin respectively. For the r_2 sample the mean number of objects was 152.5, with a maximum and minimum of 642 and 1. It should be noted that some bins covering large areas were discarded in the final plotting steps, so the final mean numbers per bin for the displayed values is slightly adjusted.

Galaxies within each bin were convolved with a Gaussian kernel prior to summation in order to facilitate the varying velocity dispersions present within a sample. Using the *astropy.convolution* python package, spectra were convolved with a kernel suitable to approximate a velocity dispersion of ~ 400 km/s (a value that was

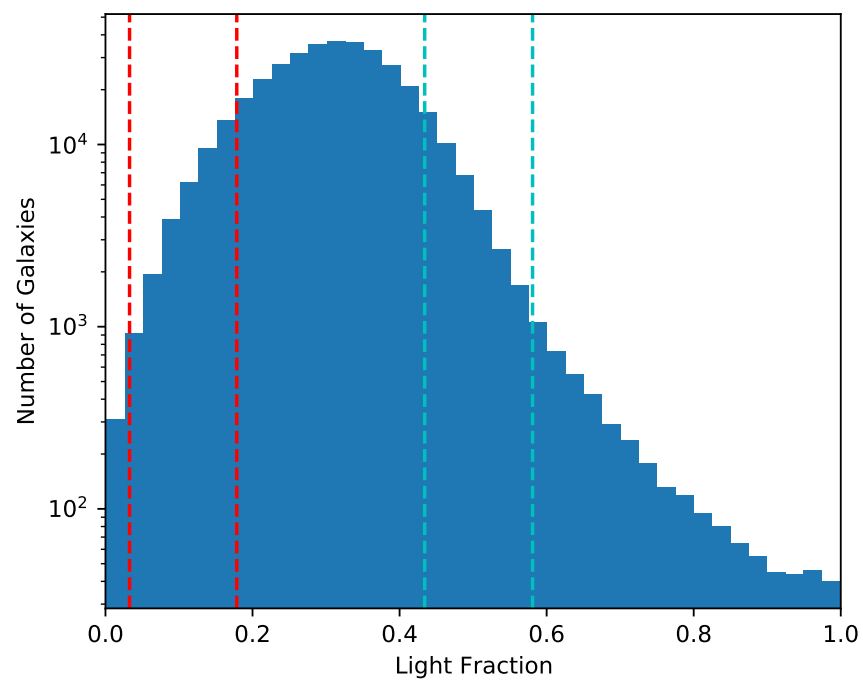


Figure 5.2: Light fraction distribution, and sample divisions for subsequent analysis with medians of 12.49% (shown between red dotted lines) and 49.98% (shown between cyan dotted lines).

above the maximum velocity dispersion naturally occurring in the sample). Theoretically this should give a recovered velocity dispersion value of 400km/s for the final summed galaxy. This is discussed further in Section 5.5.

5.3.2 Full-Spectral Fitting

To explore population properties, all final spectra were fit with model spectra through full spectral fitting. All spectra for a given bin were analysed with the full spectral fitting code pPXF (Cappellari & Emsellem 2004; Cappellari 2017) across the wavelength range 4759–6849 Å. Single stellar population (SSP) models were fit to the spectrum such that a highly accurate model fit could be produced.

In order to match with SSP binning, the spectra were rebinned from a logarithmic scale to a linear one by interpolation to the linear scale with flux conserved throughout. The SSP models were obtained from Vazdekis et al. (2012) consisting of theoretical models built from MILES and CaT spectra (Falcón-Barroso et al. 2011). A grid of the models, each at a specific age and metallicity was built, and spectra were matched to this grid. We used 636 models with M/H ranging from -2.27 to 0.4 and age ranging from 0.04 to 14.0 Gyr (Cassisi et al. 2005; Pietrinferni et al. 2006). SSP models were chosen to be revised Kroupa models with an IMF slope value of $\mu = 1.3$ (styled Mkb1.3 as per convention).

Regularisation is used in full spectral fitting to increase the physicality of the output (see Section 1.4 of the Introduction). In brief, full spectral fitting is an ill-conditioned problem, and as such there can be many degenerate solutions. Regularisation aims to find the smoothest possible of the degenerate solutions in order to present the most physical solution of other equally valid but highly nonphysical solutions which may have noisy or strongly localised weighted models. We use a simple iterative routine to find the maximum regularisation value that will provide a reduced χ^2 that is no different than 1- σ of the unregularised solution.

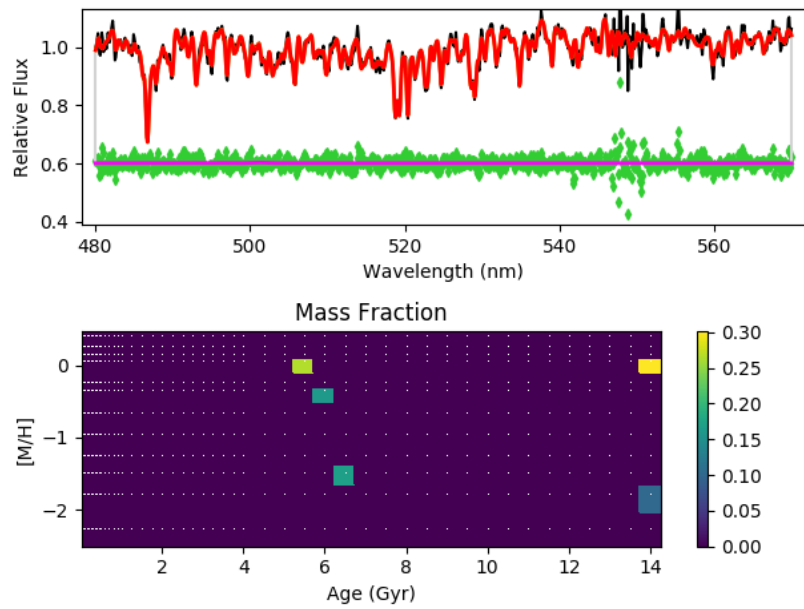


Figure 5.3: Fit of spectra with a regularisation value of 0. This is an example for an unbinned, unconvolved galaxy. The lower panel shows the simplest weighted grid of the models derived from the spectral fitting. Note that a standard SDSS fit as used in this Chapter would also include masking of sky lines and dust/gas modelling.

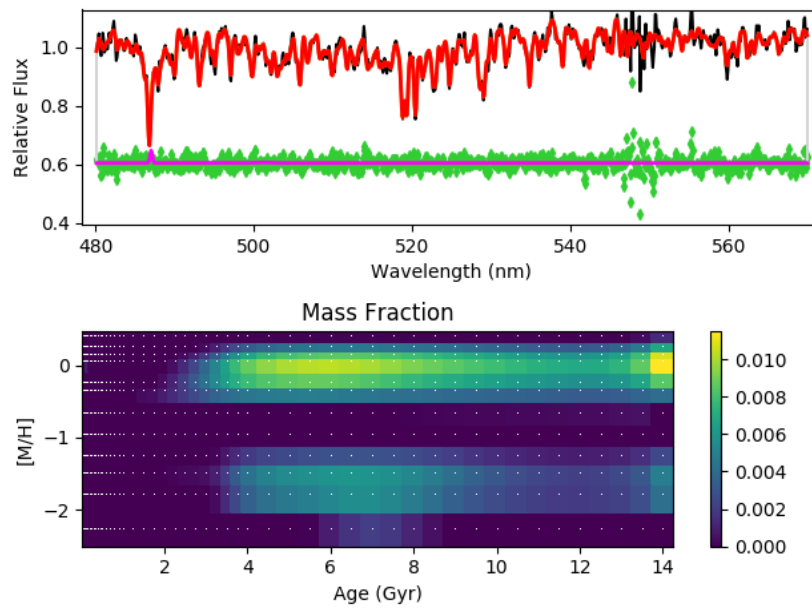


Figure 5.4: Fit of spectra with an optimal regularisation value. This is an example for an unbinned, unconvolved galaxy. The lower panel shows the smoothest solution of the models from the spectral fit. Note that a standard SDSS fit would also include masking of sky lines and dust/gas modelling.

5.3.3 Ex-situ Fraction Estimation

For each Voronoi bin of galaxies, a weighted grid of stellar models was obtained, representative of the present populations as indicated by the spectrum. This solution represents an amalgam of both the ex- and in-situ populations. At first glance, some of these ex-situ stars are instantly distinguishable as low metallicity areas appearing far later in time than the main population. These areas represent accreted populations which formed in a galaxy of lower mass, and thus according to the mass metallicity relation display lower metallicities and younger populations. Ex-situ populations in other solutions are harder to distinguish, especially amongst those where ages and metallicities of the ex-situ stars are close enough to the in-situ population properties that the two groups of stars show little or no division. These populations require more advanced treatment in order to accurately constrain ex-situ fractions.

In order to constrain which populations in a galaxy are accreted we must understand which stars differ from the expected age-metallicity relation (AMR). Modelling the chemical evolution of a galaxy according to its mass provides a baseline from which we can identify stars that are offset from this relation. This was attempted in Boecker et al. (2020b) in which a function to create flexible mass-dependent chemical enrichment templates was defined. This function can describe the chemical evolution of a galaxy dependent on its mass.

To build the function, results from Leaman et al. (2013b) were used. This work derived the AMR for Local Group dwarf galaxies, providing a template with which to fit general mass-dependent functions. As described in Boecker et al. (2020b), galaxy chemical evolution can be described as:

$$Z(t) = -p(M_*)\ln\mu(t) \quad (5.4)$$

CHAPTER 5

Where Z is the metallicity of a galaxy over time t , μ is the gas fraction within the galaxy, and $p(M_*)$ is the effective metal yield.

As per the empirical results from Leaman et al. (2013b), $p(M_*)$ can be described as:

$$\log_{10}p(M_*) = p_0 + \log_{10} \left(1 - \exp \left[- \left(\frac{M_*}{M_0} \right)^{\alpha_p} \right] \right) \quad (5.5)$$

Here, the effective yield of a galaxy is given against its stellar mass, considering constant values of p_0 which describes the asymptotic value of yield with high galaxy mass; M_0 which describes the turn-over mass; and α_p which describes the low mass slope. The variation of these parameters allow exploration of the AMR for all galaxy masses with a range of initial conditions.

To effectively describe the evolution of gas, the parameter $\mu(t)$ describes expected rates of consumption or removal of gas which are almost entirely dependent on galaxy mass and star formation rate. As such, $\mu(t)$ is described as:

$$\mu(t) = \frac{t - (13.5 - t_{\text{form}})}{t_{\text{form}}} \quad (5.6)$$

where,

$$t_{\text{form}} = \min[(14 - \log_{10}M_*)^{\alpha_t}, 13.5] \quad (5.7)$$

For a comprehensive overview of the construction of this formula, see Boecker et al. (2020b).

A powerful aspect of this technique is the ability to stochastically vary the parameters to consider uncertainty in conditions. Monte Carlo simulations can be run with variation of all fixed parameters within physical boundaries, giving a more flexible view of possible galaxy accretion history in relation to the age-metallicity plane.

5.4 Results

We run 50,000 Monte-Carlo (MC) simulations per bin to derive a mean and standard deviation in the ex-situ fraction estimation. Variables for each simulation are drawn linearly from the following parameters and ranges, $-0.2 < p_0 < 0.2$; $9.5 < \log_{10}M_0 < 11$; $0.4 < \alpha_p < 0.6$; $1.7 < \alpha_t < 2.5$. Mass is varied normally according to the standard deviation of mass estimates of all galaxies contained within a bin. An additional variance is added to the resultant function of AMR to account for the possible deviation of galaxy metallicity from purely theoretical. These ranges were defined in Boecker et al. (2020b) such that the simulated mass-metallicity relation derived from the median AMR is bounded by the observed mass-metallicity relation.

An example of this variation is shown in Figure 5.5 for the age metallicity fit for one bin of the mass size plane. Small variations in the AMR parameters can have large impacts on AMR at low ages and at high metallicity. As seen in Figure 5.6, a distribution can be drawn from the variation in AMR providing values of mean ex-situ fraction and standard deviation for each galaxy bin. Whilst discrete grid values mean that the distribution of ex-situ estimates is not entirely smooth, the mean value of ex-situ fraction and standard deviation can be well described.

By taking the mean value of ex-situ fraction derived from the MC models we can show the ex-situ fraction estimation for Voronoi binned SDSS samples. This provides a view of ex-situ fraction across the mass size plane for SDSS galaxies in a redshift range of $0.0 < z < 0.05$. This is presented in the top panels of Figure 5.7 where we show the ex-situ fraction for the Voronoi binned mass-size plane.

Both samples have a colour normalisation of 1, and as such it is immediately clear that there is an increase in ex-situ fraction when considering the r_2 sample. This is clearly shown when the difference between the two Voronoi maps is viewed. This is shown in the lower panel of Figure 5.8. In order to match the two Voronoi areas, the mass and radius range was first limited to regions in which the two samples had bins

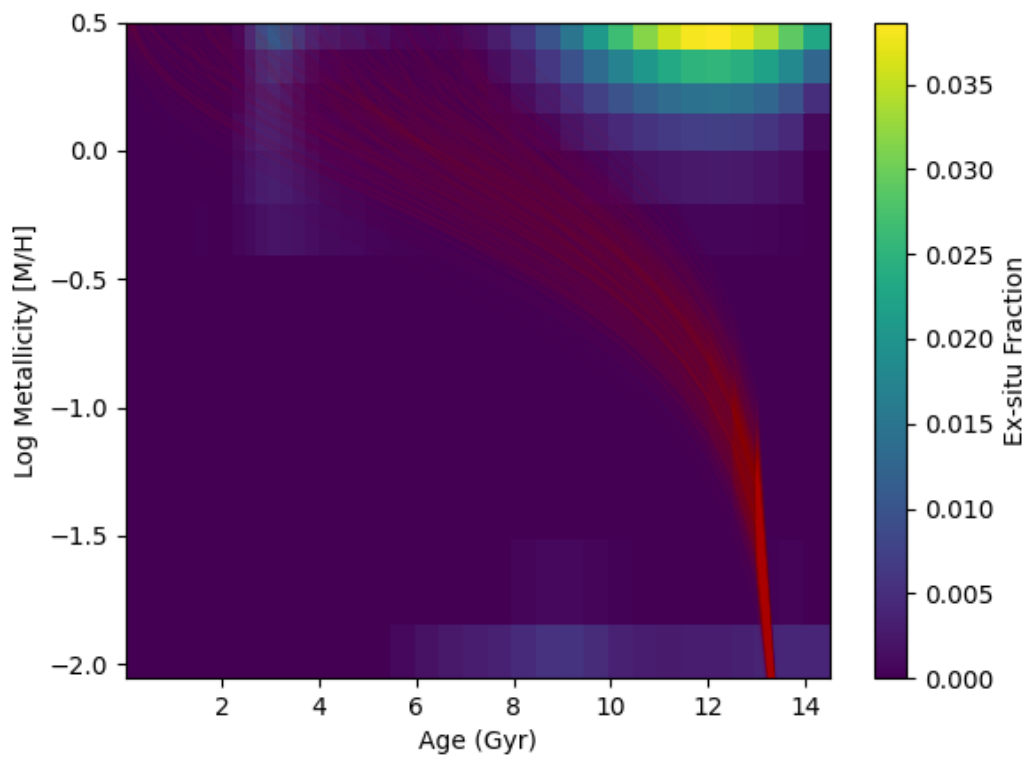


Figure 5.5: A view of the Age-Metallicity plane of one bin from the r_8 sample of SDSS galaxies. Colour shows the weight assigned to each template in the template grid. Red lines show the numerous derived AMR relations from MC simulations

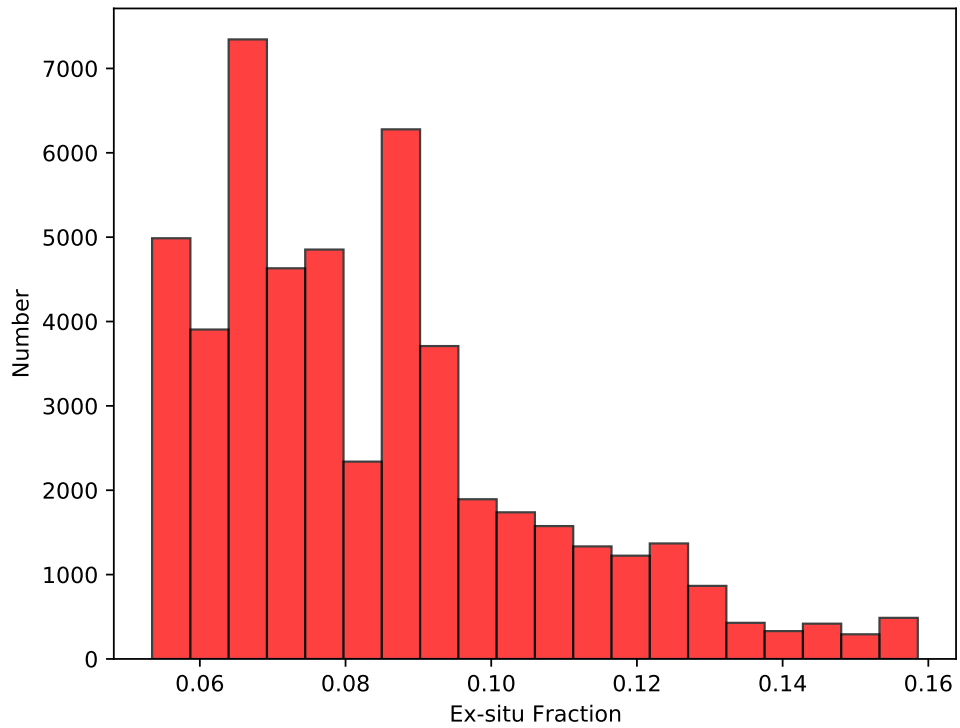


Figure 5.6: Histogram showing an example distribution of ex-situ values for 50,000 Monte Carlo simulated results for one bin (as shown in Figure 5.5). Full spectral fitting outputs a discrete grid of weighted models, and as such the recovered distribution of ex-situ values shows similarly discrete values of ex-situ estimates. Tests were run with 100,000 MC iterations with no discernible change in the distribution of recovered ex-situ fraction values.

CHAPTER 5

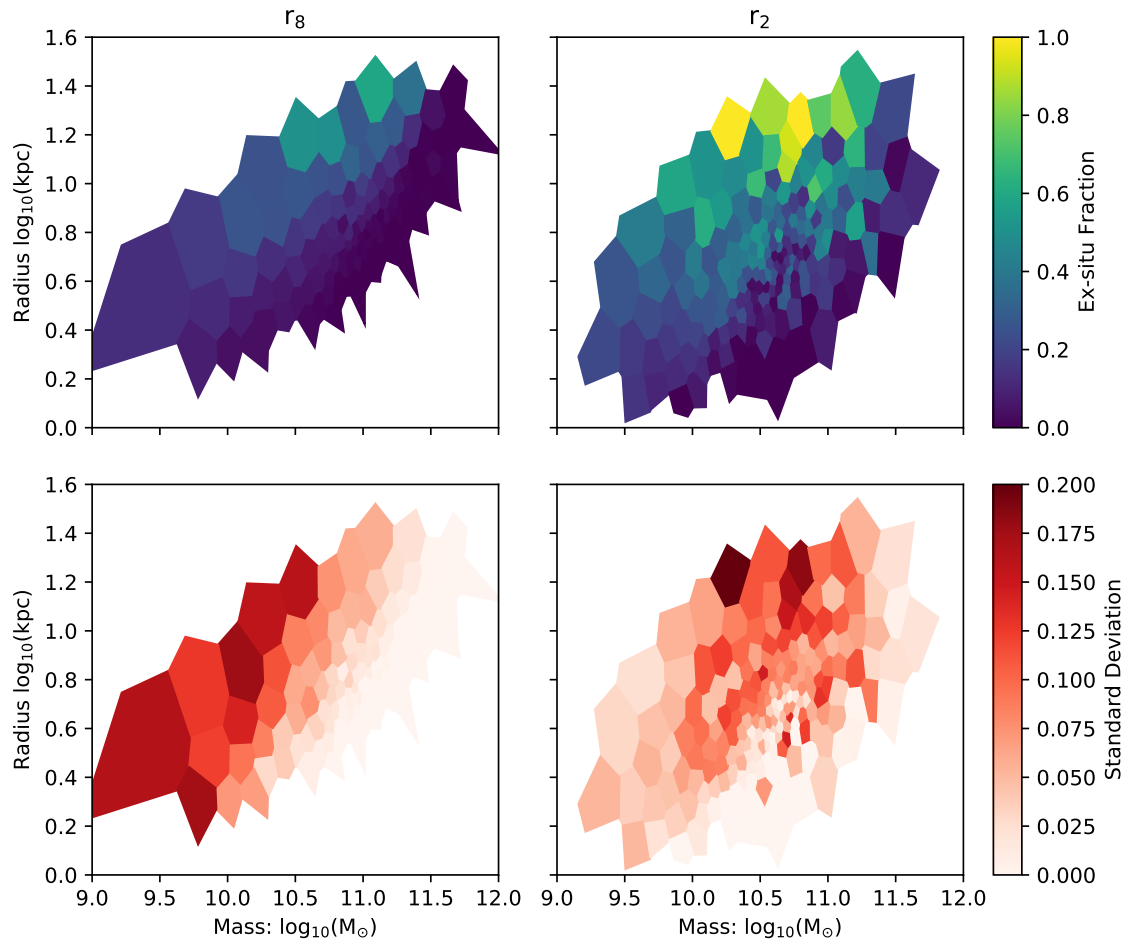


Figure 5.7: Voronoi maps showing properties regarding the r_8 and r_2 samples. Bins enclose galaxies with a summed SN of 200. Bins enclosing large areas or with vertices placed at an infinite distance were removed. In the top panels, the ex-situ fraction for both samples is shown. In the lower panels we show Voronoi maps with standard deviation of the ex-situ fraction estimate for each sample, drawn from 50,000 MC iterations per bin.

in common ($9.0_{\odot} < \log_{10}M_{*} < 12.0_{\odot}$, $0.15\text{kpc} < \log_{10}r_{1/2} < 1.45\text{kpc}$). These limited Voronoi regions were set onto a regular grid and resultant grid bins were Gaussian smoothed by 2σ , as shown in panels 1 and 2 of Figure 5.8. Final grids could be subtracted, showing regions of greater or lesser difference between samples (panel 3). Areas where bins from either sample were not represented was masked in the final subtraction map.

5.5 Discussion and Conclusions

Using full spectral fitting and modelling expected age-metallicity relations for galaxies, we have extracted the mean ex-situ fractions for galaxies across a large portion of the mass-size plane. This has been performed for two samples, one considering the central regions of galaxies, r_8 (with fibre coverage of the central 12.5% of the light profile), and a second sample considering a larger area, r_2 (with fibre coverage of the central 50% of the light profile).

Prior to summation, all spectra were convolved with a Gaussian kernel to appear as spectra from identical velocity dispersions. Figure 5.9 demonstrates the effectiveness of this step, which allows for galaxies of slightly different true velocity dispersions to be co-added. The top panels of Figure 5.9 show the original mean ex-situ fraction of all galaxies in a bin prior to convolution. We see the expected transition of lower velocity dispersion at low galaxy mass, up to higher velocity dispersions for more massive galaxies. Some trends are also visible with density. The 2nd row of panels then examines the original standard deviation in velocity dispersion per bin prior to convolution. Unsurprisingly, the standard deviation mostly scales with bin size, as larger bins encompass a greater variety of galaxies compared to small bins only encompassing similar galaxies. Standard deviation is already low with 95% of bins in each sample having standard deviations of less than 40 km/s. In the third row of panels we see the velocity dispersion recovered from each bin

CHAPTER 5

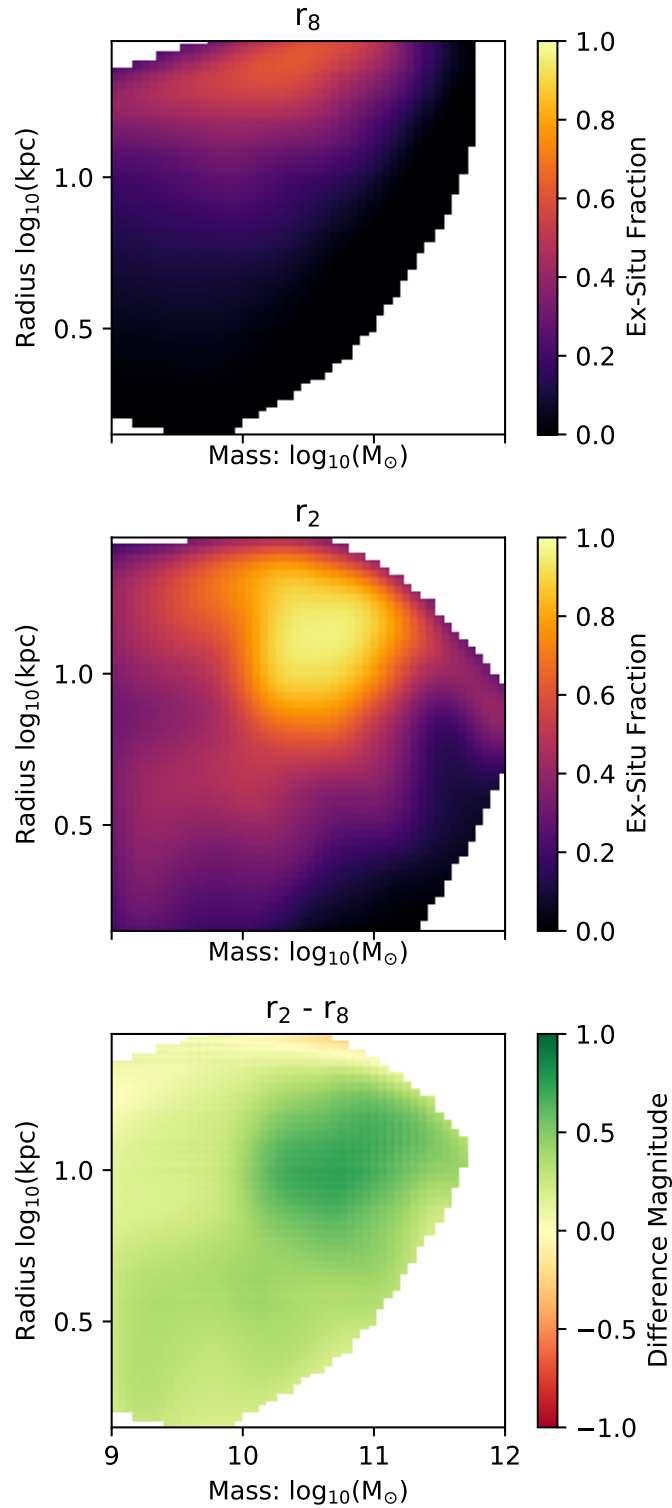


Figure 5.8: Gaussian smoothed representations of the ex-situ fraction for a fixed roughly overlapping region of both samples. The top panel shows the ex-situ fraction for a limited region of the r_8 sample, Gaussian smoothed by 2σ . The middle panel shows the same attributes for the r_2 sample over the same limited area. The lower panel shows the difference between the two samples where green is an increase with radius considered. Non overlapping regions are discarded.

CHAPTER 5

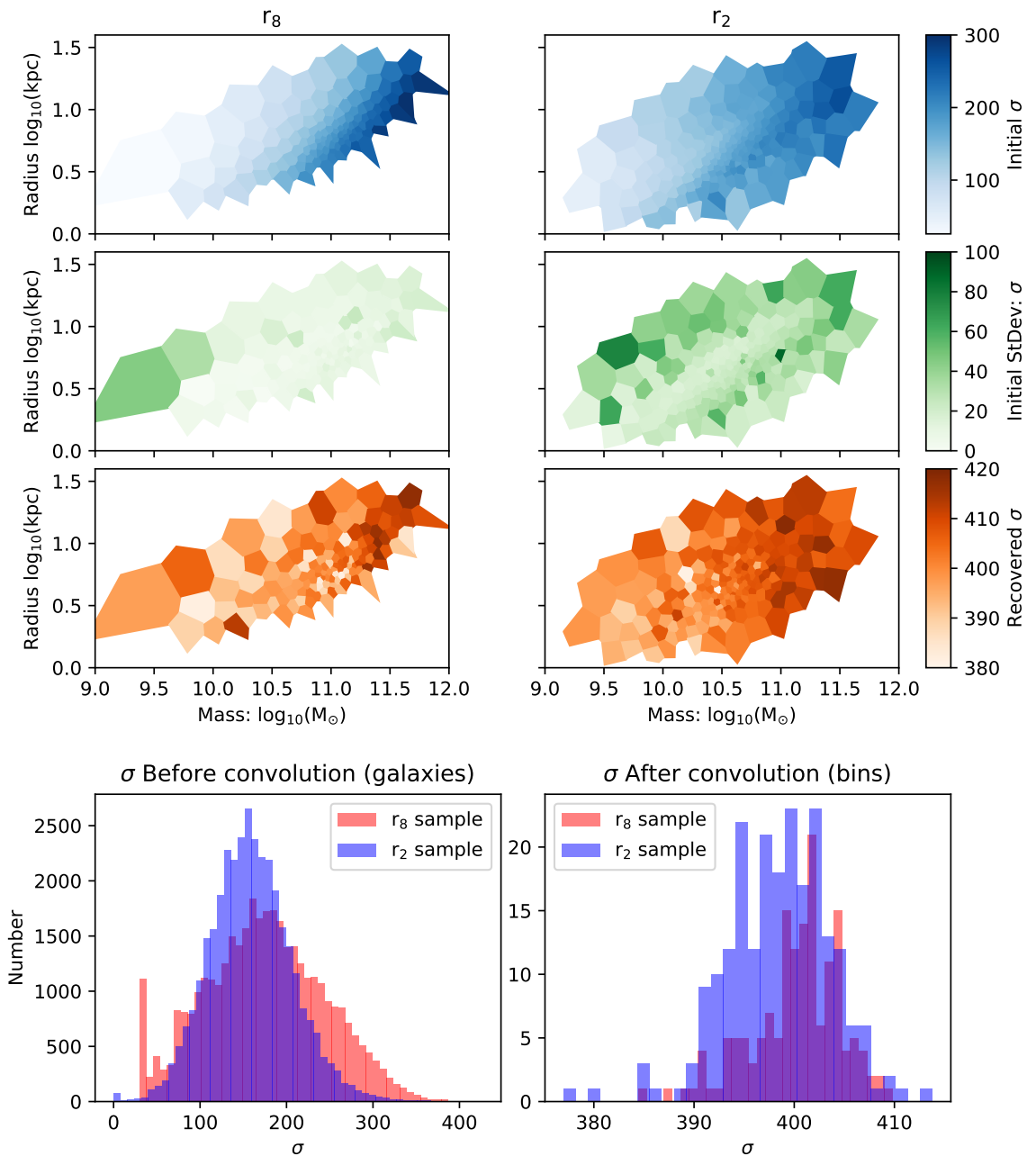


Figure 5.9: Demonstration of the convolution used to smooth spectra, in order to produce a uniform spectral resolution informed by velocity dispersion (σ). The first row of panels shows mean velocity dispersion of all galaxies in a bin. The second row of panels shows the standard deviation of those galaxies' velocity dispersion. The third row of panels shows the recovered velocity dispersion from a pPXF fit of convolved and summed spectra. Finally the fourth row shows velocity dispersion distributions before and after the convolution/summation stages.

CHAPTER 5

from a kinematically optimised pPXF fit. These show almost uniformly velocity dispersion values of 400km/s, demonstrating the success of the convolution. Some small gradient in velocity dispersion remains imprinted on the bins, however this is a tiny amount in comparison to the original values. The final row of the figure shows histograms demonstrating the before and after distribution of galaxies, across a range of velocity dispersions.

When examining the r_8 sample (Top left panel of Figure 5.7) we see generally low ex-situ fractions for all bins. There is a vertical increase in ex-situ fraction showing that more extended galaxies have higher fractions of ex-situ stars in their cores. This holds true until the most massive galaxies ($\log_{10}M_* > 11.4M_\odot$) where the most extended galaxies do not show this preference for higher ex-situ fractions in the core. This is almost certainly a result of low numbers of very massive, very extended galaxies, which are rare even for this large sample. Furthermore, extended and massive cD galaxies often have lower size estimates than is accurate, and as such these are likely missing from the samples, exacerbating the rarity. As a result, to reach the SN requirements, the Voronoi bins representing this area of the mass-size plane are large and are removed when constraining bin size to only reasonably sized bins. Despite this, there remains a trend that more massive extended galaxies tend to show the highest ex-situ fractions, though for the vast majority of galaxies in the sample, the ex-situ fraction is below 20% for the region covered.

The r_2 sample shows similar trends with mass, and radius at fixed mass. The top right panel Figure 5.7 shows a very clear increase in ex-situ fraction with galaxy extent at fixed mass. This is clearest at $\log_{10}M_* \approx 10-11M_\odot$ in which the ex-situ fraction increases from 0% to 100% over the radii covered. Again, high and extended bins show a continuation of this trend, however the regions covered by the Voronoi bins were too large to be usefully considered and so were removed.

Areas in the r_2 Voronoi sample of Figure 5.7 that show almost 100% ex-situ

CHAPTER 5

fraction are surprising considering that nearby bins in the r_8 Voronoi sample show only moderate ex-situ fractions of no more than 60%. As the r_2 sample encloses the entire galaxy, we would expect that the quantity of in-situ stars would be reflected in the bin, and show a lower fraction than 100%. A likely reason for this discrepancy is seen in maps of the standard deviation associated with each bin as shown in the lower panels of Figure 5.7. These show that those bins with the highest ex-situ fraction frequently show the greatest deviation during MC iterations, peaking at $\pm 17\%$. Bins where ex-situ stars are absent show 0 uncertainty, as these bins consist of unambiguously in-situ populations where only old and metal rich populations are present. Bins with higher ex-situ fractions tend to have more widely distributed population maps (as a result of a variety of populations arriving from external galaxies), and as such possible MC variations result in a wider array of final estimates compared to maps for purely in-situ populations. A second cause of higher standard deviation is larger bin size, which by definition collects galaxies with less specificity. As such, larger bins with high ex-situ fractions are particularly affected.

When comparing like areas of the mass size plane, Figure 5.8 shows the difference between overlapping regions. From this plot it is abundantly clear that the ex-situ fraction of stars in galaxies increases when considering greater enclosed fractions of the total galaxy light. This strongly suggests that the abundance of ex-situ fraction increases with galactocentric radius, and does so on average at all galaxy masses and radii between $9.0M_{\odot} < \log_{10}M_{*} < 12.0_{\odot}$ as seen in the lower panel of Figure 5.8. Furthermore, the increase is particularly strong for high mass, large radii galaxies, with vast increases in ex-situ fraction of the order of 50%-100%. The increase is in fact lowest for the most extended low mass galaxies, however this is a result of the galaxy centres already showing signs of a relatively high amount of ex-situ material (between 30% and 60%) suggesting that these galaxies in particular have well mixed ex-situ stars that have a strong presence in the core.

CHAPTER 5

Though the methodology presented appears to be effective, more advanced treatments could provide more robust and constrained estimates of ex-situ fraction. One powerful method would be to use tuned merger models, as was performed in Chapter 4. Due to time constraints and pandemic-induced slowdowns, the necessary models could not be added in time. As such the sufficient Monte-Carlo method was employed. By using bin-specific merger models we could provide both robust estimates of ex-situ fraction, as well as improved estimates of the uncertainty on these values. This is a planned area of continuation for the future.

Chapter 6

Thesis Overview and Discussion

6.1 Discussion

The preceding work presented in this thesis has utilised stellar populations inferred from spectroscopy and simulations to inform ideas regarding galaxy formation mechanisms. Numerous approaches have been harnessed in order to produce a robust methodology which can obtain estimates of galaxy ex-situ fraction.

Questions regarding the locations and trends of accreted stars with galaxy mass, size and galactocentric radius were first explored in Chapter 2 using cosmological simulations. This provided a window with which to examine expected values of ex-situ fractions from a theoretical view point. By doing so we have been able to first constrain the ex-situ fractions of galaxies to reasonable values. Following this, a test case was examined in Chapter 3 in order to understand the limitations, difficulties, and strengths of methods to estimate the ex-situ fractions of observed galaxies using IFU data. This provided lessons on how we could efficiently and accurately apply the methodology to a larger sample. This was then explored in Chapter 4 in which we explored extending the methodology to a larger sample of spatially resolved IFU targets, and applied a more advanced method by which to estimate uncertainty in our calculations of accreted fractions. Finally in Chapter 5 we investigated the

CHAPTER 6

application of the methodology to low resolution targets from a vast sample and explored the feasibility of such a methodology. Each subsequent chapter was able to build on and add to the wider picture of galaxy evolution in the context of accreted stars, and provided a robust view of the formation of galaxies by using their stellar populations.

In Chapter 2 we took two EAGLE simulations and extracted a sample of all galaxies between a stellar mass of $2 \times 10^7 < M_{\odot} < 1.9 \times 10^{12}$, and with a minimum of 500 stellar particles at $z=0$. All stellar particles were tracked from their time of birth until $z=0$ allowing the identification of in- or ex-situ stars in any subsequent simulated galaxy. This allowed for the exploration of a number of parameters with respect to ex-situ stars, and the chapter focussed on examining the radial trends of ex-situ stars for each galaxy; the trends with galaxy mass and size; and any trends with halo mass.

The study found clear signs that ex-situ fraction increased with galaxy mass, and with galaxy radius at fixed mass. Figure 2.5 shows how for all radial locations in the EAGLE galaxies, total ex-situ fraction increases dramatically above a stellar mass of $\log_{10} M_* > 11 M_{\odot}$. Galaxies with masses greater than $\log_{10} M_* = 12 M_{\odot}$ showed average ex-situ fractions of more than 80%, suggesting that the growth of these galaxies is almost entirely the result of accretion. Changes in ex-situ fraction with galaxy size were apparent at all positions of fixed mass, with galaxies of mass $9.5 M_{\odot} < \log_{10} M_* < 11 M_{\odot}$ showing the most pronounced difference. These galaxies showed ex-situ increases of up to 50% between the most compact and the most extended objects at fixed mass. The fact that this division was clear across the entire mass range, and at all the radial positions considered, suggests that this is a universal effect on average for all galaxies in the mass range considered.

In Chapter 3 we examined a single observational galaxy case, and explored the methodology by which to extract kinematics and population information. The

CHAPTER 6

galaxy NGC 7135 was covered by the MUSE IFU instrument, allowing for a spectro-spatial view of the galaxy with radial completeness out to around 0.6 effective radii. The galaxy was spatially binned and full spectral fitting was used to derive population information, as well as assign kinematic information to the bins. This was performed for both the stellar and the gaseous material present, giving independent insights into the galaxy composition.

NGC 7135 presented a perfect test case in which populations could be viewed. As a galaxy undergoing a merger, we had the ability to compare population results to photometric results. We were able to view populations in regions where photometry showed tidal tails and the stripped satellite galaxy core, and confirm that the population analysis found stars that would be expected in these regions.

Strong evidence to implicate historical merger events was found. Counter rotating gas was found at the galaxy core providing a clear indication that a recent merger had disturbed or deposited gas. Population analysis revealed the presence of a merging galaxy currently interacting with NGC 7135 and in the process of being fully accreted. Gas infall from this merging satellite was clearly seen as a region with high velocity dispersion. Furthermore, evidence for a significant historical merger or multiple merger event was found. This was revealed as a bi-modality in the populations, showing a well mixed population of younger stars that were not associated with the host galaxy AMR. Whilst these ex-situ stars were seen in some quantity throughout the galaxy, there was a strong radial gradient found, suggesting that many of these stars preferentially remained on the galaxy outskirts. At 0.6 effective radii, the lower limit of ex-situ fraction is placed at roughly 7%.

In Chapter 4 we advanced this analysis and applied the techniques to 13 MUSE targeted galaxies. These galaxies were extracted from the MUSE archive due to their suitable properties such as spatial coverage, quality of data, and galaxy type. Full spectral fitting was used to extract population and kinematic information of the stars

CHAPTER 6

from these galaxies. Following this, models were run to approximate the resultant expected population map, and using this the ex-situ fractions and uncertainties on these values could be extracted for every galaxy. This provided a spatially resolved view of accreted populations for galaxies across a range of masses and radii.

For all galaxies in the sample, the ex-situ fraction increased with galactocentric radius. In some cases this increase was small, only showing a 5-10% increase in the most unchanging ex-situ profile. In other cases, the increase was as much as 100% with 3 effective radii. As in Chapter 2, this increase seemed to scale with galaxy mass, and galaxy size at fixed mass. The galaxies showing the greatest ex-situ fraction in the outskirts, and the greatest radial increase, tended to be more extended, or more massive, or a combination of the two.

Finally in Chapter 5 we explore the ex-situ trends present for a large samples of SDSS galaxies. These galaxies are sorted by fibre coverage with respect to the galaxy light profile, and sub-samples are created which gather galaxies that have $\sim 12.5\%$ (r_8) or $\sim 50\%$ (r_2) light fraction. This allows us to examine basic radial trends, as the r_8 sample galaxies are assumed to represent galaxy cores, whilst the r_2 galaxies cover a larger area and reach further afield in the galaxy. Galaxies from each sample are separately binned by Voronoi binning such that high SN spectra representing discrete areas of the mass-size plane can be examined.

Views of the ex-situ fraction of SDSS galaxies across the mass size plane revealed an increase in ex-situ fraction especially with mass. This was true also with radius of a galaxy at fixed mass. All mass-size positions that were represented by both the r_8 and the r_2 samples were found to have an increasing ex-situ fraction with radius.

The common result from all individual chapters in this thesis is the increase in ex-situ fraction with galactocentric radius. This result is found to exist in simulated EAGLE galaxies; basic studies of accreted populations in NGC 7135; more advanced

CHAPTER 6

studies of multiple MUSE galaxies; and in the statistically robust SDSS samples. The SDSS results alone highlight this with the difference between the inner regions of the light profile and outer regions showing a clear increase in ex-situ fraction (see Figure 5.7). Despite this, the radial difference is at a very low resolution, arguably the lowest possible two-dimensional resolution, with only two bins. The power of this method comes from the pure statistical advantage over other methods, meaning that despite the very low resolution, both bins are well constrained. In contrast to this, a view of individual MUSE galaxies presented extraordinarily high spatial resolution, but very poor statistical resolution. By attacking the question of radial gradients of stellar populations in observed galaxies from two very different angles, we are able to provide detailed spatial information regarding accreted stars. Simultaneously we can show that this is a well sampled sub-sample of the broader galaxy population in the local universe.

The similarities of these results are summarised in Figure 6.1 which shows the ex-situ fraction of sample galaxies at $2r_e$ (or in the case of the SDSS dataset, within a circularised half-light radius). Here it is abundantly clear that there are trends with mass and size found for each dataset. The datasets cover slightly different mass ranges, however there is an almost inevitable off-set especially in stellar mass between all 3 datasets, as mass was calculated using different methods for each dataset. In all three cases there is a general trend that ex-situ fraction increases with both galaxy size and galaxy mass. This is slightly less clear in the central panel of SDSS derived values, as the ex-situ fraction appears to reduce for the most massive objects, however as discussed in the relevant chapter, this is most likely an effect of the rarity of massive extended galaxies within the SDSS sample, and as such we only see the most compact of the high mass galaxies (which the EAGLE simulations indicate show far lower ex-situ fractions than normal or extended galaxies of the same mass).

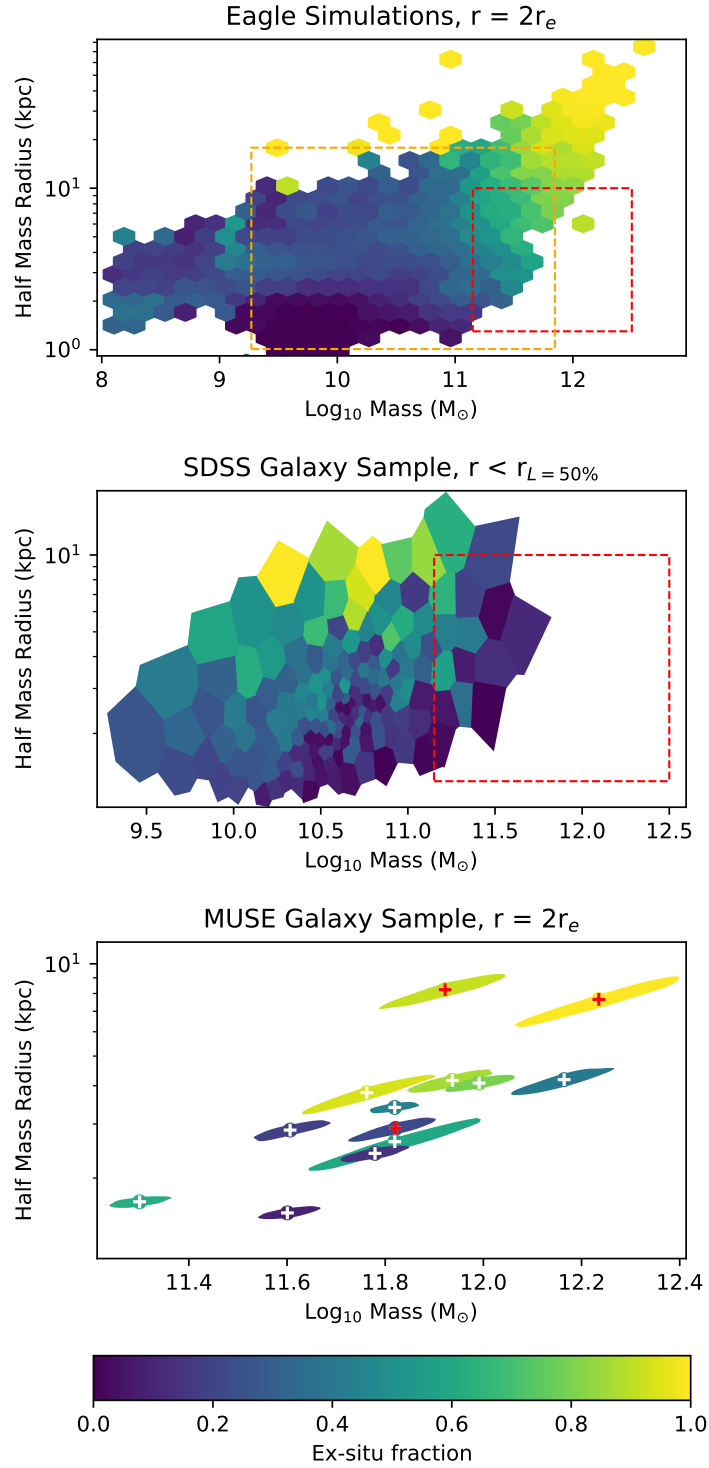


Figure 6.1: Comparison of the mass-size plane for 3 different datasets as presented in this thesis. Mass and size axes use the same scaling but different limits. The red dashed box shows the approximate area of the MUSE dataset (lowest panel). The orange dashed box shows the approximate area of the SDSS dataset (middle panel). The top and bottom panels the ex-situ fraction of stars within a boundary of $2r_e \pm 0.05r_e$, the middle panel considers all stars within a circular radius encompassing half of the full galaxy light.

CHAPTER 6

The build up of ex-situ fractions in line with galactocentric radius, as seen in the chapters of this thesis, is in line with predictions and emerging observational analysis in literature. Simulators have long discussed the two-phase scenario of stellar build up, where accreted stars are deposited onto the outskirts of in-situ galaxy cores (Oser et al. 2010; Pillepich et al. 2015; Pulsoni et al. 2020; Remus & Forbes 2021) and this is also found in Chapter 2. Observationally, reports of population gradients and features indicating accretion or interaction are frequently found in literature (Trujillo & Pohlen 2005; Auger et al. 2011; Pérez et al. 2013; Van Der Burg et al. 2015). Similarly in Chapter 3, counter rotation (a possible signature of a major merger) is found in as many as 40% of S0 galaxies observed (Rubin 1994; Davis et al. 2011; Coccato et al. 2015; Bassett et al. 2017), suggesting that mergers play a key role in the evolution and formation of galaxies.

Indeed the result that we find in Chapters 2, 4 and 5 that the most massive or extended galaxies can have up to 90% ex-situ fractions is also seen in simulations (e.g. Rodriguez-Gomez et al. (2016)). The fact that the observational results are so similar to the simulated results both from Chapter 2 and literature give weight to the accuracy of the MUSE and SDSS derived results. These results clearly point to a model of galaxy evolution in which an Early Type galaxy increases in size by accreting ex-situ stars whilst maintaining a largely in-situ core, as is described in the two-phase assembly scenario.

Whilst the observational results point to an improved ability to estimate ex-situ fractions of galaxies using both IFU and integrated galaxy data, many weaknesses remain. One particular weakness lies in the resolution and validity of the SSP models used in the full spectral fitting. These models show remarkable ability to reproduce many galaxy spectra to high precision, however they lack resolution in some areas. For instance at the very old, very metal rich region of the age-metallicity grid, there

CHAPTER 6

are only a very few models with poor age resolution (with resolution of 0.5 Gyr at age > 4 Gyr for the BaSTI based MILES models Vazdekis et al. 2010). These 0.5 Gyr steps encompass huge ranges of history in which stars were being born at an incredible rate (Madau & Dickinson 2014). As a result, old populations and especially old in-situ dominated galaxies such as red nuggets (Damjanov et al. 2009) appear highly localised in population maps. This is problematic when considering mergers between galaxies with old populations, as the ability to distinguish and separate stellar populations is significantly diminished, due to the low resolution.

Furthermore, the SSP models used are based on empirical observations of stars in the Milky Way. This gives highly physical results for populations of well studied and well sampled Milky Way-like populations, however deviations from these populations become fraught with difficulties. The further away from empirical observations a stellar population grid element is, the greater the risk that some error or inconsistency has been introduced. This is especially the case for very young, very low metallicity stars; and for very old, metal rich stars. Mostly this is down to a scarcity of these stars in the Milky Way and the inability to resolve such stars in other galaxies.

Largely the only practical solution to this problem is improved observations of rare stars. Though models will most likely improve, and the theoretical side of stellar modelling will become increasingly stable, the only real empirical fix will be to be able to resolve stars in galaxies further afield and include them in statistical samples for SSP models. Though many galaxies are currently available, the sample of rare stars is nonetheless small. High powered and high resolution telescopes and instruments such as the James Webb Space Telescope and the Extremely Large Telescope will expand the available pool of resolved stars by which to compose these samples, and will hopefully begin to improve the models for rare but important stellar populations.

CHAPTER 6

There is also a risk of degeneracy arising from the SSP models chosen. This could occur in cases where multiple solutions could be found to comprise a specific spectrum. For instance, a galaxy with high $[\text{Mg}/\text{Fe}]$ could be fit with two components, one with the correct Mg amount, and one with the correct Fe amount. This however would belie the true story where one component with the desired Mg and Fe ratio is used. Small tests were performed in this work to explore degeneracies especially arising in non-standard metallicity cases. Despite the dangers associated with full spectral fitting, the regularisation routines included within pPXF perform remarkably well in finding stable solutions that are both smooth and physical. This was able to overcome the specific cases of degeneracy tested.

A further large limitation of the current implementation of the methodology is a result of the choice of IMF. We assume fixed IMF values for samples, as is common in literature. Despite this, it is increasingly clear that galaxies show signs of varied IMFs dependent on galaxy type, mass and environment. Massive early type galaxies especially are known to exhibit non-Kroupa-like IMFs (see e.g. Cappellari et al. 2013; Smith 2014; Vaughan et al. 2018). As a result it is difficult to justify a choice of fixed IMF or an assumption of a perfectly Milky Way-like IMF. One solution for this may be to use IMF sensitive regions (such as from Smith et al. 2015) of the spectrum to derive a suitable IMF on a case by case basis. This represents an entirely new degree of freedom in the fitting of SSP models and so increases the complexity by an entire dimension. Slightly computationally simpler methods could also be used in which a first guess of IMF is made based on sensitive spectral features. Then specific areas of the parameter space would be allowed to vary within ranges of possible IMFs such that IMF could vary dependent on the populations being considered. Despite the complications introduced, this may prove to be a worthwhile exercise in order to accurately describe galaxies outside of our own neighbourhood.

CHAPTER 6

As with any field of science, the future development will likely scale with advancements in technology and instrumentation. Previously mentioned advanced telescopes will enable a greater insight into almost all areas of astronomy, both as a result of deeper and more distance samples, as well as improved resolution and data quality. Nonetheless there are plenty of advancements possible without the need for new technology, but simply a more extensive use of current technology.

One aspect that would greatly improve the work set out in this thesis would be a dedicated survey using IFU data with galaxy coverage out to large galaxy radii. Current surveys mostly focus on the brightest areas of a galaxy, which only necessitates short observation times for quick results. Despite this, it is clear that observations that do not go out to at least 2 effective radii are missing vast quantities of information pertaining to the history of the galaxy. A volume limited sample of resolved galaxies with contiguous IFU data from the core to the outskirts would allow for a statistically useful view of galaxies with respect to their populations, and changes in populations with galactocentric radius.

Existing surveys that have lower spatial resolutions but already good number statistics are also available to be mined for data. The MaNGA survey for instance has large number of galaxies available to be examined with lower resolution than MUSE but with greater coverage of galaxy parameters such as mass, size and morphology. Only a small portion of these observations have large enough radial coverage to be useful however, and therefore a dedicated IFU survey would be the most ideal option.

Further useful areas of work would be explicit test on galaxies of known populations. One possible case of this would be to evaluate the populations present in a galaxy with resolvable stars. Galaxies such as Centaurus A have observations of resolved stars (Crnojević et al. 2016, 2019) which could be used as a test case for

CHAPTER 6

population analysis. Further possibilities for this could come by measuring the population in so called ‘red-nugget’ galaxies (Damjanov et al. 2009; Zolotov et al. 2015; Ferré-Mateu et al. 2017). These pristine remnant galaxies should show no accretion and purely the oldest populations. This has already been shown in the context of globular clusters which would normally be expected to show bimodal colour distributions. The distributions of GCs around relic galaxies has been shown to lack this bimodality (Beasley et al. 2018; Alamo-Martínez et al. 2021) and only red GCs are found. This strongly supports the idea that these galaxies are relics of galaxy cores that have not experienced any meaningful accretion. Population analysis such as is presented here would be an interesting view into this case.

6.2 Conclusions

The chapters included in this thesis have explored the theory, feasibility, and applications for understanding the formation of galaxy evolution using stellar populations. This has largely focussed on identifying stars that have arrived to a galaxy by means of accretion, through mergers or close flybys.

In Chapter 2 we explore the theoretical distributions of ex-situ stars in galaxies according to the EAGLE simulations. We find clear trends of increasing ex-situ fraction with both mass and size, with the most massive galaxies ($>1 \times 10^{12} M_{\odot}$) showing ex-situ fractions of on average 80% but in some cases as exceeds $>90\%$. Further trends were found with galaxy environment where galaxies in the highest mass group/cluster halos would show a lower ex-situ fraction at fixed mass, compared to galaxies in lower mass group/cluster halos.

Following this, in Chapter 3 we analyse MUSE data of the galaxy NGC 7135. We find evidence of at least one historical merger (occurring at around 6-10Gyr ago), and an ongoing modern merger. The stellar populations are left imprinted with ex-situ stars, which we separate using a simple division of populations. Gas counter rotation is found in the core and is linked to historical merger activity. The ex-situ component of the populations is found to increase with radius.

Thirdly, in chapter 4 we use 13 galaxies observed with MUSE to estimate ex-situ fractions in massive galaxies across a range of galaxy size and mass. Using new stellar population modelling techniques we identify the fractions and location of ex-situ stars in these galaxies, creating spatially resolved maps of kinematics, populations and ex-situ fractions. We find an increase in ex-situ fraction for more massive galaxies, as well as more extended galaxies at fixed mass.

Finally in Chapter 5 we measure the ex-situ fractions of galaxies across a large area of the mass-size plane, using spatially low resolution data with high number statistics. We find a clear increase in ex-situ fraction with both mass and galaxy

CHAPTER 6

size, as well as an increase of ex-situ fraction when examining a larger area of the galaxy, suggesting that ex-situ stars are remaining preferentially on the galaxy outskirts.

Overall we find a clear preference for accreted stellar material to lie in the outer regions of galaxies. The fraction of ex-situ material appears to increase with radius. This is a likely result of the ‘two-phase’ scenario of growth in which ex-situ stars build up a galaxy following its formation as an in-situ core. The most massive and most extended galaxies are the greatest culprits in this formation by cannibalism. Massive extended galaxies are found in all chapters to show high ex-situ fractions, often increasing to almost 100% ex-situ fraction in the outer regions.

Using the populations properties of galaxies in conjunction with merger models, we have presented a viable means by which to estimate ex-situ fractions. This has been used in application to IFU data of resolved nearby galaxies. By extending this sample to a larger number of galaxies we can hope to improve both the statistical and mass-size representation of the analysis, and infer properties for galaxies on a wider basis.

Chapter A

Appendix of Chapter 2

A.1 Confirmation of Host Halo Properties

Many substructure identification algorithms, including the Subfind algorithm used here, struggle to identify self-bound substructures against high-density backgrounds. As shown by Knebe et al. (2011), this can result in the spurious loss of mass from the outskirts of substructures as their orbit takes them close to the centre of their host halo. Since ex-situ stellar mass is preferentially located in the outskirts of galaxies, this effect has the potential to induce a host halo mass dependence on the *apparent* ex-situ fraction of satellites at fixed stellar mass.

To confirm that this was not a driving effect of the result in Figure 2.7, we restricted a sample to all satellites embedded within halos of mass $M_* > 10^{14}M_\odot$ (solid red line of Figure 2.7) which would include the most severely impacted galaxies by a potential misidentification issue. By binning galaxies by radial location, as a fraction of the halo radius ($r_{crit200}$) we could investigate if there were discernible differences in ex-situ fraction for satellites closer to the halo centre.

As shown in Figures A.1 and A.2 there is no impact on the results from any such misidentification effect in the samples used in this study.

This was further confirmed by excluding satellite galaxies in which the extent of the subhalo dark matter component was comparable to that of the stellar component. As a result of the greater extent of the dark matter compared to the stellar component, this Subfind issue would affect the dark matter earlier than for the stars. By excluding the satellites in which $(r_{sm0.5} / r_{dm0.5}) > 0.55$ (where $r_{sm0.5}$ and $r_{dm0.5}$ are the stellar and dark matter half mass radii respectively) we confirmed that we continued to see the effect as seen in Figure 2.7.

This is shown in Figure A.3 where the sample was restricted to satellites in which $(r_{sm0.5} / r_{dm0.5}) < 0.55$ (exclusion of 7.5% of the original sample). The effect shown in Figure 2.7 persists, where at a fixed mass, more massive halos contain satellites of a lower ex-situ fraction. Thus we can confirm that this is most likely a physical

CHAPTER A

result of the simulation, rather than from numerical error.

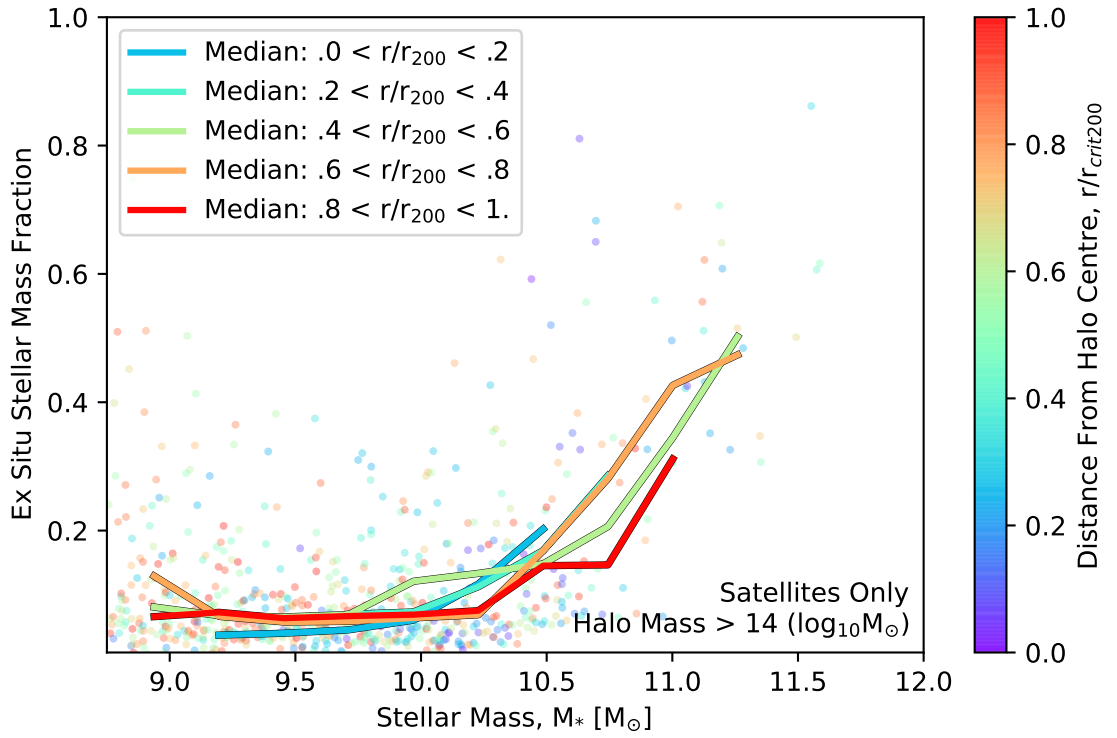


Figure A.1: Ex-situ fraction within 100kpc for $z=0$ satellite galaxies with >500 stellar particles and where $M_* > 10^{14} M_\odot$. Ex-situ fraction is shown against stellar mass, and split by distance from the halo centre. Individual objects are coloured by the fraction of the distance from the centre of the halo to which they belong, between 0 and 1 $r/r_{crit200}$. Solid lines show the median position of the ex-situ fraction for objects within 5 bins of fractional radial location in the halo, across 0.25 dex wide bins of stellar mass. There are a minimum of 3 objects per bin, and an average of 14 objects per bin.

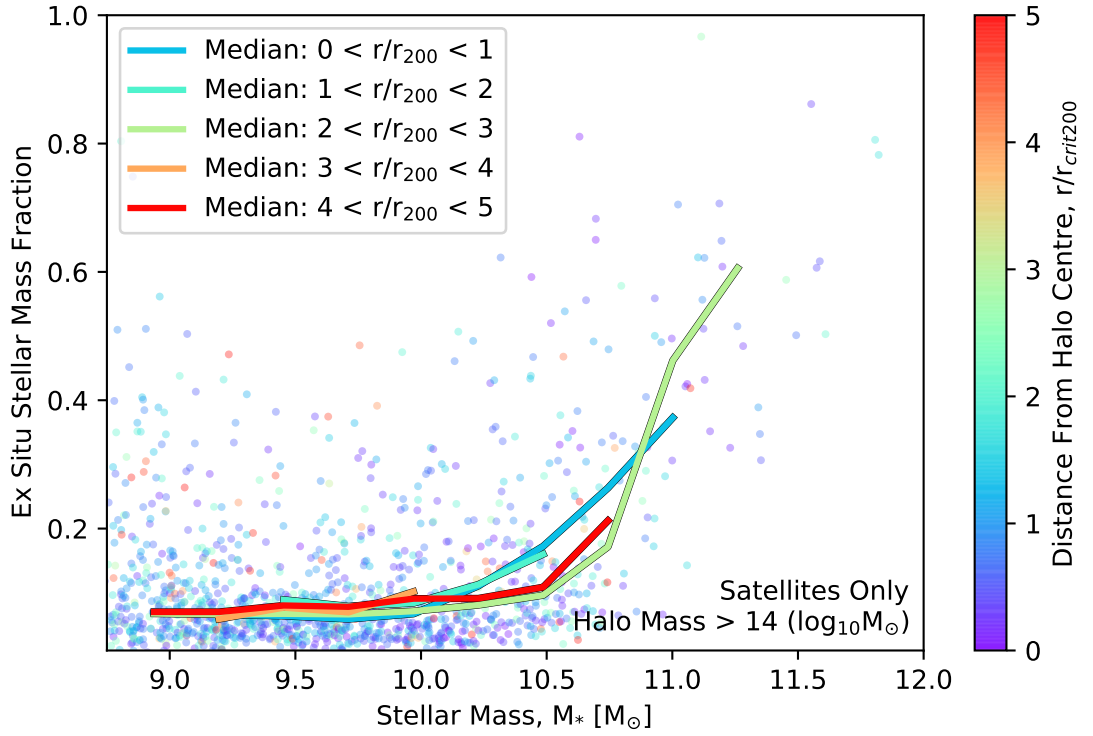


Figure A.2: Ex-situ fraction within 100kpc for $z=0$ satellite galaxies with >500 stellar particles and where $M_* > 10^{14} M_\odot$. Ex-situ fraction is shown against stellar mass, and split by distance from the halo centre. Individual objects are coloured by the fraction of the distance from the centre of the halo to which they belong between 0 and 5 $r/r_{crit200}$. Solid lines show the median position of the ex-situ fraction for objects within 5 bins of fractional radial location in the halo, across 0.25 dex wide bins of stellar mass. There are a minimum of 3 objects per bin, and an average of 86 objects per bin.

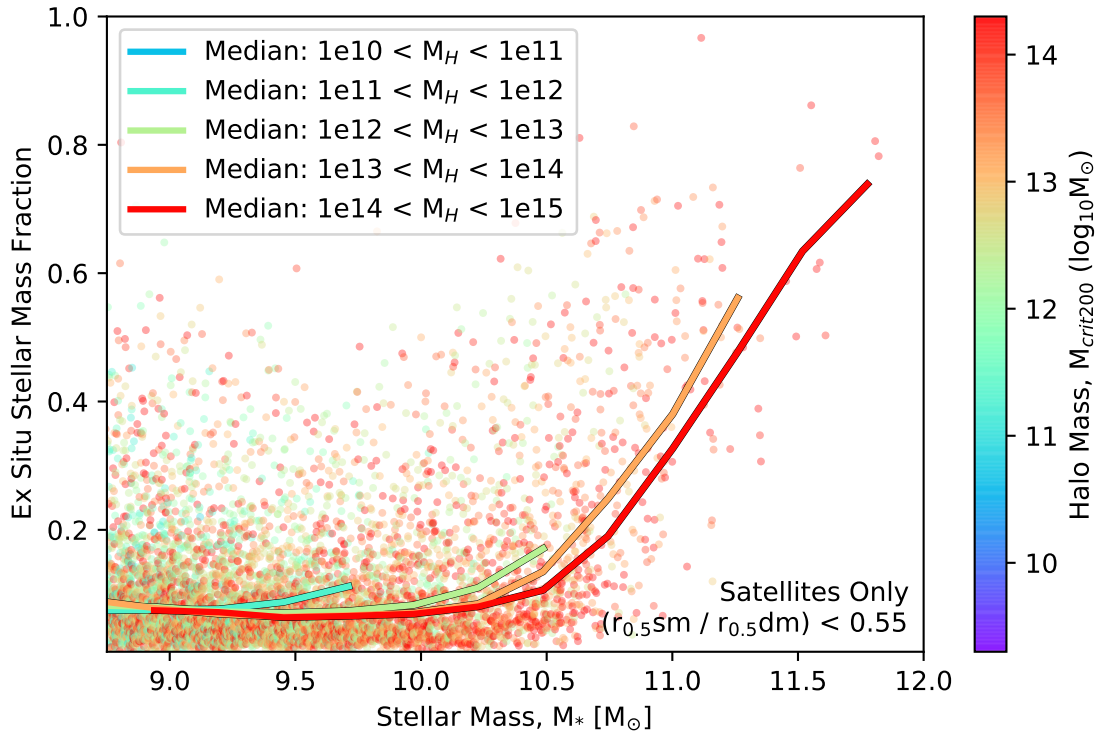


Figure A.3: Ex-situ fraction within 100pkpc for all $z=0$ satellite galaxies with >500 stellar particles where $r_{sm0.5} / r_{dm0.5} < 0.55$. Ex-situ fraction is shown against stellar mass, and split by total halo mass. Individual objects are coloured by the mass of the halo to which they belong. Solid lines show the median position of the ex-situ fraction for objects within 5 bins of parent halo mass, across 0.25 dex wide bins of stellar mass. There are a minimum of 5 objects per bin, and an average of 220 objects per bin.

A.2 Tabulated Values

Table A.1: Constants for V band surface brightness to ex-situ fraction functions for the stellar mass range $8 < \log_{10}M_{\odot} < 12.5$ in Equation 10. Surface brightnesses (μ_V) of 19 - 27 magnitudes per square arcsecond are shown.

μ_V	a	b	c	d
Red Sequence Galaxies				
19	1.763	11.177	0.991	-0.098
20	2.968	10.871	0.780	-0.015
21	3.463	10.718	0.776	0.014
22	3.168	10.600	0.799	0.030
23	2.889	10.421	0.813	0.031
24	3.124	10.282	0.772	0.073
25	3.195	10.207	0.726	0.136
26	2.960	10.020	0.720	0.152
27	3.957	10.130	0.759	0.119
Blue Sequence Galaxies				
19	8.308	10.989	0.357	0.030
20	8.715	10.900	0.360	0.035
21	3.548	11.191	0.816	0.040
22	2.909	11.258	1.127	0.034
23	3.591	10.960	0.804	0.084
24	4.119	10.642	0.704	0.083
25	4.953	10.491	0.645	0.120
26	4.585	10.349	0.677	0.130
27	6.329	10.369	0.654	0.174

CHAPTER A

Table A.2: Constants for V band co-variance matrix (Equation 11) to surface brightness functions for the stellar mass range $8 < \log_{10} M_{\odot} < 12.5$. Surface brightnesses (μ_V) of 19 - 27 magnitudes per square arcsecond are shown.

μ_V	α	β	γ	δ	ϵ	ζ	η	θ	ι	κ
Red Sequence Galaxies										
19	2.475	-0.202	-0.940	0.396	0.130	0.087	-1.69E-03	3.72E-01	3.72E-01	7.54E-02
20	2.507	0.027	-0.254	0.138	0.030	-0.004	1.02E-02	3.35E-02	3.35E-02	1.33E-02
21	2.419	-0.013	-0.135	0.062	0.020	0.001	3.84E-03	1.36E-02	1.36E-02	4.82E-03
22	1.865	-0.014	-0.119	0.053	0.021	0.002	3.82E-03	1.34E-02	1.34E-02	4.60E-03
23	1.481	-0.001	-0.112	0.055	0.024	0.000	4.98E-03	1.42E-02	1.42E-02	5.49E-03
24	1.745	0.015	-0.105	0.059	0.022	-0.002	5.25E-03	1.16E-02	1.16E-02	5.40E-03
25	1.843	0.023	-0.101	0.059	0.021	-0.002	5.34E-03	1.02E-02	1.02E-02	5.13E-03
26	1.642	0.062	-0.118	0.082	0.026	-0.008	9.55E-03	1.37E-02	1.37E-02	8.34E-03
27	3.586	0.175	-0.250	0.211	0.032	-0.023	2.39E-02	3.18E-02	3.18E-02	2.70E-02
Blue Sequence Galaxies										
19	30.214	-0.153	-0.344	0.092	0.009	0.004	7.30E-04	7.30E-03	-1.79E-03	1.25E-03
20	31.215	-0.120	-0.266	0.069	0.007	0.002	6.30E-04	5.06E-03	-1.25E-03	9.52E-04
21	4.200	-0.527	-0.758	0.063	0.096	0.124	-4.90E-03	1.75E-01	-1.05E-02	2.23E-03
22	2.608	-0.643	-1.039	0.055	0.202	0.315	-9.64E-03	5.12E-01	-1.92E-02	2.60E-03
23	2.999	-0.280	-0.379	0.034	0.047	0.051	-1.13E-03	6.69E-02	-4.35E-03	1.48E-03
24	3.835	-0.133	-0.214	0.039	0.020	0.013	6.01E-04	1.94E-02	-3.12E-03	1.82E-03
25	5.902	-0.077	-0.172	0.044	0.013	0.005	1.11E-03	1.03E-02	-2.50E-03	1.84E-03
26	5.005	-0.053	-0.167	0.055	0.014	0.004	1.78E-03	1.11E-02	-3.59E-03	2.71E-03
27	15.856	-0.012	-0.300	0.116	0.012	0.002	2.48E-03	1.32E-02	-5.10E-03	4.16E-03

CHAPTER A

Table A.3: Constants for B band surface brightness to ex-situ fraction functions for the stellar mass range $8 < \log_{10}M_{\odot} < 12.5$ in Equation 10. Surface brightnesses (μ_B) of 19 - 27 magnitudes per square arcsecond are shown.

μ_B	a	b	c	d
Red Sequence Galaxies				
19	1.793	11.144	0.981	-0.098
20	3.131	10.863	0.764	-0.004
21	3.495	10.718	0.772	0.020
22	3.181	10.595	0.799	0.031
23	2.913	10.418	0.810	0.033
24	3.139	10.279	0.772	0.073
25	3.239	10.206	0.724	0.137
26	2.944	10.015	0.727	0.146
27	3.010	10.109	0.493	0.363
Blue Sequence Galaxies				
19	8.879	10.981	0.351	0.031
20	8.276	10.899	0.367	0.034
21	3.488	11.209	0.851	0.039
22	2.853	11.260	1.137	0.033
23	3.194	10.966	0.861	0.062
24	4.039	10.636	0.712	0.078
25	4.944	10.489	0.646	0.120
26	4.440	10.347	0.684	0.125
27	4.639	10.391	0.715	0.129

CHAPTER A

Table A.4: Constants for B band co-variance matrix (Equation 11) to surface brightness functions for the stellar mass range $8 < \log_{10} M_{\odot} < 12.5$. Surface brightnesses (μ_B) of 19 - 27 magnitudes per square arcsecond are shown.

μ_B	α	β	γ	δ	ϵ	ζ	η	θ	ι	κ
Red Sequence Galaxies										
19	2.455	-0.144	-0.893	0.394	0.116	0.060	7.08E-03	3.39E-01	3.39E-01	7.55E-02
20	2.463	0.005	-0.208	0.106	0.026	-0.001	7.31E-03	2.46E-02	2.46E-02	9.39E-03
21	2.428	-0.017	-0.129	0.057	0.019	0.002	3.46E-03	1.28E-02	1.28E-02	4.35E-03
22	1.880	-0.014	-0.118	0.053	0.021	0.002	3.83E-03	1.33E-02	1.33E-02	4.60E-03
23	1.506	-0.001	-0.111	0.055	0.024	0.000	4.93E-03	1.39E-02	1.39E-02	5.42E-03
24	1.764	0.015	-0.105	0.059	0.021	-0.002	5.23E-03	1.16E-02	1.16E-02	5.39E-03
25	1.898	0.023	-0.100	0.059	0.021	-0.002	5.22E-03	1.00E-02	1.00E-02	5.05E-03
26	1.628	0.063	-0.120	0.083	0.026	-0.008	9.84E-03	1.41E-02	1.41E-02	8.64E-03
27	1.501	0.075	-0.140	0.072	0.027	-0.006	2.38E-03	5.04E-03	5.04E-03	4.00E-03
Blue Sequence Galaxies										
19	35.578	-0.142	-0.340	0.094	0.008	0.003	7.25E-04	6.44E-03	-1.65E-03	1.19E-03
20	27.422	-0.124	-0.267	0.069	0.008	0.003	6.56E-04	5.52E-03	-1.34E-03	1.00E-03
21	3.908	-0.539	-0.784	0.058	0.104	0.139	-5.05E-03	2.01E-01	-1.06E-02	2.07E-03
22	2.558	-0.661	-1.063	0.056	0.217	0.337	-1.05E-02	5.44E-01	-2.07E-02	2.72E-03
23	2.438	-0.313	-0.419	0.038	0.067	0.074	-2.31E-03	9.54E-02	-6.47E-03	1.88E-03
24	3.675	-0.134	-0.216	0.040	0.021	0.013	5.94E-04	2.03E-02	-3.28E-03	1.89E-03
25	5.884	-0.077	-0.172	0.044	0.013	0.005	1.12E-03	1.03E-02	-2.51E-03	1.85E-03
26	4.658	-0.055	-0.169	0.056	0.015	0.004	1.85E-03	1.19E-02	-3.80E-03	2.83E-03
27	6.977	-0.048	-0.300	0.111	0.018	0.005	3.01E-03	2.14E-02	-7.47E-03	5.23E-03

CHAPTER A

Table A.5: Constants for R band surface brightness to ex-situ fraction functions for the stellar mass range $8 < \log_{10}M_{\odot} < 12.5$ in Equation 10. Surface brightnesses (μ_R) of 19 - 27 magnitudes per square arcsecond are shown.

μ_R	a	b	c	d
Red Sequence Galaxies				
19	1.736	11.146	0.998	-0.105
20	3.159	10.868	0.759	0.000
21	3.418	10.709	0.780	0.015
22	3.136	10.589	0.801	0.031
23	2.908	10.407	0.809	0.033
24	3.226	10.273	0.764	0.080
25	3.199	10.203	0.723	0.141
26	2.989	10.010	0.707	0.164
27	4.061	9.988	0.925	-0.061
Blue Sequence Galaxies				
19	8.759	10.983	0.352	0.031
20	8.212	10.896	0.367	0.034
21	3.252	11.227	0.899	0.029
22	3.478	11.179	0.960	0.067
23	3.290	10.934	0.835	0.064
24	4.257	10.623	0.697	0.087
25	4.859	10.473	0.642	0.122
26	4.491	10.350	0.688	0.126
27	4.493	10.300	0.631	0.176

CHAPTER A

Table A.6: Constants for R band co-variance matrix (Equation 11) to surface brightness functions for the stellar mass range $8 < \log_{10} M_{\odot} < 12.5$. Surface brightnesses (μ_R) of 19 - 27 magnitudes per square arcsecond are shown.

μ_R	α	β	γ	δ	ϵ	ζ	η	θ	ι	κ
Red Sequence Galaxies										
19	2.479	-0.157	-0.968	0.427	0.128	0.070	6.00E-03	3.92E-01	3.92E-01	8.67E-02
20	2.502	0.004	-0.205	0.105	0.026	-0.001	7.08E-03	2.39E-02	2.39E-02	9.07E-03
21	2.309	-0.016	-0.130	0.058	0.020	0.002	3.63E-03	1.34E-02	1.34E-02	4.56E-03
22	1.826	-0.013	-0.119	0.054	0.022	0.002	3.95E-03	1.37E-02	1.37E-02	4.73E-03
23	1.501	0.001	-0.111	0.056	0.024	0.000	5.02E-03	1.39E-02	1.39E-02	5.48E-03
24	1.873	0.015	-0.104	0.058	0.021	-0.002	4.99E-03	1.10E-02	1.10E-02	5.16E-03
25	1.848	0.024	-0.100	0.059	0.021	-0.003	5.34E-03	1.01E-02	1.01E-02	5.11E-03
26	1.696	0.063	-0.118	0.082	0.026	-0.008	9.46E-03	1.33E-02	1.33E-02	8.15E-03
27	1.550	0.055	-0.103	0.062	0.022	-0.005	1.95E-03	3.32E-02	3.32E-02	3.15E-03
Blue Sequence Galaxies										
19	34.443	-0.144	-0.342	0.094	0.008	0.003	7.29E-04	6.63E-03	-1.68E-03	1.21E-03
20	26.937	-0.124	-0.266	0.069	0.008	0.003	6.67E-04	5.56E-03	-1.36E-03	1.01E-03
21	3.576	-0.605	-0.881	0.063	0.138	0.188	-7.20E-03	2.72E-01	-1.39E-02	2.41E-03
22	3.336	-0.466	-0.733	0.044	0.093	0.135	-3.67E-03	2.13E-01	-8.90E-03	1.84E-03
23	2.485	-0.283	-0.375	0.035	0.057	0.060	-1.67E-03	7.65E-02	-5.38E-03	1.71E-03
24	4.115	-0.123	-0.207	0.040	0.018	0.011	7.05E-04	1.75E-02	-2.98E-03	1.82E-03
25	5.666	-0.076	-0.169	0.044	0.013	0.005	1.17E-03	1.03E-02	-2.57E-03	1.89E-03
26	4.789	-0.055	-0.171	0.056	0.015	0.004	1.83E-03	1.19E-02	-3.80E-03	2.84E-03
27	3.864	-0.044	-0.171	0.065	0.002	0.000	5.72E-04	8.13E-03	-3.97E-03	3.94E-03

CHAPTER A

Table A.7: Constants for g band surface brightness to ex-situ fraction functions for the stellar mass range $8 < \log_{10}M_{\odot} < 12.5$ in Equation 10. Surface brightnesses (μ_g) of 19 - 27 magnitudes per square arcsecond are shown.

μ_g	a	b	c	d
Red Sequence Galaxies				
19	1.794	11.147	0.981	-0.098
20	3.104	10.865	0.766	-0.006
21	3.508	10.720	0.770	0.022
22	3.164	10.594	0.800	0.030
23	2.883	10.414	0.813	0.030
24	3.146	10.280	0.771	0.074
25	3.217	10.204	0.724	0.138
26	3.126	10.030	0.706	0.163
27	8.157	10.172	0.584	0.272
Blue Sequence Galaxies				
19	8.861	10.983	0.351	0.031
20	8.249	10.899	0.367	0.034
21	3.499	11.206	0.846	0.039
22	3.373	11.197	0.993	0.060
23	3.791	10.945	0.775	0.093
24	4.149	10.636	0.704	0.083
25	4.871	10.488	0.647	0.119
26	4.609	10.350	0.678	0.130
27	4.912	10.368	0.722	0.128

CHAPTER A

Table A.8: Constants for g band co-variance matrix (Equation 11) to surface brightness functions for the stellar mass range $8 < \log_{10} M_{\odot} < 12.5$. Surface brightnesses (μ_g) of 19 - 27 magnitudes per square arcsecond are shown.

μ_g	α	β	γ	δ	ϵ	ζ	η	θ	ι	κ
Red Sequence Galaxies										
19	2.453	-0.147	-0.892	0.392	0.116	0.061	6.53E-03	3.38E-01	3.38E-01	7.49E-02
20	2.428	0.005	-0.209	0.107	0.027	-0.001	7.40E-03	2.52E-02	2.52E-02	9.53E-03
21	2.490	-0.013	-0.134	0.061	0.019	0.001	3.74E-03	1.32E-02	1.32E-02	4.68E-03
22	1.860	-0.014	-0.119	0.053	0.021	0.002	3.87E-03	1.35E-02	1.35E-02	4.65E-03
23	1.475	0.000	-0.112	0.056	0.024	0.000	5.06E-03	1.43E-02	1.43E-02	5.55E-03
24	1.772	0.015	-0.105	0.059	0.021	-0.002	5.20E-03	1.15E-02	1.15E-02	5.36E-03
25	1.871	0.023	-0.101	0.059	0.021	-0.002	5.29E-03	1.01E-02	1.01E-02	5.09E-03
26	1.831	0.056	-0.114	0.078	0.023	-0.006	8.15E-03	1.20E-02	1.20E-02	7.25E-03
27	1.836	0.042	-0.288	0.082	0.013	-0.003	4.21E-03	8.97E-03	8.97E-03	7.08E-03
Blue Sequence Galaxies										
19	35.372	-0.143	-0.341	0.094	0.008	0.003	7.22E-04	6.50E-03	-1.65E-03	1.19E-03
20	27.228	-0.124	-0.267	0.069	0.008	0.003	6.59E-04	5.53E-03	-1.35E-03	1.00E-03
21	3.919	-0.533	-0.773	0.057	0.102	0.136	-4.93E-03	1.96E-01	-1.04E-02	2.05E-03
22	3.099	-0.484	-0.767	0.044	0.105	0.156	-4.26E-03	2.48E-01	-9.84E-03	1.86E-03
23	3.436	-0.268	-0.367	0.034	0.041	0.042	-7.67E-04	5.62E-02	-3.86E-03	1.44E-03
24	3.894	-0.130	-0.213	0.039	0.020	0.012	6.34E-04	1.90E-02	-3.11E-03	1.84E-03
25	5.675	-0.078	-0.172	0.044	0.013	0.005	1.13E-03	1.05E-02	-2.56E-03	1.87E-03
26	5.072	-0.053	-0.168	0.056	0.014	0.004	1.77E-03	1.11E-02	-3.58E-03	2.71E-03
27	8.010	-0.035	-0.303	0.117	0.016	0.004	3.18E-03	2.01E-02	-7.40E-03	5.40E-03

CHAPTER A

Table A.9: Constants for r band surface brightness to ex-situ fraction functions for the stellar mass range $8 < \log_{10}M_{\odot} < 12.5$ in Equation 10. Surface brightnesses (μ_r) of 19 - 27 magnitudes per square arcsecond are shown.

μ_r	a	b	c	d
Red Sequence Galaxies				
19	1.706	11.200	1.004	-0.101
20	2.856	10.885	0.792	-0.022
21	3.547	10.727	0.766	0.018
22	3.174	10.614	0.797	0.030
23	2.897	10.434	0.815	0.030
24	3.107	10.291	0.774	0.070
25	3.249	10.211	0.729	0.131
26	3.099	10.047	0.717	0.153
27	4.346	10.055	0.761	0.109
Blue Sequence Galaxies				
19	7.743	10.999	0.365	0.028
20	9.787	10.901	0.348	0.038
21	3.727	11.151	0.746	0.040
22	2.901	11.279	1.149	0.032
23	3.937	10.971	0.770	0.101
24	4.034	10.659	0.710	0.081
25	4.956	10.493	0.645	0.119
26	4.461	10.350	0.678	0.128
27	6.727	10.358	0.634	0.168

CHAPTER A

Table A.10: Constants for r band co-variance matrix (Equation 11) to surface brightness functions for the stellar mass range $8 < \log_{10} M_{\odot} < 12.5$. Surface brightnesses (μ_r) of 19 - 27 magnitudes per square arcsecond are shown.

μ_r	α	β	γ	δ	ϵ	ζ	η	θ	ι	κ
Red Sequence Galaxies										
19	2.526	-0.259	-1.032	0.422	0.152	0.120	-1.03E-02	4.37E-01	4.37E-01	8.30E-02
20	2.525	0.042	-0.292	0.164	0.034	-0.007	1.30E-02	4.21E-02	4.21E-02	1.71E-02
21	2.555	-0.014	-0.133	0.060	0.019	0.001	3.63E-03	1.29E-02	1.29E-02	4.55E-03
22	1.873	-0.016	-0.119	0.052	0.021	0.002	3.71E-03	1.34E-02	1.34E-02	4.49E-03
23	1.490	-0.003	-0.112	0.055	0.024	0.000	4.85E-03	1.42E-02	1.42E-02	5.40E-03
24	1.725	0.014	-0.106	0.059	0.022	-0.002	5.24E-03	1.18E-02	1.18E-02	5.40E-03
25	1.911	0.022	-0.101	0.059	0.021	-0.002	5.18E-03	1.01E-02	1.01E-02	5.05E-03
26	1.790	0.054	-0.114	0.078	0.024	-0.006	8.15E-03	1.23E-02	1.23E-02	7.34E-03
27	4.289	0.175	-0.261	0.225	0.025	-0.021	2.14E-02	3.11E-02	3.11E-02	2.71E-02
Blue Sequence Galaxies										
19	25.504	-0.167	-0.349	0.091	0.010	0.004	7.17E-04	8.41E-03	-1.96E-03	1.31E-03
20	41.826	-0.109	-0.265	0.070	0.006	0.002	5.68E-04	4.25E-03	-1.08E-03	8.63E-04
21	4.460	-0.455	-0.632	0.059	0.072	0.087	-3.38E-03	1.17E-01	-7.97E-03	2.00E-03
22	2.745	-0.696	-1.153	0.060	0.223	0.357	-1.11E-02	5.94E-01	-2.23E-02	2.85E-03
23	3.896	-0.284	-0.397	0.034	0.040	0.043	-7.09E-04	5.86E-02	-3.74E-03	1.40E-03
24	3.665	-0.140	-0.220	0.039	0.021	0.014	5.07E-04	2.11E-02	-3.21E-03	1.82E-03
25	5.906	-0.078	-0.172	0.044	0.013	0.005	1.10E-03	1.03E-02	-2.49E-03	1.83E-03
26	4.705	-0.055	-0.168	0.055	0.015	0.004	1.81E-03	1.16E-02	-3.70E-03	2.76E-03
27	3.884	-0.043	-0.262	0.041	0.011	0.001	2.33E-03	1.03E-02	-4.43E-03	3.77E-03

CHAPTER A

Table A.11: Constants for i band surface brightness to ex-situ fraction functions for the stellar mass range $8 < \log_{10}M_{\odot} < 12.5$ in Equation 10. Surface brightnesses (μ_i) of 19 - 27 magnitudes per square arcsecond are shown.

μ_i	a	b	c	d
Red Sequence Galaxies				
19	1.951	11.205	0.922	-0.064
20	2.754	10.918	0.800	-0.024
21	3.644	10.736	0.755	0.020
22	3.179	10.625	0.798	0.026
23	2.932	10.453	0.814	0.031
24	3.088	10.301	0.777	0.064
25	3.174	10.214	0.736	0.124
26	3.358	10.065	0.693	0.171
27	3.443	10.110	0.600	0.250
Blue Sequence Galaxies				
19	8.421	11.007	0.358	0.031
20	9.537	10.902	0.346	0.034
21	3.991	11.096	0.660	0.041
22	2.957	11.286	1.141	0.033
23	3.173	11.025	0.898	0.061
24	3.956	10.687	0.709	0.084
25	4.926	10.509	0.654	0.115
26	4.169	10.341	0.686	0.117
27	4.145	10.367	0.634	0.170

CHAPTER A

Table A.12: Constants for i band co-variance matrix (Equation 11) to surface brightness functions for the stellar mass range $8 < \log_{10} M_{\odot} < 12.5$. Surface brightnesses (μ_i) of 19 - 27 magnitudes per square arcsecond are shown.

μ_i	α	β	γ	δ	ϵ	ζ	η	θ	ι	κ
Red Sequence Galaxies										
19	2.470	-0.201	-0.742	0.297	0.104	0.070	-1.95E-03	2.36E-01	2.36E-01	4.46E-02
20	2.425	0.028	-0.305	0.164	0.036	-0.005	1.26E-02	4.66E-02	4.66E-02	1.76E-02
21	2.718	-0.015	-0.132	0.059	0.018	0.001	3.43E-03	1.21E-02	1.21E-02	4.29E-03
22	1.878	-0.018	-0.119	0.052	0.021	0.002	3.63E-03	1.34E-02	1.34E-02	4.43E-03
23	1.526	-0.005	-0.111	0.054	0.023	0.001	4.62E-03	1.39E-02	1.39E-02	5.20E-03
24	1.702	0.013	-0.106	0.058	0.022	-0.002	5.23E-03	1.19E-02	1.19E-02	5.41E-03
25	1.815	0.022	-0.102	0.060	0.021	-0.002	5.42E-03	1.06E-02	1.06E-02	5.26E-03
26	2.082	0.038	-0.101	0.066	0.020	-0.004	5.82E-03	9.40E-03	9.40E-03	5.37E-03
27	2.110	0.042	-0.100	0.063	0.020	-0.003	5.91E-03	5.12E-03	5.12E-03	4.09E-03
Blue Sequence Galaxies										
19	32.166	-0.156	-0.372	0.104	0.009	0.004	7.81E-04	7.88E-03	-1.99E-03	1.38E-03
20	40.003	-0.108	-0.273	0.076	0.006	0.002	6.36E-04	4.48E-03	-1.21E-03	9.52E-04
21	4.918	-0.375	-0.500	0.055	0.051	0.054	-1.90E-03	6.88E-02	-5.55E-03	1.72E-03
22	2.804	-0.689	-1.148	0.058	0.214	0.346	-1.03E-02	5.79E-01	-2.09E-02	2.65E-03
23	2.393	-0.345	-0.469	0.037	0.077	0.091	-2.75E-03	1.22E-01	-6.87E-03	1.77E-03
24	3.600	-0.155	-0.232	0.038	0.024	0.017	3.69E-04	2.34E-02	-3.28E-03	1.78E-03
25	5.794	-0.081	-0.176	0.043	0.013	0.005	1.07E-03	1.08E-02	-2.53E-03	1.84E-03
26	4.050	-0.058	-0.170	0.056	0.017	0.005	1.94E-03	1.29E-02	-4.12E-03	2.98E-03
27	3.835	-0.022	-0.218	0.095	0.011	0.001	2.22E-03	9.81E-03	-4.24E-03	3.57E-03

Chapter B

Appendix of Chapter 3

CHAPTER B

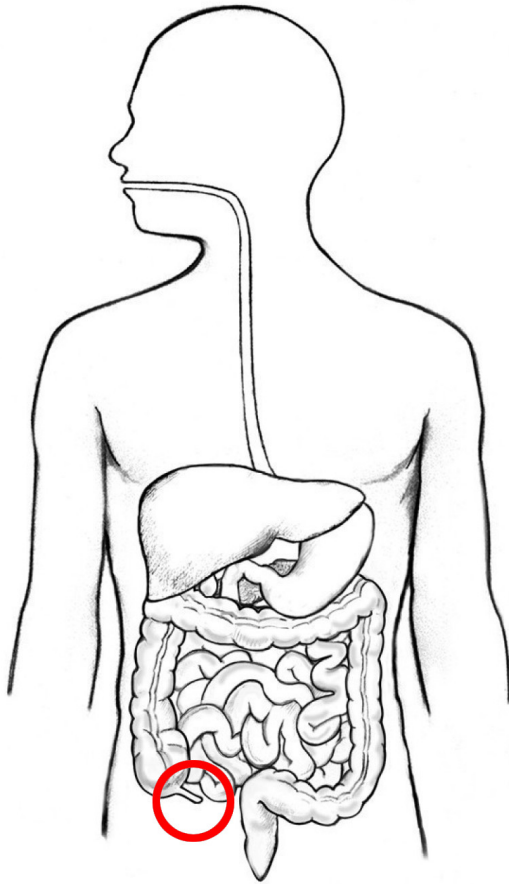


Figure B.1: Appendix

Chapter C

Appendix of Chapter 4

C.1 Galaxy Sample - Interesting Cases and Points of Note

The galaxy sample was sub-selected from the wider available MUSE data as described in Section 4.4. Figure C.1 shows this selection from available MUSE data. In this section we will lay out some points of interest and note regarding particular sample galaxies.

C.1.1 IC1459

In Figure C.5 we see a clear counter-rotating core at the centre of IC 1459. This is well known and well studied (Franx & Illingworth 1988; Cappellari et al. 2002; Prichard et al. 2019). Counter-rotation has long been associated with galaxy mergers (see e.g. Bertola et al. 1988). The galaxy appears to show nested rings of distinct populations which are particularly visible in the M/H panel of Figure C.5. This feature was questioned considering the lack of kinematic features, however the ring can clearly be seen as a region of gas experiencing starformation, for instance in H-Alpha or in H-Beta, shown in Figure C.2 of the Appendix.

C.1.2 NGC1316

NGC 1316 is a giant elliptical galaxy in the Fornax cluster, and one of the brightest radio sources present in the sky (Geldzahler & Fomalont 1984). The general galaxy morphology was extensively studied in Schweizer (1980, 1981). Mackie & Fabbiano (1998) use X-ray data to provide strong evidence from Schweizer (1981) that the galaxy underwent an intermediate merger, further evidenced by the presence of shells and strong tidal features, and evidence of accretion (Horellou et al. 2001; Serra et al. 2019).

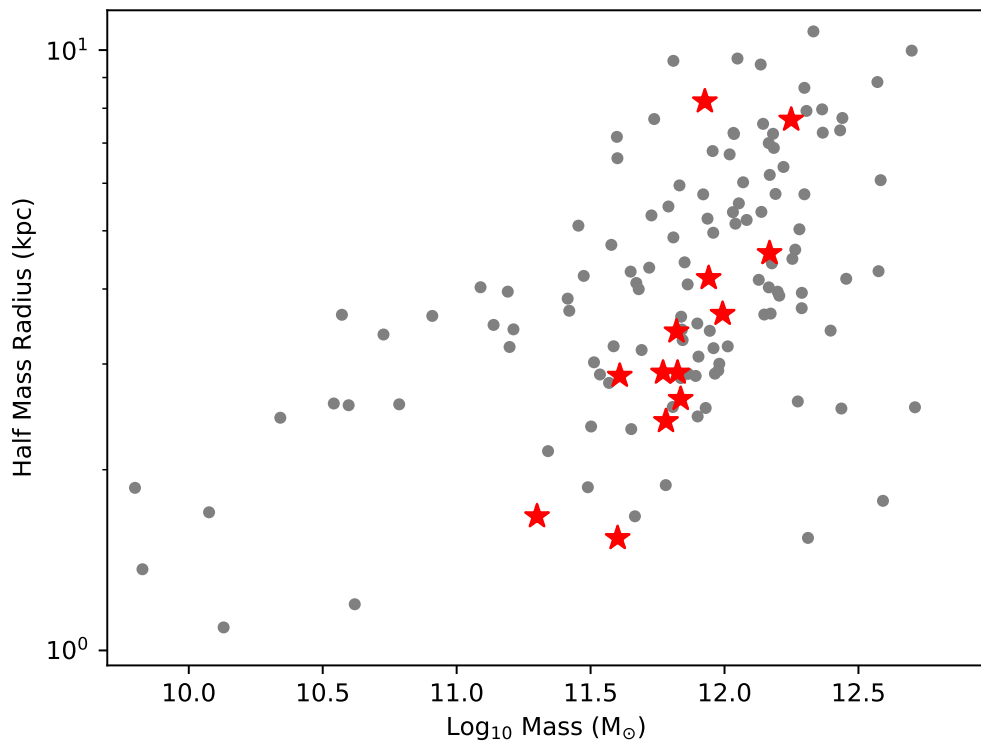


Figure C.1: Distribution of available MUSE targeted galaxies (grey dots), shown against final sample galaxies (red star) after sub-selection described in section 4.4. Distance was calculated with a simplistic Hubble law velocity calculation for non-selected galaxies. Mass and angular size were taken from 2MASS (Jarrett et al. 2003).

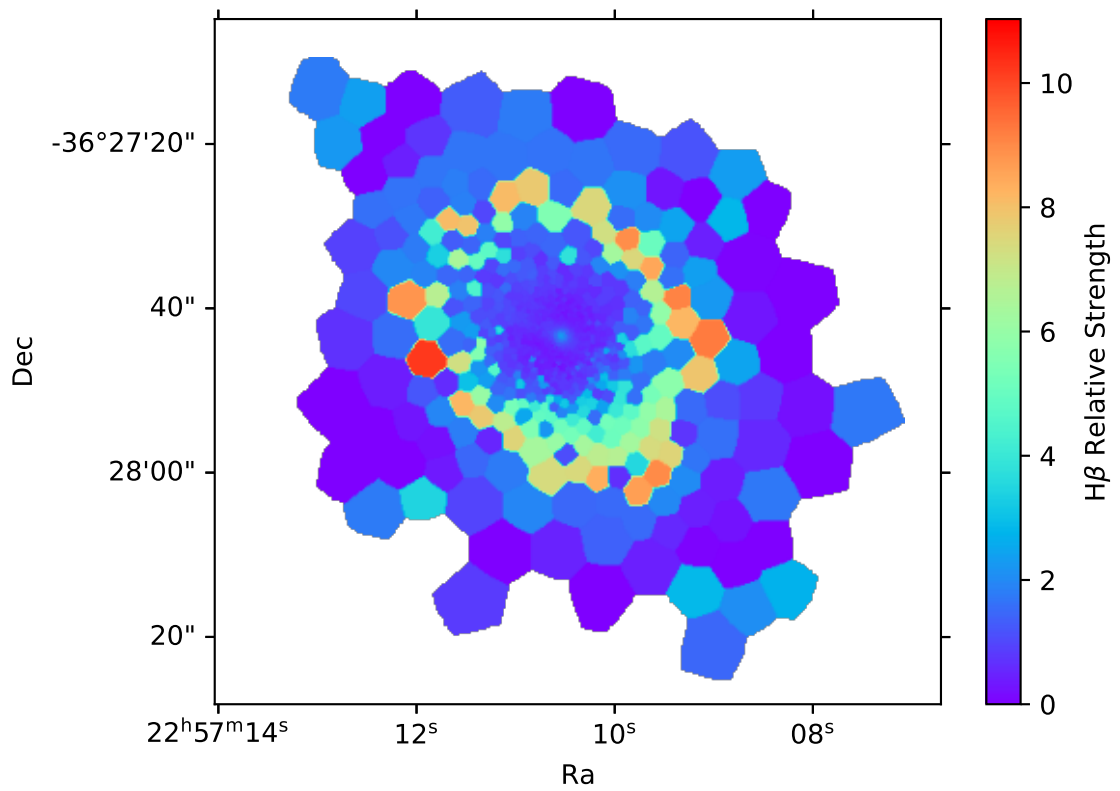


Figure C.2: H-Beta in IC 1459, showing a clear ring and matching to that seen distinctly in metallicity. Colour shows relative magnitude of H-Beta.

CHAPTER C

C.1.3 NGC1404

The elliptical galaxy NGC 1404 is located in Fornax and is one of the brighter members. NGC 1404 is known to have historical and ongoing interaction with the Fornax central galaxy NGC 1399, with a recent fly-by at around 1.1-1.3Gyr ago (Sheardown et al. 2018). The interactions between NGC 1404 and NGC 1399 appear to have resulted in the stripping of globular clusters from NGC 1404 which are now found to be associated with NGC 1399 (Bekki et al. 2003). MUSE observations of the galaxy resulted in a chance nova outburst observation seen in data taken in November 2017 (Smith 2020a). In Figure C.10 we find a double sigma spike in the centre of NGC 1404. This matches to a small area of counter-rotation also in the centre, which is the most likely cause of this double peak in dispersion.

C.1.4 NGC2992

NGC 2992 is a constituent of Arp 245, along with NGC 2993 and the dwarf galaxy A245N. NGC 2992 appears to be in the early stages of interaction (Guolo-Pereira et al. 2021). IR imaging shows a very weak stellar stream connecting NGC 2992 with NGC 2993. We see the affects of this stream in Figures C.12 and 4.6. In Figure C.12 we see younger than average populations in the lower left of the 3-6Gyr stellar age panel in the same area as the connecting stellar stream. These younger stars dilute older populations as seen in the 12-14Gyr panel. Furthermore in Figure 4.6 we see higher than average ex-situ fractions in the lower left of the panel, in the direction of the stellar stream.

C.1.5 NGC4594

NGC 4594, otherwise known as ‘The Sombrero Galaxy’ is a lenticular galaxy with an inclination of 84 degrees. Its prominent disk has made it a target of both scientific and artistic value. The dust lane presents particular challenges in full spectral fitting.

CHAPTER C

Though pPXF has advanced tools that are well equipped to deal with dust features in galaxies, the thick dust lanes in NGC 4594 appears to be too thick for pPXF to accurately handle. Residuals from the spectral fitting were on average 30% higher in the thick dusty regions, compared to residuals in the bulge. This pushed many bins above the threshold residual limit and they were excluded. This also causes issues (to a far lesser degree) in Figures of NGC 1316 and NGC 2992.

C.1.6 NGC4696

NGC 4696 is the central galaxy of the Centaurus cluster of galaxies. A clear asymmetric dust feature reaches out, visually disrupting the otherwise seemingly placid galaxy. There are also less visually distinct filaments of gas and dust seen in line-emission studies (Fabian et al. 1982; Laine et al. 2003; Sparks et al. 1989). Crawford et al. (2005) suggest the filaments are the result of buoyant gas bubbles lifting the gas from the galaxy centre, and find areas of low X-ray pressure supporting this hypothesis. Others suggest the gas features are evidence of the accretion of a gas rich galaxy (Farage et al. 2010).

C.1.7 NGC5846

NGC 5846 is a massive elliptical galaxy with a broadly spherical shape, with an axis ratio of ~ 0.95 (Jarrett et al. 2003). The galaxy is well known to be a near-by example of an AGN galaxy, with extensive studies in X-ray (Trinchieri & Goudfrooij 2002; Machacek et al. 2005). NGC 5846 is well studied largely due to both its proximity as an AGN galaxy, and its extensive globular cluster count (Forbes et al. 1996). There is strong evidence that NGC 5846 experienced a recent flyby by its visual companion, NGC 5846A. Indications hint at tidal stripping of gas and stars from a number of close companions in the associated galaxy group (Mahdavi et al. 2005; Zhu et al. 2016). In Chilingarian & Bergond (2010) a compact elliptical was identified that

CHAPTER C

had most likely been tidally stripped by NGC 5846.

C.2 Verification of Metallicity Effects

C.2.1 Eagle Simulation Verification

The methodology used to ascertain the ex-situ fractions of sample galaxies relied on an expectation of metallicity evolution with respect to ex-situ fractions, and largely ignored possible radial metallicity gradients attributed to internal mechanisms independent of the ex-situ fractions. The true interplay between in- and ex-situ populations that result in the final galaxy metallicity gradient are hugely complex and difficult to disentangle. We therefore present robust tests regarding this possible metallicity complication to ensure that our final results are valid irrespective of small underlying internal processes.

We use 718 galaxies from the EAGLE simulations (Crain et al. 2015; Schaye et al. 2015) to assess the validity of the metallicity assumptions. Galaxies were selected to be of ‘red type’ (more spheroidal and passively evolving), by selecting only galaxies with co-rotational values of $\kappa_{co} < 0.4$ (Correa et al. 2017). Galaxies were further chosen to ensure a minimum of 500 stellar particles were present within $3r_e$, and that star formation in the prior 1Gyr remained low. Each galaxy was subsequently divided into five radial bins between 0 and 5 effective radii.

For each radial bin of all galaxies, mock spectra were produced by summing weighted spectra from an AMR grid derived from stellar particles present in a galaxy radial bin. Gaussian noise was applied and spectra were convolved with Gaussian functions to replicate a spectral line width consistent with 100km/s velocity dispersion. These mock spectra were then analysed with pPXF to extract an estimated AMR. This allowed us to also ensure that degeneracy was not affecting our final results.

As it was not feasible to run simulations for each individual galaxy, ex-situ fraction was estimated using the method described in Boecker et al. (2020b). As

CHAPTER C

described in Section 4.4.2, mass dependent chemical evolution trends are used to identify which regions of the age-metallicity parameter space are likely associated with ex-situ populations. A total of 500 Monte-Carlo simulations were produced for each bin of every galaxy, providing a robust estimate to the recovered ex-situ fraction.

This recovered estimate was then measured against the true value from the EAGLE galaxies. The mean absolute difference in ex-situ estimate varied for mass bins. In the lowest and highest mass bins, ex-situ fraction was either very low or very high respectively. This allowed easy recovery of ex-situ fraction. For intermediate masses, the AMR was more complex and showed greater variation between galaxies. At the very most, the mean difference between the recovered and the true ex-situ fraction was 9.5 percentage points. Even if all galaxies in our main MUSE sample were incorrect by 9.5 percentage points, no results would be significantly affected, and a division between the ex-situ fractions of the lowest and most massive galaxies would remain.

C.2.2 Adaptive Metallicity Gradient Modelling

While galaxies show a wide diversity of radial metallicity gradients, all observations to date quantify average metallicity from the *total* stellar population light at any location (e.g., an unknown blend of in-situ and ex-situ stars). The interplay between the radial variation in ex-situ fraction that we recover, and any intrinsic radial metallicity gradients in the in-situ (and ex-situ) stars are therefore complex. We explore changes in recovery of ex-situ fractions when assuming intrinsic radial metallicity gradients, by adapting the models used as per Section 4.4.2.2. To examine possible effects in detail we have constructed a version of our analytic ex-situ fraction model grids which include spatial variations in the chemical evolution. We describe below how we use recent simulation and observational results to guide our choices

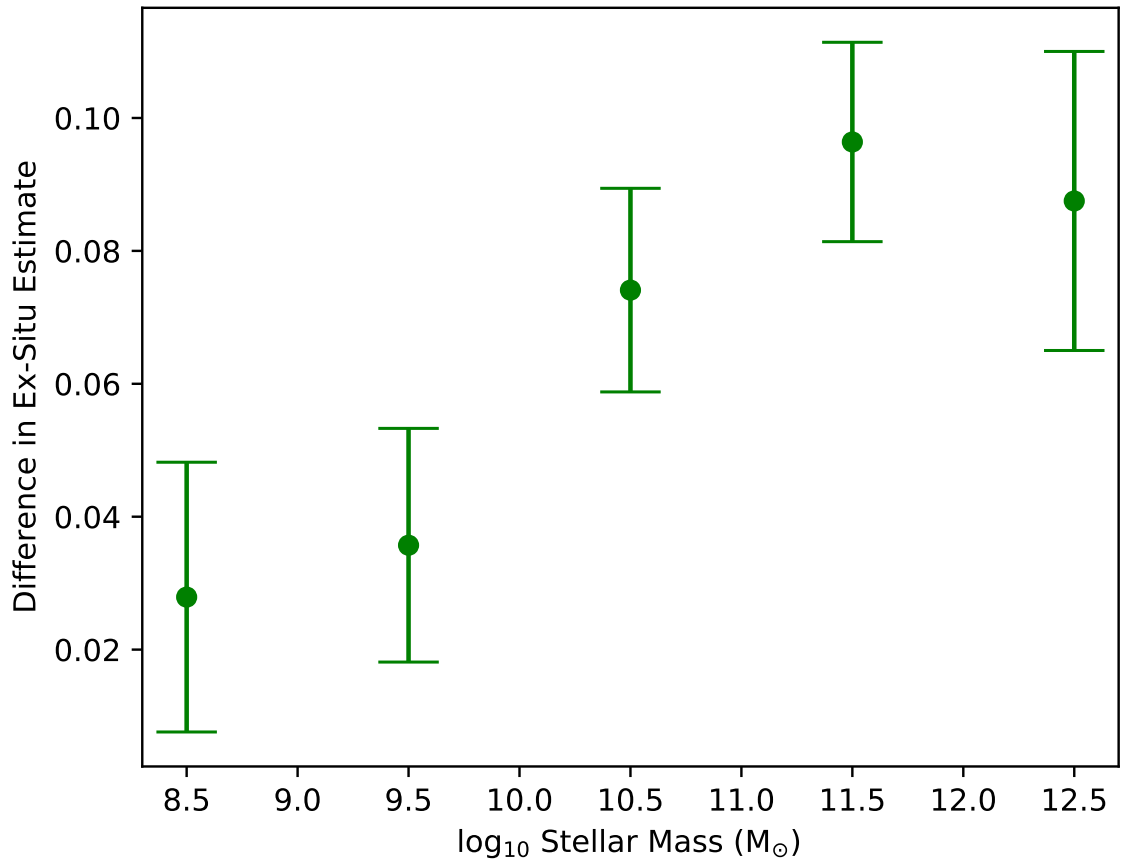


Figure C.3: Mean absolute difference of ex-situ recovery from real, shown for five stellar mass bins. A total of 718 EAGLE simulation galaxies were used, with mock spectra generated for each in 5 radial bins between 0 and 5 effective radii. The y-axis shows the value of difference between the EAGLE galaxies and the real galaxies studied in Chapter 4. Green circles indicate the mean difference in ex-situ fraction across all radial bins for all galaxies, for 5 different stellar mass bins. Error bars indicate the standard deviation in difference within the mass bin. Points are shown at the centre of their mass bin, and cover ± 0.5 dex in stellar mass.

CHAPTER C

in exploring any potential impacts of radial metallicity gradients of the in-situ and ex-situ stellar components separately.

We proceed by computing our model chemical evolution tracks for the in-situ and ex-situ stellar populations as described in Section 4.4.2.2. For a given stochastic model of many merger histories and chemical evolution histories, these produce density distributions for the ex-situ and in-situ components within the AMR grid, and these are used to decompose the returned pPXF mass fractions into ex-situ fractions. Here we simply modify this exercise to produce model density distributions of the ex-situ and in-situ components at each measured radius (0.1 R/R_e steps) within the galaxy, and modify the mean metallicity of the AMR density distributions according to a particular radial metallicity gradient.

For the in-situ component we adopt a logarithmic metallicity gradient of $d[M/H]/dR_e = -0.2$ dex/ R_e , which Zhuang et al. (2019) showed is typical for galaxies of similar mass to NGC 1380. For the ex-situ component we adopt three possible cases: i) no radial metallicity gradient, ii) the same radial metallicity gradient as the in-situ component and iii) a metallicity gradient found for only the ex-situ particles in galaxies of that mass using TNG-50 simulations (Nelson et al. (2019), Zhuang, Leaman, Pillepich, in preparation).

In each case, the final model ex-situ fraction grid was used to assign the mass density in the AMR plane (derived from pPXF) an ex-situ fraction. However this was done at every radius with a locally specified ex-situ grid tailored to that radius in each of the three cases for the radial metallicity gradients described above. The attached figure shows how these new model grids (which incorporate reasonable amounts of radial dependence on metallicity informed from observations and simulations), modify the ex-situ fraction profiles for NGC 1380. It is evident that the changes introduced by this are important, but within the systematic uncertainties due to degeneracies, regularisation, and resolution metallicity and ages of

CHAPTER C

populations. Figure C.4 shows the results of the adapted models, with coloured lines indicating the newly derived ex-situ profiles for NGC 1380. All are found to be largely within the intrinsic uncertainty, as demonstrated by the grey shaded regions.

CHAPTER C

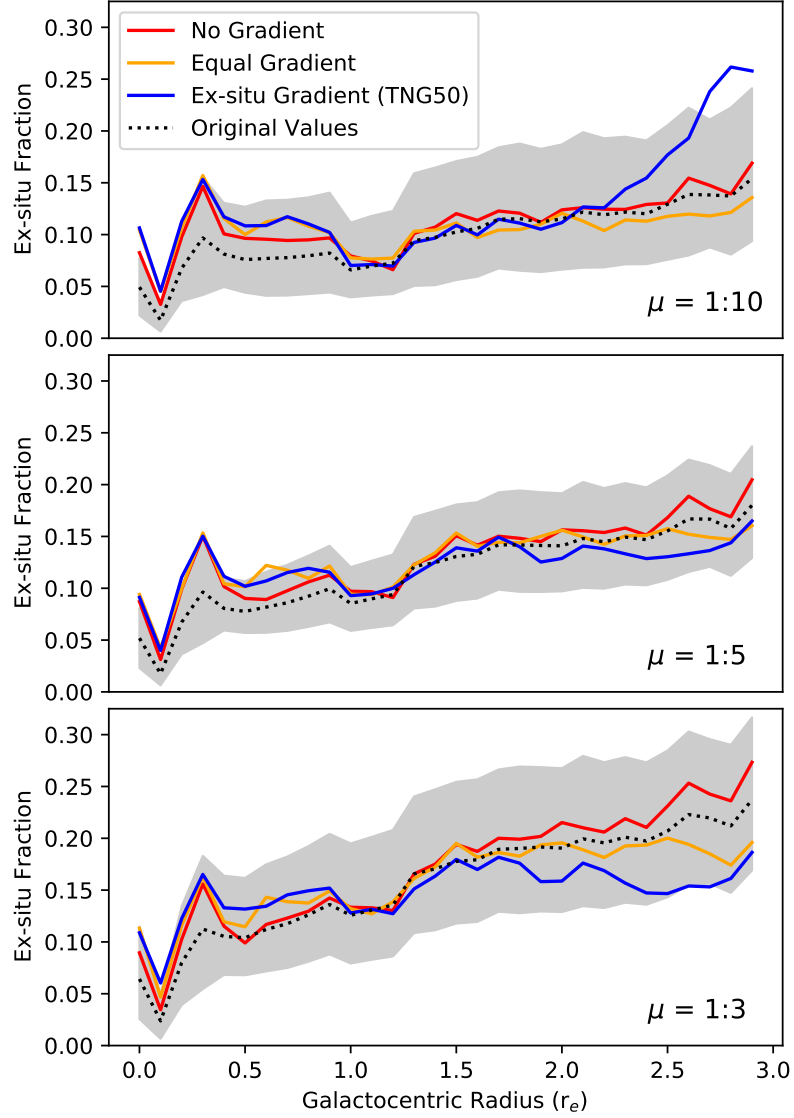


Figure C.4: Ex-situ fraction profile estimations for NGC 1380, using three different possible intrinsic metallicity gradients. The chemical evolution models were adapted according to three intrinsic metallicity cases, and their predicted ex-situ fractions were computed as described in Section 4.4.2.2. The three cases were: no radial metallicity gradient (red line); equal in-situ and ex-situ gradient magnitudes (orange line); ex-situ metallicity gradient as predicted by the TNG-50 simulations (blue line). These are overplotted on the predicted ex-situ fractions from the base models with no extra consideration of intrinsic profiles (black dotted line), with uncertainties shown with a grey highlighted region.

CHAPTER C

C.3 Galaxy Full Plots

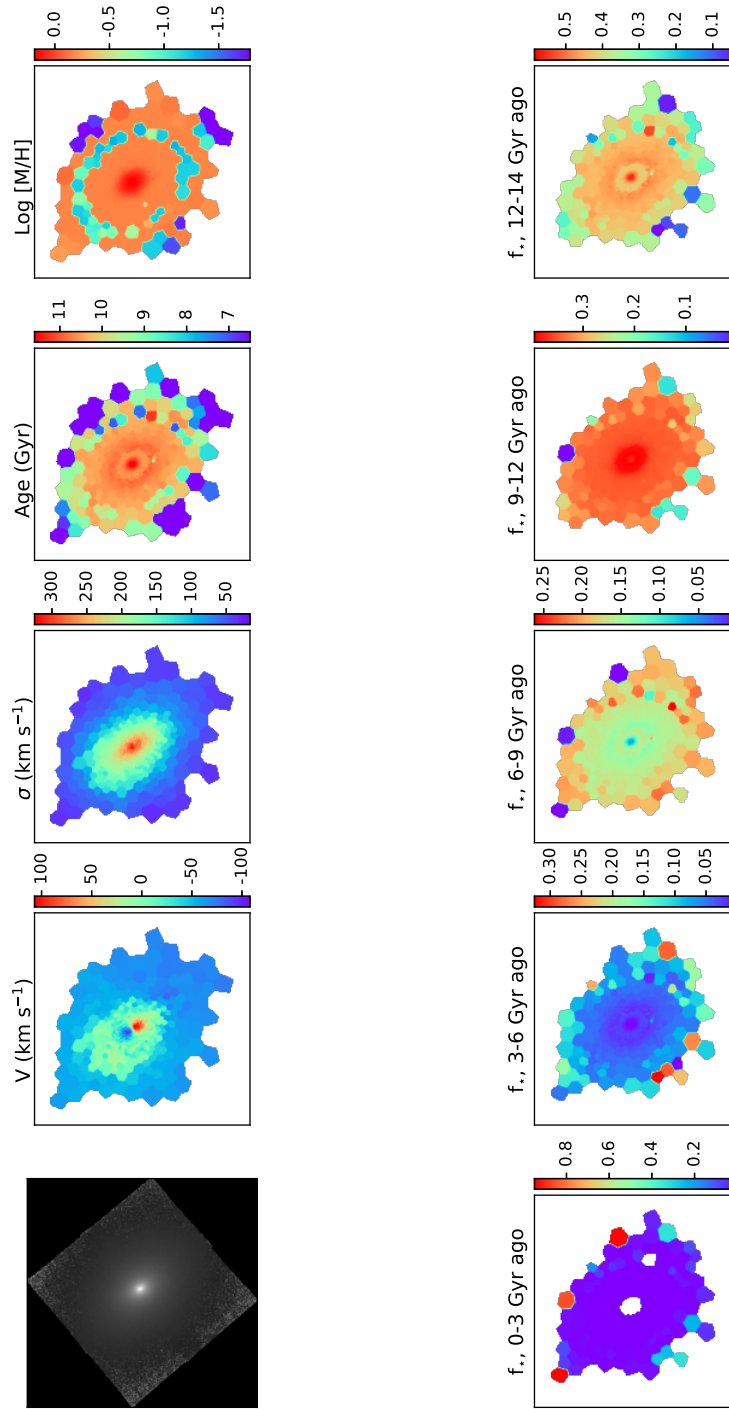


Figure C.5: IC 1459. Top left panel shows the collapsed MUSE cube. Other top row panels show stellar parameters of velocity, velocity dispersion, age, and metallicity. Lower panels show stars selected by age. Colour shows the fraction of stars in a bin that are of a specific age

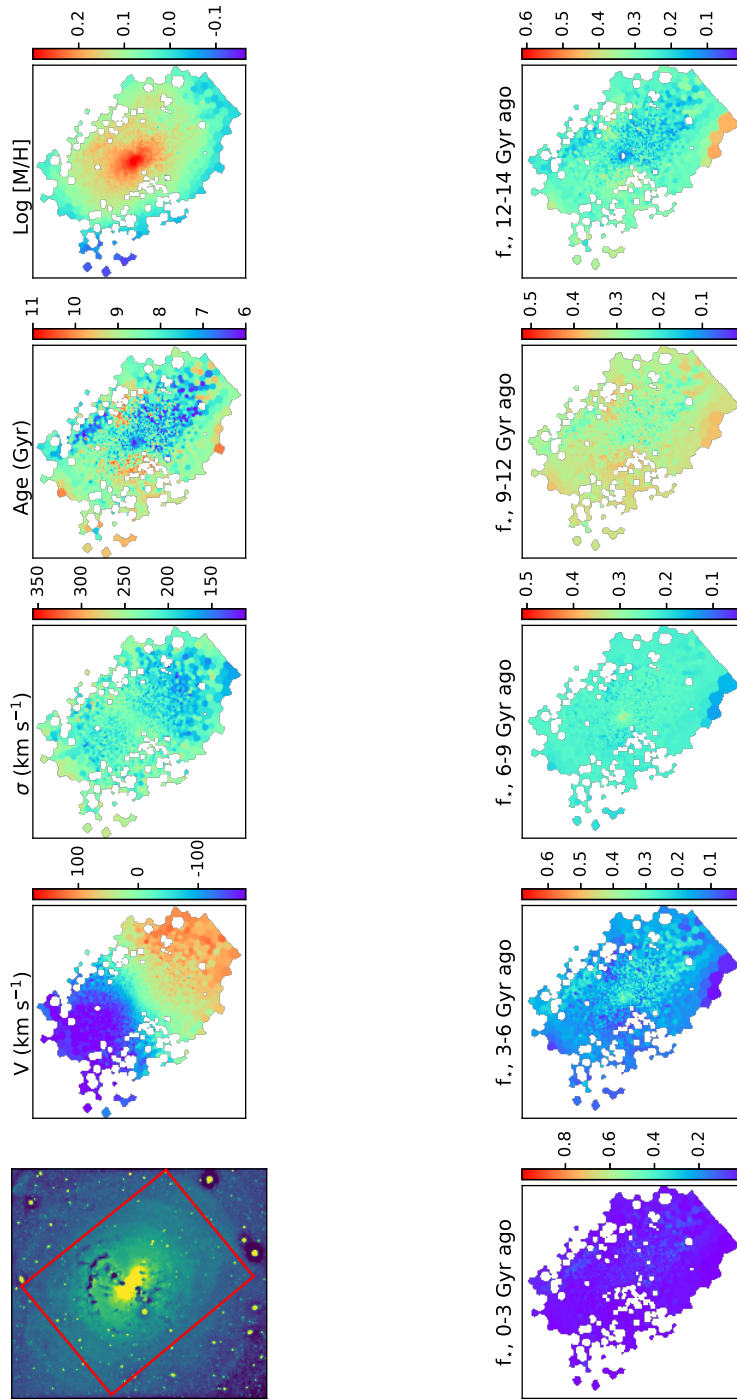


Figure C.6: NGC1316. Top left panel shows a Hubble view, with the MUSE cube footprint overlaid in red. Unsharp mask has been applied to highlight galaxy shells (unsharp amount: 25, radius: 25). Other top row panels show stellar parameters of velocity, velocity dispersion, age, and metallicity. Lower panels show stars selected by age. Colour shows the fraction of stars in a bin that are of a specific age.

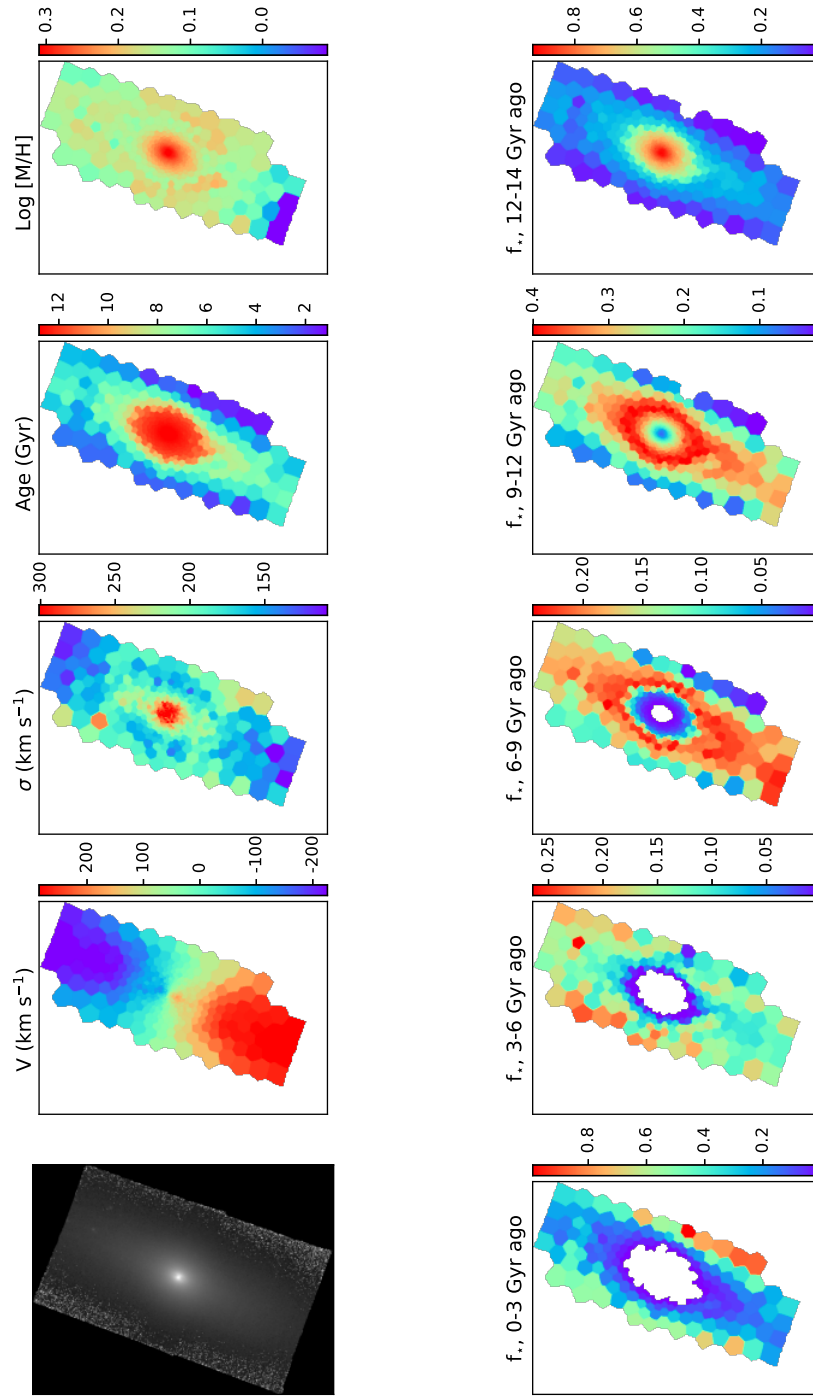


Figure C.7: NGC 1332. Top left panel shows the collapsed MUSE cube. Other top row panels show stellar parameters of velocity, velocity dispersion, age, and metallicity. Lower panels show stars selected by age. Colour shows the fraction of stars in a bin that are of a specific age

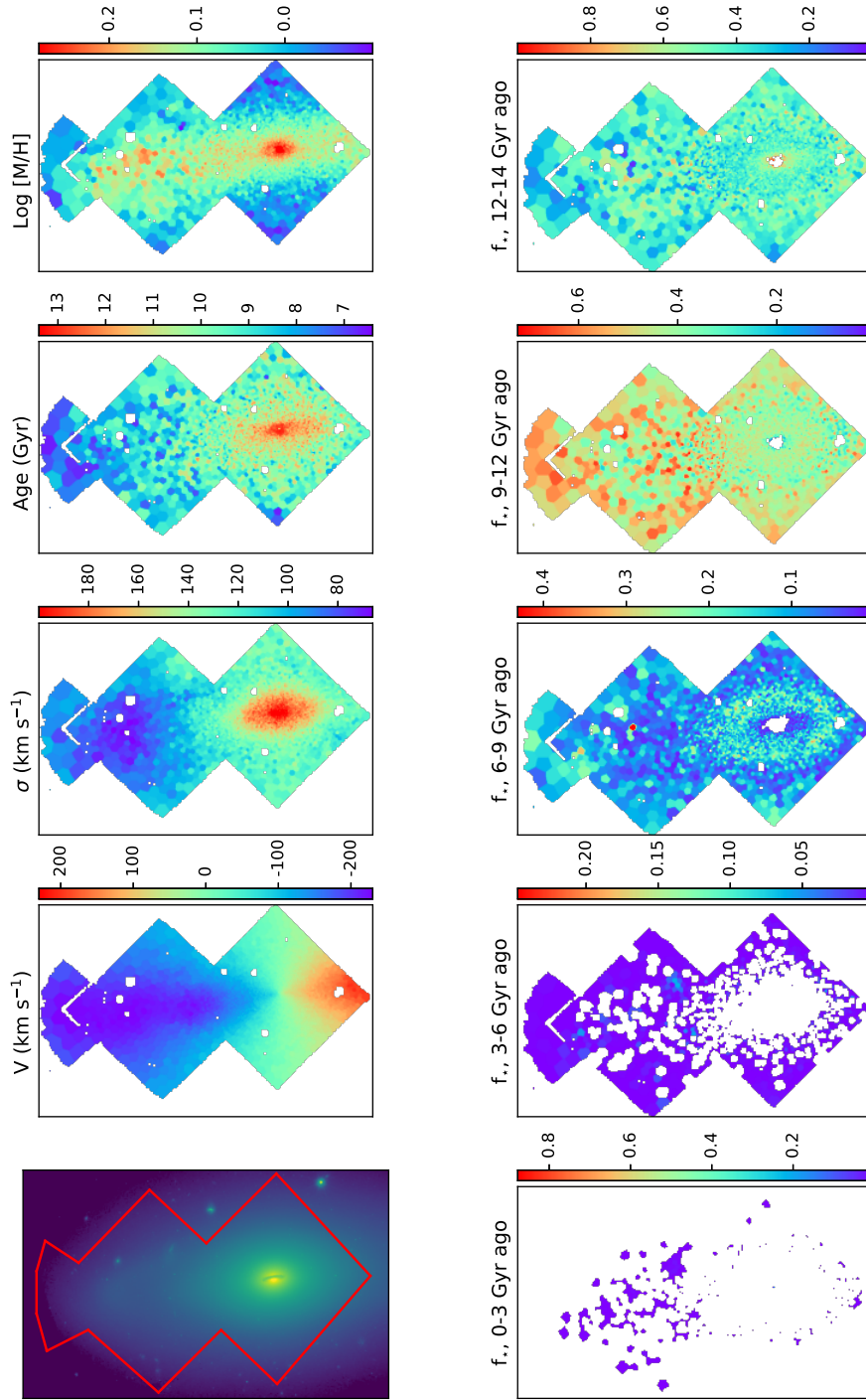


Figure C.8: NGC1380. Top left panel shows a Hubble view, with the MUSE cube footprint overlaid in red. Other top row panels show stellar parameters of velocity, velocity dispersion, age, and metallicity. Lower panels show stars selected by age. Colour shows the fraction of stars in a bin that are of a specific age.

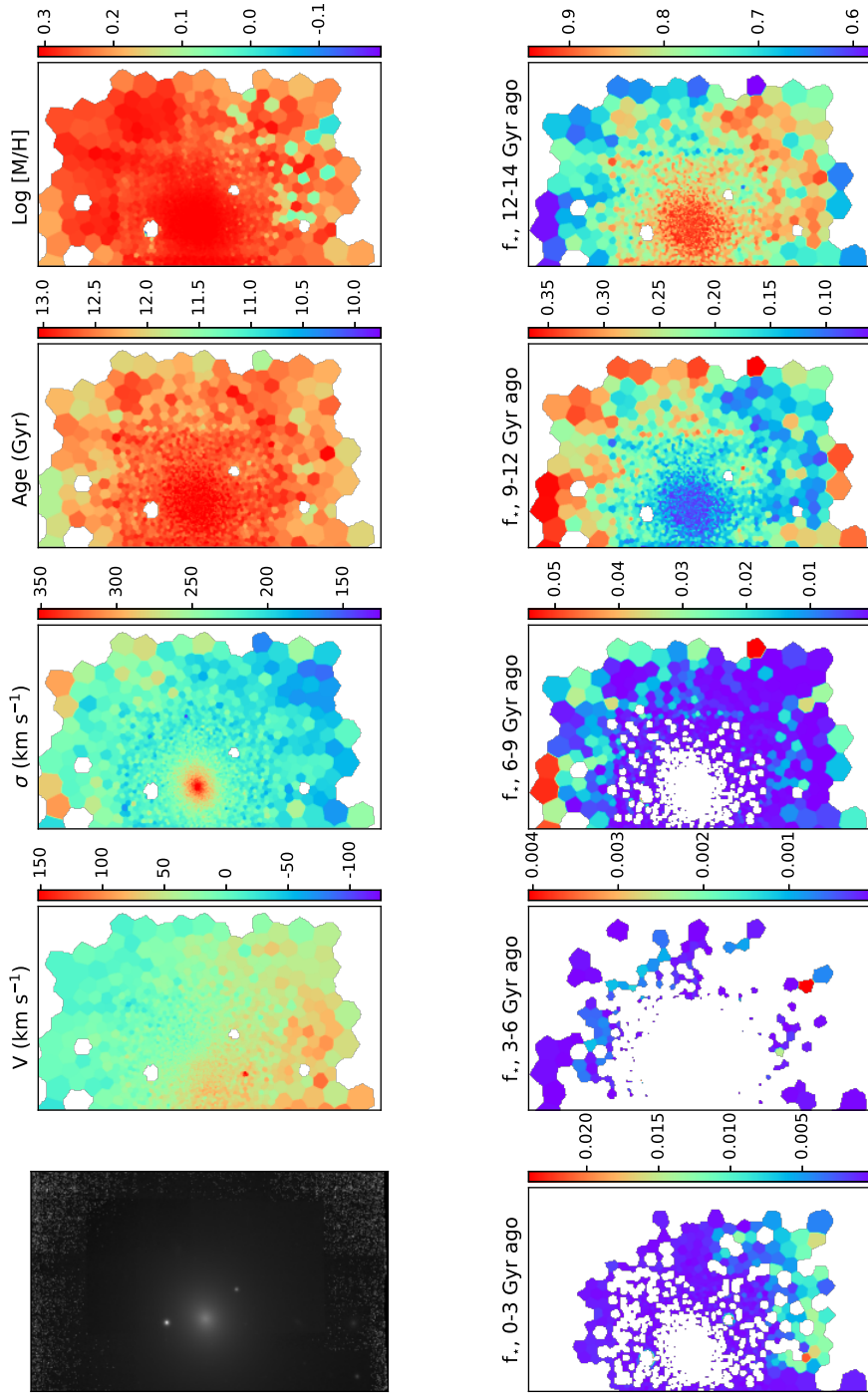


Figure C.9: NGC1399. Top left panel shows the collapsed MUSE cube. Other top row panels show stellar parameters of velocity, velocity dispersion, age, and metallicity. Lower panels show stars selected by age. Colour shows the fraction of stars in a bin that are of a specific age.

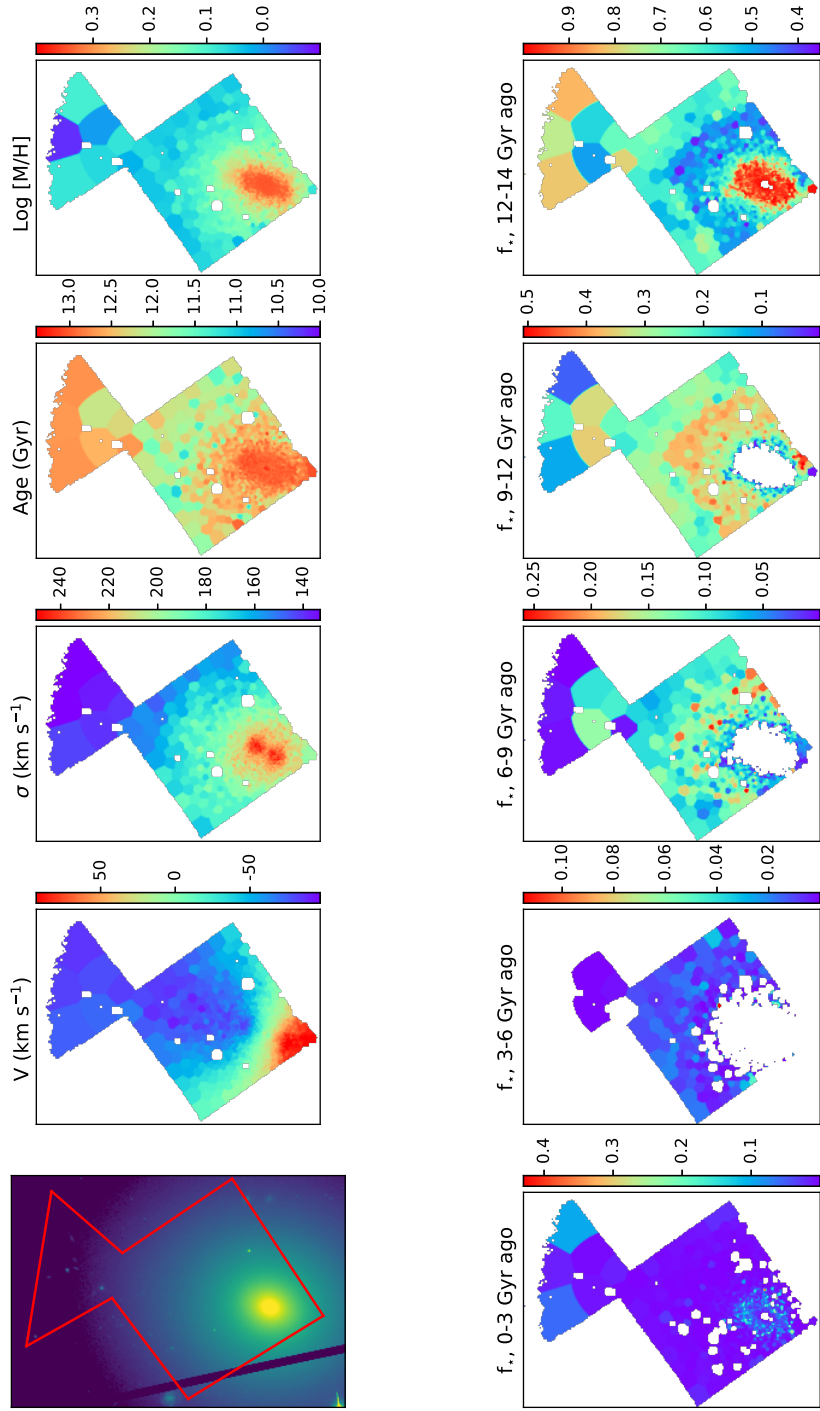


Figure C.10: NGC1404. Top left panel shows a Hubble view, with the MUSE cube footprint overlaid in red. Other top row panels show stellar parameters of velocity, velocity dispersion, age, and metallicity. Lower panels show stars selected by age. Colour shows the fraction of stars in a bin that are of a specific age.

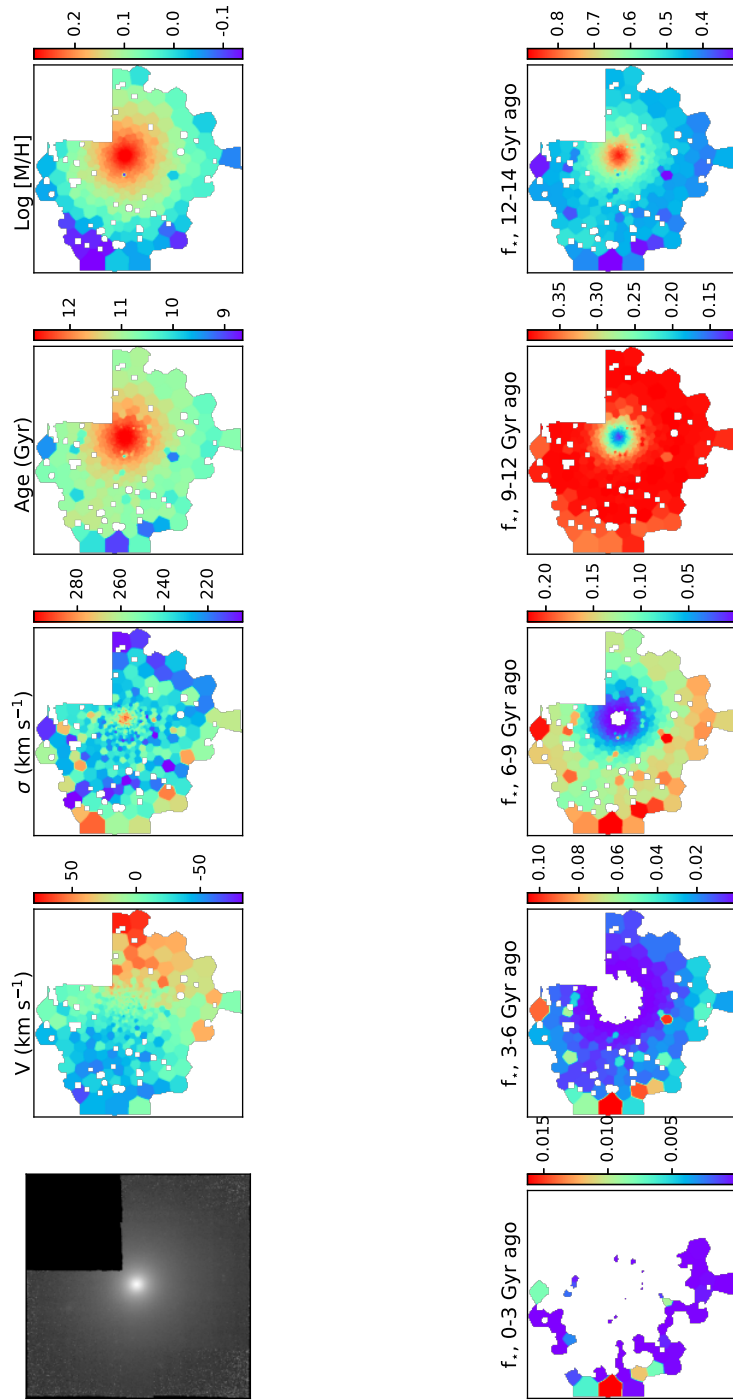


Figure C.11: NGC 1407. Top left panel shows the collapsed MUSE cube. Other top row panels show stellar parameters of velocity, velocity dispersion, age, and metallicity. Lower panels show stars selected by age. Colour shows the fraction of stars in a bin that are of a specific age.

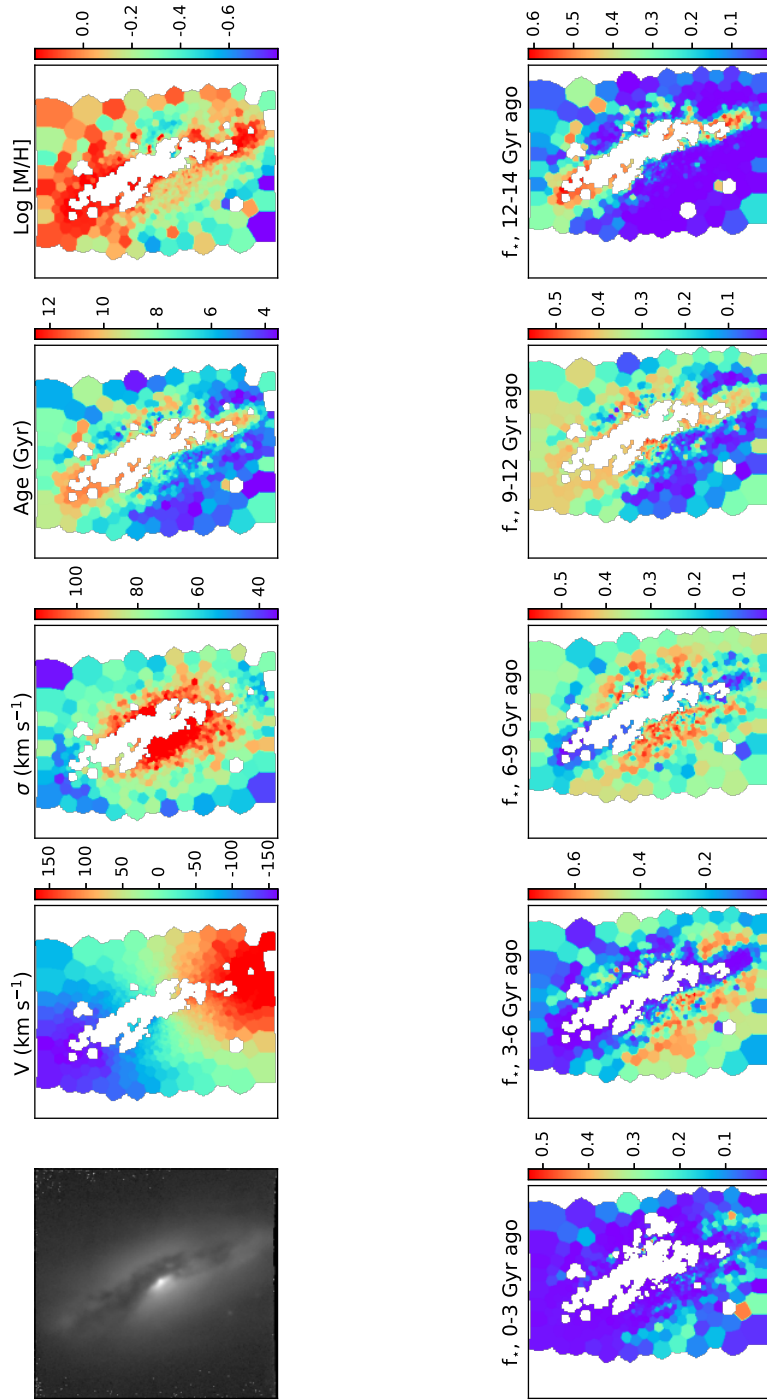


Figure C.12: NGC 2992. Top left panel shows the collapsed MUSE cube. Other top row panels show stellar parameters of velocity, velocity dispersion, age, and metallicity. Lower panels show stars selected by age. Colour shows the fraction of stars in a bin that are of a specific age.

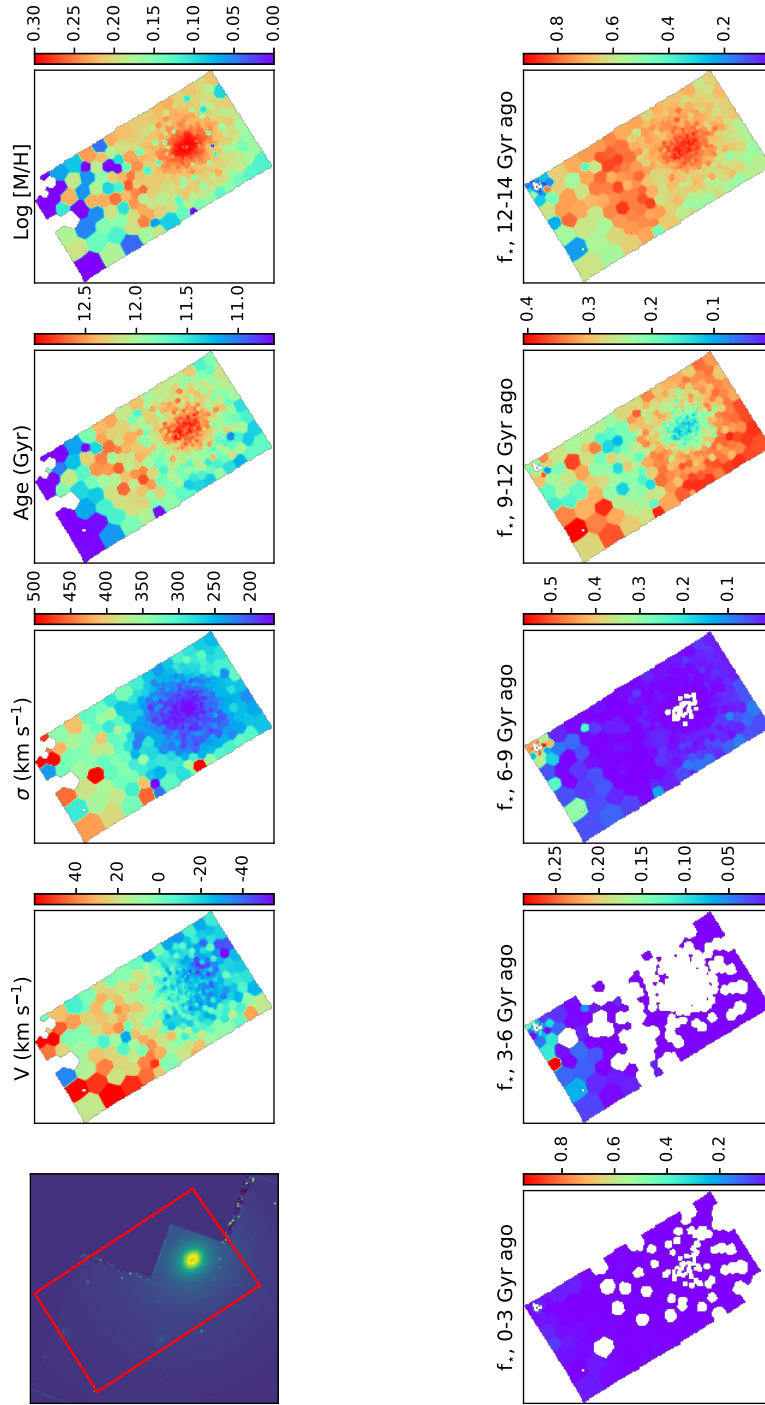


Figure C.13: NGC 3311. Top left panel shows a Hubble view, with the MUSE cube footprint overlaid in red. Other top row panels show stellar parameters of velocity, velocity dispersion, age, and metallicity. Lower panels show stars selected by age. Colour shows the fraction of stars in a bin that are of a specific age.

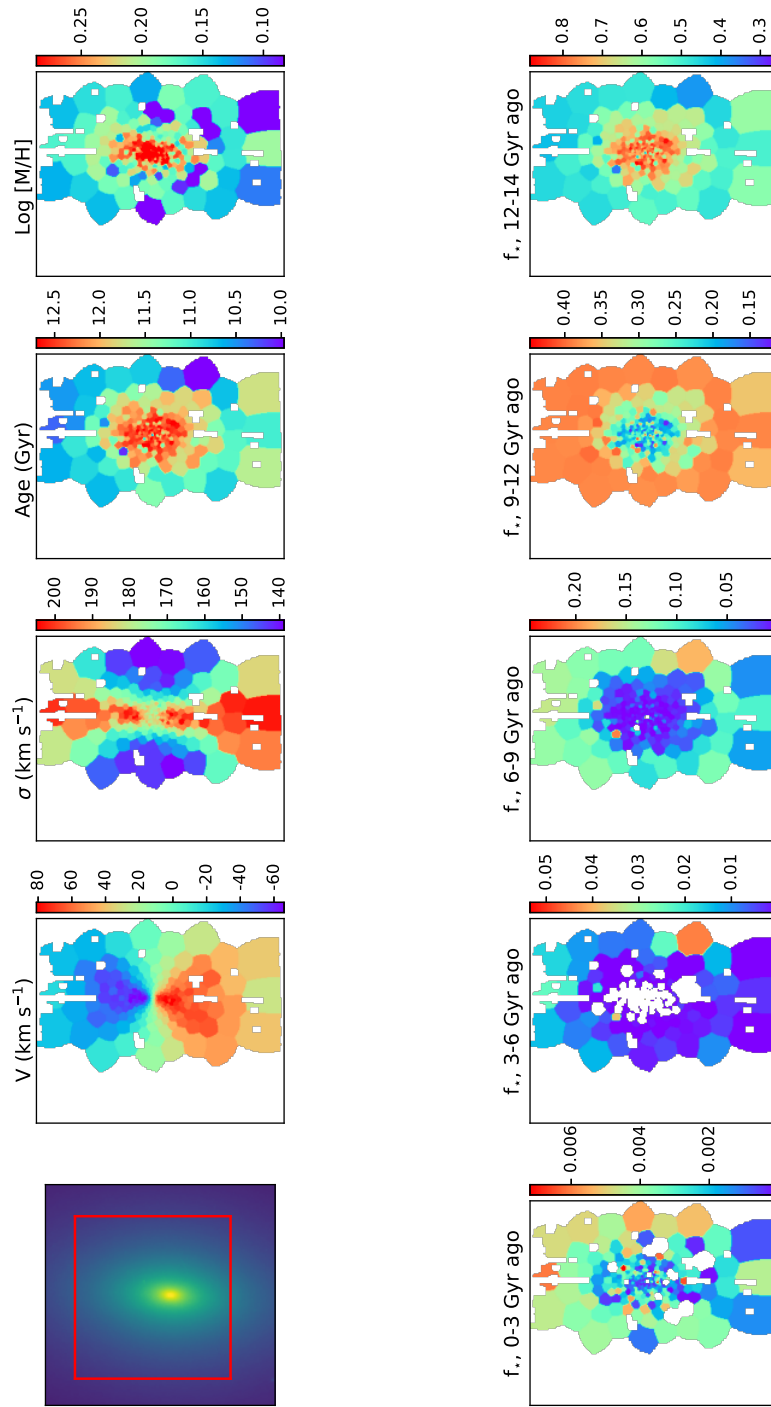


Figure C.14: NGC 4473. Top left panel shows a Hubble view, with the MUSE cube footprint overlaid in red. Other top row panels show stellar parameters of velocity, velocity dispersion, age, and metallicity. Lower panels show stars selected by age. Colour shows the fraction of stars in a bin that are of a specific age.

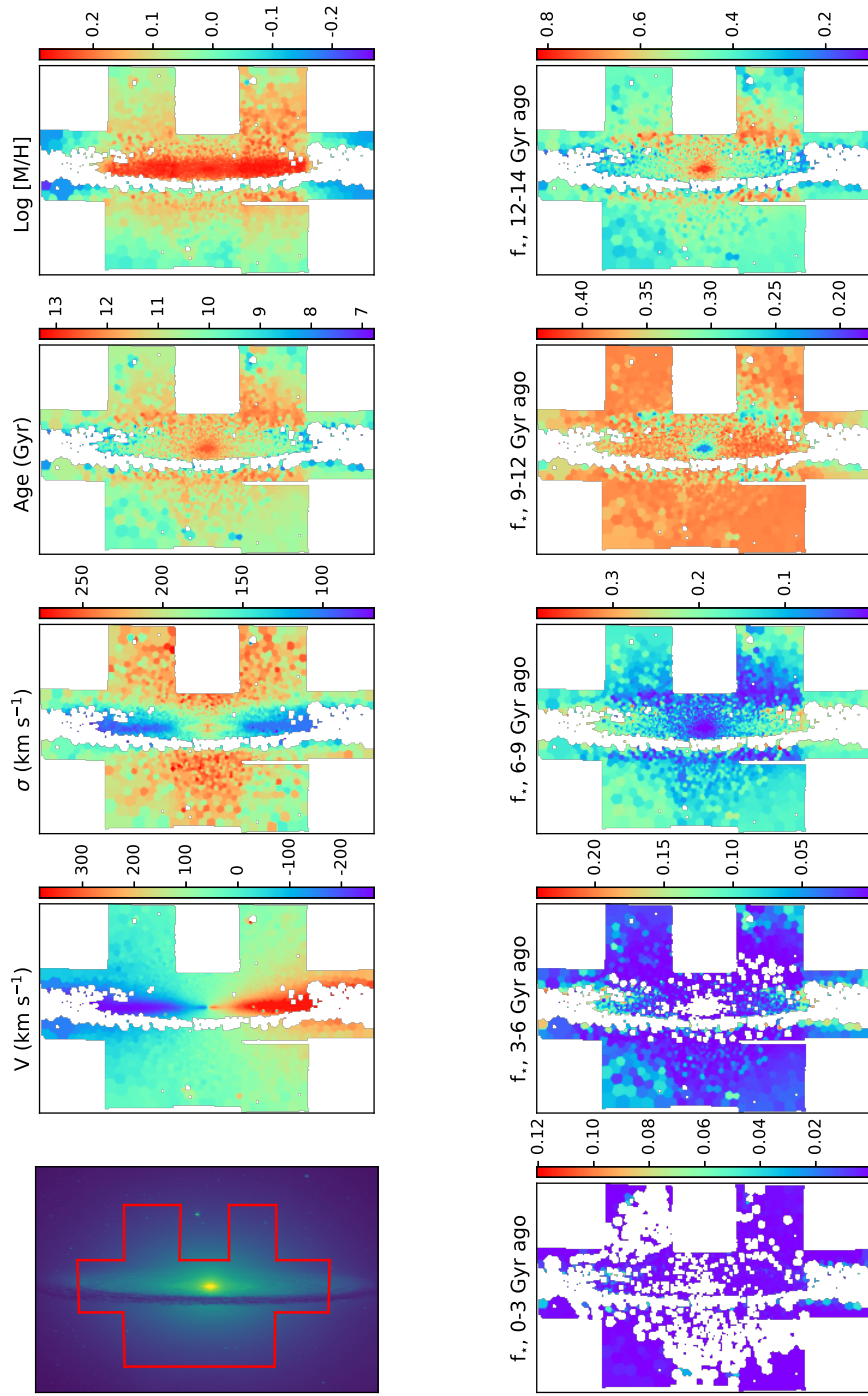


Figure C.15: NGC4594. Top left panel shows a Hubble view, with the MUSE cube footprint overlaid in red. Other top row panels show stellar parameters of velocity, velocity dispersion, age, and metallicity. Lower panels show stars selected by age. Colour shows the fraction of stars in a bin that are of a specific age.

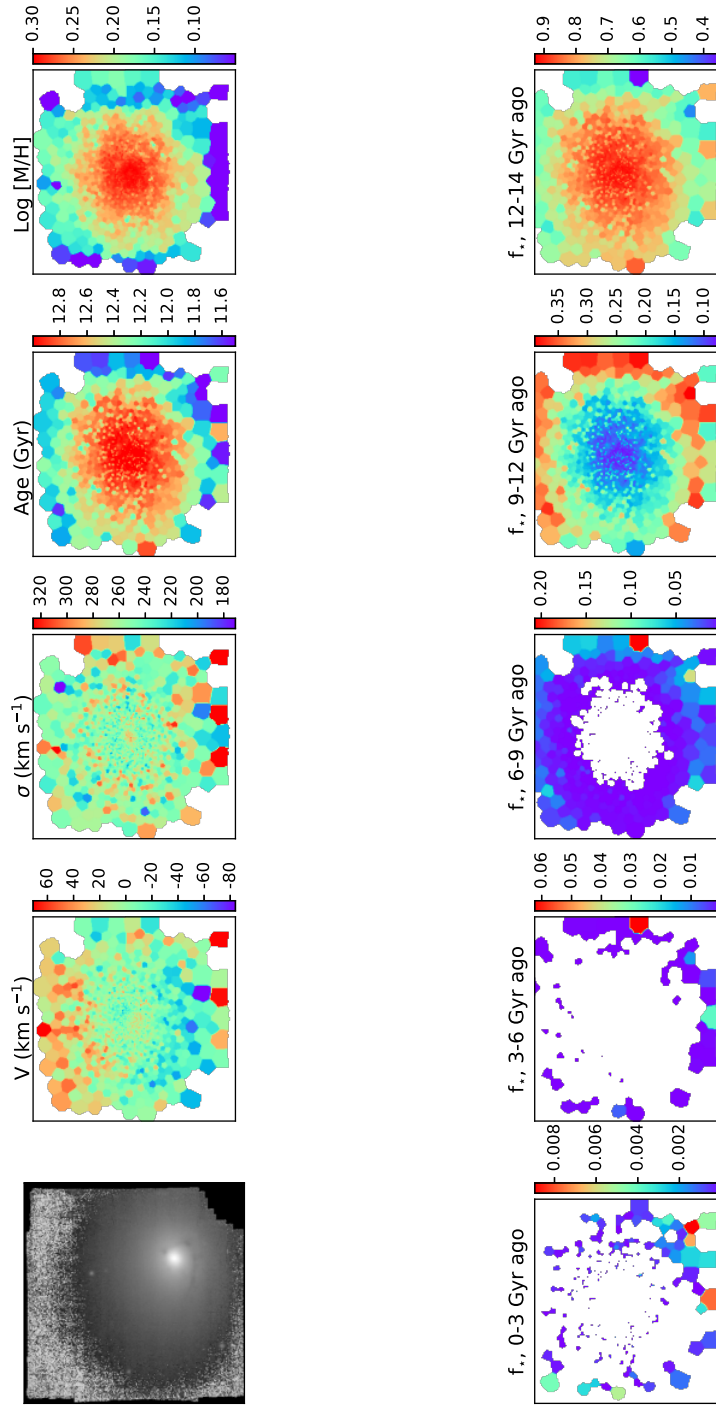


Figure C.16: NGC4696. Top left panel shows the collapsed MUSE cube. Other top row panels show stellar parameters of velocity, velocity dispersion, age, and metallicity. Lower panels show stars selected by age. Colour shows the fraction of stars in a bin that are of a specific age.

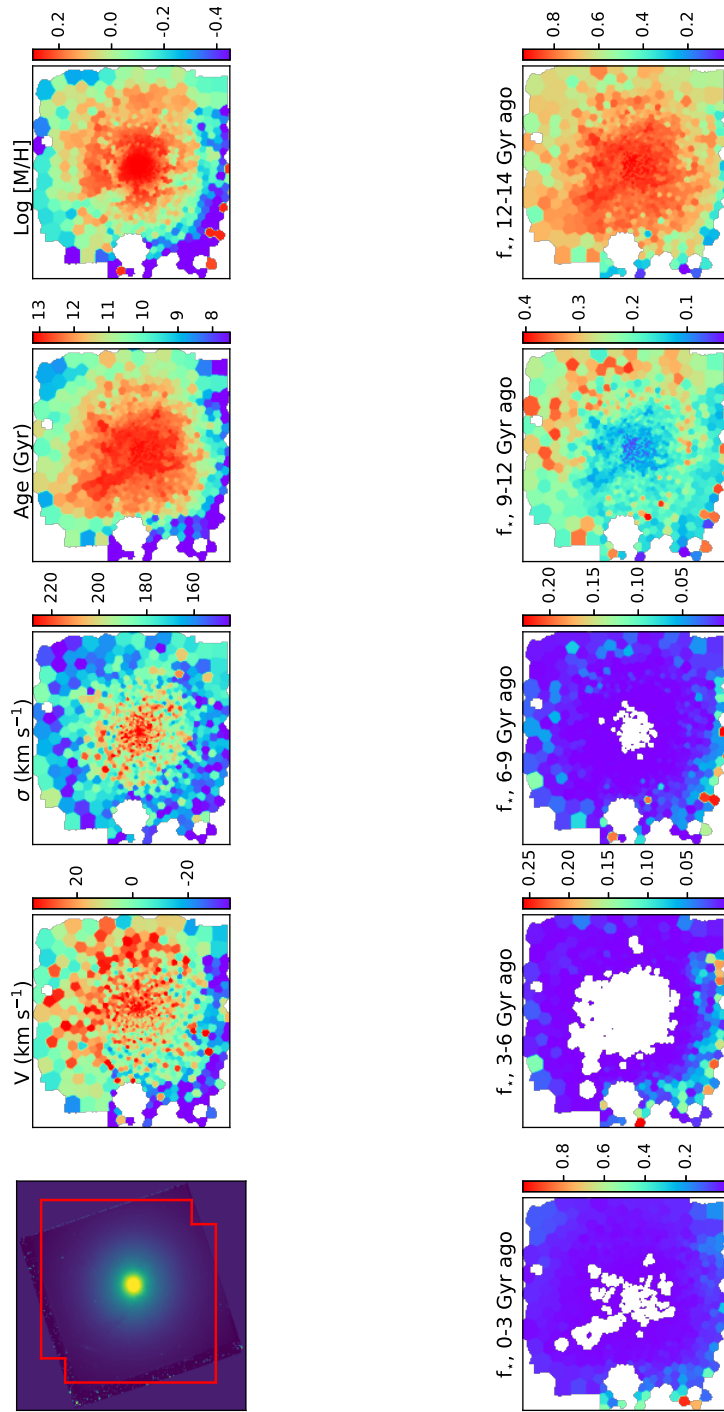


Figure C.17: NGC5846. Top left panel shows a Hubble view, with the MUSE cube footprint overlaid in red. Other top row panels show stellar parameters of velocity, velocity dispersion, age, and metallicity. Lower panels show stars selected by age. Colour shows the fraction of stars in a bin that are of a specific age.

Acknowledgements

I have far more people to acknowledge than this short portion of text could possibly contain. The work over the course of these past few years has remained tremendous fun, largely entirely due to the people I have met and talked to during the course of my studies. A huge thanks goes to my supervisor Dr Mark Norris who has supported me constantly over the past years, and whose attentiveness to his students has set me up with unrealistic standards in email reply times. A big thanks to my ESO supervisor Dr Harald Kuntschner for all his work and rapid commenting on any paper or chapters I sent his way. This work has been split across three countries so there's no way I can name everyone I would like to, but a massive thanks to the Preston crew; mis La Palma amigos, especially Belén who is my hero; and meine ESO Freunde who kept me sane during the pandemic with online beer meetings. Big thanks to my parents and family for getting me this far. Grateful acknowledgements to both Prof. Derek Ward-Thompson and the Moses Holden Studentship founder Patrick Holden for setting me up and supporting me with a studentship. Finally my hugest thanks go to Ingrid who has kept on supporting me, and who has listened to me talk about work even when she'd much rather be knitting. Lastly, a big shout-out to the Coronavirus pandemic for keeping me locked in a 12m² apartment for about a year. Probably made me focus on writing a bit more, but I will never forgive you for cancelling Oktoberfest. Speaking of which, I'm off for a beer.

Bibliography

- Ade, P. A., Ahmed, Z., Aikin, R., et al. 2016, Physical review letters
- Aguado, D., Ahumada, R., Almeida, A., et al. 2018, arXiv preprint arXiv:1812.02759
- Ahumada, R., Prieto, C. A., Almeida, A., et al. 2020, The Astrophysical Journal Supplement Series, 249, 3
- Aihara, H., Armstrong, R., Bickerton, S., et al. 2018, Publications of the Astronomical Society of Japan, 70, S8
- Alamo-Martínez, K. A., Chies-Santos, A. L., Beasley, M. A., et al. 2021, Monthly Notices of the Royal Astronomical Society, 503, 2406
- Annibali, F., Bressan, A., Rampazzo, R., et al. 2010, Astronomy & Astrophysics, 519, A40
- Arnold, J. A., Romanowsky, A. J., Brodie, J. P., et al. 2011, The Astrophysical Journal Letters, 736, L26
- Auger, M., Treu, T., Brewer, B., & Marshall, P. 2011, Monthly Notices of the Royal Astronomical Society: Letters, 411, L6
- Bacon, R., Accardo, M., Adjali, L., et al. 2010, *Proceedings of the SPIE.*, 7735, 773508
- Bacon, R., Copin, Y., Monnet, G., et al. 2001, *Mon. Not. Roy. Astron. Soc.*, 326, 23
- Bacon, R., Piqueras, L., Conseil, S., Richard, J., & Shepherd, M. 2016, MPDAF: MUSE Python Data Analysis Framework
- Bacon, R., Vernet, J., Borisova, E., et al. 2014, The Messenger, 157, 13
- Bahcall, N. A., Gramann, M., & Cen, R. 1994, *Astrophys. J.*, 436, 23
- Baldry, I. K., Glazebrook, K., Brinkmann, J., et al. 2004, The Astrophysical Journal, 600, 681
- Baldwin, C., McDermid, R., Kuntschner, H., Maraston, C., & Conroy, C. 2018, Monthly Notices of the Royal Astronomical Society, 473, 4698
- Baldwin, J. A., Phillips, M. M., & Terlevich, R. 1981, Publications of the Astronomical Society of the Pacific, 93, 5
- Barnes, J. & Hut, P. 1986, nature, 324, 446
- Barr, J., Bedregal, A., Aragón-Salamanca, A., Merrifield, M., & Bamford, S. 2007, Astronomy & Astrophysics, 470, 173
- Barrera-Ballesteros, J., García-Lorenzo, B., Falcón-Barroso, J., et al. 2015, Astronomy & Astrophysics, 582, A21
- Barro, G., Faber, S., Pérez-González, P. G., et al. 2013, The Astrophysical Journal, 765, 104
- Bassett, R., Bekki, K., Cortese, L., & Couch, J.,

- W. 2017, *Monthly Notices of the Royal Astronomical Society*, 471, 1892
- Beasley, M. A., Trujillo, I., Leaman, R., & Montes, M. 2018, *Nature*, 555, 483
- Beckwith, S. V., Stiavelli, M., Koekemoer, A. M., et al. 2006, *The Astronomical Journal*, 132, 1729
- Bekki, K. 2001, *Astrophysics and Space Science*, 276, 847
- Bekki, K., Forbes, D. A., Beasley, M. A., & Couch, W. J. 2003, *Mon. Not. Roy. Astron. Soc.*, 344, 1334
- Bell, E. F. & de Jong, R. S. 2001, *The Astrophysical Journal*, 550, 212
- Belli, S., Newman, A. B., & Ellis, R. S. 2015, *The Astrophysical Journal*, 799, 206
- Belokurov, V., Zucker, D. B., Evans, N. W., et al. 2006, *Astrophys. J. Letters*, 642, L137
- Bernard, E. J., Ferguson, A. M., Schlafly, E. F., et al. 2014, *Monthly Notices of the Royal Astronomical Society: Letters*, 443, L84
- Bertola, F., Buson, L., & Zeilinger, W. W. 1988, *Nature*, 335, 705
- Bezanson, R., Van Dokkum, P. G., Tal, T., et al. 2009, *The Astrophysical Journal*, 697, 1290
- Bigiel, F., Leroy, A., Walter, F., et al. 2011, *The Astrophysical Journal Letters*, 730, L13
- Boecker, A., Alfaro-Cuello, M., Neumayer, N., Martín-Navarro, I., & Leaman, R. 2020a, *The Astrophysical Journal*, 896, 13
- Boecker, A., Leaman, R., van de Ven, G., et al. 2020b, *Monthly Notices of the Royal Astronomical Society*, 491, 823
- Bournaud, F., Jog, C., & Combes, F. 2005, *Astronomy & Astrophysics*, 437, 69
- Boylan-Kolchin, M., Bullock, J. S., & Kaplinghat, M. 2011, *Monthly Notices of the Royal Astronomical Society: Letters*, 415, L40
- Bressan, A., Marigo, P., Girardi, L., et al. 2012, *Monthly Notices of the Royal Astronomical Society*, 427, 127
- Brodie, J. P. & Strader, J. 2006, *Annu. Rev. Astron. Astrophys.*, 44, 193
- Bryant, J., Croom, S., Van De Sande, J., et al. 2019, *Monthly Notices of the Royal Astronomical Society*, 483, 458
- Bundy, K., Bershady, M. A., Law, D. R., et al. 2014, *The Astrophysical Journal*, 798, 7
- Bundy, K., Fukugita, M., Ellis, R. S., et al. 2009, *The Astrophysical Journal*, 697, 1369
- Cales, S. L. & Brotherton, M. S. 2015, *Monthly Notices of the Royal Astronomical Society*, 449, 2374
- Capelo, P. R. & Dotti, M. 2017, *Monthly Notices of the Royal Astronomical Society*, 465, 2643
- Capelo, P. R., Volonteri, M., Dotti, M., et al. 2015, *Monthly Notices of the Royal Astronomical Society*, 447, 2123
- Cappellari, M. 2013, *The Astrophysical Journal Letters*, 778, L2
- Cappellari, M. 2017, *Mon. Not. Roy. Astron. Soc.*, 466, 798
- Cappellari, M. & Copin, Y. 2003, *Monthly Notices of the Royal Astronomical Society*, 342, 345

- Cappellari, M. & Emsellem, E. 2004, *Publications of the ASP.*, 116, 138
- Cappellari, M., McDermid, R. M., Alatalo, K., et al. 2013, *Monthly Notices of the Royal Astronomical Society*, 432, 1862
- Cappellari, M., Verolme, E., Van Der Marel, R., et al. 2002, *The Astrophysical Journal*, 578, 787
- Carraro, G. & Chiosi, C. 1994, *Astronomy and Astrophysics*, 287, 761
- Carraro, G., Ng, Y. K., & Portinari, L. 1998, *Monthly Notices of the Royal Astronomical Society*, 296, 1045
- Cassisi, S., Pietrinferni, A., Salaris, M., et al. 2005, arXiv preprint astro-ph/0509543
- Chabrier, G. 2003, *Publications of the Astronomical Society of the Pacific*, 115, 763
- Chilingarian, I. V. & Bergond, G. 2010, *Monthly Notices of the Royal Astronomical Society: Letters*, 405, L11
- Choi, E., Ostriker, J. P., Naab, T., Oser, L., & Moster, B. P. 2015, *Monthly Notices of the Royal Astronomical Society*, 449, 4105
- Choksi, N., Gnedin, O. Y., & Li, H. 2018, *Monthly Notices of the Royal Astronomical Society*, 480, 2343
- Cid Fernandes, R., González Delgado, R., Storchi-Bergmann, T., Martins, L. P., & Schmitt, H. 2005, *Monthly Notices of the Royal Astronomical Society*, 356, 270
- Cid Fernandes, R., Mateus, A., Sodré, L., Stasińska, G., & Gomes, J. M. 2005, *Mon. Not. Roy. Astron. Soc.*, 358, 363
- Ciotti, L. 1991, *Astronomy and Astrophysics*, 249, 99
- Ciotti, L. & Bertin, G. 1999, *Astron. Astrophys.*, 352, 447
- Claret, A. & Torres, G. 2016, *Astronomy & Astrophysics*, 592, A15
- Clauwens, B., Schaye, J., & Franx, M. 2016, *Monthly Notices of the Royal Astronomical Society*, 462, 2832
- Clauwens, B., Schaye, J., Franx, M., & Bower, R. G. 2018, *Mon. Not. Roy. Astron. Soc.*, 478, 3994
- Cleveland, W. S. & Devlin, S. J. 1988, *JASA*, 83, 596
- Coccatto, L., Fabricius, M., Morelli, L., et al. 2015, *Astronomy & Astrophysics*, 581, A65
- Collaboration, P., Ade, P., Aghanim, N., Armitage-Caplan, C., et al. 2014, *Astron. Astrophys.*, 571, A16
- Colless, M. et al. 2003, arXiv preprint astro-ph/0306581
- Comerón, S., Salo, H., Janz, J., Laurikainen, E., & Yoachim, P. 2015, *Astron. Astrophys.*, 584, A34
- Conroy, C. & Gunn, J. E. 2010, *The Astrophysical Journal*, 712, 833
- Conroy, C., Gunn, J. E., & White, M. 2009a, *The Astrophysical Journal*, 699, 486
- Conroy, C., White, M., & Gunn, J. E. 2009b, *The Astrophysical Journal*, 708, 58
- Cook, B., Conroy, C., Pillepich, A., Rodriguez-Gomez, V., & Hernquist, L. 2016, *The Astrophysical Journal*, 833, 158

- Cordier, D., Pietrinferni, A., Cassisi, S., & Salaris, M. 2007, *Astron. J.*, 133, 468
- Correa, C. A., Schaye, J., Clauwens, B., et al. 2017, *Mon. Not. Roy. Astron. Soc.*, 472, L45
- Cortesi, A., Merrifield, M., Coccato, L., et al. 2013, *Monthly Notices of the Royal Astronomical Society*, 432, 1010
- Crain, R. A., Schaye, J., Bower, R. G., et al. 2015, *MNRAS*, 450, 1937
- Crawford, C., Hatch, N., Fabian, A., & Sanders, J. 2005, *Monthly Notices of the Royal Astronomical Society*, 363, 216
- Crnojević, D., Sand, D., Bennet, P., et al. 2019, *The Astrophysical Journal*, 872, 80
- Crnojević, D., Sand, D., Spekkens, K., et al. 2016, *The Astrophysical Journal*, 823, 19
- Daddi, E., Renzini, A., Pirzkal, N., et al. 2005, *The Astrophysical Journal*, 626, 680
- Dalcanton, J. J., Williams, B. F., Lang, D., et al. 2012, *The Astrophysical Journal Supplement Series*, 200, 18
- Damjanov, I., McCarthy, P. J., Abraham, R. G., et al. 2009, *The Astrophysical Journal*, 695, 101
- Davis, T. A., Alatalo, K., Sarzi, M., et al. 2011, *Monthly Notices of the Royal Astronomical Society*, 417, 882
- Davison, T. A., Kuntschner, H., Husemann, B., et al. 2021a, *Monthly Notices of the Royal Astronomical Society*, 502, 2296
- Davison, T. A., Norris, M. A., Leaman, R., et al. 2021b, *Monthly Notices of the Royal Astronomical Society*, 507, 3089
- Davison, T. A., Norris, M. A., Pfeffer, J. L., Davies, J. J., & Crain, R. A. 2020, *Monthly Notices of the Royal Astronomical Society*, 497, 81
- Delgado, R. M. G. & Fernandes, R. C. 2010, *Monthly Notices of the Royal Astronomical Society*, 403, 797
- Di Matteo, P., Bournaud, F., Martig, M., et al. 2008, *Astronomy & Astrophysics*, 492, 31
- Dolfi, A., Forbes, D. A., Couch, W. J., et al. 2020, *Monthly Notices of the Royal Astronomical Society*, 495, 1321
- dos Reis, S. N., Buitrago, F., Papaderos, P., et al. 2020, *Astronomy & Astrophysics*, 634, A11
- Dotter, A., Chaboyer, B., Jevremović, D., et al. 2008, *The Astrophysical Journal Supplement Series*, 178, 89
- Du, M., Debattista, V. P., Ho, L. C., et al. 2019, *The Astrophysical Journal*, 875, 58
- Dubois, Y., Pichon, C., Welker, C., et al. 2014, *MNRAS*, 444, 1453
- Duc, P.-A., Cuillandre, J.-C., Karabal, E., et al. 2015, *Monthly Notices of the Royal Astronomical Society*, 446, 120
- Ebeling, H., Stephenson, L. N., & Edge, A. C. 2014, *The Astrophysical Journal Letters*, 781, L40
- Edwards, L. O., Salinas, M., Stanley, S., et al. 2020, *Monthly Notices of the Royal Astronomical Society*, 491, 2617
- Eliche-Moral, M. d. C., Rodríguez-Pérez, C., Borlaff, A., Querejeta, M., & Tapia, T. 2018,

- Astronomy & Astrophysics, 617, A113
- Ellison, S. L., Mendel, J. T., Scudder, J. M., Patton, D. R., & Palmer, M. J. 2013, Monthly Notices of the Royal Astronomical Society, 430, 3128
- Fabian, A., Atherton, P., Taylor, K., & Nulsen, P. 1982, Monthly Notices of the Royal Astronomical Society, 201, 17P
- Fahrion, K., Lyubenova, M., Hilker, M., et al. 2020, Astronomy & Astrophysics, 637, A27
- Faifer, F. R., Escudero, C. G., Scalia, M. C., et al. 2017, *Astron. Astrophys.*, 599, L8
- Faifer, F. R., Forte, J. C., Norris, M. A., et al. 2011, Monthly Notices of the Royal Astronomical Society, 416, 155
- Fakhouri, O., Ma, C.-P., & Boylan-Kolchin, M. 2010, Monthly Notices of the Royal Astronomical Society, 406, 2267
- Falc3n-Barroso, J., S3nchez-Bl3zquez, P., Vazdekis, A., et al. 2011, Astronomy & Astrophysics, 532, A95
- Farage, C., McGregor, P., Dopita, M., & Bicknell, G. 2010, The Astrophysical Journal, 724, 267
- Fasano, G., Poggianti, B. M., Couch, W. J., et al. 2000, The Astrophysical Journal, 542, 673
- Fernandes, R. C. & Delgado, R. M. G. 2010, Monthly Notices of the Royal Astronomical Society, 403, 780
- Ferr3-Mateu, A., Trujillo, I., Mart3n-Navarro, I., et al. 2017, Monthly Notices of the Royal Astronomical Society, 467, 1929
- Ferreras, I., Scott, N., La Barbera, F., et al. 2019, Monthly Notices of the Royal Astronomical Society, 489, 608
- Fitts, A., Boylan-Kolchin, M., Bullock, J. S., et al. 2018, MNRAS, 479, 319
- Forbes, D. A. & Bridges, T. 2010, Monthly Notices of the Royal Astronomical Society, 404, 1203
- Forbes, D. A., Brodie, J. P., & Huchra, J. 1996, arXiv preprint astro-ph/9612172
- Forbes, D. A., Pastorello, N., Romanowsky, A. J., et al. 2015, Monthly Notices of the Royal Astronomical Society, 452, 1045
- Forbes, D. A. & Remus, R.-S. 2018, Monthly Notices of the Royal Astronomical Society, 479, 4760
- Forbes, D. A., Spitler, L. R., Strader, J., et al. 2011, Monthly Notices of the Royal Astronomical Society, 413, 2943
- Franx, M. & Illingworth, G. D. 1988, The Astrophysical Journal, 327, L55
- Fukugita, M., Hogan, C., & Peebles, P. 1998, The Astrophysical Journal, 503, 518
- Furlong, M., Bower, R. G., Crain, R. A., et al. 2016, MNRAS, 465, 722
- Furlong, M., Bower, R. G., Theuns, T., et al. 2015, MNRAS, 450, 4486
- Gallazzi, A., Charlot, S., Brinchmann, J., White, S. D., & Tremonti, C. A. 2005, Monthly Notices of the Royal Astronomical Society, 362, 41
- Ge, J., Mao, S., Lu, Y., Cappellari, M., & Yan, R. 2019, *Mon. Not. Roy. Astron. Soc.*, 485,

- 1675
- Geldzahler, B. & Fomalont, E. 1984, *The Astrophysical Journal*, 89, 1650
- Genel, S., Vogelsberger, M., Springel, V., et al. 2014, *MNRAS*, 445, 175
- Genzel, R., Tacconi, L., Lutz, D., et al. 2015, *The Astrophysical Journal*, 800, 20
- Gingold, R. A. & Monaghan, J. J. 1977, *Monthly notices of the royal astronomical society*, 181, 375
- Goddard, D., Thomas, D., Maraston, C., et al. 2017, *Monthly Notices of the Royal Astronomical Society*, 466, 4731
- Greene, J. E., Janish, R., Ma, C.-P., et al. 2015, *The Astrophysical Journal*, 807, 11
- Greene, J. E., Murphy, J. D., Comerford, J. M., Gebhardt, K., & Adams, J. J. 2012, *Astrophys. J.*, 750, 32
- Greene, J. E., Murphy, J. D., Graves, G. J., et al. 2013, *The Astrophysical Journal*, 776, 64
- Greene, J. E., Veale, M., Ma, C.-P., et al. 2019, *The Astrophysical Journal*, 874, 66
- Gu, M., Conroy, C., Law, D., et al. 2018, *arXiv e-prints*, arXiv:1810.13242
- Guérou, A., Emsellem, E., Krajnović, D., et al. 2016, *Astron. Astrophys.*, 591, A143
- Gunn, J., Carr, M., Rockosi, C., et al. 1998, *The Astronomical Journal*, 116, 3040
- Gunn, J. E. & Gott, J. Richard, I. 1972, *Astrophys. J.*, 176, 1
- Guolo-Pereira, M., Ruschel-Dutra, D., Storchi-Bergmann, T., et al. 2021, *Monthly Notices of the Royal Astronomical Society*, 502, 3618
- Gupta, A., Tran, K.-V., Cohn, J., et al. 2020, *The Astrophysical Journal*, 893, 23
- Hawking, S. W. & Ellis, G. F. R. 1973, *The large scale structure of space-time*, Vol. 1 (Cambridge university press)
- Hill, G. J., MacQueen, P. J., Smith, M. P., et al. 2008, *Proceedings of the SPIE.*, 7014, 701470
- Ho, L. C., Li, Z.-Y., Barth, A. J., Seigar, M. S., & Peng, C. Y. 2011, *The Astrophysical Journal Supplement Series*, 197, 21
- Hood, C. E., Kannappan, S. J., Stark, D. V., et al. 2018, *Astrophys. J.*, 857, 144
- Hopkins, P. F., Kereš, D., Oñorbe, J., et al. 2014, *MNRAS*, 445, 581
- Horellou, C., Black, J., Van Gorkom, J., et al. 2001, *Astronomy & Astrophysics*, 376, 837
- Huang, S., Ho, L. C., Peng, C. Y., Li, Z.-Y., & Barth, A. J. 2013a, *The Astrophysical Journal*, 766, 47
- Huang, S., Ho, L. C., Peng, C. Y., Li, Z.-Y., & Barth, A. J. 2013b, *The Astrophysical Journal Letters*, 768, L28
- Huang, S., Leauthaud, A., Greene, J. E., et al. 2018, *Monthly Notices of the Royal Astronomical Society*, 475, 3348
- Hubble, E. 1926, *Contributions from the Mount Wilson Observatory/Carnegie Institution of Washington*, 324, 1
- Hubble, E. 1927, *The Observatory*, 50, 276
- Hung, C.-L., Hayward, C. C., Smith, H. A., et al. 2016, *The Astrophysical Journal*, 816, 99
- Husser, T.-O., Kamann, S., Dreizler, S., et al.

- 2016, *Astronomy & Astrophysics*, 588, A148
- Iyer, K. G., Tacchella, S., Genel, S., et al. 2020, *Monthly Notices of the Royal Astronomical Society*, 498, 430
- Jackson, T. M., Pasquali, A., La Barbera, F., More, S., & Grebel, E. K. 2021, arXiv preprint arXiv:2102.02241
- Jarrett, T., Chester, T., Cutri, R., Schneider, S., & Huchra, J. 2003, *The Astronomical Journal*, 125, 525
- Jennings, Z. G., Romanowsky, A. J., Brodie, J. P., et al. 2015, *Astrophys. J. Letters*, 812, L10
- Jiang, L., Helly, J. C., Cole, S., & Frenk, C. S. 2014, *Mon. Not. Roy. Astron. Soc.*, 440, 2115
- Johnson, B. D., Weisz, D. R., Dalcanton, J. J., et al. 2013, *The Astrophysical Journal*, 772, 8
- Kacharov, N., Neumayer, N., Seth, A. C., et al. 2018, *Mon. Not. Roy. Astron. Soc.*, 480, 1973
- Kado-Fong, E., Greene, J. E., Hendel, D., et al. 2018, *The Astrophysical Journal*, 866, 103
- Karademir, G. S., Remus, R.-S., Burkert, A., et al. 2019, *Monthly Notices of the Royal Astronomical Society*, 487, 318
- Keel, W. C. 1985, *Astron. J.*, 90, 2207
- Kennicutt Jr, R. C. 1998, *The Astrophysical Journal*, 498, 541
- Kirby, E. N., Cohen, J. G., Guhathakurta, P., et al. 2013, *The Astrophysical Journal*, 779, 102
- Kirshner, R. P., Oemler Jr, A., Schechter, P. L., & Smetman, S. A. 1981, *The Astrophysical Journal*, 248, L57
- Kluge, M., Neureiter, B., Riffeser, A., et al. 2020, *The Astrophysical Journal Supplement Series*, 247, 43
- Knebe, A., Knollmann, S. R., Muldrew, S. I., et al. 2011, *Monthly Notices of the Royal Astronomical Society*, 415, 2293
- Knowles, A. T., Sansom, A. E., Coelho, P., et al. 2019, *Monthly Notices of the Royal Astronomical Society*, 486, 1814
- Kobayashi, C. 2004, *Monthly Notices of the Royal Astronomical Society*, 347, 740
- Kormendy, J., Fisher, D. B., Cornell, M. E., & Bender, R. 2009, *The Astrophysical Journal Supplement Series*, 182, 216
- Krajinović, D., Cappellari, M., & McDermid, R. M. 2018, *Mon. Not. Roy. Astron. Soc.*, 473, 5237
- Kroupa, P. 2001, *Monthly Notices of the Royal Astronomical Society*, 322, 231
- Kroupa, P. 2002, *Science*, 295, 82
- Kruijssen, J. M. D., Pfeffer, J. L., Crain, R. A., & Bastian, N. 2019, *Mon. Not. Roy. Astron. Soc.*, 486, 3134
- Kruijssen, J. M. D., Pfeffer, J. L., Reina-Campos, M., Crain, R. A., & Bastian, N. 2018, *Monthly Notices of the Royal Astronomical Society*, 486, 3180
- La Barbera, F., Ferreras, I., de Carvalho, R. R., et al. 2012, *Mon. Not. Roy. Astron. Soc.*, 426, 2300
- Lacey, C. & Cole, S. 1993, *Monthly Notices of the Royal Astronomical Society*, 262, 627
- Lacey, C. & Cole, S. 1994, *Monthly Notices of*

- the Royal Astronomical Society, 271, 676
- Lackner, C. N., Cen, R., Ostriker, J. P., & Joung, M. R. 2012, *MNRAS*, 425, 641
- Lagos, C. d. P., Crain, R. A., Schaye, J., et al. 2015, *Mon. Not. Roy. Astron. Soc.*, 452, 3815
- Lagos, C. d. P., Schaye, J., Bahé, Y., et al. 2018, *Monthly Notices of the Royal Astronomical Society*, 476, 4327
- Laine, S., van der Marel, R. P., Lauer, T. R., et al. 2003, *The Astronomical Journal*, 125, 478
- Lange, R., Driver, S. P., Robotham, A. S. G., et al. 2015, *Mon. Not. Roy. Astron. Soc.*, 447, 2603
- Larsen, S. S., Brodie, J. P., Huchra, J. P., Forbes, D. A., & Grillmair, C. J. 2001, *The Astronomical Journal*, 121, 2974
- Lauberts, A. 1982, *ESO/Uppsala survey of the ESO(B) atlas*
- Law, D. R., Yan, R., Bershad, M. A., et al. 2015, *The Astronomical Journal*, 150, 19
- Layden, A. C. & Sarajedini, A. 2000, *The Astronomical Journal*, 119, 1760
- Leaman, R., VandenBerg, D. A., & Mendel, J. T. 2013a, *Monthly Notices of the Royal Astronomical Society*, 436, 122
- Leaman, R., Venn, K. A., Brooks, A. M., et al. 2013b, *The Astrophysical Journal*, 767, 131
- Leauthaud, A., George, M. R., Behroozi, P. S., et al. 2012, *The Astrophysical Journal*, 746, 95
- Lee, J. C., De Paz, A. G., Tremonti, C., et al. 2009, *The Astrophysical Journal*, 706, 599
- Leroy, A. K., Walter, F., Sandstrom, K., et al. 2013, *The Astronomical Journal*, 146, 19
- Lewis, A., Munshi, D., Adam, R., et al. 2016, *Astronomy and Astrophysics*, 596, A108
- Lewis, A. R., Dolphin, A. E., Dalcanton, J. J., et al. 2015, *The Astrophysical Journal*, 805, 183
- Li, H., Mao, S., Cappellari, M., et al. 2018, *Monthly Notices of the Royal Astronomical Society*, 476, 1765
- Li, Z. & Han, Z. 2008, *The Astrophysical Journal*, 685, 225
- Lofthouse, E., Kaviraj, S., Conselice, C. J., Mortlock, A., & Hartley, W. 2016, *Monthly Notices of the Royal Astronomical Society*, stw2895
- Lotz, J. M., Jonsson, P., Cox, T., et al. 2011, *The Astrophysical Journal*, 742, 103
- Lucy, L. B. 1977, *The astronomical journal*, 82, 1013
- Ludlow, A. D., Schaye, J., Schaller, M., & Richings, J. 2019, *MNRAS*, 488, L123
- L’Huillier, B., Combes, F., & Semelin, B. 2012, *Astronomy & Astrophysics*, 544, A68
- Ma, C.-P., Greene, J. E., McConnell, N., et al. 2014, *The Astrophysical Journal*, 795, 158
- Machacek, M., Dosaj, A., Forman, W., et al. 2005, *The Astrophysical Journal*, 621, 663
- Mackereth, J. T., Schiavon, R. P., Pfeffer, J., et al. 2019, *Monthly Notices of the Royal Astronomical Society*, 482, 3426
- Mackey, A. D., Ferguson, A. M. N., Huxor, A. P., et al. 2019, *Monthly Notices of the*

- Royal Astronomical Society, 484, 1756
- Mackie, G. & Fabbiano, G. 1998, *The Astrophysical Journal*, 115, 514
- Madau, P. & Dickinson, M. 2014, *Annual Review of Astronomy and Astrophysics*, 52, 415
- Mahdavi, A., Trentham, N., & Tully, R. B. 2005, *The Astrophysical Journal*, 130, 1502
- Makino, J. & Hut, P. 1997, *Astrophys. J.*, 481, 83
- Malhan, K., Ibata, R. A., & Martin, N. F. 2018, *Monthly Notices of the Royal Astronomical Society*, 481, 3442
- Malin, D. & Carter, D. 1983, *The Astrophysical Journal*, 274, 534
- Maller, A. H., Katz, N., Kereš, D., Davé, R., & Weinberg, D. H. 2006, *The Astrophysical Journal*, 647, 763
- Mancillas, B., Duc, P.-A., Combes, F., et al. 2019, *Astronomy & Astrophysics*, 632, A122
- Maraston, C. 2005, *Mon. Not. Roy. Astron. Soc.*, 362, 799
- Marigo, P., Girardi, L., Bressan, A., et al. 2008, *Astronomy & Astrophysics*, 482, 883
- Marinacci, F. & Vogelsberger, M. 2015, *Monthly Notices of the Royal Astronomical Society: Letters*, 456, L69
- Marino, A., Rampazzo, R., Bianchi, L., et al. 2011, *Monthly Notices of the Royal Astronomical Society*, 411, 311
- Martin, G., Kaviraj, S., Devriendt, J. E. G., Dubois, Y., & Pichon, C. 2018, *Mon. Not. Roy. Astron. Soc.*, 480, 2266
- Martinez-Delgado, D., Cooper, A. P., Roman, J., et al. 2021, arXiv preprint arXiv:2104.06071
- Martínez-Delgado, D., Peñarrubia, J., Gabany, R. J., et al. 2008, *Astrophys. J.*, 689, 184
- Martins, L. P., Lima-Dias, C., Coelho, P. R., & Laganá, T. F. 2019, *Monthly Notices of the Royal Astronomical Society*, 484, 2388
- Massari, D., Koppelman, H. H., & Helmi, A. 2019, *Astronomy & Astrophysics*, 630, L4
- McAlpine, S., Helly, J. C., Schaller, M., et al. 2016, *Astronomy and Computing*, 15, 72
- McGaugh, S. S. & Schombert, J. M. 2014, *Astron. J.*, 148, 77
- Mentz, J. J., La Barbera, F., Peletier, R. F., et al. 2016, *Mon. Not. Roy. Astron. Soc.*, 463, 2819
- Mihos, C. & Hernquist, L. 1995, arXiv preprint astro-ph/9512099
- Moffat, A. 1969, *Astronomy and Astrophysics*, 3, 455
- Monachesi, A., Gómez, F. A., Grand, R. J. J., et al. 2019, *Mon. Not. Roy. Astron. Soc.*, 485, 2589
- Monreal-Ibero, A., Arribas, S., Colina, L., et al. 2010, *Astronomy & Astrophysics*, 517, A28
- Moore, B., Katz, N., Lake, G., Dressler, A., & Oemler, A. 1996, *Nature*, 379, 613
- Morales, G., Martínez-Delgado, D., Grebel, E. K., et al. 2018, *Astronomy & Astrophysics*, 614, A143
- Moreno, J., Torrey, P., Ellison, S. L., et al. 2015, *Monthly Notices of the Royal Astronomical*

- Society, 448, 1107
- Morton, T. D. 2015, *Astrophysics Source Code Library*, ascl
- Naab, T., Johansson, P. H., & Ostriker, J. P. 2009, *The Astrophysical Journal Letters*, 699, L178
- Navarro-González, J., Ricciardelli, E., Quilis, V., & Vazdekis, A. 2013, *Mon. Not. Roy. Astron. Soc.*, 436, 3507
- Nelson, D., Pillepich, A., Genel, S., et al. 2015, *Astronomy and Computing*, 13, 12
- Nelson, D., Pillepich, A., Springel, V., et al. 2019, *Monthly Notices of the Royal Astronomical Society*, 490, 3234
- Nevin, R., Blecha, L., Comerford, J., et al. 2021, arXiv preprint arXiv:2102.02208
- Norris, M. A., Escudero, C. G., Faifer, F. R., et al. 2015, *Mon. Not. Roy. Astron. Soc.*, 451, 3615
- Norris, M. A., Sharples, R. M., & Kuntschner, H. 2006, *Mon. Not. Roy. Astron. Soc.*, 367, 815
- Norris, M. A., Van de Ven, G., Schinnerer, E., et al. 2016, *Astrophys. J.*, 832, 198
- Ocvirk, P., Pichon, C., Lançon, A., & Thiébaud, E. 2006, *Monthly Notices of the Royal Astronomical Society*, 365, 74
- Onodera, M., Renzini, A., Carollo, M., et al. 2012, *Astrophys. J.*, 755, 26
- Oser, L., Ostriker, J. P., Naab, T., Johansson, P. H., & Burkert, A. 2010, *Astrophys. J.*, 725, 2312
- Oyarzún, G. A., Bundy, K., Westfall, K. B., et al. 2019, *The Astrophysical Journal*, 880, 111
- Padoan, P. & Nordlund, Å. 2002, *The Astrophysical Journal*, 576, 870
- Park, S., Sohn, B. W., & Sukyoung, K. Y. 2013, *Astronomy & Astrophysics*, 560, A80
- Pelliccia, D., Lemaux, B. C., Tomczak, A. R., et al. 2019, *Monthly Notices of the Royal Astronomical Society*, 482, 3514
- Peng, E. W., Jordán, A., Côté, P., et al. 2006, *The Astrophysical Journal*, 639, 95
- Percival, S. M., Salaris, M., Cassisi, S., & Pietrinferni, A. 2009, *Astrophys. J.*, 690, 427
- Pérez, E., Fernandes, R. C., Delgado, R. G., et al. 2013, *The Astrophysical Journal Letters*, 764, L1
- Pietrinferni, A., Cassisi, S., Salaris, M., & Castelli, F. 2004, *Astrophys. J.*, 612, 168
- Pietrinferni, A., Cassisi, S., Salaris, M., & Castelli, F. 2006, *The Astrophysical Journal*, 642, 797
- Pietrinferni, A., Cassisi, S., Salaris, M., Percival, S., & Ferguson, J. W. 2009, *Astrophys. J.*, 697, 275
- Pillepich, A., Madau, P., & Mayer, L. 2015, *The Astrophysical Journal*, 799, 184
- Pillepich, A., Nelson, D., Hernquist, L., et al. 2018, *Monthly Notices of the Royal Astronomical Society*, 475, 648
- Pinna, F., Falcón-Barroso, J., Martig, M., et al. 2019, *A&A*, 623, A19
- Poci, A., McDermid, R. M., Zhu, L., & van de Ven, G. 2019, *Mon. Not. Roy. Astron. Soc.*,

- 487, 3776
- Pont, F. & Eyer, L. 2004, *Monthly Notices of the Royal Astronomical Society*, 351, 487
- Pota, V., Brodie, J. P., Bridges, T., et al. 2015, *Mon. Not. Roy. Astron. Soc.*, 450, 1962
- Prichard, L. J., Vaughan, S. P., & Davies, R. L. 2019, *Monthly Notices of the Royal Astronomical Society*, 488, 1679
- Puglisi, A., Daddi, E., Brusa, M., et al. 2021, *Nature Astronomy*
- Pulsoni, C., Gerhard, O., Arnaboldi, M., et al. 2020, *Astronomy & Astrophysics*, 641, A60
- Qu, Y., Helly, J. C., Bower, R. G., et al. 2017, *Monthly Notices of the Royal Astronomical Society*, 464, 1659
- Querejeta, M., Eliche-Moral, M. d. C., Tapia, T., et al. 2015, *Astronomy & Astrophysics*, 579, L2
- Quilis, V. & Trujillo, I. 2013, *The Astrophysical Journal Letters*, 773, L8
- Ragone-Figueroa, C., Granato, G. L., Murante, G., Borgani, S., & Cui, W. 2013, *Monthly Notices of the Royal Astronomical Society*, 436, 1750
- Rampazzo, R., Marino, A., Tantalò, R., et al. 2007, *Monthly Notices of the Royal Astronomical Society*, 381, 245
- Rampazzo, R., Omizzolo, A., Uslenghi, M., et al. 2020, *Astronomy & Astrophysics*, 640, A38
- Rampazzo, R., Plana, H., Longhetti, M., et al. 2003, *Mon. Not. Roy. Astron. Soc.*, 343, 819
- Rejkuba, M., Harris, W., Greggio, L., et al. 2014, *The Astrophysical Journal Letters*, 791, L2
- Remus, R.-S. & Forbes, D. A. 2021, arXiv preprint arXiv:2101.12216
- Rich, J. A., Kewley, L. J., & Dopita, M. A. 2011, *The Astrophysical Journal*, 734, 87
- Rodriguez-Gomez, V., Pillepich, A., Sales, L. V., et al. 2016, *Monthly Notices of the Royal Astronomical Society*, 458, 2371
- Romanowsky, A. J., Strader, J., Brodie, J. P., et al. 2012, *Astrophys. J.*, 748, 29
- Rood, H. 1988, *Annual review of astronomy and astrophysics*, 26, 245
- Rood, H. J. 1987, *Publications of the Astronomical Society of the Pacific*, 99, 921
- Rosito, M. S., Tissera, P., Pedrosa, S., & Lagos, C. D. 2019, *Astronomy & Astrophysics*, 629, L3
- Rubin, V. C. 1994, *The Astronomical Journal*, 108, 456
- Ruiz-Lara, T., Beasley, M. A., Falcón-Barroso, J., et al. 2018, *Mon. Not. Roy. Astron. Soc.*, 478, 2034
- Salaris, M., Cassisi, S., Pietrinferni, A., Kowalski, P. M., & Isern, J. 2010, *Astrophys. J.*, 716, 1241
- Sales, L. V., Navarro, J. F., Schaye, J., et al. 2010, *Mon. Not. Roy. Astron. Soc.*, 409, 1541
- Sales, L. V., Navarro, J. F., Theuns, T., et al. 2012, *Monthly Notices of the Royal Astronomical Society*, 423, 1544
- Salpeter, E. E. 1955, *The Astrophysical Journal*, 121, 161
- Samir, R., Reda, F., Shaker, A., Osman, A., &

- Amin, M. 2016, *NRIAG Journal of Astronomy and Geophysics*, 5, 277
- Santucci, G., Brough, S., Scott, N., et al. 2020, *The Astrophysical Journal*, 896, 75
- Saracco, P., Longhetti, M., & Andreon, S. 2009, *Monthly Notices of the Royal Astronomical Society*, 392, 718
- Sarzi, M., Iodice, E., Coccato, L., et al. 2018, *A&A*, 616, A121
- Saulder, C., van den Bosch, R. C., & Mieske, S. 2015, *Astronomy & Astrophysics*, 578, A134
- Scalo, J. M. 1986, *Fundamentals of cosmic physics*, 11, 1
- Schawinski, K., Dowlin, N., Thomas, D., Urry, C. M., & Edmondson, E. 2010, *The Astrophysical Journal Letters*, 714, L108
- Schawinski, K., Urry, C. M., Simmons, B. D., et al. 2014, *Monthly Notices of the Royal Astronomical Society*, 440, 889
- Schaye, J., Crain, R. A., Bower, R. G., et al. 2015, *Monthly Notices of the Royal Astronomical Society*, 446, 521
- Schaye, J., Crain, R. A., Bower, R. G., et al. 2015, *Mon. Not. Roy. Astron. Soc.*, 446, 521
- Schiavon, R. P., Barbuy, B., Rossi, S. C., & Milone, A. 1997, *The Astrophysical Journal*, 479, 902
- Schlafly, E. F. & Finkbeiner, D. P. 2011, *The Astrophysical Journal*, 737, 103
- Schweizer, F. 1980, *The Astrophysical Journal*, 237, 303
- Schweizer, F. 1981, *The Astrophysical Journal*, 246, 722
- Scott, N., Brough, S., Croom, S. M., et al. 2017, *Monthly Notices of the Royal Astronomical Society*, 472, 2833
- Seigar, M. S., Graham, A. W., & Jerjen, H. 2007, *Monthly Notices of the Royal Astronomical Society*, 378, 1575
- Serra, P., Maccagni, F., Kleiner, D., et al. 2019, *Astronomy & Astrophysics*, 628, A122
- Sersic, J. L. 1968, Cordoba
- Shankar, F., Buchan, S., Rettura, A., et al. 2015, *The Astrophysical Journal*, 802, 73
- Shanks, T., Metcalfe, N., Chehade, B., et al. 2015, *Monthly Notices of the Royal Astronomical Society*, 451, 4238
- Shaviv, G. & Salpeter, E. E. 1973, *The Astrophysical Journal*, 184, 191
- Sheardown, A., Roediger, E., Su, Y., et al. 2018, *The Astrophysical Journal*, 865, 118
- Shen, S., Mo, H. J., White, S. D. M., et al. 2003, *Mon. Not. Roy. Astron. Soc.*, 343, 978
- Shipp, N., Drlica-Wagner, A., Balbinot, E., et al. 2018, *The Astrophysical Journal*, 862, 114
- Simons, R. C., Papovich, C., Momcheva, I., et al. 2020, arXiv e-prints, arXiv:2011.03553
- Sinha, M. & Holley-Bockelmann, K. 2012, *The Astrophysical Journal*, 751, 17
- Skrutskie, M., Cutri, R., Stiening, R., et al. 2006, *The Astronomical Journal*, 131, 1163
- Smith, R. J. 2014, *Monthly Notices of the Royal Astronomical Society: Letters*, 443, L69
- Smith, R. J. 2020a, *Monthly Notices of the Royal Astronomical Society: Letters*, 494, L1

- Smith, R. J. 2020b, *Annual Review of Astronomy and Astrophysics*
- Smith, R. J., Alton, P., Lucey, J. R., Conroy, C., & Carter, D. 2015, *Monthly Notices of the Royal Astronomical Society: Letters*, 454, L71
- Smith, R. J., Lucey, J. R., & Carter, D. 2012, *Monthly Notices of the Royal Astronomical Society*, 426, 2994
- Solomon, P. & Barrett, J. 1991, in *Symposium-International Astronomical Union, Vol. 146*, Cambridge University Press, 235–241
- Spada, F., Demarque, P., Kim, Y.-C., Boyajian, T., & Brewer, J. 2017, *The Astrophysical Journal*, 838, 161
- Sparks, W., Macchetto, F., & Golombek, D. 1989, *The Astrophysical Journal*, 345, 153
- Spavone, M., Capaccioli, M., Napolitano, N. R., et al. 2017, *Astronomy & Astrophysics*, 603, A38
- Spavone, M., Krajnović, D., Emsellem, E., Iodice, E., & den Brok, M. 2021, On the assembly history of massive galaxies. A pilot project with VEGAS deep imaging and M3G integral field spectroscopy
- Spolaor, M., Hau, G. K., Forbes, D. A., & Couch, W. J. 2010, *Monthly Notices of the Royal Astronomical Society*, 408, 254
- Spolaor, M., Proctor, R. N., Forbes, D. A., & Couch, W. J. 2009, *The Astrophysical Journal Letters*, 691, L138
- Springel, V. 2005, *Monthly notices of the royal astronomical society*, 364, 1105
- Tacchella, S., Diemer, B., Hernquist, L., et al. 2019, *Monthly Notices of the Royal Astronomical Society*, 487, 5416
- Tacconi, L., Neri, R., Genzel, R., et al. 2013, *The Astrophysical Journal*, 768, 74
- Taylor, P. & Kobayashi, C. 2017, *Monthly Notices of the Royal Astronomical Society*, 471, 3856
- Thilker, D. A., Bianchi, L., Schiminovich, D., et al. 2010, *The Astrophysical Journal Letters*, 714, L171
- Thob, A. C. R., Crain, R. A., McCarthy, I. G., et al. 2019, *Mon. Not. Roy. Astron. Soc.*, 485, 972
- Thomas, D., Maraston, C., & Bender, R. 2003, *Monthly Notices of the Royal Astronomical Society*, 339, 897
- Tojeiro, R., Heavens, A. F., Jimenez, R., & Panter, B. 2007, *Mon. Not. Roy. Astron. Soc.*, 381, 1252
- Trayford, J. W., Theuns, T., Bower, R. G., et al. 2015, *Mon. Not. Roy. Astron. Soc.*, 452, 2879
- Trinchieri, G. & Goudfrooij, P. 2002, *Astronomy & Astrophysics*, 386, 472
- Trujillo, I., Ferré-Mateu, A., Balcells, M., Vazdekis, A., & Sánchez-Blázquez, P. 2013, *The Astrophysical Journal Letters*, 780, L20
- Trujillo, I. & Pohlen, M. 2005, *The Astrophysical Journal*, 630, L17
- Tully, R. B. & Fisher, J. R. 1988, *Nearby galaxies catalog* (Cambridge University Press)
- Twarog, B. A. 1980, *The Astrophysical Journal*, 242, 242

- Ueda, J., Iono, D., Yun, M. S., et al. 2014, *The Astrophysical Journal Supplement Series*, 214, 1
- Van Der Burg, R. F., Hoekstra, H., Muzzin, A., et al. 2015, *Astronomy & Astrophysics*, 577, A19
- van der Wel, A., Franx, M., van Dokkum, P. G., et al. 2014, *Astrophys. J.*, 788, 28
- Van Dokkum, P., Quadri, R., Marchesini, D., et al. 2006, *The Astrophysical Journal Letters*, 638, L59
- Van Dokkum, P. G., Abraham, R., & Merritt, A. 2014, *The Astrophysical Journal Letters*, 782, L24
- van Dokkum, P. G., Bezanson, R., van der Wel, A., et al. 2014, *Astrophys. J.*, 791, 45
- Van Dokkum, P. G., Franx, M., Kriek, M., et al. 2008, *The Astrophysical Journal Letters*, 677, L5
- Vaughan, S. P., Davies, R. L., Zieleniewski, S., & Houghton, R. C. 2018, *Monthly Notices of the Royal Astronomical Society*, 479, 2443
- Vazdekis, A., Ricciardelli, E., Cenarro, A., et al. 2012, *Monthly Notices of the Royal Astronomical Society*, 424, 157
- Vazdekis, A., Sánchez-Blázquez, P., Falcón-Barroso, J., et al. 2010, *Monthly Notices of the Royal Astronomical Society*, 404, 1639
- Ventou, E., Contini, T., Bouché, N., et al. 2017, *Astronomy & Astrophysics*, 608, A9
- Villaume, A., Romanowsky, A. J., Brodie, J., & Strader, J. 2019, *The Astrophysical Journal*, 879, 45
- Vogelsberger, M., Genel, S., Springel, V., et al. 2014, *Nature*, 509, 177
- Vogelsberger, M., Genel, S., Springel, V., et al. 2014, *Mon. Not. Roy. Astron. Soc.*, 444, 1518
- Vorontsov-Vel'Yaminov, B. A. & Arkhipova, V. P. 1974, *Trudy Gosudarstvennogo Astronomicheskogo Instituta*, 46, 1
- Weilbacher, P. M., Palsa, R., Streicher, O., et al. 2020, *Astron. Astrophys.*, 641, A28
- Wellons, S., Torrey, P., Ma, C.-P., et al. 2016, *Monthly Notices of the Royal Astronomical Society*, 456, 1030
- Westmeier, T., Braun, R., & Koribalski, B. 2011, *Monthly Notices of the Royal Astronomical Society*, 410, 2217
- Wilkinson, D. M., Maraston, C., Goddard, D., Thomas, D., & Parikh, T. 2017, *Monthly Notices of the Royal Astronomical Society*, 472, 4297
- Wu, Y., Xiang, M., Chen, Y., et al. 2021, *Monthly Notices of the Royal Astronomical Society*, 501, 4917
- Yoon, S.-J., Yi, S. K., & Lee, Y.-W. 2006, *Science*, 311, 1129
- York, D. G., Adelman, J., Anderson Jr, J. E., et al. 2000, *The Astronomical Journal*, 120, 1579
- Zahid, H. J., Sohn, J., & Geller, M. J. 2018, *The Astrophysical Journal*, 859, 96
- Zaw, I., Farrar, G. R., & Greene, J. E. 2009, *The Astrophysical Journal*, 696, 1218
- Zheng, Z., Wang, H., Ge, J., et al. 2017, *Monthly Notices of the Royal Astronomical Society*,

465, 4572

Zhu, L., Romanowsky, A. J., van de Ven, G.,
et al. 2016, *Monthly Notices of the Royal Astro-*
nomical Society, 462, 4001

Zhuang, Y., Leaman, R., van de Ven, G., et al.
2019, *Monthly Notices of the Royal Astro-*
nomical Society, 483, 1862

Zinn, R. 1985, *The Astrophysical Journal*, 293,
424

Zolotov, A., Dekel, A., Mandelker, N., et al.
2015, *Monthly Notices of the Royal Astro-*
nomical Society, 450, 2327

Zolotov, A., Willman, B., Brooks, A. M., et al.
2009, *Astrophys. J.*, 702, 1058